

WASHINGTON UNIVERSITY
THE HENRY EDWIN SEVER GRADUATE SCHOOL
DEPARTMENT OF COMPUTER SCIENCE AND ENGINEERING

UNDERSTANDING THE HYDRODYNAMICS AND PERFORMANCE OF
ANAEROBIC DIGESTERS

by

Mehul S. Vesvikar

Prepared under the direction of Professor Muthanna H. Al-Dahhan

A dissertation presented to the Henry Edwin Sever Graduate School of
Washington University in partial fulfillment of the
requirements for the degree of
DOCTOR OF SCIENCE

August 2006

Saint Louis, Missouri

WASHINGTON UNIVERSITY
THE HENRY EDWIN SERVER GRADUATE SCHOOL
DEPARTMENT OF CHEMICAL ENGINEERING

ABSTRACT

UNDERSTANDING THE HYDRODYNAMICS AND PERFORMANCE OF
ANAEROBIC DIGESTERS

by

Mehul S. Vesvikar

ADVISOR: Professor Muthanna H. Al-Dahhan

August 2006

St. Louis, Missouri

Anaerobic digestion is an efficient way of treating animal wastes and biomass byproducts to reduce its pollution threat and obtain energy in the form of methane. The high failure rate of anaerobic digesters coupled with the lack of fundamental research prohibits the widespread use of anaerobic digestion. Assessing the role of mixing in performance of anaerobic digesters and its influence on digester design, scale and operation via experimental and modeling studies is the focus of this work. The energy consumption and ease of operation criteria led to the selection of gaslift digester mixed by gas recirculation. Performance studies in laboratory and pilot-scale digesters treating cow manure show that large-scale experimentation is required to obtain reliable information for design and scale-up of digesters. For the first time, Computer automated radioactive particle tracking (CARPT) and Computational Fluid Dynamics (CFD) are used to study the effects of operating variables, designs, internals, and scales on the mixing pattern and hydrodynamics of the anaerobic digesters. The comparison of dead zone volumes, circulation times and eddy diffusivities obtained from CARPT and CFD show that gaslift digester with draft tube diameter half of the reactor diameter and multiple point sparger provides better mixing than other digester configurations. CARPT and CFD data complemented the performance studies and conclude that the geometric similarity and equal power input per unit volume is not sufficient to obtain the same digester performance at two different scales. Further, successful development and implementation of multiple-particle tracking (MP-CARPT) in this work will overcome the limitations of single-particle CARPT in future research on dense multiphase systems including anaerobic digesters. The knowledge gained from this dissertation will be useful for further investigations that can lead to efficient operation of anaerobic digesters by the potential end users.

*Dedicated to
my dear Aae (Mom) and Baba (Dad)*

Contents

List of Tables	vi
List of Figures	vii
Acknowledgements.....	viii
Preface	ix
1 Thesis Format	1
1.1 Margins.....	1
1.2 Page Numbers.....	1
1.3 Body Text	2
1.4 Titles and Headings.....	2
1.4.1 Chapter Titles	2
1.4.2 Section Headings.....	3
1.4.3 Subsection Headings	3
1.4.4 Headings for Divisions Smaller than Subsections	3
1.5 Figures and Tables.....	4
1.6 Lists	4
1.7 Footnotes and Endnotes	5
1.8 Quotations.....	5
1.9 Equations.....	5
2 Parts of the Thesis	7
2.1 Front Matter.....	7
2.1.1 Title Page.....	7
2.1.2 Abstract Page.....	8
2.1.3 Copyright Page.....	8
2.1.4 Dedication.....	9
2.1.5 Table of Contents	9
2.1.6 List of Tables.....	9
2.1.7 List of Figures.....	10
2.1.8 List of Abbreviations.....	10
2.1.9 Glossary or Nomenclature	10
2.1.10 Acknowledgements.....	10
2.1.11 Preface	11
2.2 Text	11
2.3 Back Matter	11
2.3.1 Appendices.....	11
2.3.2 References	12
2.3.3 Vita.....	12

2.3.4	Short Title Page.....	12
3	Citing References.....	13
3.1	Paranthetical References.....	13
3.1.1	Author-Date System.....	13
3.1.2	Numbered Referneces.....	14
3.2	Reference List	14
Appendix A	The English Language and Other Confusing Things	15
Appendix B	Procedures and Deadlines	16
Appendix C	Thesis Format Checklist.....	18
Appendix D	Special Notes for MS WORD Users	19
References	22
Vita	23

List of Tables

Table 1.1: Thesis Formatting Options	6
Table 2.1: Required and Optional Thesis Components.....	8

List of Figures

Figure1.1 Just a Figure.....**Error! Bookmark not defined.**

Nomenclature

a	Constant	-
A	Cross sectional area	m^2
D	Draft tube diameter	m
d	Distance	m
d	Diameter of bubble	m
f	Function	-
g	Acceleration due to gravity	m/s^2
g	Gravity vector	m/s^2
H	Liquid level in the reactor	m
h	Draft tube height	m
h	Specific static enthalpy	J/kg
K	Constant	-
k	Kinetic energy	$dynes/cm^2$
k	Turbulent kinetic energy	m^2/s^2
M	Interfacial force term	N/m^3
N	Number	-
N _p	Number of phases	-
P	Pressure	N/m^2
p	Static pressure	N/m^2
p _{ref}	Reference pressure	N/m^2
p _{tot}	Total Pressure	N/m^2
Q	Volumetric flow rate	m^3/s
r _α	Volume fraction of phase α	-
R ₀	Universal gas constant	$l.atm/kmol.°K$
S _M	Momentum source	N/m^3
S _{MS}	Mass source	$kg/m^3 s$
T	Tank/ reactor diameter	m
t	Time	<i>Sec</i>
t	Time	<i>s</i>
T	Temperature	$°K$
U	Superficial velocity	m/s
U	Velocity	m/s
u	Fluctuating velocity component in turbulent flow	m/s
u'	Fluctuating velocity	m/s
V	Volume	m^3
w	Molecular weight	$kg/kmol$

Greek symbols

ρ	Density	Kg/m^3
ε	Holdup	-

Subscripts/ Superscripts

θ	Azimuthal
avg	Average
b	Bottom
c	Circulation
ct	Circulation time
d	Downcomer
g	Gas
G	Gas
int	Interval
L	Liquid
max	Maximum
min	Minimum
r	Riser/radial
S	Solid
z	Axial

Acronyms

AD	Anaerobic digestion
ADrs	Anaerobic digesters
ALR	Airlift loop reactor
BOD	Biological oxygen demand
CARPT	Computer automated radioactive particle tracking
CFD	Computational fluid dynamics
Co-60	Cobalt with mass number 60 (radioactive)
COD	Chemical oxygen demand
CT	Computed tomography
CTD	Circulation time distribution
CTDF	Circulation time distribution function
EALR	External airlift loop reactor
GC	Gas chromatography
HRT	Hydraulic retention time

IALR	Internal airlift loop reactor
LS	Laboratory-scale
MP-CARPT	Multiple particle CARPT
NIM	Nuclear instrument modules
ORNL	Oak Ridge National Laboratory
PCI	Peripheral component interconnect
PMT	Photo multiplier tube
PS	Pilot-scale
SBCR	Slurry bubble column reactor
Sc-46	Scandium with mass number 46 (radioactive)
TFA	Timing filter amplifier
TS	Total solids
TVS	Total volatile solids
VFA	Volatile fatty acids

Acknowledgements

Five years of graduate life felt like five decades at one point, but now that it's over, they seem shorter than a moment. Long or short, stressful or joyous, tedious or enlightening, depressing or motivating, these years will always be remembered. I am thankful to everyone and everything that accompanied me in my journey towards the doctorate.

My advisor, Prof. Muthanna Al-Dahhan, deserves first acknowledgement for the support, advice, help, and enthusiasm that he showered on me. He introduced me to the world of multi-tasking and made me an inhabitant there. I thank him with a deep sense of gratitude for showing me the path towards my destination.

I also want to take this opportunity to thank Prof. Milorad Dudukovic and Prof. P. A. Ramachandran for their guidance and help throughout my studies and also for being on my defense committee. I also want to thank my other committee members, Dr. Largus Angenent, Dr. Daniel Giammar, and Dr. David Depaoli for investing their precious time to read my thesis and offering their thoughtful comments and suggestions.

I wish to acknowledge the DOE for its financial support and ANSYS for providing the CFX software. I also wish to thank the whole Oak Ridge National Laboratory group, including Dr. Alan Wintenber, Dr. Abhijeet Borole, Dr. Chuck Alexander, Dr. Thomas Klasson, Dr. David Depaoli, and others for their contribution towards the development of the new MP-CARPT and for conducting digester experimental runs. I am thankful to Dr. Khursheed Karim, who provided lot of help and guidance during the initial and intermediate stages of this project. I wish to thank Ryan Mackin and Rebecca Hoffmann for helping me with the experimental work.

This journey would not have been the same without my fellow passengers, the CREL students and scholars. Although it is not possible to mention every name, a few need special recognition. Debangshu has always been there to brainstorm with me and offer very much needed criticism, as well as meaningless but stress-relieving chit-chat. Rajneesh, Satish, Huping, and Ashfaq always offered their help in spite of their busy schedules. My other friends Saurabh, Mao, RC, Vidya, Rahul, Radmila, Lu Han and many others have made a great contribution by their encouraging presence and delightful company.

I cannot thank enough the department secretaries, Rose, Mindy, Jean, Ruth and Angela, for their timely help, always offered with a big smile and warm greetings. I wish to thank Steve Picker, Jim Linders, and Pat Harkins for their help with the fabrication, design and the setup of the experiments. I also wish to thank Prof. Jim Ballard from the Technical Writing Center for providing me with help and guidance on writing. I cannot forget my TA experience and all my students, who always made me feel like a student myself, and helped me enjoy the teaching process while I was learning with them. Three of them, Amy, Kristin and Rebecca will always be the “Charmed” (or the charming) ones.

This acknowledgement would be incomplete without the mention of the friends who were there for me at every turn to guide me and to hold me at every ups and downs of this journey. Without their support, encouragement, love or sheer presence, this would have never been possible. My roommates and dearest friends, Swapnil and Mukund; my loving friends, Shilpi, Sukanya and Tanika; my buddies Samir, Anand and Abhishek; my American friends, Angie and Ed; the “old is gold” ones, Sanket, Nandu, Medha, Subodh, Sagar, Vivek, and Sreepriya; the best one, Rahul Mahajan; my soulmate, Sarita; my mentor, Prof. J.B. Joshi; the only one, Sharada Vahini; all my neighbors and friends from India, my grandma, aunts and uncles, cousins, nephews

and nieces, and innumerable others share a special place in my heart, my life and my accomplishments.

There are no words to express my feeling towards my family - Deepa, Dada, Tai, Aaee and Baba. Their selfless love and unshaken trust in me has brought me this and every other success in my life. My dear sister has been a constant source of inspiration to face obstacles bravely, with a smile. My father sacrificed everything he had to provide me with anything I wanted with the only expectation of seeing me successful. Every time I see my mom, my faith becomes stronger in the saying "God could not be everywhere, so he created mother." I owe everything I am and I will be to my mother. Thanking my family would be disrespectful, so I ask for their blessings.

Finally, I bow down in front of Him and pray that He gives the peace, love, knowledge, joy and fulfillment to everyone that he has bestowed upon me.

वक्रतुन्द महाकाय सूर्यकोटिसमप्रभ ।

निर्विघ्नं कुरु मे देव सर्वकार्येषु सर्वदा ॥

Vakratunda Mahakaaya Suryakoti Samaprabha |

Nirvighnam Kuru Mey Deva Sarva Kaaryeshu Sarvada ||

Meaning: The Lord Ganesh, with the curved trunk and a mighty body, who has the luster of a million suns. I pray to thee Oh Lord, to remove the obstacles from all the actions I intend to perform.

Mehul S. Vesvikar

Washington University in St. Louis

May 2006

Chapter 1

Introduction

1.1 Introduction and Motivation

The growth and concentration of the livestock industries provide a large source of affordable and renewable energy also requiring safe disposal of the large quantities of animal waste (manure) generated at dairy, swine, and poultry farms. According to 1997 census, in the United States itself over 900 million tons of such waste is produced every year (USDA, 2003). Unsafe and improper disposal of decomposable animal waste causes major environmental pollution problems, including surface and groundwater contamination, odors, dust, and ammonia leaching. There is also threat from methane emissions, which contribute to the greenhouse effect. The increasing growth of animal industries has resulted in the formulation of new laws and regulations governing safe handling and disposal of animal waste. A survey of dairy and swine farms in the country reaffirmed that Anaerobic Digestion (AD) is a technology with considerable potential. Ignoring caged layer poultry, about 426 metric tons of methane is potentially recoverable from 3,000 dairy and swine farms in 19 states of the United States (Lusk, 1998).

Over the past 25 years, AD processes have been developed and applied to a wide array of industrial and agricultural wastes to reduce pollution and recover methane (Speece, 1996; Ghosh, 1997). AD is a process of conversion of biomass to biogas, a mixture of methane and carbon dioxide, involving several biological steps occurring slowly (Parkin

and Owen, 1986), more details are given in Chapter 2. Byproduct of AD is a semisolid residue which can be used as a fertilizer.

AD has been implemented on only a small percentage of farms in the United States. One of the important reasons for this is the high rate of failure of farm based digesters, (Lusk, 1998). These high failure rates can be attributed mostly to poor design (Lusk, 1998) and absence of a well acclimated microbial community (Angenent et al., 2002).

The performance of ADrs is affected primarily by the retention time of digestible slurry (substrate) in the digester and the degree of contact between incoming substrate and a viable bacterial population. These parameters are functions of the hydraulic regime (mixing) in the reactors. Mixing in the digester is required to distribute organisms, substrate, and nutrients uniformly, to transfer heat, and to maintain uniform pH. Thus, mixing is regarded as essential in ADrs (Meynell, 1976; Sawyer and Grumbling, 1960). Furthermore, mixing aids in particle size reduction as digestion progresses and in the removal of gas from the mixture. Mixing is also required to prevent stratification and scum formation. In short, adequate mixing provides a uniform environment, one of the keys to good digestion (Parkin and Owen, 1986).

The effects of mixing on the AD process are not well understood and the information available is contradictory. This discrepancy and contradiction regarding the role of mixing in ADr performance needs to be resolved through carefully planned experimentation. Karim et al. (2005a and 2005b) concluded from a series of their extensive laboratory-scale performance experiments that pilot-scale experiments are required to reach unambiguous conclusions. Mixing can be accomplished by a variety of mechanical mixers, by recirculation of the digester contents, or by recirculation of the produced biogas using recirculation pumps. Gas-mixed digesters are easy to operate and require comparatively less energy for mixing (Casey, 1986; Kondandt and Roediger, 1977; Lee et al., 1995; Morgan and Neuspiel, 1958). Therefore, by comparing the

performance of identically operated gas-mixed ADRs in both mixed and unmixed modes, the true effect of mixing was evaluated (Appendix A).

The performance of an ADR is affected by mixing at larger scales of operation, thus the knowledge of the hydrodynamics is important in the design and scale-up of such ADRs. The hydrodynamics are in turn affected by the geometry and the physical properties of the system, along with operating conditions. The digesters mixed by recirculation of biogas are commonly referred as gaslift internal loop reactors in the literature. The gaslift loop reactors are equipped with a concentric draft tube and gas sparger to create liquid movement. They are tall, with slurry level to reactor diameter (L/D) ratio normally greater than two. These reactors are extensively used in industrial chemical and biochemical applications. Thus vast information of hydrodynamics of these reactors is available in literature. The digesters have low L/D ratio, approximately equal to one. The hydrodynamic information of low L/D ratio gaslift loop reactors is not available in literature, although effect of L/D on hydrodynamics is very important. Thus studying the hydrodynamics of low L/D ratio gaslift internal loop reactors is necessary. Some of the other important parameters which can affect the mixing pattern inside such type of digester includes, biogas recycling rate, bottom clearance of the draft tube, slope of the hopper bottom, draft tube to tank diameter ratio, position and type of gas sparger and solids loading rate.

ADRs are highly opaque systems due to the presence of the solids and the dense color of the biomass, which creates problems in using common experimental techniques to reveal hydrodynamic information. Thus advanced non-invasive techniques such as Computer Automated Radioactive Particle Tracking (CARPT) and Computed Tomography (CT) have to be used to “see” inside the digester, (Karim et al., 2004).

A wide variety of solids is encountered in ADRs treating animal waste, such as husk, straw, and fibers coming from the feed, and sand particles, saw dust, wood shavings/chips, rice hulls etc. from bedding material. Due to these solids, regions of

very slow flow or even solids settling in the digester are highly possible. If CARPT is applied in such situations, the single radioactive particle can represent only one type of solids, and slow flows will reduce the data collection rate. In addition, solids settling can bring data collection to a halt. The data collection rate, representation of more than one solids type, and ability to deal with settling can be greatly improved by the introduction of multiple tracers that can be tracked simultaneously. Furthermore, Multiple-particle tracking (MP-CARPT) can offer other important advantages, such as the capability to simultaneously track the motion of particles of different sizes, shapes, densities. It can also determine segregation of particles and probe particle interactions. The techniques can be of valuable use in other process applications as well, such as slurry bubble columns, gas-solid or gas-liquid fluidized beds, solid-liquid stirred tanks, etc.

Although advanced non-invasive techniques are very useful in understanding the hydrodynamics of digesters, these techniques are time consuming, expensive, and are not always available. Thus, it is hard to use these experiments to characterize all digester configurations and operating conditions. As an alternative, Computational Fluid Dynamics (CFD) code, once it is validated, proves to be a valuable and efficient tool to understand and evaluate the hydrodynamics of digesters. For multiphase systems, like ADrs, CFD can be used with confidence for design and scale-up only after validation with the experimental data, which can be obtained by CARPT and CT.

Advanced non-invasive experimental techniques and computational modeling together can provide valuable information about the digester hydrodynamics. Further, if this information is intended to be used with confidence for the design of ADrs, then scale-up studies are necessary. A general rule in industry is that the scale of operation has a significant impact on the performance of reactor and process equipment, as the mixing scales are affected by scale of the operation. However, the effects of digester scale on digester mixing pattern/intensity have not been studied and quantified. Thus experimentation on the pilot scale is required to test the applicability of the laboratory

scale results at large scales, in order to use this data efficiently for design of commercial/farm scale ADrs.

To provide information regarding the effective design and scale-up of ADrs and to evaluate the feasibility of different design and operating conditions, further research related to the mixing and hydrodynamics of ADrs is necessary. Advanced non-invasive experimental techniques and rigorous computational modeling approaches performed on laboratory and pilot scale digesters can fill the missing gaps in the literature regarding the hydrodynamics of digester.

1.2 Objectives

The primary objectives of this study are to advance the understanding of Anaerobic Digester (ADr) hydrodynamics to evaluate various operating conditions, and to assess the effect of the digester's design and scale on their hydrodynamics. To achieve this, hydrodynamic knowledge (gained from experiments and computational modeling) and performance knowledge (obtained from digester performance studies, Appendix A) can be used together. Knowledge of the hydrodynamics will provide the preferable operating conditions to obtain good mixing performance. The integration of the performance, experimental and computational studies is shown in Figure 1.1.

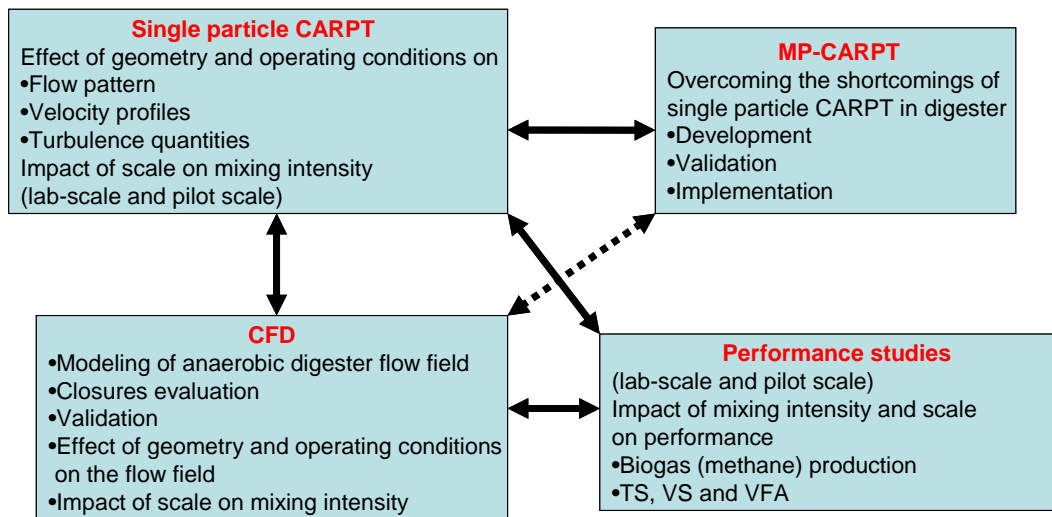


Figure 1.1 Integration of the performance and hydrodynamics of anaerobic digesters

The specific techniques and procedures of these studies are described in the following sections.

1.2.1 Single Particle CARPT and CFD Studies

The impact of mixing intensity in small and large digesters on the performance of ADrs mixed by gas recirculation was studied (Appendix A). The findings of this study showed that the performance of laboratory-scale digesters is not affected by mixing, but the performance of pilot-scale digesters is significantly affected by mixing. The laboratory-scale digesters show better performance than the pilot-scale digesters in terms of methane production. Thus, only large-scale digesters should be used to study the performance and to obtain reliable data that can be used for the design for the design of digesters.

Therefore, single particle CARPT and CFD were used to:

- Study the flow pattern and detailed hydrodynamics of ADrs at laboratory and pilot scales using real cow manure and equipped with a draft tube and a sparger

to allow mixing by gas recirculation. The CARPT data was also used as a benchmark for validation of CFD models.

- To investigate the effect of gas flow rate, shape of tank bottom, draft tube diameter to tank diameter ratio, type of sparger, solids content of the slurry, and scale on the mixing pattern and hydrodynamics of the digester.

1.2.2 Development and Validation of MP-CARPT

With the help of Oak Ridge National Laboratory (ORNL), single particle tracking technique currently used in Chemical Reaction Engineering Laboratory (CREL) was advanced to:

- Develop a multiple-particle tracking technique (MPCARPT), where up to eight radioactive tracer particles can be tracked simultaneously.
- Modify and develop new electronics to reduce the overall cost of the equipment and electronics as compared to the original single particle CARPT.
- Validate and implement this technique.

1.3 Thesis Organization

Chapter 2 provides a literature survey of anaerobic digestion and the performance and design of anaerobic digesters. It reviews the hydrodynamics of internal gaslift loop reactors. Chapter 3 introduces the new MP-CARPT technique, and describes its validation and implementation. Chapter 4 outlines CARPT investigations for two scales of digester and also discusses the findings of the experiments related to hydrodynamics and scale-up. Chapter 5 outlines the CFD efforts to simulate the flow in ADRs. Chapter 6 summarizes the research findings and makes recommendations for future work.

Chapter 2

Background

2.1 Introduction

The importance of anaerobic digestion and the need for a better understanding of the design and scale-up of anaerobic digesters have been discussed in Chapter 1. The role of mixing and hydrodynamics in the performance of anaerobic digesters has also been introduced. The aim of this chapter is to briefly document the literature related to the anaerobic digestion process, the design of anaerobic digesters, and their hydrodynamics.

2.2 Anaerobic Digestion

2.2.1 Pollution and Anaerobic Digestion

Growth and concentration of the livestock industry in the US create opportunities for the proper disposal of the large quantities of manures generated at dairy, swine, and poultry farms. The potential pollutants from decomposing livestock manures are Biological Oxygen Demand (BOD), pathogens, nutrients, methane, and ammonia emissions. The major pollution problems associated with these wastes are surface and groundwater contaminations and surface air pollution caused by odors, dust and ammonia. There is also concern about the contribution of methane emissions to global climate change.

The methane contained in biogas is a potent greenhouse gas, 21 times more harmful than carbon-dioxide in causing the greenhouse effect. The Environmental Protection Agency (EPA) has estimated that the atmospheric concentration of methane, has more than doubled in the past two centuries, and is now is increasing 1% per year (Lusk, 1998).

Consequently, manure management systems that enable pollution prevention are necessary. Moreover, the EPA passed the Concentrated Animal Feeding Operations (CAFOs) Rule in December 2003, requiring the Nation's largest CAFOs to acquire Clean Water Act permits. This forces CAFO's to develop manure management plans that ensure proper management and land application of manure (Hoffmann, 2005; Moser and Roos, 1997).

Several animal waste treatments are practiced, including chemical treatment, incineration, aerobic biological fermentation and Anaerobic Digestion (AD). AD offers several advantages over other waste treatment processes (Chynoweth et al., 1993). AD converts odor-causing materials (food source for methane-producing bacteria) in organic matter to methane and carbon-dioxide, which are odorless. Odor reduction using Anaerobic Digesters (ADrs) can be a cost-effective alternative compared to aeration, chemicals. or enzyme treatments. In fact, the biogas produced can be a by-product of a system designed for odor control. Odor control is the main reason livestock farmers have installed ADRs in the US.

With better management practices, methane from manure can be a clean, renewable source of energy. Depending on the digestion process, the methane content of biogas is generally between 55% - 80%. The remaining composition is primarily carbon dioxide, with trace quantities (0-15,000 ppm) of corrosive hydrogen sulfide and water (Lusk, 1998).

The animal manure is rich in nitrogen, but the nitrogen is bound up in proteins and is not readily available to plants without undergoing biological conversion. During the digestion process, much of the organic bound nitrogen is released as ammonia. The digestant left after the digestion process has combined nitrogen, phosphorus, and potassium percentages ranging from 3-4.5% on a dry matter basis and can be spread directly onto farmland for its nutrient value. Due to the lower viscosity of digestant as compared to the raw manure, it penetrates faster into the soil. Soil ammonium adsorption is also high, hence, washout is low. Thus, the by-product of the AD process proves to be a very good soil fertilizer.

Biomass is a form of renewable energy, unlike fossil fuels such as oil, natural gas and coal. Vanishing reserves of fossil fuels and increasing demand for energy make it critical to consider the use of renewable energy. Based on life-cycle cost analysis of proven anaerobic digesters (ADrs) producing biogas and nutrient rich by-product slurry, an avoidable livestock production liability can become a profit-making asset.

2.2.2 Anaerobic Digestion Mechanism

The primary objective of anaerobic digestion is the stabilization of organic matter, with a concurrent reduction in odors, pathogen concentration, and mass of solid organic material. This is accomplished through biological conversion of organics to methane and carbon dioxide in an oxygen-free environment. Conversion of organics to methane involves five groups of bacteria carrying out rather specific reactions. Conceptually, anaerobic digestion can be represented in a three step process for simplicity (Hill, 1982; Parkin and Owen, 1986). The three-stage process (shown in Figure 2.1) involves: (1) hydrolysis, liquefaction and fermentation; (2) hydrogen and acetic acid formation; (3) methane formation.

Hydrolysis, Liquefaction and Fermentation

Hydrolysis and liquefaction of complex and/or insoluble organics are necessary to convert these materials to a size and form that can pass through bacterial cell walls for use as energy or nutrient sources.

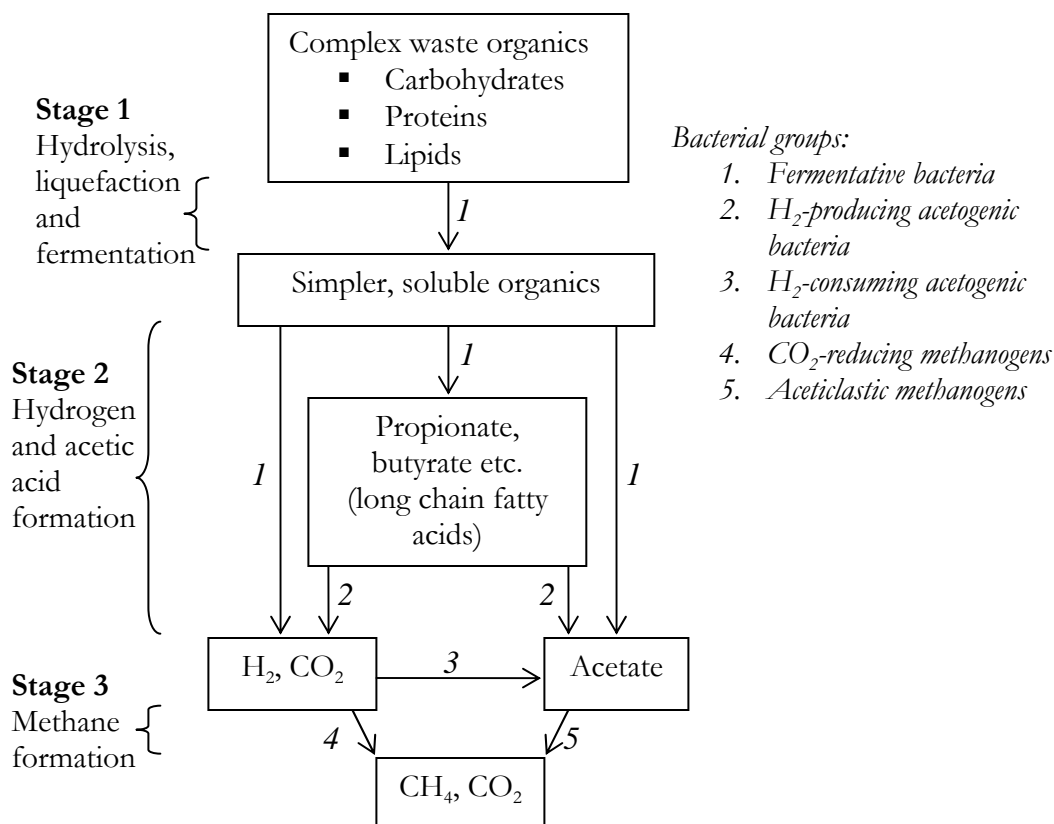


Figure 2.1 Three-stage anaerobic digestion mechanism

Hydrolysis and liquefaction are accomplished by extracellular, hydrolytic enzymes produced and excreted by the bacterial population for this specific purpose. It is important to recognize that stabilization of complex organics cannot occur unless this initial hydrolysis step is functioning properly. Therefore the overall rate of stabilization and methane fermentation can be limited by the hydrolysis rate of complex organics.

Once complex organics are hydrolyzed, they are fermented to long chain organic acids, sugars, amino acids, and eventually to smaller organic acids such as propionic, butyric, and valeric acid. This phase is commonly called the ‘acid-forming’ or fermentation

phase, and also results in essentially no stabilization. The population of bacteria responsible for acid production, called acetogenic bacteria, may be facultative anaerobes (viable in the presence of oxygen), strict or obligate anaerobes (to which oxygen is toxic), or a combination of both. Acetic acid, hydrogen, and carbon dioxide are also formed during the production of organic acids.

Hydrogen is inhibitory to many of the acid-forming bacteria and must be removed from the system if acid production is to continue. Fortunately, hydrogen is an energy source for some methanogenic bacteria and is rapidly consumed in the reduction of carbon dioxide to methane. The optimum pH of acidogenic bacteria is 5.2 to 6.5, and its specific growth rate is around 2 days (Demirer and Chen, 2004).

Hydrogen and Acetic Acid Formation

Hydrogen is produced by fermentative bacteria and consumed by acetogenic bacteria. Acetate is also produced by these groups, as well as by acetogenic bacteria. Hydrogen plays a key role in regulating organic acid production and consumption. If the partial pressure of hydrogen exceeds 10^{-4} atm, methane production is inhibited and the concentration of organic acids (e.g., propionic and butyric) will increase. Thus, to maintain efficient anaerobic digestion of sludges to methane, hydrogen levels must be maintained below this level. A syntrophic association with a large, stable population of CO_2 -reducing methanogens will ensure maintenance of low hydrogen concentrations. Because of its key regulatory role, hydrogen offers promise as a process performance indicator. Acetogenic bacteria grow very slowly, with a minimum doubling time of 3.6 days (Demirer and Chen, 2004).

Methane Formation

Waste stabilization occurs during the methanogenic phase by conversion of the acetic acid into methane, which is essentially insoluble in water and readily separates from the sludge as a gas which leaves the system. Carbon dioxide is also produced, and either escapes as gas or is converted to bicarbonate alkalinity. Methanogenic bacteria are strict

anaerobes to which oxygen is inhibitory. One of the most important characteristics of the methanogenic phase is that very few substrates can act as energy sources for the various methanogens. Of these, acetic acid and hydrogen serve as the major substrates. Methanogenic bacteria, which are very sensitive to environmental stresses, grow more slowly than acidogenic bacteria, and at a rate similar to acetogens (Demirer and Chen, 2004).

Methane formed in anaerobic digestion comes from acetate cleavage (Equation 2.1) and from reduction of carbon dioxide by CO₂-reducing methanogens using hydrogen as their energy source (Equation 2.2).



2.2.3 Anaerobic Digesters (ADrs)

In practice, ADRs are operated in both mixed and unmixed modes. The choice of operation also depends on the type of waste. Dairy and swine manure management systems are often liquid or slurry based, which simplifies the necessary manure movement.

ADr designs can be classified as two main types, unmixed and complete-mix digesters. (Complete-mix digester is a generally used misnomer since it indicates only the provision of an additional form of mixing but does not imply complete mixing of the digester contents). ADRs used on farms are also commonly classified as continuous fed or batch fed (Gunaseelan, 1997; Parkin and Owen, 1986). As the name suggests, no mixing is provided in unmixed ADRs. Unmixed ADRs are operated in two main designs, plug-flow and anaerobic lagoon digesters. The choice between the two is mostly governed by the solids content of the waste. There are also other modifications of

designs and operation of ADrs, such as a fixed film digester or an anaerobic filter, and temperature-phased digesters (Gunaseelan, 1997).

Complete-Mix Digesters

Complete-mix digester vessels are insulated and maintained at a constant elevated temperature, in the mesophilic (77°F to 104°F) or thermophilic (122°F to 149°F) range. The digester vessel is usually a round insulated tank, above or below ground, and made from reinforced concrete, steel or fiberglass. Heating coils with circulating hot water can be placed inside the digester or, depending on the consistency of the feedstock, the contents can be circulated through an external heat exchanger to maintain the desired temperatures. They can be mixed by a motor driven mixer, a liquid recirculation pump, or by biogas recirculation (see Figure 2.2). A gas tight cover (floating or fixed) traps the biogas. The complete mixed digester is best suited to process manure with 3-10% total solids. Retention time is usually 10 to 20 days. The biogas created by the digester can be used to heat the digester to the desired temperature (McNeil, 2005).

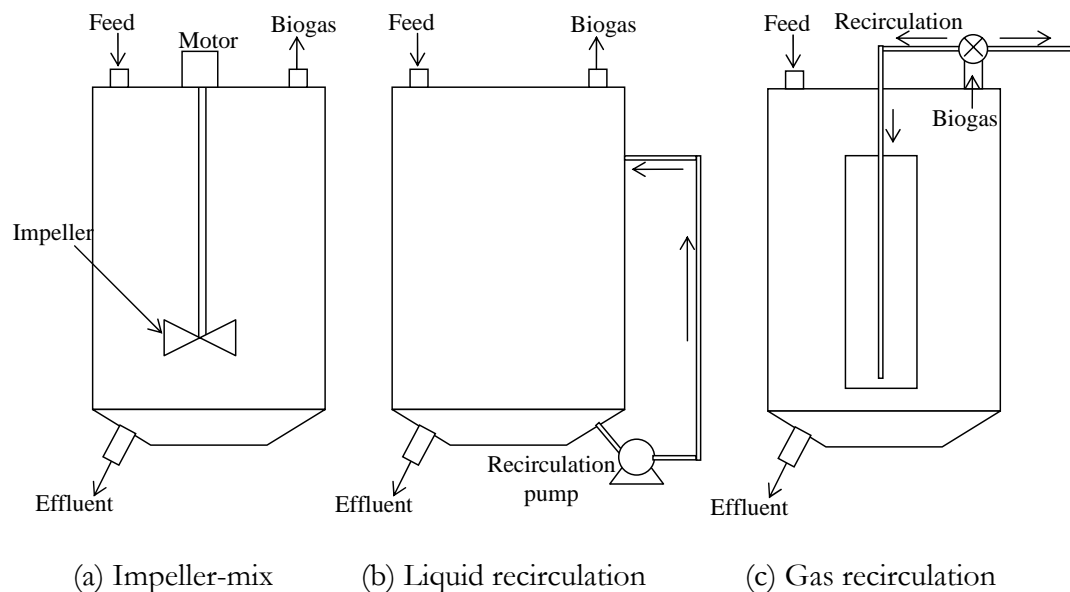


Figure 2.2 Modes of mixing in complete-mix digesters

Gaslift digesters are popular in AD applications because they offer several advantages over other designs of complete-mix digesters (Carroll and Ross, 1984). Gas recirculation digesters do not have any moving parts, which makes cleaning and maintenance easy. Sealing the digester to avoid leakage of biogas or contamination by air is very difficult in case of impeller mixed digesters. Power consumption is a very important factor in selection of digester design. The power required to drive the impeller motors is significantly higher than the power required for pumping the gas. The energy required to run the digester should be kept to minimum to maximize the energy gain from the biogas produced by the digester. Since the slurry used in complete-mix digesters has solids, slurry recirculation needs special pumps that can handle slurry and also needs higher power.

Non-uniform dispersion of mixing energy causes problems such as solids settling to the bottom and formation of a floating layer at the top. Thus, the distribution of mixing energy throughout the digester volume is key in the selection of a mixing system (Casey, 1986). Spreading a relatively low energy input throughout the highly viscous manure slurry is not an easy task. This is especially true for concentrated power inputs such as impellers and slurry recirculation systems. These systems show high shear rate and hence high power dissipation rate near the input location, and shear rate tapers off with distance from the power input location. In the case of slurry recirculation systems, the mixing input usually leads to a mass circulation of the digester contents, with consequent uneven shear stress and relatively poor performance in preventing float layer formation. High shear stress is also detrimental to the microorganisms. Gas recirculation systems provide low shear distributed throughout the digester volume due to distribution of the dissipated power input.

Another important factor is the interaction between the separate mixing effects of the evolved biogas and that of the imposed mixing. Ideally, their mixing effects should be complementary. This will not be the case with a slurry recirculation system or an impeller mixed system. By contrast, in a gaslift digester the pumped biogas rises

vertically upwards, carrying slurry upwards with it, thus facilitating evolution of biogas bubbles. Hence, digester mixed by gas recirculation seems to be best option within complete-mix digesters.

2.2.4 Importance of Mixing in Anaerobic Digestion

Number of factors affects the performance and efficiency of AD, such as temperature, pH, feed characteristics, feed rate and feeding mode, toxicity, and mixing in the digester. Hoffmann (2005) and Parkin and Owen (1986) have explained this in detail. Parkin and Owen (1986) provided a check list of key factors that govern bacterial growth and thus, the AD's performance. Favorable conditions for the following factors will maximize chances for achieving optimum design and efficient operation: 1) optimum retention time, 2) adequate mixing (bacteria-substrate contact), 3) proper pH, 4) proper temperature control, 5) adequate concentration of proper nutrients, 6) absence (or assimilation) of toxic materials, and 7) proper feed characteristics. Factors one to five are directly related to mixing in the digester. Thus, we will review the effect of mixing on AD performance in this discussion.

Despite the slow bioreaction rate, the reasons for providing mixing in digesters are to provide efficient utilization of the entire digester volume, to prevent stratification and temperature gradients, to maintain uniform pH, to disperse metabolic end products and any toxic materials contained in the influent sludge, and to maintain intimate contact between the bacteria, bacterial enzymes, and their substrates (Bello-Mendoza and Sharratt, 1998; Casey 1986; Meynell, 1976; Parkin and Owen, 1986; Sawyer and Grumbling, 1960; Smith et al., 1996). Additional concerns associated with inefficient mixing are foaming and scum formation, and excessive solids deposition. Mixing also helps in evolution of biogas bubbles. In short, adequate mixing provides a uniform environment, one of the keys to good digestion.

Inefficient mixing decreases effective system volume, which reduces the sludge retention time (SRT) and pushes the system towards failure. Studies with full-scale digesters have shown that inefficient mixing may reduce the effective volume of the digester by as much as 70%, leaving an actual volume utilization of only 30% (Monteith and Stephenson, 1981). Parkin and Owen (1986) illustrated the effect of the SRT on digester performance and proved that inefficient mixing causes digester failure. From a digester study at a larger scale, James et al. (1980) also suggest that mixing is required for efficient operation of the digester to avoid settling and flocculation.

The optimum pH of acidogenic bacteria is 5.2 to 6.5, and the specific growth rate is around 2 days. Acetogenic bacteria grow very slowly, with a minimum doubling time of 3.6 days. Methanogenic bacteria, the group of anaerobes most sensitive to environmental stresses, grow more slowly than acidogenic bacteria, at a rate similar to acetogens (Demirer and Chen, 2004). The optimum pH environment for methanogens is 7.5-8.5. ADrs are generally operated in fed-batch or batch mode. If the added feed concentration is not kept uniform throughout the digester volume, then fast growing acidogenic bacteria will produce acids at a higher rate than the rate at which acids can be consumed by acetogenic or methanogenic bacteria. Increasing acids concentration lowers the pH, killing the methanogenic activity and pushing the digester towards failure. Thus fast and uniform distribution of feed is required through proper mixing (Merchuk and Gluz, 1999).

In spite of the crucial role played by mixing in the operation of ADrs, contradictory findings in small scale digesters are reported in the literature about the necessity of mixing and the mixing intensity required to enhance the digester performance. Chen et al. (1990) found that a non-mixed digester exhibited a higher methane yield than a continuously mixed digester. Ho and Tan (1985) reported greater gas production for a continuously mixed digester than for an unmixed digester for palm oil mill effluents. Dague (1970) observed that shifting from continuous mixing to intermittent mixing resulted in significantly higher gas production during the anaerobic treatment of a liquid

municipal waste stream. Ben-Hasson et al. (1985) observed a 75% lower methane production rate from a continuously mixed reactor than from an unmixed reactor when treating dairy cattle manure anaerobically. Pierkiel and Lanting (2004) observed in a pilot-scale digester that higher volumetric power input induces stronger mixing, reducing the hydraulic retention time and raising biological activity.

While discussing the importance of mixing in digesters, it has to be remembered that some degree of internal mixing is always present in all ADrs. The evolution of biogas bubbles creates some amount of mixing. Under favorable conditions - at high gas evolution rates and in the absence of readily floatable solids or low solids content - evolved biogas may provide sufficient process mixing on own, thus eliminating the need for an external mixing input. However, in the case of slurries, self-mixing cannot be relied upon to prevent the development of bottom deposits or a floating scum layer. Some mixing of digester contents also takes place during the addition of feed and removal of effluent; however this mixing is intermittent in nature, unlike the continuous mixing provided by evolving biogas.

Karim et al. (2005a, 2005b) and Hoffmann (2005) conducted a range of systematic experiments on 6-inch diameter laboratory-scale units to assess the effect of mixing on the digesters' performance. Karim (2005a) operated several digesters with conical bottoms; fed with slurry containing 5% or 10% (i.e., 50 or 100 gm/L) total solids with different mode of mixing and with different geometries. The mode of mixing or the digester geometry showed no significant effect on the performance of the digesters. They concluded that the true effect of mixing cannot be observed at laboratory scales, and more performance experiments need to be performed at larger scales to arrive at confirmatory conclusions.

The impact of mixing intensity in small and large digesters on the performance of ADrs mixed by gas recirculation was studied (Appendix A). The findings of this study showed that the performance of laboratory-scale digesters is not affected by mixing, but the

performance of pilot-scale digesters is significantly affected by mixing. The laboratory-scale digesters showed better performance than the pilot-scale digesters in terms of methane production. And thus it was concluded that only large-scale digesters should be used to study the performance and to obtain reliable data that can be used for the design of digesters.

Reactor configuration itself does not play an important role in causing changes in the microbial community (Morgan et al., 1991). The effect of reactor configuration on the performance of ADrs is due to changes in the hydrodynamics or mixing performance. For example, higher shear produced by impeller mixed digesters is harmful to the microorganisms, or a reactor configuration causing higher dead zones can reduce the effective reactor volume, thus reducing the effective sludge retention time (SRT) and causing digester failure. Tilche and Vieira (1991) observed a change in process performance upon scale-up and related it to a change in mixing patterns. Smith et al. (1996) also observed a change in digester performance upon scale-up. They conducted tracer studies and measured dead zone volumes and concluded that the change in hydrodynamics of the digester upon scale-up results in a change in their performance.

Thus, the hydrodynamics or mixing performance of a digester is important in understanding, designing and scale-up of ADrs. The next section discusses the hydrodynamics of gaslift digesters.

2.3 Gaslift Digesters

Gaslift loop reactors are used in digester applications to provide mixing by recirculation of gas. For digester applications the reactor height (slurry level) is maintained approximately equal to the reactor diameter. For gaslift loop reactors, conventionally used in chemical or biochemical industrial applications, the reactor height to diameter ratio (H/T) is normally greater than two. (In this discussion, low H/T (approximately equal to one) gaslift loop reactors will be referred to as gaslift digesters). Because of the

prominent use of high H/T ratio gaslift loop reactors in industry, much information on gaslift loop reactors is available. In contrast, there is very little information on gaslift digesters ($H/T \cong 1$). Thus, it is difficult to evaluate the effect of H/T ratio on the mixing and hydrodynamics of gaslift loop reactors. The liquid or slurry level in the gaslift loop reactors is one of the important parameters affecting the hydrodynamics (Merchuk et al., 1996).

Since the gaslift loop reactors and the gaslift digesters are basically the same type of reactors operating with the same working principle, their global hydrodynamic behavior should not be considerably different. The global hydrodynamic characteristics such as the nature of the flow pattern, flow regimes, the nature of correlations and equations to determine hydrodynamic parameters (holdup, circulation velocities, circulation time, turbulence parameters, transport coefficients), are not expected to be considerably affected by the change in H/T ratio. However the effect of operating conditions on the flow pattern, flow regime transition criteria, constants and exponents in correlations, and hydrodynamic parameters will be different for considerably different H/T ratios.

Knowledge of gaslift loop reactors will be helpful in understanding the hydrodynamics of gaslift digesters. Thus the hydrodynamics of gaslift loop reactors is discussed in the following sections.

2.3.1 Gaslift Loop Reactors

Gaslift Loop Reactors (GLR) can be divided into two main types on the basis of their structure (Figure 2.3), external gaslift loop reactors (EGLR) and internal gaslift loop reactors (IGLR)

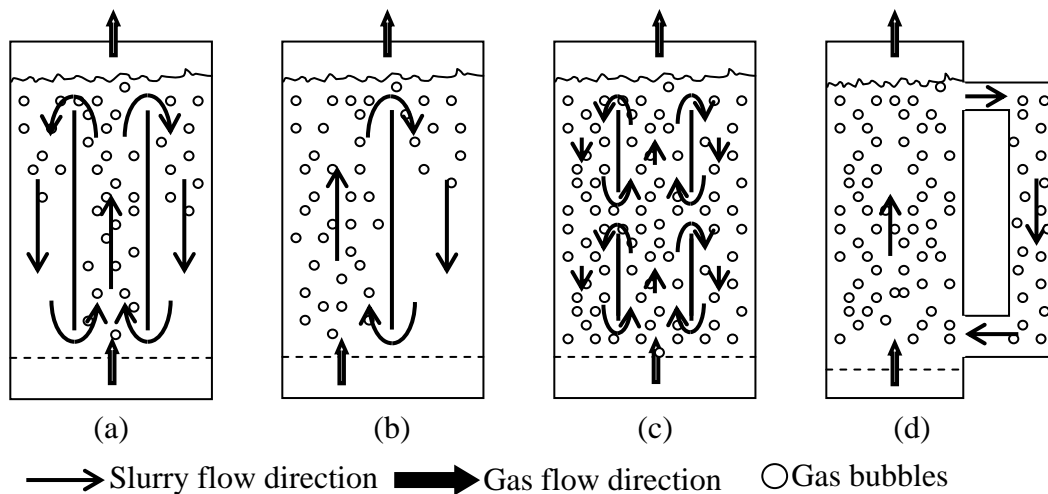


Figure 2.3 Types of GLR (a) Concentric tube IGLR, (b) Split IGLR
(c) Stages IGLR (d) External GLR

In EGLRs circulation takes place through separate and distinct conduits, whereas in IGLRs a baffle or concentric tube is placed strategically in a single vessel to create the channels required for the circulation. The designs of both types of reactors can be modified further, leading to variation in hydrodynamics, in the extent of gas disengagement from the fluid, and in the flow rates of various phases. Some of the variations of IGLR are rectangular and square cross-sectioned gaslift, split-cylinder gaslift, concentric-tube gaslift, and multiple concentric tubes. (see Figure 2.3).

Advantages of GLRs

Advantages offered by GLRs are discussed below:

- **Low shear stress:** The uniformly distributed, low shear stress present in GLRs is one of their most important advantages, and makes them popular for biological applications. In GLRs the gas is injected at a single point, but the direct contribution of gas injection to the hydrodynamics of the system is small. Circulation of liquid and gas is created by the difference in the gas holdup between the riser and the downcomer, which creates a pressure difference at the bottom of the equipment.

$$\Delta P = \rho_l g(\varepsilon_r - \varepsilon_d) \quad (2.3)$$

The pressure difference forces the fluid from the bottom of the downcomer towards the riser, generating circulation. Since the average gas holdup along the length of the riser and downcomer contributes to the pressure difference, there are no focal points of energy dissipation, and thus shear distribution is homogeneous throughout the GLR. In contrast, in bubble columns and stirred tanks, the energy source inducing fluid motion is focal. The shear forces in bubble columns are highest adjacent to the gas sparger and dissipate with distance from the sparger. In stirred tanks, a region of very high shear exists near the impeller, which decreases with increasing distance from the impeller. Thus GLRs are used in biological systems where microorganisms are very sensitive to shear.

- **Simple design:** GLRs are mechanically simple in design, without any rotating internal parts. The absence of a shaft and the associated sealing, which is always a weak element from the point of view of sterility, confers on the GLR an obvious advantage over stirred tanks. The vertical orientation of these reactors, as well as lack of internals, facilitates easier cleaning and sterilization.
- **Low energy consumption:** The energy consumption per unit volume to create circulation and mixing is significantly lower in GLRs than in stirred tanks and bubble columns. Unlike bubble columns, the injected gas velocity does not decide the liquid velocities; rather the difference in gas holdup creates liquid circulation. Thus, even very low gas velocities can initiate liquid circulation in the whole reactor. The injected gas serves the dual functions of aeration and agitation, which promotes efficiency in the overall energy balance and eliminates the need for a separate expenditure of energy for agitation.
- GLRs show good mass transfer and heat transfer characteristics and are easily adaptable to three-phase systems.

2.3.2 Hydrodynamics in Gas-Solid-Liquid IGLRs

The interconnections between the design variables, the operating variables, and the observable hydrodynamic variables in an IGLR are shown schematically in Figure 2.4 (adapted from Merchuk et al., 1996). The design variables are the reactor height, the D/T ratio, the geometrical design of the gas-liquid separator, and the bottom clearance of the draft tube (it is proportional to the free area for flow in the bottom and represents the resistance to flow in this part of the reactor). The main variables are primarily the gas input rate and, to a lesser extent the top clearance of the draft tube from the liquid surface. These two independent variables set the conditions that determine the liquid velocity in the IGLR via the mutual influence of pressure drop and holdup. Viscosity is not shown as independent variable because in the case of gas-liquid mixtures, it is a function of the gas holdup (and of liquid velocity in the case of non-Newtonian liquids), and because in a real process it will change with time due to changes in compression of liquid.

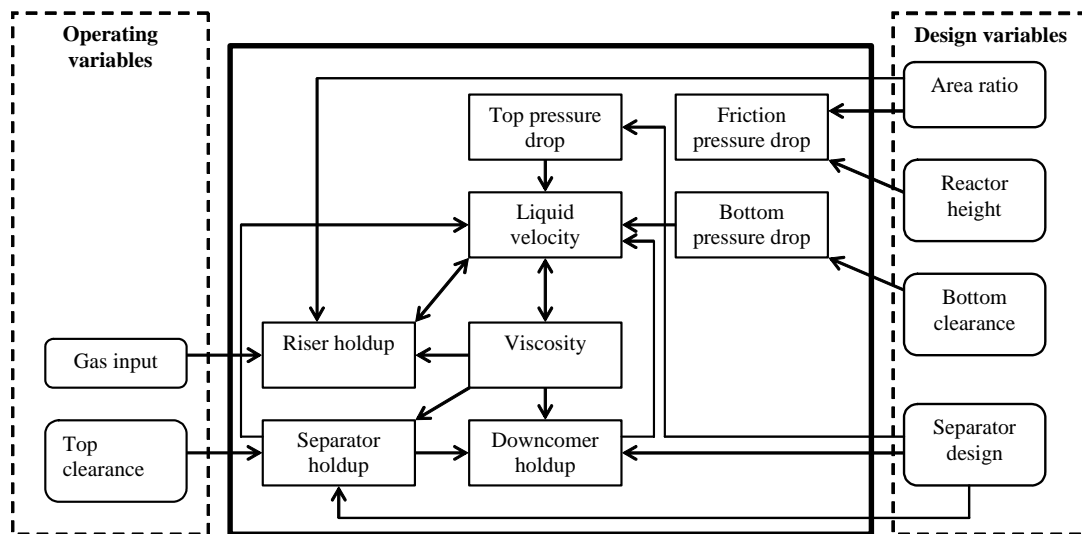


Figure 2.4 Relationship between independent and dependent variables in the hydrodynamics of IGLRs

Because of the advantages of IGLRs, they are becoming increasingly popular in three phase gas-liquid-solid applications. Recent literature has focused on the hydrodynamics and modeling of three phase IGLRs (Feitkenhauer et al., 2003; Freitas et al., 1999; Heijnen et al., 1997; Kennard and Janekeh, 1991; Klein et al., 2003a and 2003b; Lu et al., 1995; Luo, 2005; Merchuk et al. 2003; Merchuk and Shechter, 2003; Petersen and Margaritis, 2001; Siegel and Robinson et al., 1992; Sun et al., 2005; Trilleros et al., 2005). This literature discusses the effect of solids of varying densities ranging from lighter than water to heavier than glass (0.8 to 4.5 g/cc), on the hydrodynamics of IGLR. The consensus exists between all the researchers that, if the density of the solids is higher than that of the liquid, liquid rising velocity will be smaller and the holdup of solids in the riser will be larger than in the downcomer, and vice-versa. The presence of solids however, always diminishes the driving force for circulation, independently of their density.

The importance of the gas holdup in gaslift reactors is twofold: 1. The value of the gas holdup gives an indication of the potential for mass transfer; and 2. The difference in the gas holdup between the riser and the downcomer generates the driving force for liquid circulation. It should be stressed, however, that when referring to gas holdup as the driving force for liquid circulation, only the total volume of gas is relevant. This is not the case for mass transfer phenomena, in which case the interfacial area is of paramount importance, and therefore some information on bubble size distribution is required for complete understanding of the process. Because gas holdup values vary within a reactor, average values, referring to whole volume of the reactor, are usually reported. Values referring to a particular section, such as the riser or the downcomer, are much more valuable, since they provide a basis for determining liquid velocity and mixing. The geometric design of the IGLR has a significant influence on the gas holdup. Changes in D/T ratio will change the liquid and gas residence time in each part of the reactor and hence their contributions to the overall holdup. Gas holdup increases with decreasing D/T .

The liquid velocity is one of the most important parameters in the design of IGLRs. It affects the gas holdup in the riser and downcomer, the mixing time, the mean residence time of the gas phase, the interfacial area, and the mass and heat transfer coefficients. Circulation in IGLRs is induced by the difference in hydrostatic pressure between the riser and the downcomer as a consequence of a difference in gas holdup. Unlike gas holdup, liquid velocity is not an independent variable, because the gas flow rate is the only variable that can be manipulated. The geometry of the reactor also influences the liquid velocity, but this remains constant during operation. Experiments have been carried out in devices specially designed to artificially change the resistance to flow, with the aim of studying the effect of the velocity at a fixed rate of aeration (Merchuk and Stein, 1981). The information emerging from these experiments indicates that an increase in the liquid velocity leads to a decrease in the mean residence time of bubbles in the riser. In practice, when the gas flow is increased, the higher liquid velocity increases the carryover of the bubbles from the gas separator into the downcomer. The carryover dampens the liquid flow by reducing the hydrostatic driving force. As a result, the overall change in liquid velocity is tempered.

One of the major factors in the design of IGLRs is the effect of the geometry of the system on the various characteristics of the flow phases. Reactor geometry affects overall performance, and is also influenced by the operating variables and fluid dynamic properties (explained in Figure 2.4). Geometric variables that affect the hydrodynamic performance of IGLR are draft tube diameter to reactor diameter ratio (D/T), liquid height to reactor diameter ratio (H/T), draft tube top and bottom clearance, draft tube height (b), shape of the bottom, location and geometry of sparger, etc.

Trilleros et al. (2005) proposed several correlations to predict the effect of D/T and b/H on the liquid velocity and gas holdup. Comparing the exponents of each term in the correlations, he concluded that the effect of physical properties of the GLS system on the hydrodynamics is more important than the effect of geometry. The cross-sectional area of the draft tube determines the superficial fluid velocity in the reactor. In

three-phase systems it also plays an important role in determining the minimum velocity necessary to fluidize the solid particles. It has been shown that to achieve optimum gas holdup, D/T should be greater than 0.75 (Kennard and Janekeh, 1991; Weiland, 1984). Rousseau and Bu'Lock (1980) have shown that minimal mixing time is achieved when D/T is between 0.6 and 1; this has been confirmed by Lin et al. (1976). Weiland (1984) states that D/T of less than 0.6 should only be used if high liquid velocities in the draft tube are required to avoid sedimentation of large microbial aggregates. Kojima et al. (1999) observed an increase in liquid velocity with an increase in D/T .

To study the effect of top and bottom clearance, D/T , and h/D , Gavrilescu and Tudose (1998b) performed experiments on three scales of IGLRs, with volumes ranging from 0.07 to 5.2 m³. They found that the draft tube clearance and D/T have major influences on liquid superficial velocity, circulation time, friction coefficient, and the radial profiles of liquid velocity and gas holdup. Interestingly, Kojima et al. (1999) found no effect of draft tube clearance on the liquid circulation velocity, whereas Luo (2005) found from CARPT and CT experiments that both the top and bottom clearance has significant impact on the liquid circulation and gas holdup in IGLRs. Lu et al. (1995) found that liquid velocity increased with increase in draft tube height, whereas the effect of static liquid height on liquid velocity was negligible. Kojima et al. (1999) also confirmed that liquid velocity increases with an increase in draft tube height, but no explanation was provided for this behavior.

2.4 Scale-up of IGLRs

A thorough knowledge of mixing behavior is of particular importance during the process of scale-up from laboratory-scale to industrial-scale IGLRs. In small scale reactors, due to ease of mixing, it is easier to maintain the optimal conditions of pH, temperature, and substrate concentration required for maximum productivity. However, because of the compromises made during scale-up, it is difficult to keep the same

hydrodynamic conditions established in the laboratory-scale. Thus, full-scale mixing may not be as good as mixing on a laboratory-scale.

Merchuk and Gluz (1999) pointed out two main groups of problems encountered in scale-up of bioreactors. First, economic and mechanical limitations make it difficult to maintain the same high power input per unit volume in large scale reactors that is used in laboratory-scale units. This problem is not encountered in ADRs, because power input is kept to minimum for economical operation. Second, the lack of knowledge of hydrodynamics of large-scale reactors prevents design of bioreactors from first principles. Thus, simplistic hydrodynamic models and empirical correlations are used for scale-up.

Despite of many successful full-scale applications of IGLRs (the Pachuca tank used in metallurgy; the waste water treatment at Gist Brocades, The Netherlands; the production of single cell proteins by Pruteen process, Klein et al., 2001), the use of GLRs is limited. One of the most important reasons is lack of reliable scale-up models or scale-up methods to predict key operational parameters in the range of different geometries and operational conditions. Blazej et al. (2004); Gavrilesco and Tudose (1998); Heijnen et al. (1997); Merchuk et al. (1996) and Merchuk and Gluz (1999) are among the few who have addressed the scale-up issues of IGLR.

Heijnen et al. (1997) reported that the flow regimes occurring in IGLR are the same for all scales of reactors (ranging from a liter to 100 m³), but flow regime transition conditions are not the same for all scales. Blazej et al. (2004) performed experiments on three different scales of IGLR, ranging from 10.5 liters to 200 liters, and concluded that larger reactor volumes operating in the bubble recirculation regime provide higher liquid circulation velocities and higher, more uniformly distributed gas holdup than smaller reactors. Better performance of large scale reactors was attributed to lower values of friction factors from the walls and internals. Heijnen et al. (1997) made similar observations with a pilot-scale (400 liters) and full-scale (284 m³) IGLR. Merchuk et al.

(1996) observed higher gas holdup and lower liquid circulation velocities in a larger reactor (300 m^3) than a smaller scale one (30 m^3).

Gavrilescu and Tudose (1998) encountered the change in hydrodynamics of the system when passing from laboratory to larger scales. As the reactor scale increased from 70 liters to 2.5 m^3 , the overall gas holdup decreased, whereas from 2.5 to 5.2 m^3 no effect of scale on the gas holdup was seen. They also observed that the influence of the geometry of the system on the flow of different phases is important in design and scale-up of IGLRs (see Figure 2.4).

Merchuk et al. (1996) presented an extensive list of design, operational, and hydrodynamic variables and interconnections between them; the effect of these variables on each other is important in scale-up of IGLRs.

Although the above knowledge of IGLRs cannot be directly extrapolated to gaslift digesters, it can help in understanding the challenges involved in their design and scale-up. In a specific well-mixed laboratory-scale digester, the optimum growth rate of microorganisms or the optimum production rate of a specific product usually relates to well-defined environmental conditions, such as pH range, temperature, substrate level and limiting factors. Laboratory-scale digesters are very attractive for experimentation because of their convenient small size, ease of operation, and low cost. They are also efficiently mixed and thus contain a uniform environment. These characteristics make them valuable in estimating kinetic parameters and nutrient and alkalinity requirements, and in discovering potential problems like toxicity. Small-scale experiments performed to reveal the hydrodynamics provide insight into flow patterns and the shape of velocity and holdup profiles. On the other hand, experimentation on a large scale digester is necessary to elucidate the operational problems and difficulties, such as the effects of improper mixing (Ben-Hasson and Ghaly, 1989, Karim et al., 2005a & 2005b).

The literature on IGLRs is focused on phenomenological hydrodynamic modeling and validation of these models through experiments (Freitas et al., 1999; Garcia et al., 1996; Garcia et al., 1999; Heijnen et al., 1997; Klein et al., 2003; Sun et al., 2005 and many others). Hydrodynamic models are used to predict the two most important design parameters, liquid circulation velocity and gas holdup. Another prevalent approach in designing IGLRs is formulating correlations, to evaluate desired quantities such as liquid velocity, gas holdup and mass transfer coefficients, by correlating the experimental data (Choi et al., 1996; Feitkenhauer et al., 2003; Kojima et al., 1999; Miron et al., 2004; Trilleros et al., 2005; Gavrilescu and Tudose, 1998a, 1998b; Wei et al., 2000; Wen et al., 2005).

If a hydrodynamic model is formulated from first principles, it can offer many advantages such as ease and reliability of reactor design and scale-up and the ability to predict the effect of operating conditions. However, such formulations are made difficult by the inherent geometric complexity of the system and by the fact that these processes typically involve turbulent flow (Saez et al., 1998). As a result, these models rely on one or more input parameters that are fitted from the experimental data or obtained from empirical correlations. Therefore, hydrodynamic models, just like empirical correlations, cannot be used for or extrapolated to different geometries, scales, and operating conditions (Cockx et al., 1997; van Baten et al., 2003).

Considering the shortcomings of conventional experiments, phenomenological models, and empirical correlations, advanced non-invasive experimental techniques like Computer Automated Radioactive Particle Tracking (CARPT) and Computed Tomography (CT) are required to understand the hydrodynamics of IGLRs in detail. CARPT provides knowledge of flow patterns, velocity profiles and turbulence parameters, while CT provides local or averaged phase holdup. Karim et al. (2004) and Luo (2005) applied CARPT and CT for visualizing flow patterns and phase holdup profiles in an IGLR type anaerobic digester. Laser Doppler Velocimetry (LDV) and

Ultrasound Doppler Velocimetry (UDV) can also be used under limited conditions for obtaining flow patterns and velocity and holdup profiles, Vial et al. (2003).

Advanced non-invasive experimental techniques like CARPT and CT help to understand the hydrodynamics in more detail, but their application is limited by time and resource constraints. Thus these techniques cannot be used to evaluate the effect of every parameter on the hydrodynamics. This is where Computational Fluid Dynamics (CFD) can be utilized, once they are validated.

For single-phase systems, CFD models and closures are well established and validated with benchmark experimental data, so that CFD can be used with a high level of confidence for simulating single-phase systems. However, this is not the case with multiphase systems. The complex flow structure and interactions within different phases, in addition to the turbulence, make it very difficult to develop models for multiphase systems that can mimic reality. The closures used for these equations are modeled hypothetically or correlated from experimental data and thus cannot be universally applied to all cases. Multiphase CFD simulations need to be developed for individual situations and validated against experimental data. Once the CFD results are validated for a particular system, CFD can be used to optimize the system by varying parameters and operating conditions to achieve proper design and scale-up.

Only a few CFD modeling attempts are described in the literature on IGLRs (Bagatin et al., 1999; Blazej et al., 2004a; Cockx et al., 1999; Glover et al., 2003; Jakobsen et al., 1993; Luo (2005); Mudde and Van Den Akker, 2001; Oey et al., 2001 and 2003b; Svendsen et al., 1992; van Baten et al., 2003a and 2003b). Some of the researchers (Mudde and Van Den Akker, 2001; Oey et al., 2001) compared CFD predictions with the results of a 1D mechanical energy balance model. This cannot be a conclusive way to evaluate the predictions of the CFD model, because of the over-simplifying assumptions and empiricism involved with 1D hydrodynamics models.

Few other researchers have compared CFD results with experimental data. The comparison has been done mostly for the overall liquid circulation velocity and/or overall gas holdup in the riser and/or downcomer section (Bagatin et al., 1999; Blazej et al., 2004a; Glover et al., 2003; van Baten et al., 2003a and 2003b). The predictions of average quantities match very well with the experimental data in most cases. But CFD is put to real test to make conclusive evaluations, when the predicted local quantities, like liquid velocity profiles or gas holdup profiles, are compared with experimental values. The comparison in this case is often satisfactory qualitatively and only reasonable quantitatively. Svendsen et al. (1992) compared liquid velocity profiles and reported unsatisfactory predictions of CFD simulations in the case of IGLRs.

Blazej et al. (2004a) simulated 2D flow in IGLR using the algebraic slip model and compared the simulated predictions with the experimental data. The average liquid velocities were obtained by magnetic tracer particle method, and the average gas hold up was measured by an inverted U-tube manometer. Computational predictions for liquid velocity and gas holdup in the riser matched reasonably with the experimental data, but the computations always overpredicted the liquid velocities and gas holdup at higher gas superficial velocities. This was attributed to lack of proper modeling of gas entrainment in the downcomer region at high gas flow rates. To resolve this issue, Glover et al. (2003) performed 3D simulations in a similar system and found that it increased the accuracy of predictions in downcomer region but the predictions in the riser section were less accurate than the predictions of 2D simulations.

van Baten et al. (2003a) performed both 2D and 3D simulations for different configurations of IGLR and observed that the geometry effects were properly accounted for by the CFD model. van Baten et al. (2003b) and Bagatin et al. (1999) found that the scale effects were accounted for by CFD, in addition to the geometry effect. This feature of CFD is very helpful in design and scale-up of IGLRs and needs to be evaluated further.

2.5 Summary

The literature review of the anaerobic digestion process has helped to highlight the importance of mixing in the process. Considering the advantages and disadvantages offered by various designs of ADrs, a digester mixed by gas recirculation was selected for experimental studies.

Gaslift digesters are geometrically similar to the IGLR, with the exception of the L/D ratio. For gaslift digesters, the L/D ratio is normally close to one, whereas for IGLRs it is greater than two. Because of the considerable literature available related to IGLRs, their hydrodynamics related to flow regimes, gas hold holdup, liquid velocity, liquid mixing, etc. was discussed. The G-L mass transfer characteristics were not discussed because in the case of ADrs, the gas is recirculated only to facilitate liquid mixing. Mass transfer of gas in the liquid phase is not important. Due to lack of information about low L/D ratio IGLRs, the hydrodynamics of gaslift digesters is not known in detail, making their design and scale-up difficult. This is the main motivation behind studying the hydrodynamics of gaslift digesters (low L/D ratio IGLRs) using experimental and computational techniques.

To understand the impact of mixing, hydrodynamic experiments need to be conducted on the selected digester configuration. CARPT and CT were identified as suitable techniques for revealing hydrodynamics of ADrs. In addition, CFD can also be used to study the hydrodynamics of ADrs, but the CFD models need to be evaluated against the experimental data obtained from CARPT and CT. The hydrodynamics of a reactor are significantly affected by its scale of operation; thus, to get a true feel for the magnitudes of hydrodynamic variables like phase velocity and holdup and turbulence parameters in full scale reactors, experimentation/modeling on larger scale is necessary. If these kinds of experiments/modeling are carried out on both small and large scale, the comparison of these results can help in design and scale-up of ADrs.

Chapter 3

Multiple-Particle Tracking Technique: Development, Validation and Implementation

3.1 Introduction and Motivation

The CARPT technique has been utilized for a number of years at the CREL to map flow fields and mixing in various opaque single phase and multiphase systems using a single radioactive tracer particle. Useful hydrodynamic information can be obtained from CARPT studies. CARPT appears to be an ideal technology for application to opaque systems like anaerobic digesters as well. However, the nature of the slurry and the flow in the digester presents some technical challenges that were not encountered in the previous applications of CARPT, including:

1. With gaslift digester designs studied and demonstrated in the chapter 4, we observed very slow flows in some portions of the digesters. These slow flows may have caused possible solids settling. This caused two difficulties: (a) data collection was very slow in certain portions of the reactor and/or under certain operating conditions, and (b) the tracer particle settled in more than one instances and thus caused a halt to data collection. These problems are enhanced with increase in the scale of operation.

2. The slurry in the anaerobic digester consists of particles having different properties (size, shape, and density), while the current CARPT technique used only single-particle tracking.

Thus the data collection process was slow and all the required information such as the hydrodynamic behavior of the solids of different physical properties, the segregation and interaction of the solid particles, could not be obtained by tracking a single radioactive particle.

The current CARPT data-acquisition assembly has many components, which not only makes it bulky, but also expensive. The assembly and the synchronization of the components of single particle CARPT unit is very time consuming and laborious. Since the CARPT was introduced at the CREL in 1990 by Yubo Yang, Moslemian and Devenathan, very few things have been changed with the CARPT hardware. Thus, a development of a new system was required, which will not only extend the capabilities and overcome few of the limitations of the current CARPT system, but will also improve the current CARPT assembly, in terms of accuracy and cost.

The data collection rate and the capability to deal with the settling of the tracer can be greatly improved by the introduction of multiple tracers that can be tracked simultaneously. Multiple-particle tracking can be pursued by introduction of particles containing different isotopes emitting gamma radiation of different energies that can be discriminated. In addition to speeding up the data collection rate for slow flows and reducing the impact of the particle settling, multiple-particle tracking will offer other important advantages, such as the capability to simultaneously track the motion of particles of different size, shape, and density, determining segregation of particles, and probing particle interactions. Use of the advanced technology in designing a new system will also provide an opportunity to make the new assembly compact, cheaper, faster, and easy to operate and understand.

The multiple-particle tracking technique will be a valuable tool for characterization of number of multiphase processes/reactor systems of industrial interests, which use a range of particles with different properties. For example, gas-solid fluidized beds are widely used in process industries for large-scale applications like coal gasification to small scale, polymer and pharmaceutical, production (Lee et al., 2005). These reactors contain a large amount of solids with a wide range of sizes and some times different densities; characterization of flow of these solids of different physical properties can provide valuable information for designing and understanding these systems. Similarly MP-CARPT can be very useful in the evaluation of multiphase processes in GLS and LS fluidized beds, stirred tanks, slurry bubble columns, etc.

To accomplish the above objectives, a new data acquisition system for tracking multiple radioactive particles was designed and manufactured. Because of its ability to track more than one radioactive particle, it was named as Multiple-Particle Tracking Technique and abbreviated as MP-CARPT after CARPT. The system was developed with the help of the team from the Oak Ridge National Laboratory (ORNL) consisting of electronic engineers, software engineers and nuclear engineers. Dr. Alan Wintenberg designed the hardware and electronics, Dr. Lloyd Clonts designed the acquisition software, and Dr. Chuck Alexander provided the input on the radiation and radioactive particles. Dr. David Depaoli oversaw the activities at the ORNL as a Co-PI with Dr. Muthanna Al-Dahhan as project PI. The hardware was assembled at the CREL and the necessary modifications to hardware and software were also made at the CREL.

This chapter covers the validation and implementation of the MP-CARPT. Various issues related to the design and selection of the MP-CARPT system and its components are discussed in this chapter. The details of the hardware and software are provided in the Appendix B. The procedure and the guidelines to operate the MP-CARPT unit is also explained in the Appendix B. The principle of the MP-CARPT, results of the validation and implementation are presented in the following discussion.

3.2 Selection of Radioactive Sources

A number of characteristics should be considered carefully for the selection of the radioactive sources to be used in the MP-CARPT experiments. Following are the main considerations:

- 1. Gamma energy peak:** The MP-CARPT works on the principle of discrimination between different sources based on the gamma energy peak (explained in detail in next section). This requires that the gamma peaks of different particles should be well separated from each other. At least one peak of any one particle should be completely separated from all other peaks of other particles. In addition to that, for MP-CARPT to work, no more than two gamma peaks of two different particles should be overlapped. This criterion narrows the radioactive sources as possible candidates for the MP-CARPT.
- 2. Half-life period:** The activity of a radioactive source is reduced by 50% in time equal to its half-life. Half-life of a radioactive particle can be in the range of few seconds to many years. Since each experiment takes at least a period of 48 hours, neglecting the technical difficulties, the half-life of possible radioactive candidate should be preferably more than 48 hours. But considering the time required for the shipping of activated source, legal formalities, particle preparation, etc., only sources with the half-life of over a month are suitable for the experimentation. Relatively longer half-life guarantees multiple use of particle and reduces the costs of frequent activation. On the contrary, very long half-life means a longer liability on the part of the user for its protection, handling and maintenance.
- 3. Physical state:** The radioactive source to be used as a tracer in must be easy to handle and be able to mimic the phase to be tracked. It cannot be miscible with the system. Thus radioactive sources existing in gas or liquid phase are not suitable for the MP-CARPT. Radioactive sources available in solid phase, such that the density of source can be adjusted (explained in next section), are suitable candidates. In

addition, a radioactive source should also be recoverable after the experimentation, thus it has to be in a solid state or in a solid composite particle. Liquid tracers can be used if enclosed properly in a leak proof casing, but until the safe procedures to do so are identified and benchmarked, and approval is obtained from the Radiation Safety Department, the radioactive sources available in solid state are the only viable choices at this time.

- 4. Density:** The density of the radioactive tracer should match the phase being tracked. For this reason the density of the source is manipulated in different ways to make it either lighter or heavier to match the density of the phase to be tracked. A radioactive source (in solid state) can be coated with suitable material or it can be enclosed in a tiny plastic ball to adjust its density. But if the density of the radioactive source is very high, it would not be easy to adjust its density to the required value. Density is certainly a factor important in the selection of the radioactive source, but it is dependent on the requirements of system to be studied.
- 5. Personnel safety:** The safety of the personnel handling and using the radioactive material is of prime importance. Excessive exposure to radiation causes serious health problems. Thus, the selected radioactive source should possess minimum health risks. It should be easy to handle and easy to clean up in case of contamination.

There are many other considerations in the selection of radioactive source such as physical and chemical properties of the source, cost, ease of availability, ease of activation and legal formalities. The Radiation Safety Department at Washington University controls the possession and use of any radioactive material. The radioactive source should pass the approval of the Radiation Safety Department before being used.

Table 3.1 gives a condensed list of radioactive sources that may or may not be suitable for the MP-CARPT. Only the elements occurring in a solid form with a half life greater than 30 days and less than 5 years are listed in the Table 3.1. The sources which do not

produce gamma or with very low percentage of gamma production are also not listed in Table 3.1.

Table 3.1 List of possible radioactive candidates to be used for MP-CARPT (obtained from Wang, 1969)

Element (mass number)	Half life	Gamma energy MeV (%)	Density (g/cc)	Comments
Beryllium (7)	53d	0.48(10)	1.8	Poisonous
Sodium (22)	2.58y	0.511(180),1.27(100)	0.97	Reactive with water
Scandium (46)	84d	0.89(100), 1.12 (100)	2.9	Can be used
Manganese (54)	303d	0.83(100)	7.3	Can be used
Cobalt (56)	77.3d	0.85(100)-3.3(13)	8.7	Many gamma energies, not suitable
Cobalt (57)	267d	0.12(87), 0.14(11)	8.7	Very low gamma energies
Cobalt (58)	71d	0.81(99), 1.7(0.6)	8.7	Can be used
Cobalt (60)	5.26y	1.17(100),1.33(100)	8.7	suitable
Zinc (65)	245d	1.12(49)	7.1	Low gamma percentage
Selenium (75)	120d	0.14(57), 0.27(60)	4.8	low gamma energies
Rubidium (83)	83d	0.53(93), 0.79(1)	1.5	Spontaneously flammable in air, explosive in water
Rubidium (84)	33d	0.9(74), 0.5(42)	1.5	
Strontium (85)	64d	0.51(100)	2.6	Reactive with water
Yttrium (88)	108d	0.9(91), 1.84(100)	4.5	Suitable
Zirconium (95)	65d	0.72(49),0.76(49)	6.4	Can be used
Niobium (95)	35d	0.77(100)	8.6	Can be used
Ruthenium(103)	40d	0.5(88), 0.61(6)	12.2	Very high density
Antimony (124)	60d	0.6(97), 1.7(50),8 to 2.1	6.68	Many gamma energies
Cesium (134)	2.1y	0.6(98), 0.8(98)	1.87	Explosive in water, reacts with air
Cerium (139)	140d	0.165(80)	6.9	Very low gamma energy
Hafnium (175)	70d	0.34(85)	11.4	Low gamma energy, high density
Osmium (185)	94d	0.65(80), 0.88(14)	22.48	Heaviest element, oxide is poisonous
Iridium (192)	74d	0.32(80), 0.47(49)	22.4	Extremely high density

Upon careful consideration of all the above criteria, Co-60 and Sc-46 were selected for dual-particle tracking. High-energy gamma peak of Co-60 is completely distinguished from other gamma peaks of Sc-46, which satisfies the most crucial criterion. The half life of Sc-46 is only 84 days, which is suitable. Co-60 has a very long half life of 5.27 years is not desirable from safety consideration, but is suitable for frequent use at no additional cost of activation. Co-60 and Sc-46 are both available in solid state with densities of 8.9 and 2.98 g/cm³, respectively. Co-60 is heavier, due to which smaller size particles are required. Smaller the particle, longer is the activation time and harder it is to handle. Thus, Co-60 and Sc-46 may not be the ideal candidates, but they are the best possible alternatives that meet most of the requirements mentioned above at this time for the development, validation and implementation of the MP-CARPT.

3.3 MP-CARPT electronics

Figure 3.1 below shows the schematic of the new MP-CARPT electronics. The connections of the electronics components are shown in Figure 3.2. The MP-CARPT unit essentially consists of detectors, formed by a photomultiplier tube (PMT) connected to the base amplifier. This base amplifier is powered by a power supply unit and the output signal from the base amplifier goes to timing filter amplifier (TFA) input for amplification. Both power supply unit and timing amplifier sit in a NIM bin. Each timing amplifier has 8 channels (one for each detector). The timing amplifier is connected to the pulse processor card (one card is required for one timing amplifier, thus 8 detectors need only one card). The pulse processor card functions as a discriminator, scaler and an interface to the PC. This pulse processor card sits in a compact PCI box and it is connected to the back plane of compact PCI which also holds a PC on a card.

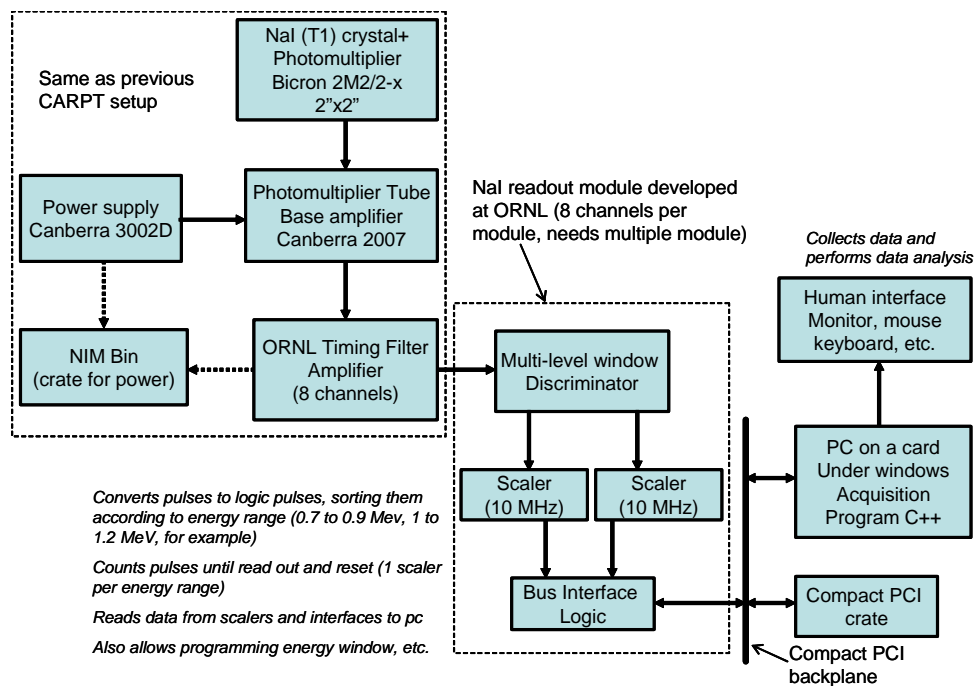


Figure 3.1 MP-CARPT electronics

A single C++ program compiled and run by the user performs the data acquisition according to the needs of the user. Each component of the MP-CARPT unit, its operation and its functions are explained in Appendix B.

Even though the list of electronics is long, it is all contained in only two boxes/crates. This reduces the wiring connections and avoids the lengthy set-up procedures. Less number of components also cuts the costs significantly. Cost estimation of MP-CARPT electronics and its comparison with the cost of the single particle CARPT unit shown in Table 3.2 shows the cost savings of \$ 25,000 obtained with new unit for set-up of 16 detectors. Moreover, the new electronics is advanced, thus it is more efficient and faster in data acquisition.

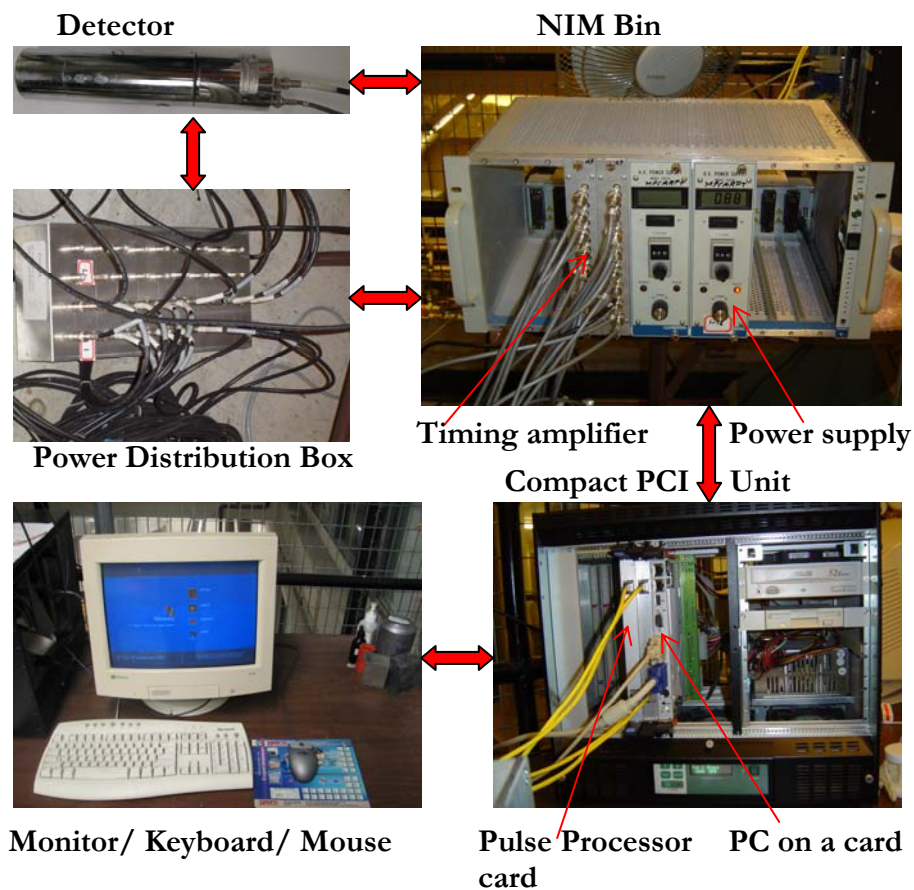


Figure 3.2 MP-CARPT electronics components and connections

3.4 MP-CARPT Validation

3.4.1 Tracking Stationary Particles

The MP-CARPT technique, its principles, operation, and data-processing will be discussed here in reference to the tracking of stationary Co-60 and Sc-46 particles, both for the single-particle tracking and dual-particle tracking. By tracking stationary particles at known locations, the error in the reconstruction can be evaluated and the MP-CARPT electronics and reconstruction algorithm can be validated.

Table 3.2 Cost comparison of old and new unit for 16 detectors

Component	Old single particle CARPT unit		New MP-CARPT unit	
	quantity	cost (USD)	quantity	cost (USD)
PMT and its base	16	16,080	16	16,080
TFA	16 (at \$1,100 each)	17,600	2 (at \$1,200 each)	2,400
Power supply	1	1,540	1	1,540
NIM Bin	2	4,550	1	2,275
Computer	1	500	1 (PC on a card)	5,500
Power Cables	20	200	20	200
Signal Cables	16	1,704	16	1,704
Other Cables	16 (at \$55 each)	880	8 (at \$4 each)	32
Pulse Processor Module	1	15,450	2 (at \$2,000 each)	4,000
Total		58,504		33,731
Savings	\$24,775			

Experimental set-up

16 number of NaI detectors were mounted circumferentially on a stand in 8 columns. Each column had two detectors mounted one over other and separated by 3.9 inches. Two consecutive columns were 45° apart, thus covering whole 360° by 8 columns. The arrangement of detectors is shown schematically in Figure 3.3a and a photograph is shown in Figure 3.3b.

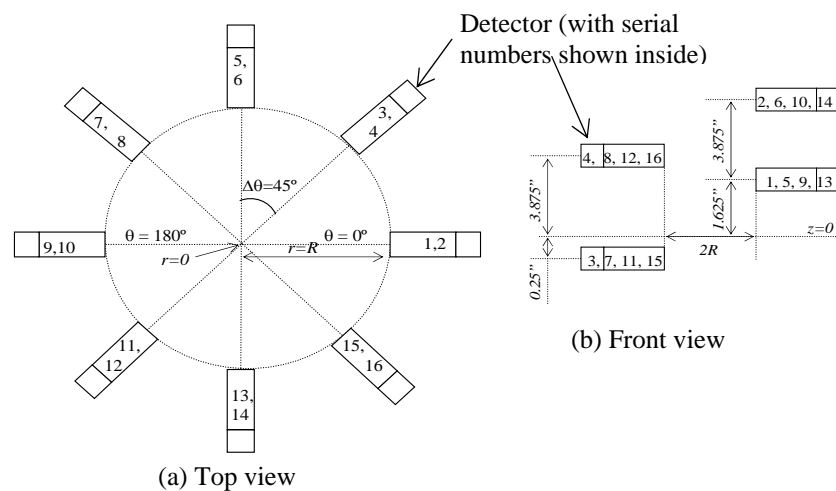


Figure 3.3a Schematic of the arrangement of detectors on detector stand

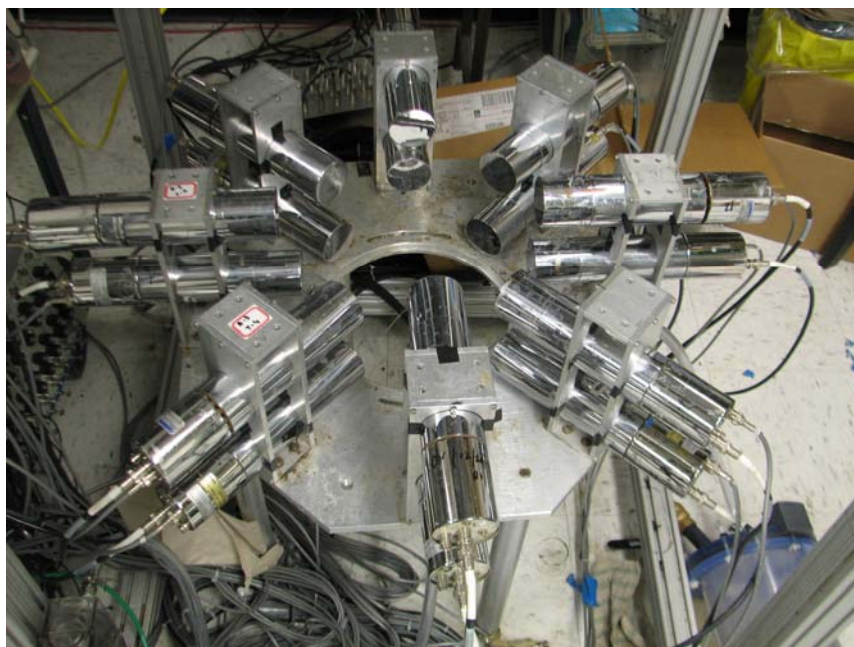


Figure 3.3b Photograph of detector stand

An automated calibration device was used for carrying out the calibration. The device is equipped with a rod to hold the radioactive source at one end. This rod is connected to three separate motors for independent movement of rod in axial, radial and azimuthal direction. The design and details of calibration device are given in detail by Luo (2005).

Co-60 and Sc-46 were used as the radioactive sources. 100 μm Co-60 particle with approximate activity of 100 μCi was enclosed in a 1mm polypropylene ball. The Sc-46 particle was 150 μm in diameter with approximate activity of 150 μCi was also enclosed in a 1 mm polypropylene ball. Enclosing the particles in plastic balls makes it convenient to handle and see the particles and also ensures safe handling.

Principle and Methodology

Gamma peaks obtained by recording the photon counts of Sc-46 and Co-60 in fine mode (fine mode records the counts of all energies as opposed to coarse mode, where only the counts in a selected energy window are recorded) are shown in Figure 3.3. The procedure to obtain scans and operate the MP-CARPT unit is explained in Appendix B. To obtain the counts for generating gamma peaks, the radioactive sources can be placed anywhere within the vicinity of all the detectors, but not too close to the detectors.

The counts obtained from radioactive particles are additive. The total counts of Sc-46 and Co-60 obtained individually are equal to the counts obtained from both sources together, illustrated and proved by Figure 3.4. Figure 3.4 reveals one more important point that forms the principle for discriminating between different radioactive sources. The high energy peak of Co-60 (1.332 MeV) is completely distinguished from other peaks of Sc-46. Thus, if counts of Sc-46 and Co-60 are obtained in such a way that the high energy counts of Co-60 are recorded separately, then reconstruction of Co-60 is a trivial problem similar to reconstruction of single particle in CARPT (see CARPT manual, 2005 for details of reconstruction of single particle tracking). The additive property of counts can be used for reconstruction of Sc-46 particle.

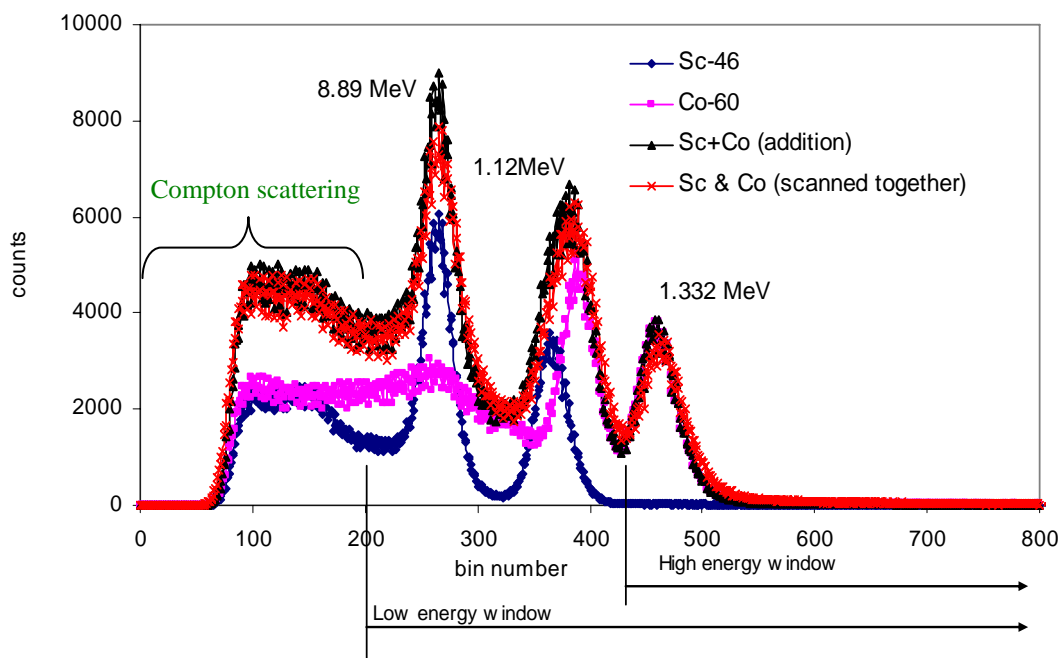


Figure 3.4 Gamma peaks of Sc-46 and Co-60 individually, together and summation of individual counts

Selection of energy windows

The counts of high energy and low energy peaks are separated by setting up the energy windows for discriminator. The new MP-CARPT unit is capable of recording counts in eight separate energy windows. The lower and upper limit of each window can be specified by the user; the windows can also be overlapped if necessary. This gives us the ability of tracking eight different radioactive sources simultaneously. However, tracking and reconstruction of only two radioactive sources is discussed here. Once dual particle tracking is tested and validated then this technique can be extended easily to track more than two radioactive sources.

The first step in the MP-CARPT is to obtain position of energy peaks of Sc-46 and Co-60 for each detector, as shown in Figure 3.4. The limits of energy window for calibration and tracking experiment are obtained from Figure 3.4. The complete energy spectrum is spread from 0 to 1023 bins by discriminator. Lower and higher limit of high

energy window can be 425th and 600th bin, respectively. Thus all the counts corresponding to the energy level from 425th to 600th bin (both inclusive) will be recorded in high energy window. The higher limit can be extended till 1023rd bin, this will necessarily make no difference because the counts of both the sources are zero from bin number 525. But the lower limit has to be specified higher than 425th bin, as only this way the counts of Co-60 can be recorded distinctly without any overlapping from Sc-46. The lower and higher limit for low energy window can be 200th and 425th bin, respectively. Again the lower limit can be as low as bin number zero. But the Compton scatter present in lower bin numbers below 200 introduces error during reconstruction and has to be avoided (see CARPT manual, 2005 for more discussion on Compton scatter). The lower limit can be set as 315th bin to exclude Compton scattering by Sc-46 as well; but it has to be remembered that low span of energy window reduces the number of counts in the window. Lower counts also introduce error in the reconstruction. If the activity of the sources used is high, then the low span of energy window is acceptable. Very high activity of sources however, will cause the problem of peak shift (discussed in Appendix B).

All these points should be considered carefully to select the limits of energy windows. Every detector can have different specifications of limits of energy windows based on the detector settings. Thus, synchronization of detectors is not required when using MP-CARPT unit. Synchronization of detectors means matching the position of gamma peaks for all the detectors. Synchronization of detectors (traditionally referred to as MCA in the CREL) is a major time consuming step with old single particle CARPT unit. A set of 16 detectors needed about 24 to 48 hours for synchronization, more number of detectors required more time. With the new unit, the energy peaks as shown in Figure 3.4 can be obtained even in a fraction of second, but to obtain enough number of counts, the counts should be obtained for at least 15 seconds. 60 seconds of data acquisition is more than sufficient for obtaining Figure 3.4 in all cases; this time is independent of number of detectors. Thus, MP-CARPT unit offers a huge time-saving advantage over the old unit.

Calibration

Two sets of calibration are required for (stationary or moving) dual particle tracking; one for each source, Sc-46 and Co-60, separately. Same limits of energy windows and data acquisition frequency should be used for both calibration and tracking. The suitable value of data acquisition frequency is selected, 50 Hz (50 samples per second) in this case. The data acquisition frequency can be changed by adjusting the acquisition time for each sample in the acquisition program (data acquisition time of 0.02 seconds corresponds to sampling frequency of 50 Hz). Data acquisition frequency cannot be too high or too low for tracking moving particles. Very high values, normally above 100 Hz, introduce noise in the acquired data. The lower limit of allowable acquisition frequency depends on the maximum velocity of moving particle in the system. Low frequencies can cause error in reconstruction, referred to as dynamic bias (Rammohan et al. 2001, Rammohan, 2003).

For calibration, each particle is placed individually (in absence of other source) at several known locations and tracked until desired number of samples are obtained. The data is acquired in coarse mode for the calibration and experiment (details given in Appendix B). The average of all the samples for each calibration location is used for reconstruction. Thus, maximum possible number of samples should be obtained during calibration for better accuracy. 512 number of samples were generally obtained for each calibration location at acquisition frequency of 50 Hz.

The number of calibration points depends on the geometry of the system. Maximum possible number of calibration points should be used. Generally, the geometry of system is divided into number of cells in radial, azimuthal and axial direction as shown in Figure 3.5, the calibration points can be located at either at the centers of the cells or at the nodes of the cells for convenience. The closer the calibration points, more the number of calibration points, thus lesser is the error in reconstruction of particle positions. 250 calibration points were used for tracking stationary particle, in this case. The cylindrical coordinates of calibration points are listed in Table 3.3.

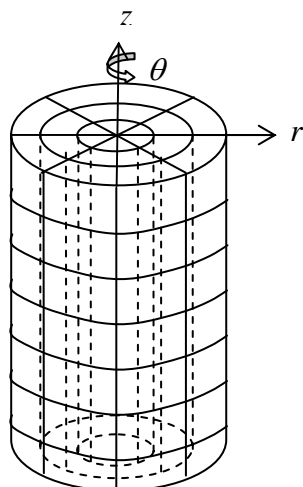


Figure 3.5 Grids for calibration points/locations

Table 3.3 Cylindrical coordinates of calibration points

r (inch)	θ (degrees)	Z (inch)	# of calibration points
0	0	0 to 4.5 (with Δz of 0.5)	$1 \times 1 \times 10 = 10$
1	0 to 330 (with $\Delta\theta$ of 30)	0 to 4.5 (with Δz of 0.5)	$1 \times 12 \times 10 = 120$
2	0 to 330 (with $\Delta\theta$ of 30)	0 to 4.5 (with Δz of 0.5)	$1 \times 12 \times 10 = 120$
Total number of calibration points			250

The calibration process is fully automated and done with the help of calibration device (Luo, 2005). Calibration device is equipped with rod, which can be moved in radial, azimuthal and axial direction with the help of three separate motors. Radioactive particle is placed in a small plastic vial and the vial is attached to the end of the rod during calibration. The movement of motor is computerized and the motor movement program is integrated with data acquisition program. Thus, the calibration location (r , θ and z) is recorded automatically along with data acquisition.

This way the calibration for each particle is carried out separately. The calibration locations for both the particles should preferably be the same, but it is not required to be the same. If counts of Sc-46 and Co-60 together at 'position x ' are required, they can

be readily evaluated by summing up the individual counts of Sc-46 and Co-60, each recorded at the same 'position x '.

The calibration data is obtained in two separate energy windows as explained earlier. Figure 3.6a and 3.6b shows the calibration plot for Sc-46 and Co-60, respectively, for both energy windows for a given detector. The ordinate in Figure 3.6a and 3.6b is the averaged value of counts obtained for 512 samples. The abscissa is the distance of a source from a given detector. The number of counts varies inversely with the distance from the detector; the counts recorded are higher when the source is nearer the detector and vice-a-versa. In Figure 3.6b, for Sc-46, the counts in high energy window are very low; they should be ideally zero, as the Sc-46 peaks do not fall in the high energy window (see Figure 3.4). Non-zero counts are recorded due to the background radiation or the random nature of radioactivity and introduce error in the reconstruction.

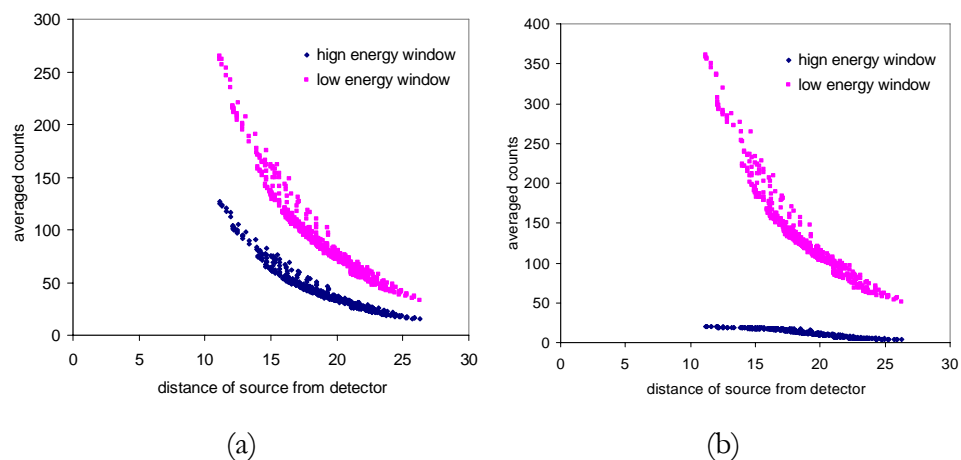


Figure 3.6 (a) calibration plot for Co-60 (b) calibration plot for Sc-46

Stationary Tracking experiment

During the actual tracking experiment, Co-60 and Sc-46 particles were placed together at 48 known locations and counts data was obtained in coarse mode. The limits of low and high energy windows and the data acquisition frequency were equal to what was used during calibration. 64 samples of data at frequency of 50 Hz were obtained for

each of 48 known locations. 48 locations were strategically selected, such that only 50% of the locations were same as calibration locations. Reconstruction of non-calibrated locations helps to test the accuracy of the reconstruction algorithm. The particles were placed at $r=1$ inch, $\theta=0^\circ$ to 345° with $\Delta\theta=15^\circ$, and $z=2$ and 3 inches, thus total $1 \times 24 \times 2 = 48$ locations.

Traditionally for tracking a moving particle in any reactor system, the particle is released into the system and it is tracked for at least a period of 24 hours at a suitable data acquisition frequency. The particles were kept at known stationary locations in this experiment for validation of the technique and to evaluate the error in the reconstruction.

Reconstruction

Obtaining the location of the radioactive particles from the acquired count data is called particle position reconstruction. The reconstruction algorithm is shown in Figure 3.7. Since the limits of high energy window are selected such that only counts of Co-60 are recorded in that window, the reconstruction procedure of Co-60 is exactly similar to that of single particle CARPT. Reconstruction procedure of single particle tracking is explained in short here, see CARPT manual (2005) for more details.

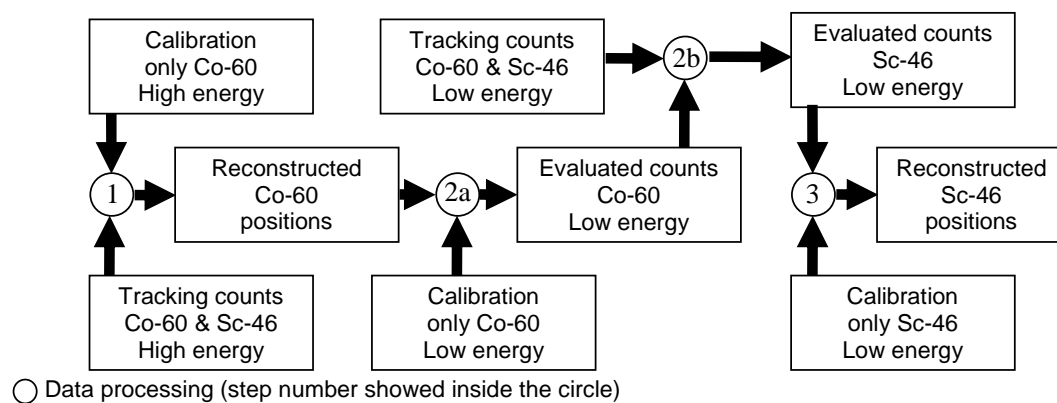


Figure 3.7 Reconstruction algorithm for dual-particle tracking

The first step is to reconstruct the Co-60 positions. The calibration curve of Co-60 (for high energy window) is fitted using spline fitting and spline coefficients are obtained for each detector. Using these coefficients, if the counts of Co-60 in high energy window for a particular detector are known, the distance of particle from a given detector can be evaluated. Then the counts from the experiment are used to calculate the distance of the particle from each detector using spline fit coefficients. Now we have N number (equal to number of detectors) of known distances and three unknown coordinates (x, y and z) to evaluate (see equation 5.1).

$$d_i = \sqrt{(x - x_i)^2 + (y - y_i)^2 + (z - z_i)^2} \quad \text{for } i = 1 \text{ to } N \quad (5.1)$$

where, d_i is the distance of particle from i^{th} detector

(x_i, y_i, z_i) are the coordinates of i^{th} detector

N is the number of detectors

Thus, it becomes a problem of solving a system of N nonlinear equations using a least square approximation method to evaluate three unknowns (where $N > 3$). The least square approximation function is given in equation 5.2.

$$f(x, y, z) = \sum_{i=1}^N \left\{ \left[(x - x_i)^2 + (y - y_i)^2 + (z - z_i)^2 \right] - d_i^2 \right\} \quad (5.2)$$

The reconstructed positions evaluated in this manner are then filtered to remove any noise in the processed data, encountered due to the random nature of radioactivity. More details of reconstruction and filtering are given in CARPT manual (2005). An alternate, more accurate method of reconstruction was formulated by Bhusarapu (2005). But this method is computationally very time-consuming.

Next step is to obtain the counts of Sc-46 only from the low energy window. The counts in low energy window are contributed both by Co-60 and Sc-46. If we can

estimate the counts of Co-60 in the low energy window, the counts of Sc-46 can be obtained by subtracting the counts of Co-60 from the total counts of low energy window. Again spline fitting can be used here. By knowing the distance of Co-60 particle from a particular detector, the number counts recorded by given detector can be evaluated by using spline fit coefficients. Since we want to evaluate counts of Co-60 from low energy window, the calibration curve of Co-60 for low energy window is used here. The distances of Co-60 particle are known because the Co-60 locations are ALR eady reconstructed in step one. For each experimental data, the Co-60 counts in low energy window are evaluated and then subtracted from the total counts of low energy window. Thus, we end up with counts of only Sc-46 in low energy window.

Step three, is to reconstruct the positions of Sc-46. It is exactly similar to step one, since the counts are known, and calibration curve (for Sc-46 low energy window) is available.

The reconstructed positions of Co-60 and Sc-46 (tracked together) using above reconstruction method are shown in Figure 3.8a and 3.8b, respectively. The error in reconstruction of Co-60 is less than 5% for x and y coordinates whereas 15% for z coordinates because the calibration grid in z direction was coarser than in x and y direction. The error in reconstruction of Co-60 is less than Sc-46 because the Sc-46 counts do not interfere with Co-60 in high energy window. But the error in reconstruction of Sc-46 is less than 5% for x-coordinates, about 25% for y-coordinates and 20% for z-coordinates. This error is very large and unacceptable. There are two main reasons for this large error in reconstruction of Sc-46.

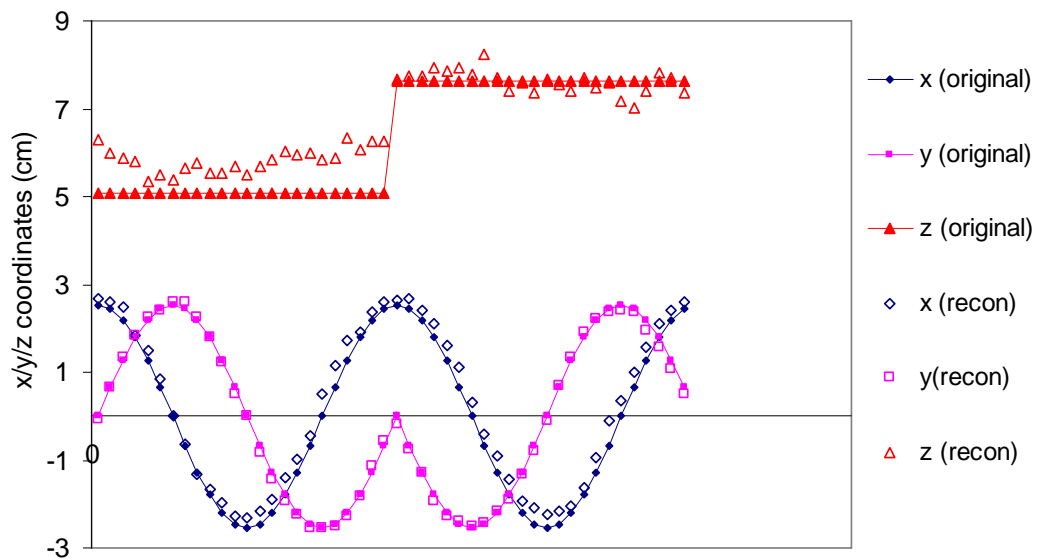


Figure 3.8a Reconstructed positions of Co-60 and comparison with original experimental positions

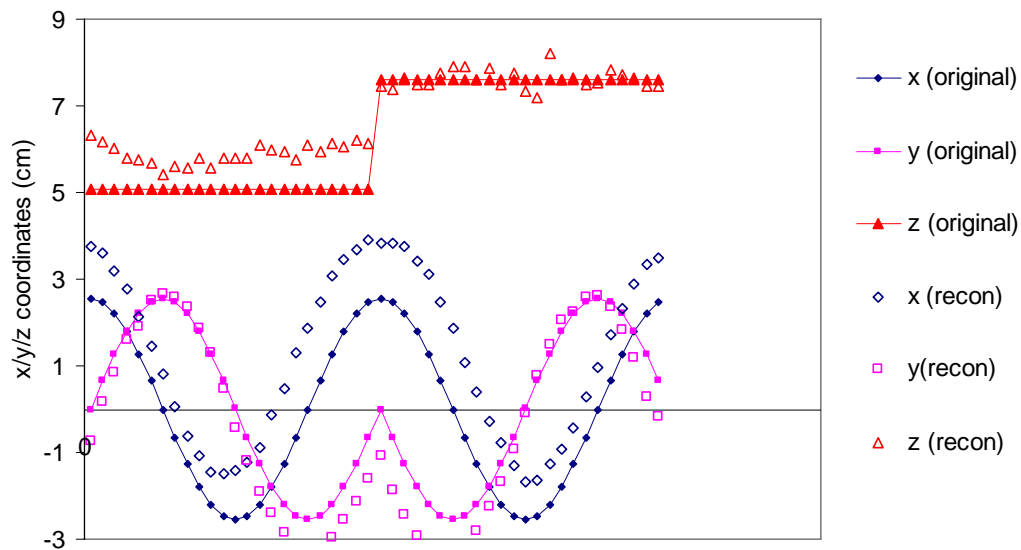


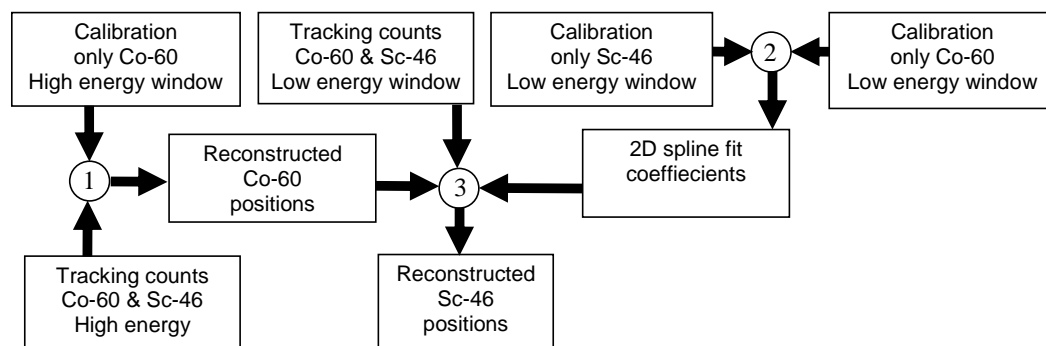
Figure 3.8b Reconstructed positions of Sc-46 and comparison with original experimental positions

First, the reconstructed Co-60 positions are used in the reconstruction of Sc-46. The small error in Co-60 reconstructed positions contributes and amplifies the error caused due to numerical approximations during reconstruction and due to the random nature

of radioactivity. The second reason for large error is due to the subtraction of counts carried out in step two of reconstruction (see step 2b in Figure 3.7). The result of subtraction is sometimes a negative number, which is treated as zero counts in reconstruction program and introduces error. Recall that the calibration counts are average of large number of samples where as the experimental counts are very random in nature, which is the main reason of error in reconstruction. Therefore, a new methodology for particle reconstruction is needed.

New Reconstruction Methodology

To avoid the large error in the reconstruction of Sc-46, the subtraction of counts of Co-60 from total low energy window counts has to be avoided. Thus, a new reconstruction scheme has been developed. Since the Co-60 reconstruction involves negligible error, same procedure as described before (step 1) can be used for Co-60 reconstruction. A new reconstruction algorithm for Sc-46 positions is described below and shown in Figure 3.9.



○ Data processing (step number showed inside the circle)

Figure 3.9 Modified reconstruction algorithm for dual-particle tracking

2D (two-dimensional) spline fitting is done using three variables, the total counts of Co-60 and Sc-46, distance of Co-60, and distance of Sc-46 from a particular detector. By knowing two of these variables, third unknown can be evaluated by the spline coefficients obtained through 2D spline fitting. Distance of Co-60 from any detector is

known, because Co-60 positions are reconstructed. Total counts of Co-60 and Sc-46 are available in low energy window from tracking experiment. Thus, the third unknown distance of Sc-46 from every detector can be evaluated using 2D spline fit coefficients. Important point to note here is, distances of Sc-46 are directly obtained from spline fitting. The step to obtain counts by subtraction is eliminated. Thus the error in reconstruction due to subtraction as well as obtaining distances from Sc-46 counts is eliminated.

The first task would be to generate a 2D spline fit plane. Calibration counts of only Co-60 and only Sc-46 from low energy window can be added to obtain total counts of Co-60 and Sc-46 in low energy window, as shown below.

Calibration counts of Co-60 for i^{th} detector, $C_i = [c_1 \quad c_2 \quad c_3 \dots c_j \dots \quad c_n]_i$

Calibration counts of Sc-46 for i^{th} detector, $S_i = [s_1 \quad s_2 \quad s_3 \dots s_j \dots \quad s_n]_i$

Total counts of Co-60 and Sc-46 for i^{th} detector,

$$T_i = \begin{bmatrix} t_{1,1} & t_{1,2} & \dots t_{1,k} \dots & \dots & t_{1,n} \\ t_{2,1} & t_{2,2} & \dots & \dots & \dots \\ \dots t_{j,1} \dots & \dots & t_{j,k} & \dots & t_{j,n} \\ \dots & \dots & \dots & \dots & \dots \\ t_{n,1} & t_{n,2} & \dots & \dots & t_{n,n} \end{bmatrix}_i \quad \text{where, } t_{j,k} = c_j + s_k$$

Where c_j are the counts of Co-60 at the calibration location j

s_k are the counts of Sc-46 at the calibration location k

$t_{j,k}$ are the total counts of Co-60 and Sc-46 with Co-60 at the calibration location j and Sc-46 at the calibration location k

n is the total number of calibration points

Every count c_j in matrix C_i is associated with distance $d_{j,i}^c$ i.e. distance of Co-60 at j^{th} location from i^{th} detector. Similarly, every count s_j in matrix S_i is associated with distance $d_{j,i}^s$ i.e. distance of Sc-46 at j^{th} location from i^{th} detector, such that;

Distance of Co-60 calibration locations from i^{th} detector,

$$D_i^c = [d_{1,i}^c \quad d_{2,i}^c \quad \dots d_{j,i}^c \dots \quad d_{n,i}^c]$$

Distance of Sc-46 calibration locations from I^{th} detector,

$$D_i^s = [d_{1,i}^s \quad d_{2,i}^s \quad \dots d_{j,i}^s \dots \quad d_{n,i}^s]$$

Using matrix D_i^c , D_i^s and T_i , 2D spline fit plane can be generated and spline fit coefficients can be obtained. Unlike 1D spline fitting, we have generated a calibration plane, as shown in Figure 3.10, instead of a calibration curve.

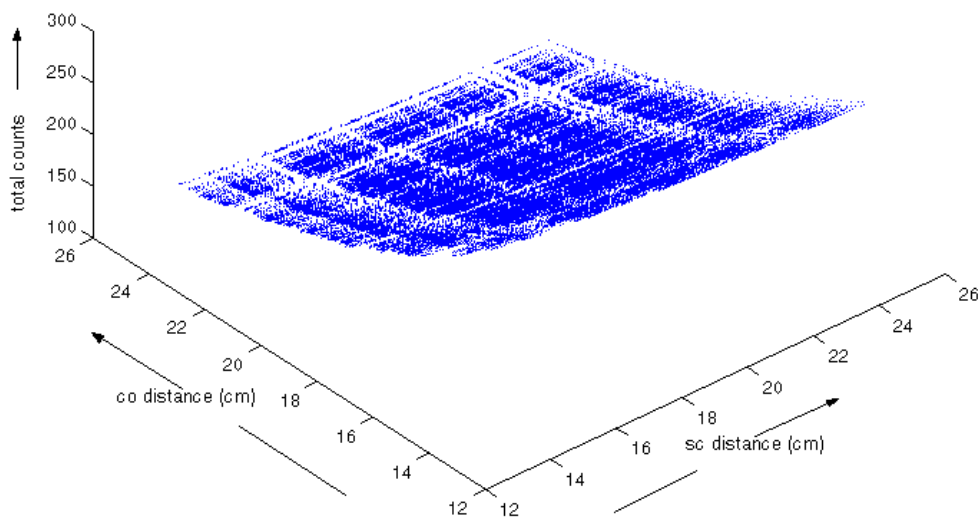


Figure 3.10 Calibration plane for detector 1 for low energy window total counts of Co-60 and Sc-46.

Next, using the total counts of Co-60 and Sc-46 in low energy window from tracking experiment and corresponding reconstructed distance of Co-60 for each count data, distance of Sc-46 from each detector can be evaluated. Again, as described above, by least square approximation of these distances, coordinates of Sc-46 can be evaluated.

The reconstruction of Sc-46 locations using this new algorithm is shown in Figure 3.11. There is significant improvement in the reconstructed positions with new algorithm as compared to one with old algorithm. The error in reconstruction of x and y coordinates

is very small as compared to error in z co-ordinate. This is due to the larger calibration grid size (1 inch) in z direction (see Table 3.3).

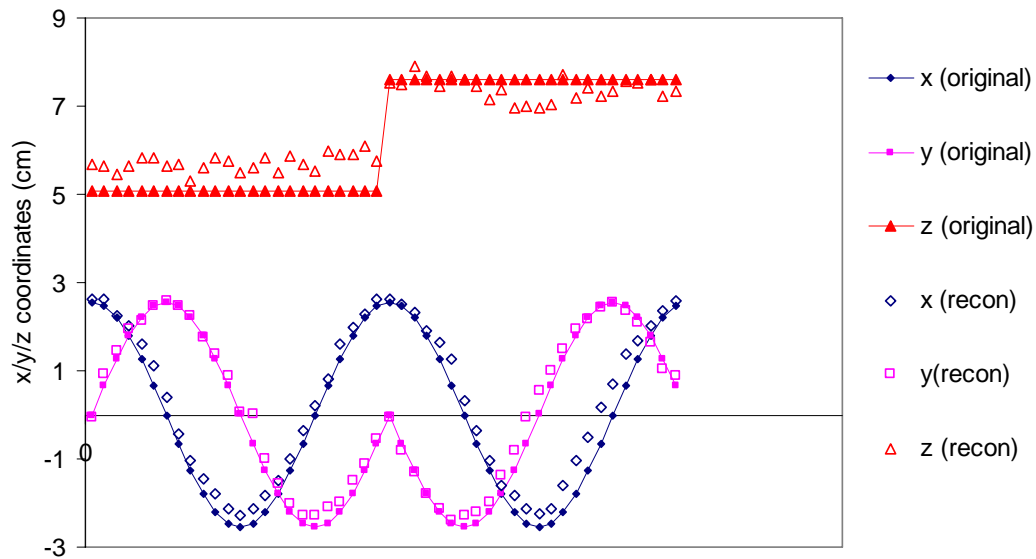


Figure 3.11 Comparison of original Sc-46 locations with reconstructed positions using new algorithm

The results of reconstruction of Co-60 and Sc-46 scanned together with the new MP-CARPT unit shows that the MP-CARPT unit can be satisfactorily used to track two particles simultaneously. Thus the new technique MP-CARPT is validated for tracking two stationary radioactive sources successfully. In the next section this technique will be implemented to track Co-60 and Sc-46 together moving independently in a cold reactor system.

3.4.2 Tracking Particles in Motion

Both old single particle CARPT and MP-CARPT units were used for this validation experiment. The objective was to evaluate the results of new unit with the benchmarked data obtained by old CARPT unit and ensure that new unit is providing correct results for tracking moving particles.

Experimental set-up

An acrylic tank of 15.2 cm diameter and 34 cm in height, as shown in Figure 3.12, was used for this experiment. Tank was equipped with a sparger to circulate air and draft tube with 7.6 cm diameter and 14 cm height. Tank was filled with water upto a level of 22 inches. Air was sparged at a rate of 5 lpm. The tank was placed on a detector stand in the center surrounded by 16 NaI detectors arranged circumferentially.

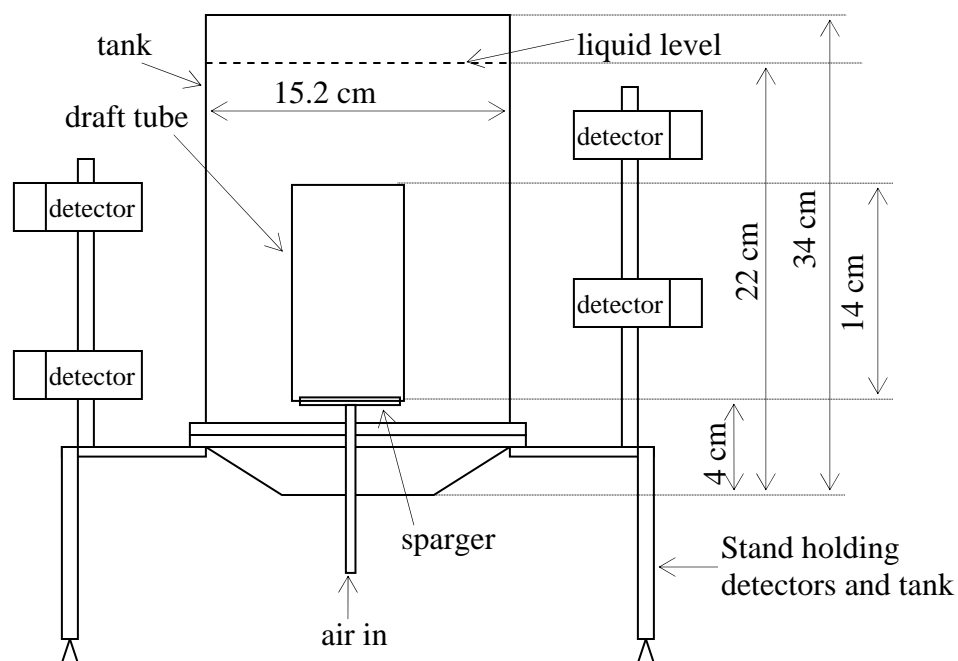


Figure 3.12 Experimental set-up for dual particle tracking

Co-60 and Sc-46 were used as the radioactive sources. 100 μm Co-60 particle with approximate activity of 100 μCi was enclosed in a 1mm polypropylene ball to adjust its density equal to that of water. The Sc-46 particle was 150 μm in diameter with approximate activity of 150 μCi was also enclosed in a 1 mm polypropylene ball. The density of both particles was adjusted equal to that of water to mimic the water phase.

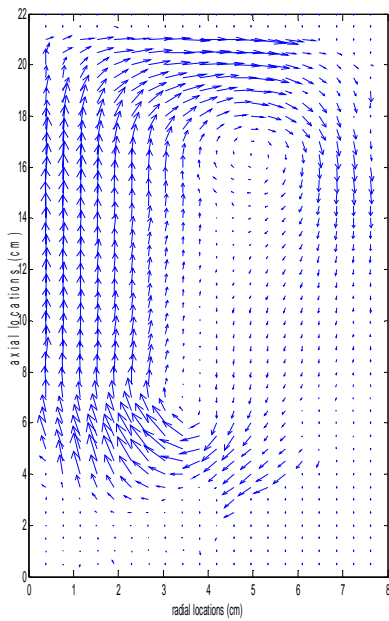
Both old single particle CARPT unit and new MP-CARPT unit was used to track the Co-60 and Sc-46 particles individually. MP-CARPT unit was used to track Co-60 and Sc-46 together. For MP-CARPT unit, the limits of low energy window were set from bin number 200 to 425, whereas the limits of high energy window were from bin number 425 to 600. Calibration was done separately for old and new unit at 500 different known locations for individual Co-60 and Sc-46 particle using both units. The data acquisition frequency was 50 Hz.

Co-60 and Sc-46 were tracked individually with the old and new unit and together with new unit. For the tracking experiment radioactive particles were introduced in the system and data for every condition with both units was acquired for a period of 24 hours at a frequency of 50 Hz.

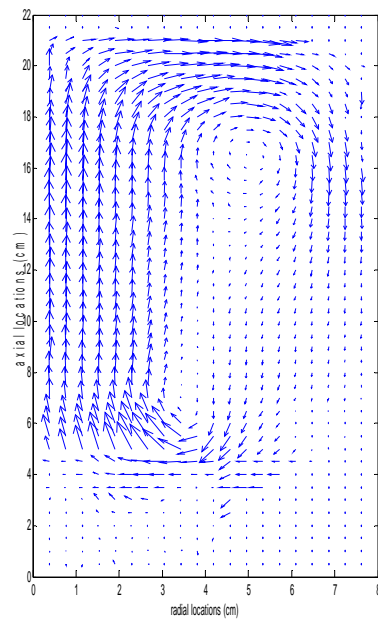
Reconstruction Results

The modified algorithm (Figure 3.9) was used for reconstruction of Sc-46 positions from the dual particle tracking data. For all other tracking experiments, the reconstruction was treated as in single particle tracking. The reconstructed position data is actually the instantaneous position data for the particle. Since the acquisition frequency is known (50 Hz), the time lap between 2 consecutive positions is also known (0.02 seconds). The instantaneous position data can be processed to obtain instantaneous velocities. Time averaged, azimuthally averaged axial and radial velocities can be obtained from instantaneous velocity data and this can used to obtain time averaged flow pattern of moving particles and turbulence quantities. Post-processing of reconstructed data is explained in detail in the CARPT manual (2005).

The flow patterns obtained from each of the tracking experiment viz. for Co-60 and Sc-46 with old CARPT unit, Co-60 and Sc-46 tracked separately with new MP-CARPT unit and Co-60 and Sc-46 tracked together with new MP-CARPT unit are shown in Figure 3.13a to 3.13f, respectively. All the flow patterns look more or less the same and actual difference between the data is not clearly noticeable.

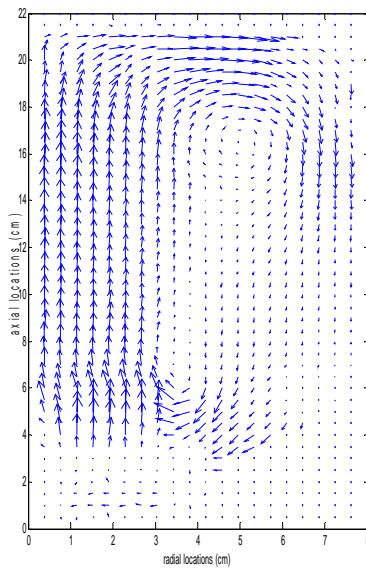


(a) Co-60

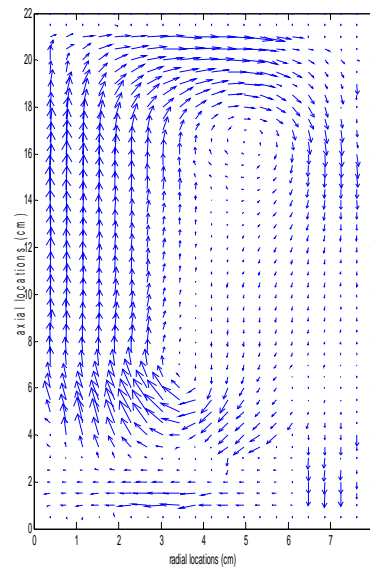


(b) Sc-46

Figure 3.13a & 3.13b Flow pattern obtained from single particle CARPT unit for Co-60 and Sc-46, respectively

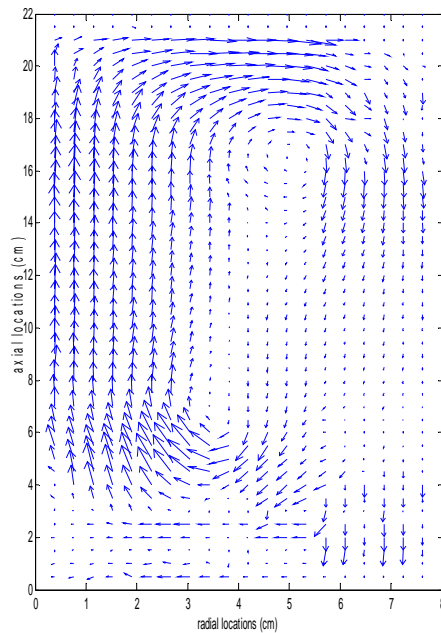


(c) Co-60

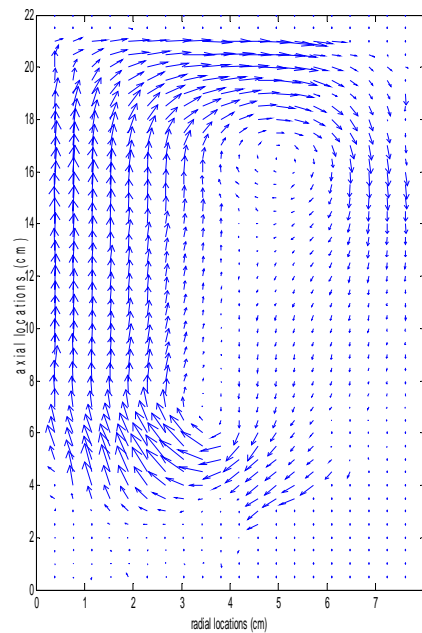


(d) Sc-46

Figure 3.13c & 3.13d Flow pattern obtained from MP-CARPT unit for Co-60 and Sc-46, tracked separately, respectively



(e) Co-60



(f) Sc-46

Figure 3.13e & 3.13f Flow pattern obtained from MP-CARPT unit for Co-60 and Sc-46, tracked together, respectively.

Radial profiles of average axial velocity can be compared to evaluate the quantitative differences between the data obtained from old unit and new unit, and between the single particle tracking and dual particle tracking. Figure 3.14 shows the comparison of time averaged azimuthally averaged axial velocities at the center of the tank for Co-60 and Sc-46 particles for different set of experiments. The magnitude of axial velocity is slightly different for every case, but this error is acceptable and is within the range associated with CARPT itself.

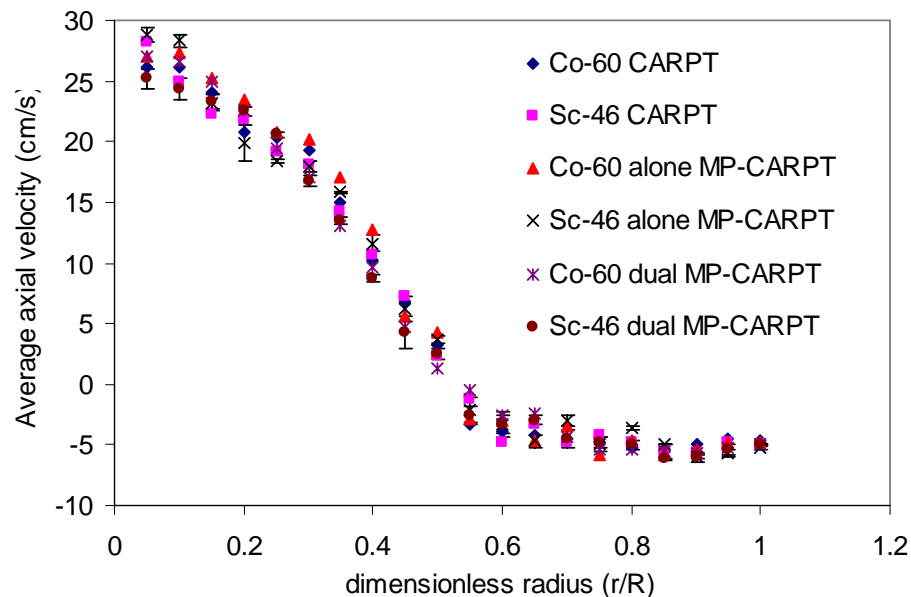


Figure 3.14 Comparison of time averaged azimuthally averaged axial velocity at the center of the tank

3.4.3 Tracking Two Moving Particles with Different Densities

Majority of the processes of industrial interest are multiphase in nature and normally consists of solid particles suspended in liquid or gas phase. In such processes it is of particular interest to evaluate the effect of presence of one phase on the hydrodynamics of the other phase. This can be done using the single particle CARPT by repeating the tracking for each phase separately as only one phase can be tracked at a time. Using the MP-CARPT both phases can be tracked together at the same time, thus the time required for such experiments is considerably reduced. However there are certain limitations in performing such experiments, especially to track liquid phase in a LS or GLS system. These limitations will be discussed in the following sections.

To demonstrate the use of MP-CARPT to track two tracers representing different phases a low L/D (slurry level to reactor diameter ratio $\cong 1$) slurry bubble column

reactor (SBCR) with low solids loadings was used. SBCR consists of solids moving in a liquid phase due to the sparging of a gas.

Experimental set-up

A six-inch diameter acrylic cylindrical vessel shown in Figure 3.15 was used for this study. The system was operated as a slurry bubble column reactor (SBCR). The distributor plate had 139 holes of 1.32 mm diameter each, arranged in a triangular pitch of 1 cm. The distributor plate had open area of 1.04%. The tank was filled with 4 liters of water. 40 gms of 300 micron glass spheres (2.5 gm/cc density) were added to the water, such that slurry had 1 % (by weight) solids. Air was sparged at the rate of 50 SCFH, such that superficial gas velocity in the tank was 2.154 cm/sec. The average gassed liquid height was 22 cm.

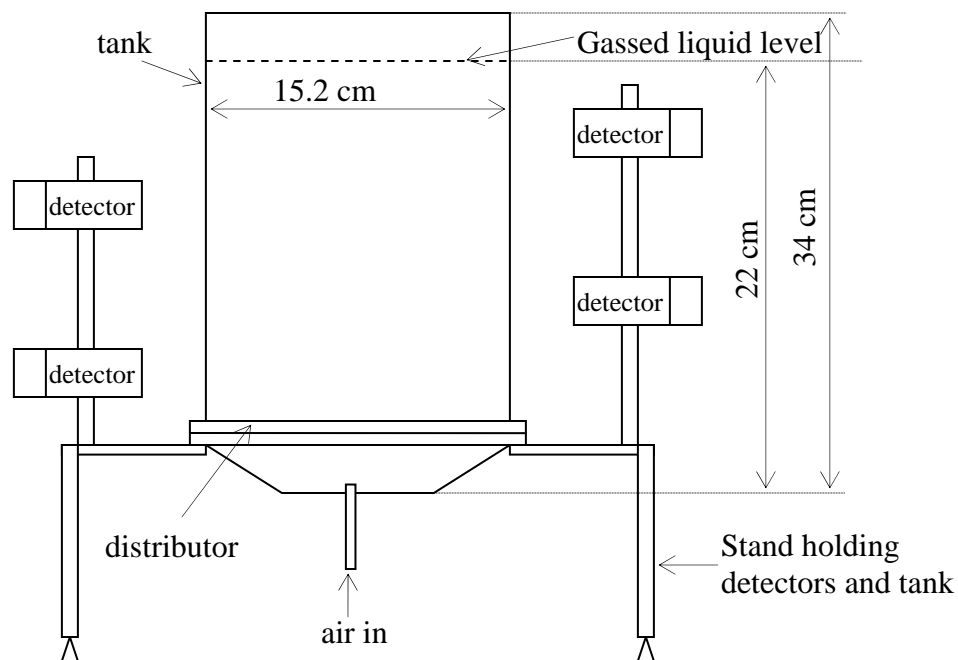


Figure 3.15 Experimental set-up for tracking two particles with different densities

A 300 μm Sc-46 particle with approximate activity of 100 microCi was used to mimic the solid phase. The Sc-46 particle was actually 276 μm in diameter and then coated

with polypropylene up to 300 μm to adjust its density to 2500 Kg/m^3 . The Co-60 particle was 100 μm in diameter and 100 μCi in strength. Co-60 particle was enclosed in a 1mm polypropylene ball and its density was adjusted to 1000 Kg/m^3 using glue to fill the air gap. The Co-60 particle was used to mimic water used as the liquid phase.

Similar 16-detector set-up (shown in Figure 3.3) was used in this study as used in the previous experiments. Three sets of experiments were performed, all of them using MP-CARPT unit. Two experiments where Co-60 and Sc-46 particles were tracked separately as liquid phase and solid phase, respectively. Then both the particles were released in the system and were tracked together in the third experiment. This allowed the validation of results of dual-particle tracking of different densities against the single-particle tracking results.

527 calibration points were obtained for each particle and 512 samples were collected for each calibration point at data acquisition frequency of 50 Hz. The limits of low energy window were set from bin number 250 to 475, whereas the limits of high energy window were from bin number 475 to 640.

In each of the three experiments particles were tracked for total of 20 hours at frequency of 50 Hz.

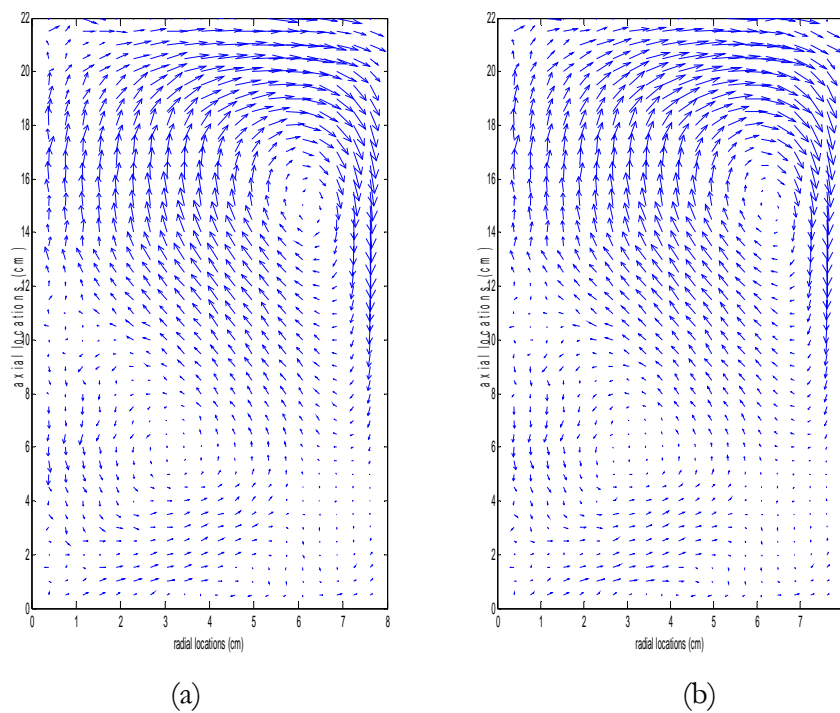
Results

Single-particle tracking reconstruction algorithms were used for single-particle tracking and for Co-60 reconstruction in dual-particle tracking, whereas the modified algorithm was used for reconstruction of Sc-46 in dual-particle tracking. The flow patterns obtained for Sc-46 and Co-60 are shown in Figure 3.16a to 3.16d. The flow patterns for Co-60 from single-particle and dual-particle tracking look the same. This is also the case for Sc-46 particles. It is very interesting to note that the flow patterns for a low L/D SBCR are significantly different than the flow patterns of solid or liquid phase in a high L/D SBCR. The flow patterns in a high L/D SBCR were obtained by Novica (2003).

Figure 3.17 shows the radial profile of azimuthally averaged axial velocity at the center of the column. The error bars are also shown in Figure 3.17. The dual particle tracking experiment was repeated to obtain the error. It can be seen that the difference between velocities obtained from the single-particle and dual-particle tracking is not significant as it is less than the error associated with the reconstructed data.

The error associated with Sc-46 reconstruction is more than the error associated with Co-60. The reasons for this were explained before.

These results show the ability of the new MP-CARPT unit to track two radioactive particles of different densities. However, it has to be remembered that the solid fraction in the system was kept low to 1%, so that the collisions between the Sc-46 particle tracking liquid phase and the solids in the system can be kept to minimum. If the solids hold up is too high then the true hydrodynamics of liquid phase cannot be obtained due to the interference created by solids in the system to the tracer mimicking liquid phase.



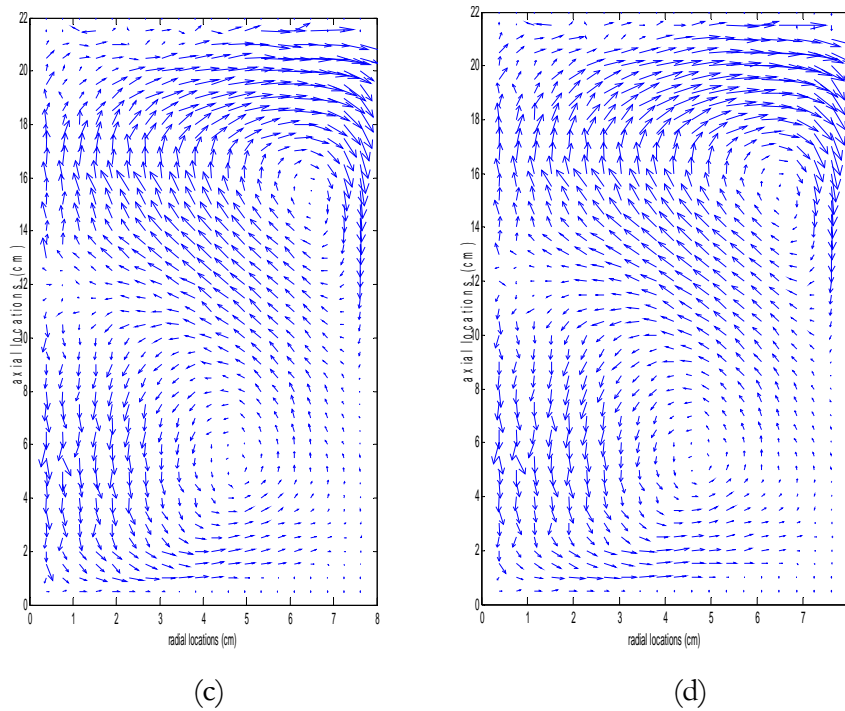


Figure 3.16 (a) Co-60, single-particle tracking (b) Co-60, dual-particle tracking
(c) Sc-46, single-particle tracking (d) Sc-46, dual-particle tracking

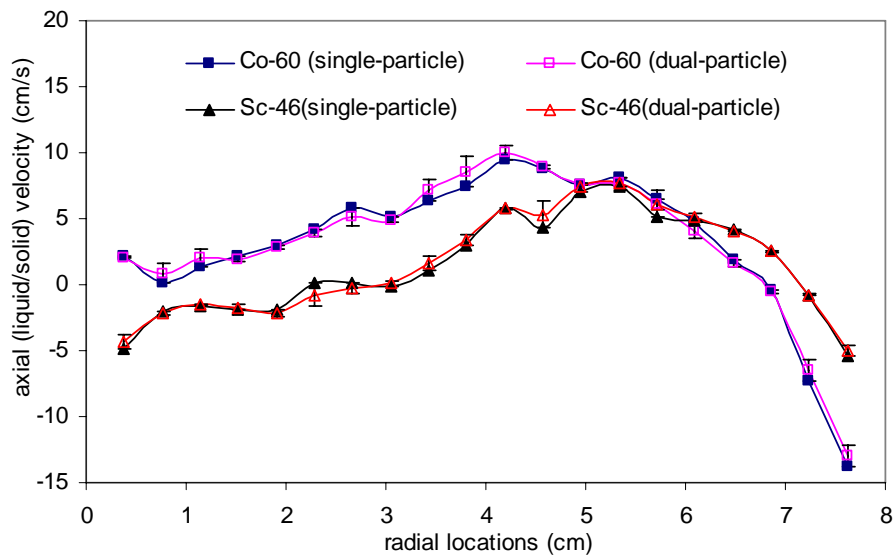


Figure 3.17 Comparison of axial velocity profiles obtained from single-particle and dual-particle tracking for Co-60 and Sc-46 with different densities.

3.4 Summary and Recommendations

New MP-CARPT unit offers number of advantages over the old single particle CARPT unit. The new unit is compact, cheaper, faster, and easy to use and operate. It provides ability to track eight different radioactive sources simultaneously.

The MP-CARPT electronics and technique was validated to track two stationary particles simultaneously. A new reconstruction algorithm was developed which shown very small error in reconstruction of Co-60 and Sc-46 particles. The validation was taken further to next step to track two moving particles representing the same liquid phase. The MP-CARPT was successful in tracking two particles in motion as well. Next, two radioactive particles of different densities, one mimicking liquid phase and other solid phase, were tracked in SBCR. The particles representing different phases could also be tracked simultaneously using MP-CARPT unit.

The solids fraction in SBCR was kept low to 1% to obtain true hydrodynamic information of liquid phase. When tracking two different phases, ex. solid and liquid, care should be taken to design the experiment in such a way that the tracer follows the represented phase as closely as possible. Collisions of tracer representing liquid phase with the solid particles in the system can be minimized by using very low solids fraction.

MP-CARPT can be used conveniently to track two or more solids phases in a system with different properties (for example size, shape or density). However, how much difference in size or density of tracers is required so that the tracers can provide true hydrodynamics of phase being tracked needs to be evaluated. This issue can be addressed by tracking tracers of same size and different densities or same density and different sizes and observing the difference in hydrodynamics.

Having validated the dual particle tracking, this technique can be easily extended to track more than two radioactive sources simultaneously. The current unit is capable of tracking maximum of eight sources at a time, but it is limited due to availability and suitability of radioactive sources for this technique.

The error in the reconstruction of the MP-CARPT can be further reduced by some modifications of the experimental set-up, procedures, and the reconstruction algorithms. If the number of detectors for tracking are increased, such that the detector are packed closely together, then the error in the reconstruction will be reduced due to increased spatial resolution (CARPT manual, 2005). The current MP-CARPT reconstruction algorithm is based on the principle of addition of the calibration counts of Co-60 and Sc-46 obtained separately to represent the counts obtained together. Instead if the calibration is performed with the Co-60 and Sc-46 particles present together, keeping one particle fixed at one location and placing other particle at all the calibration locations one by one and thus covering all the possible permutations, then more accurate calibration region can be obtained. This calibration technique will take into consideration the effect of presence of two particles together on their total counts. The reconstruction method developed by Bhusarapu (2005) can be also be used for the increased accuracy.

Since the technique is validated and the protocols for operation of MP-CARPT unit are understood, a manual for MP-CARPT is prepared. This manual will help future novice users to understand and operate the MP-CARPT electronics and also and provide guidelines to process the raw data obtained from tracking experiments using the new electronics.

Chapter 4

CARPT Studies:

Laboratory-Scale and Pilot-Scale

4.1 Introduction and Motivation

The results of the performance studies (Appendix A) showed that the scale of operation has a significant effect on the performance of digesters. Mixing affects the performance of large-scale digesters but not of laboratory-scale digesters. Performance of digesters is partly governed by the mixing characteristics/ hydrodynamics inside the digester, which in turn is affected by the scale of operation. To evaluate the effect of scale on the hydrodynamics information of hydrodynamics in the digester is required. As mentioned in chapter 2, the hydrodynamic information about the low L/D ratio gaslift digesters is lacking. Thus, there is need to investigate the hydrodynamics of these gaslift digesters in detail. Due to opaque nature of the slurry in the digester, advanced non-invasive techniques like Computer Automated Radioactive Particle Tracking (CARPT) and Computed Tomography (CT) are needed to discern the hydrodynamics of digester. CARPT provides 3D flow pattern, velocity profiles and turbulence parameters, while CT provides time averaged cross sectional phase holdup distribution. This chapter is focused on the digester hydrodynamic investigation using CARPT measurements performed on laboratory-scale and pilot-scale digesters, which are geometrically similar

to the digesters used in performance studies. However, the phase holdup distribution study using CT at same conditions of CARPT is part of other doctoral thesis (by Rajneesh Varma at CREL). The geometric and operating conditions are varied to evaluate their effect. Flow patterns, liquid velocity profiles, turbulence parameters such as shear stress, turbulent kinetic energy, and eddy diffusivities were evaluated to understand the nature of the flow in the digesters at two scales and differentiate between them. Mixing intensity is quantified in terms of dead space volume and turbulent diffusivities to understand the effect of scale.

4.2 Experimental Set-up

4.2.1 Laboratory-scale

A six inch (15.24 cm) diameter acrylic tank equipped with a draft tube and a conical bottom with a slope of 25° , as shown in Figure 4.1a was used as a digester. The geometry of the digester and the operating conditions were maintained similar to the performance experiments described in Appendix A. The slurry level was 22 cm and working liquid volume was 3.78 liters. Gas was introduced at the bottom of the tank using a sparger. Two different types of spargers were used; viz., a single point sparger and a cross sparger. Single point sparger was a pipe with a single opening of 5 mm diameter, while the cross sparger had 4 holes (facing towards the bottom of the tank) of 1.7 mm each. Schematic of the cross sparger is shown in Figure 4.1b. Four arms of cross sparger extended inside the draft tube and covered 50 % of the draft tube cross sectional area. The spacing of sparger hole from the center of the tank was $\sqrt{2}D/2$; where D is the diameter of the draft tube. Draft tube diameter was changed from 3.8 cm to 7.6 cm and 11.4 cm, such draft tube diameter to tank diameter ratio (D/T) is 0.25, 0.5 and 0.75 respectively. The length of the arms of cross sparger was also changed with respect to the draft tube diameter.

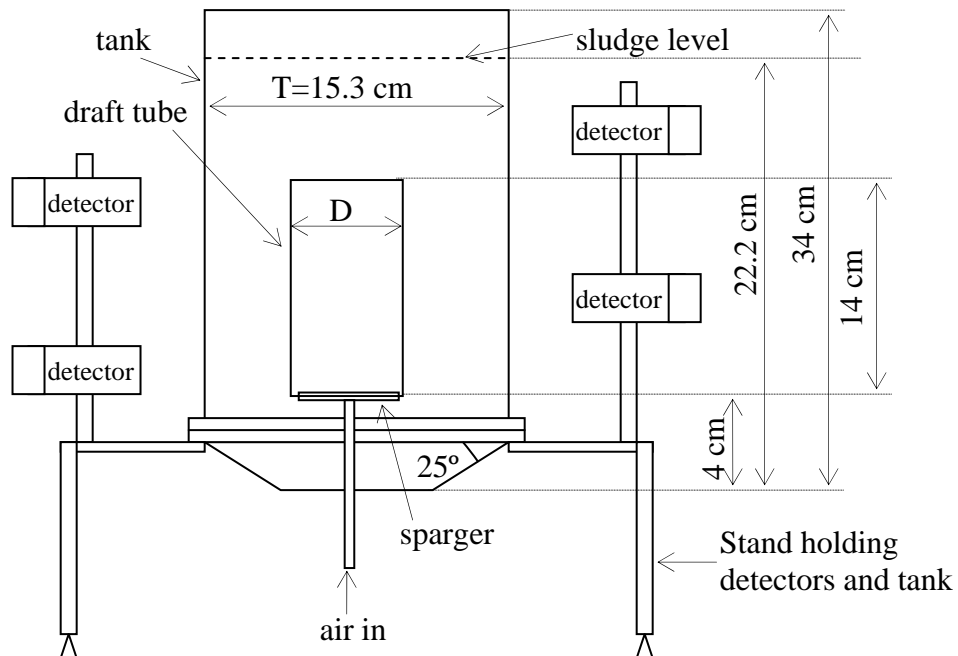


Figure 4.1a Digester geometry

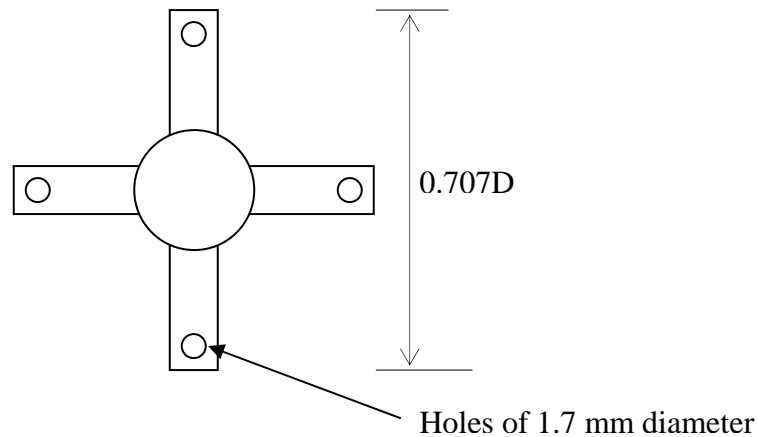


Figure 4.1b Cross sparger (top view, D is the diameter of the draft tube)

The experiments were conducted with slurry obtained from dairy waste. The slurry was screened to eliminate larger solids and then diluted to adjust the total solids concentration to 100 g/l (or 10% solids). To account for mixing created by the gas sparging only, anaerobic biogas production was hindered using sodium azide (2g/l).

Air was used as gas phase; air can be used to mimic biogas in digester. Biogas is a mixture of methane and carbon-dioxide, thus there is no significant difference in density of air and biogas. (Density of air at atmospheric pressure and room temperature is 1.18 Kg/m^3 , whereas biogas with 60% methane and 40% CO_2 has density of 1.11 Kg/m^3 at standard conditions). The air flow rate was varied from 1 lpm to 3 lpm. These flow rates resulted in superficial gas velocity (based on tank diameter) of 0.91 and 2.74 mm/sec, respectively. The gas flow rate of 1 lpm corresponds to energy input density of 8 W/m^3 (minimum suggested by US, EPA 1979 for proper digester mixing). At this low gas superficial velocity the IGLR operates in regime one called as bubbly flow regime or no gas entrainment regime (Heijnen et al., 1997; Pironti et al., 1995; Siegel, 1992; van Benthum et al., 1999).

CARPT experiments were performed in accordance to experiments carried out by Karim et al. (2004). $150 \mu\text{m}$ diameter Sc-46 particle with approximate activity of $200 \mu\text{Ci}$, enclosed in 1 mm diameter polypropylene ball was used as a tracer. The density of particle was adjusted close to that of water by using epoxy-resin to fill the air gap inside the ball. The density of the sealed tracer particle was checked by determining its terminal settling velocity in water. The tracer particle represented both the liquid in the slurry (water) and the microorganisms; microorganisms have density close to that of water. The solid particles and microorganisms in the slurry are small enough to behave similar to liquid flow elements, thus the two-phase solid-liquid slurry behaves like a single phase in which the fluid phase and the solid phase are in thermal equilibrium state and flow with the same velocity rather than a conventional solid-liquid mixture (Wen et al., 2005 and Klein et al., 2003).

Sixteen numbers of NaI detectors were arranged surrounding the six inch digester as shown in Figure 4.1a. A picture of experimental set-up is shown in Figure 4.2. First of all calibration was performed in situ by positioning the tracer particle at 400 known positions and spline fit curves were generated. An automated calibration device was used for this purpose (the details of calibration device are given by Luo, 2005). After

that the tracer particle was released into the digester and the track data were collected at a frequency of 50 Hz for 24 hours followed by data processing and reconstruction of the tracer particle trajectories. More details of CARPT and reconstruction algorithms are discussed by Karim et al. (2004) and Luo (2005) and detailed information is available in CARPT manual (2005).

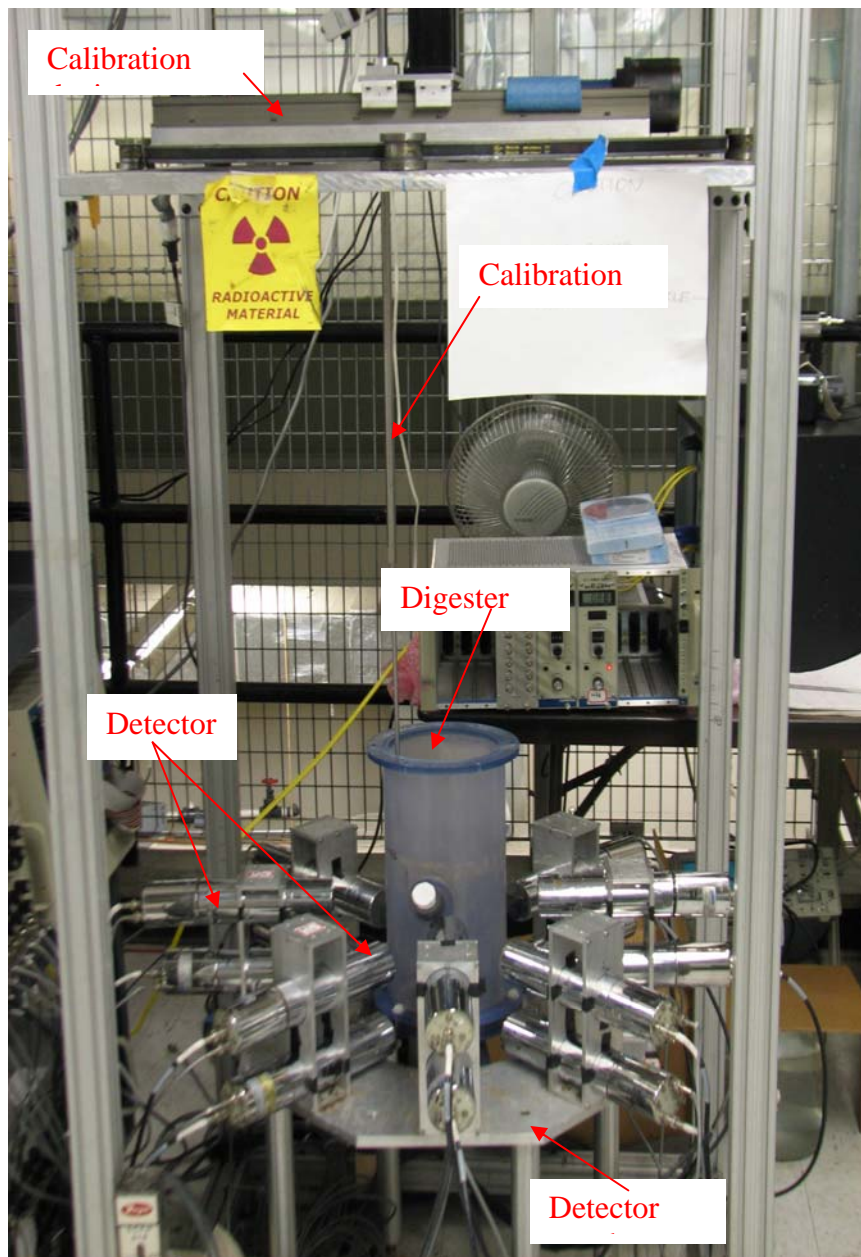


Figure 4.2 Photograph of laboratory-scale digester experimental set-up

Total five CARPT runs were performed; the operational details are given in Table 4.1. The operating conditions were varied in order to study the effect of gas recirculation rate, draft tube diameter and type of sparger. Vesvikar and Al-Dahhan (2005) carried out CFD studies on similar digester configuration and studied the effect of gas recirculation rate and draft tube diameter. They concluded that the gas recirculation rate did not show any appreciable effect on the liquid velocity may be because of the non-uniform local gas distribution. Thus both non-uniform single-point sparger and a uniform multi-point cross sparger were used in this study. Effect of gas flow rate was studied for cross sparger and the effect of sparger type on the hydrodynamics was studied at the lowest gas flow rate.

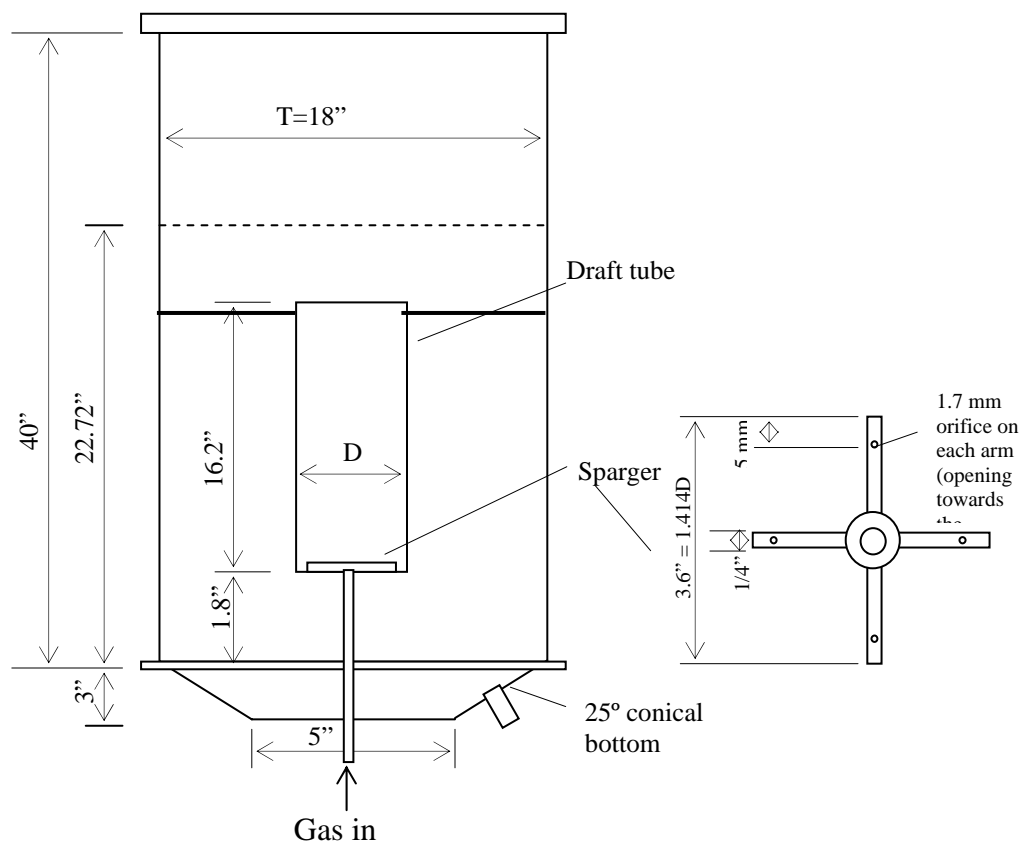
Table 4.1 Details of CARPT experiments for laboratory-scale digester

Experiment no.	Gas flow rate (lpm)	Total solids in the slurry (g/l)	D/T ratio	Sparger geometry
L1	1	100	0.25	Cross
L2	3	100	0.25	Cross
L3	1	100	0.5	Cross
L4	1	100	0.75	Cross
L5	1	100	0.25	Single point

4.2.2 Pilot-scale

An 18-inch (45.72 cm) diameter acrylic tank was used as a pilot-scale digester; it was geometrically similar to the laboratory-scale digester. The working volume of pilot-scale digester was 97 liters; whereas it was 3.78 liters for laboratory-scale digester (volumetric scale-up ratio of approximately 25 was employed). Digester was equipped with a draft tube and a conical bottom with a slope of 25°, as shown in Figure 4.3a. Air was recirculated at the bottom of the tank using a sparger. Two different types of spargers were used; viz., a single point sparger and a cross sparger. Single point sparger was a

pipe with a single opening of $\frac{3}{4}$ inch diameter, while the cross sparger had 4 holes of 2.2 mm each (facing downwards towards the bottom of the tank). Schematic of the cross sparger is shown in Figure 4.3b. Four arms of cross sparger extended inside the draft tube and covered 50 % of the draft tube cross sectional area. The spacing of sparger hole from the center of the tank was $\sqrt{2D}/2$; where D is the diameter of the draft tube. Draft tube diameter was changed from 11.5 cm to 34.3 cm, such that draft tube diameter to tank diameter ratio (D/T) is 0.25 and 0.75, respectively. The overall diameter of sparger was also changed in accordance with the draft tube diameter.



(a) Pilot-scale digester

(b) Cross-sparger

Figure 4.3a & 4.3b Digester geometry and cross sparger geometry

The experiments were conducted with similar slurry obtained from dairy waste, which was used for laboratory-scale experiment. The slurry was screened to eliminate larger

solids and then diluted to adjust the total solids to desired concentration, 50 gm/l (5% solids) or 100 g/l (10% solids). To account for mixing created by the gas sparging only, anaerobic biogas production was hindered using sodium azide (2g/l).

Air was used as the gas phase for the same reasons as explained in the section 4.2.1; air flow rate was varied from 4.5 lpm to 9 lpm and 18 lpm. These flow rates resulted in superficial gas velocity (based on tank diameter) of 0.45 mm/sec to 0.91 mm/sec and 1.82 mm/sec, respectively. Gas flow rate of 9 lpm corresponds to energy input density of 8 W/m³ (minimum suggested by US, EPA 1979 for proper digester mixing) and superficial gas velocity of 0.91 mm/sec, similar to laboratory-scale digester for gas flow rate of 1 lpm. At this low gas superficial velocity the IGLR operates in regime one also known as bubbly flow regime or no gas entrainment regime (Heijnen et al., 1997; Siegel and Robinson, 1992; van Benthum et al., 1999).

CARPT experiments were performed in accordance to experiments carried out in laboratory-scale digester. 150 µm diameter Sc-46 particle with approximate activity of 250 µCi, enclosed in 1 mm diameter polypropylene ball was used as tracer. The density of particle was adjusted close to that of water by using epoxy-resin to fill the air gap inside the ball. The tracer particle represented both the liquid in the slurry (water) and the microorganisms, which has density close to that of water.

24 numbers of NaI detectors were arranged surrounding the pilot-scale digester as shown in Figure 4.4. First of all calibration was performed in situ by positioning the tracer particle at 500 known positions, using an automated calibration device, and spline fit curves were generated. After that the tracer particle was released into the digester and the track data were collected at a frequency of 50 Hz for 24 hours followed by data processing and reconstruction of the tracer particle trajectories (see CARPT manual, 2005).



Figure 4.4 Photograph of CARPT set-up for pilot-scale digester

Total ten CARPT runs were performed; the operational details are given in Table 4.2. The operating conditions were varied in order to study the effect of gas recirculation rate, draft tube diameter, and type of sparger. CARPT was performed on laboratory-scale digester configuration to study the effect of sparger type, gas recirculation rate and draft tube diameter. Similar studies were carried out at pilot-scale for comparison with laboratory-scale hydrodynamic performance. In addition, effect of solids content in the slurry on the hydrodynamics was also investigated.

Table 4.2 Details of CARPT experiments for pilot-scale digester

Experiment no.	Gas flow rate (lpm)	Total solids in the slurry (g/l)	D/T ratio	Sparger geometry
P1	4.5	100	0.25	Cross
P2	9	100	0.25	Cross
P3	18	100	0.25	Cross
P4	4.5	100	0.75	Cross
P5	9	100	0.75	Cross
P6	18	100	0.75	Cross
P7	4.5	100	0.25	Single point
P8	9	100	0.25	Single point
P9	18	100	0.25	Single point
P10	9	50	0.25	Cross

4.3 Results

4.3.1 Laboratory-scale

Flow Pattern and Liquid Velocity Profile

Figure 4.5 shows the flow pattern inside the digester for experiment L1 (Table 4.1); digester with D/T ratio of 0.25, cross sparger, and gas flow rate of 1 lpm. The overall flow pattern consists of two circulation loops; the bigger circulation loop extends from the top of the digester to the bottom of draft tube, and it is directed upwards inside the draft tube. Another smaller circulation loop exists at the top of the draft tube close to

the surface. The liquid moves upward in the center and downwards towards the wall. There are big dead zones outside the draft tube and close to the digester wall having very low or zero velocities (represented with smaller arrows or dots in Figure 4.5). This flow pattern has been reported and discussed in detail by Karim et al. (2004) and Vial et al. (2002). Similar flow patterns were observed for experiment L2 to L5, and will be discussed in the following sections.

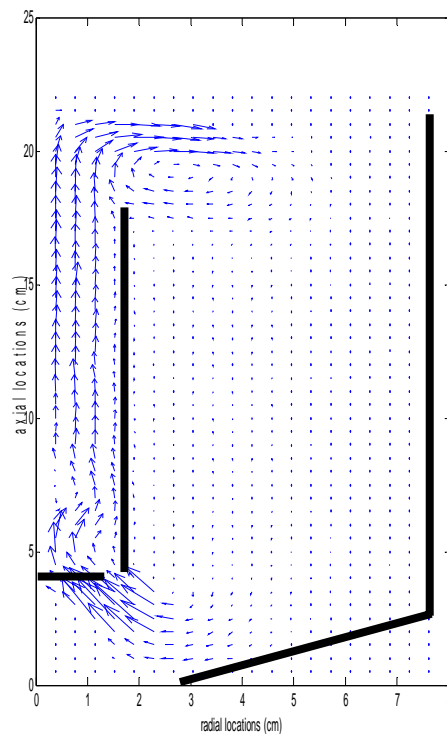


Figure 4.5 Flow pattern for experiment L1
($D/T=0.25$, 1 lpm gas flow rate, cross sparger)

Radial profile of time averaged azimuthally averaged axial liquid velocity at different axial locations is shown in Figure 4.6. The level of $z=2$ cm represents the horizontal level inside the conical bottom region at 2 cm from the bottom of the digester, similarly $z=4$ cm is just below the draft tube, $z=11$ cm is at the centre of the draft tube or tank, and $z=18$ cm is just above the draft tube. The velocities are positive inside the draft tube and negative outside the draft tube, indicating the upward and downward motion

of the liquid, respectively. The velocities are zero near the wall region and near the bottom of the digester which shows the location of the dead zones. Higher velocities inside the draft tube are due to the turbulence created by the gas bubbles rising inside with high velocities and the maximum axial liquid velocities existed near the sparger hole openings. Similar liquid velocity profiles were obtained by Karim et al. (2004) for 8 inch diameter gas recirculation digester.

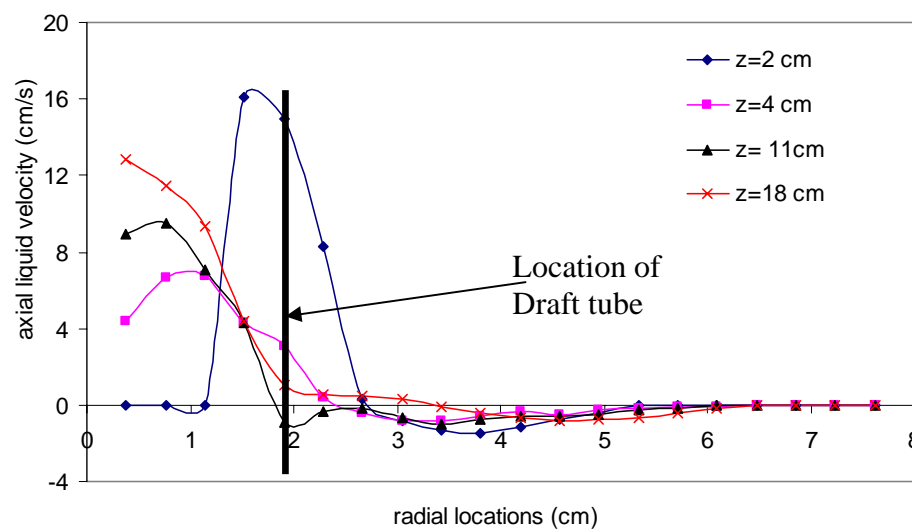


Figure 4.6 Circumferentially averaged axial liquid velocity radial profile for experiment L1

Effect of Gas Flow Rate

The effect of gas flow rate on the liquid velocity is shown in Figure 4.9. It is clear from Figure 4.7 that the time averaged axial liquid velocity in the riser increases significantly with the increase in the gas flow rate. However, increase in liquid velocity in the downcomer was negligible. As mentioned before, due to very low superficial gas velocities, the digester was operating in regime one. In this regime, as the gas superficial velocity is increased, increasing gas hold up in the riser increases the driving force for the liquid flow, and thus increasing the liquid velocity (Heijnen et al., 1997). At higher gas flow rates corresponding to regime two, the gas bubbles coalesce and also occupy some part of downcomer, without any substantial increase in liquid velocity. The liquid

velocity in downcomer should also increase with increasing gas flow rate in regime 1, but the magnitude of increase depends on the flow area in downcomer. With D/T of 0.25, because of large flow area of downcomer, the increase in liquid velocity with increase in gas flow rate is not appreciable. This effect of gas superficial velocity on average liquid circulation velocity was observed by many researchers (Freitas et al., 1999; Klein et al., 2003; Lu et al., 1995; Sun et al., 2005; Wen et al., 2005).

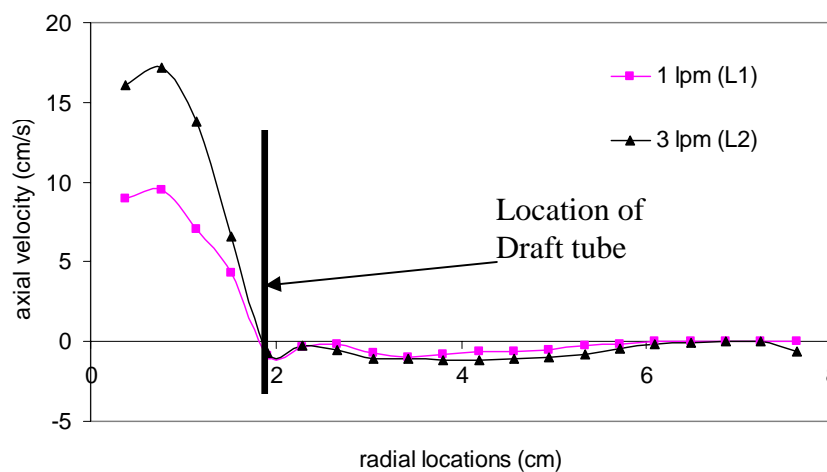


Figure 4.7 Effect of gas flow rate on axial liquid velocity (L1 and L2) at the center of the tank ($z=11$ cm)

The increase in the liquid velocity with gas flow rate depends on the distribution of gas in the draft tube. If the gas holdup is uniform inside the draft tube, higher liquid velocities can be obtained in the downcomer region due to better gas-liquid dispersion. This information about gas hold-up profile can be obtained from CT, which is a part of the other doctoral thesis by Rajneesh Varma.

Effect of Draft Tube Diameter

The cross sectional area of draft tube determines the superficial velocity of gas in the riser. Therefore, its size becomes a key parameter, which influences the hydrodynamics of IGLRs. In three-phase systems like digesters, it also plays an important role in

determining the minimum velocity necessary to fluidize the solid particles. Kennard and Janekeh (1991) reported that $D/T > 0.75$ is required to achieve optimum gas hold up. This value is best for aerobic fermenters, since the fluid has a minimum residence time in the downcomer where bubble concentration is low. Minimal mixing time is achieved, when $0.6 < D/T < 1$. $D/T < 0.6$ should be used if high liquid velocities in the riser are required in order to avoid sedimentation of heavy solid particles or large microbial aggregates. Trilleros et al. (2005) correlated his experimental data in pilot-scale IGLR and found that the effect of D/T on liquid velocity is more important than the effect of draft tube height or solid or liquid holdup in the riser. Thus, the effect of D/T on liquid velocity is investigated here.

Figure 4.8 shows the flow pattern obtained for D/T ratios of 0.5 and 0.75 (experiment L3 and L4, Table 4.1), respectively. The overall flow pattern in digester with larger draft tube diameter is different as compared to the one with smaller draft tube. There is one circulation loop inside the draft tube (figure 4.8a and 4.8b), which is absent in digester with smaller draft tube diameter ($D/T=0.25$), Figure 4.5. There are two other circulation loops present, one stronger loop at the top of the digester and other weaker loop outside the draft tube. The circulation is very good inside the draft tube, but poor outside the draft tube region; for D/T of 0.75 (Figure 4.10b) almost no liquid movement is observed outside the draft tube.

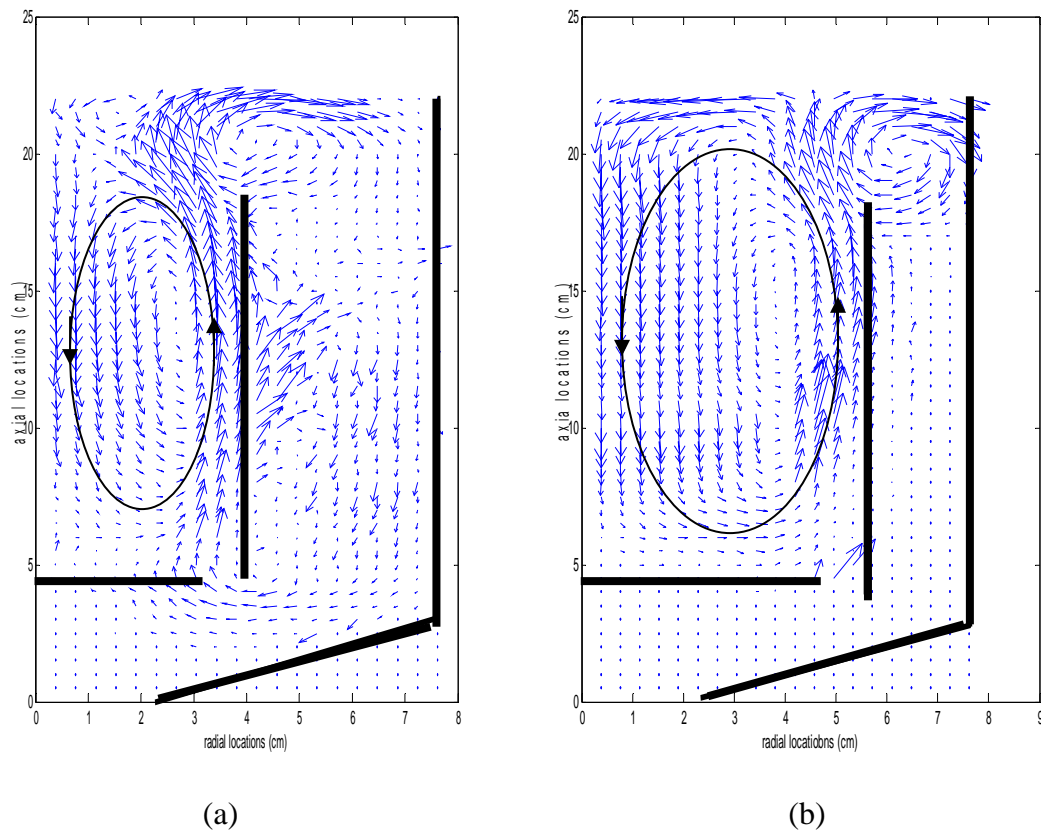


Figure 4.8 Effect of draft tube diameter on the flow pattern

(a) $D/T=0.5$, L3 (b) $D/T=0.75$, L4

The presence of the circulation loop inside the draft tube exists would be due to the cross sparger design and large diameter of the riser. The sparger holes are spaced at 5.4 cm and 8.1 cm away from the center of the draft tube for D/T of 0.5 and 0.75, respectively. That means the gas is sparged away from the center and close to sparger walls. The rising gas bubbles close to riser walls, carries liquid upwards with it. The dispersed sparging created by the cross sparger, creates an additional loop inside the draft tube. Thus, the liquid flow is directed downwards in the center and upwards near the wall. This behavior is not seen in the Figure 4.5 for D/T of 0.25. For D/T of 0.25, the arms of sparger extend only for a very short length (2.75 cm from the center) and the cross sparger behaves more like a single point sparger (concentrated sparging at the

center) due to smaller diameter. This will be explained further in next section under effect of the sparger design.

Effect of D/T ratio on the time averaged liquid axial velocity radial profiles at the bottom of the draft tube and at the center of the tank is shown in Figure 4.9a and 4.9b, respectively. These figures show the magnitudes of axial velocity inside the digester, the axial liquid velocities are higher at the center of draft tube. The velocities at the bottom of the tank are low for D/T of 0.5 but for D/T of 0.75 these velocities are practically zero, indicating the dead zones. The negative velocities for D/T of 0.5 outside the draft tube region, indicates the downward velocities and existence of circulation loop.

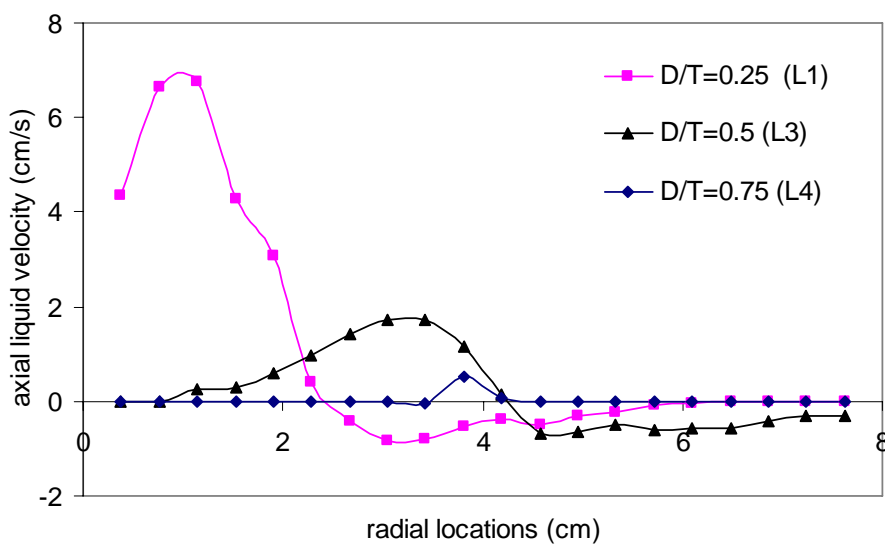


Figure 4.9a Effect of draft tube diameter on the axial liquid velocity at the bottom of the draft tube, $z=4$ cm, (experiment no L1, L3 and L4)

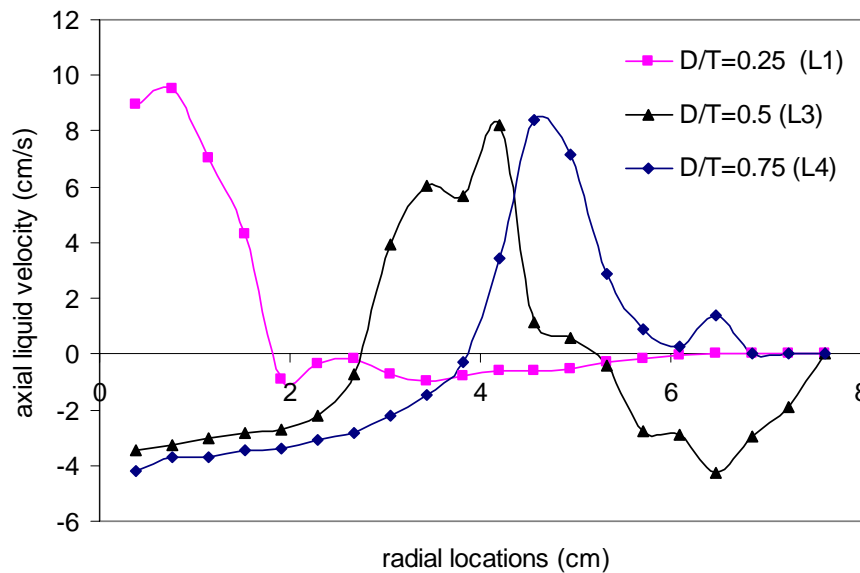


Figure 4.9b Effect of draft tube diameter on the axial liquid velocity at the center of the draft tube, $z=11$ cm, (experiment L1, L3 and L4)

As the D/T ratio increases, the magnitude of axial velocity inside the draft tube decreases. This was expected, with same gas flow rate as the area for flow increases with the increasing draft tube diameter the velocity decreases, according to Bernoulli's principle. This was also observed by Kojima et al. (1999), Kennard and Janekeh (1991), and Merchuk and Gluz (1999).

One would expect that as D/T increases, the liquid velocity in the downcomer should increase due to reduction in flow area. But higher D/T also means larger riser cross section, lower riser gas holdup at the same superficial gas velocity (i.e. lower gas velocity based on the riser diameter) and hence lower driving force for the liquid circulation. That is why, an optimum D/T exists for achieving higher liquid velocities in the downcomer.

Feitkenhauer et al. (2003) suggested that the riser and downcomer should have same equivalent diameter to minimize the energy loss by friction, this also prevents higher liquid velocities in one part of reactor and hence higher energy dissipation.

Effect of Sparger Geometry

Since the overall flow pattern and hydrodynamics of gaslift digester depends on the gas hold up and gas hold up is partly decided by the design of sparger, the effect of sparger at the digester conditions design on hydrodynamics of gaslift digester is very important. In spite of this, effect of sparger design in IGLR is not often discussed in literature. Becker et al. (1994) investigated the effect of sparger geometry on the hydrodynamics of IGLR using CFD. He found that a multipoint sparger creates higher gas holdup as compared to a single point sparger. Whereas, Merchuk (1986) only varied the hole diameters of multipoint sparger and found no effect on gas holdup or liquid velocity in 2D split GLR.

The flow pattern for digester with pipe sparger and D/T of 0.25 (experiment L5) shown in Figure 4.10 is similar to flow pattern obtained for experiment L1 and L2, Figure 4.5. No effect of sparger on the flow pattern was observed for D/T ratio of 0.25. In experiments L1 and L2 the effect of sparger is not very important due to smaller draft tube diameter (D/T ratio of 0.25). As explained in the previous section, the arms of cross sparger extend only for a very short length (2.75 cm from the center) and cover a small area inside the draft tube with D/T of 0.25. The gas distribution is concentrated at the center of the tank over a small region, see Figure 4.1. This may be the reason for absence of the internal circulation loop in the draft tube with D/T of 0.25. As the draft tube diameter increases, the length of arms of sparger extend away from center and each other and create more dispersed sparging, see Figure 4.11. This gives rise to the internal circulation loop inside the draft tube, which becomes more prominent with increasing draft tube diameter.

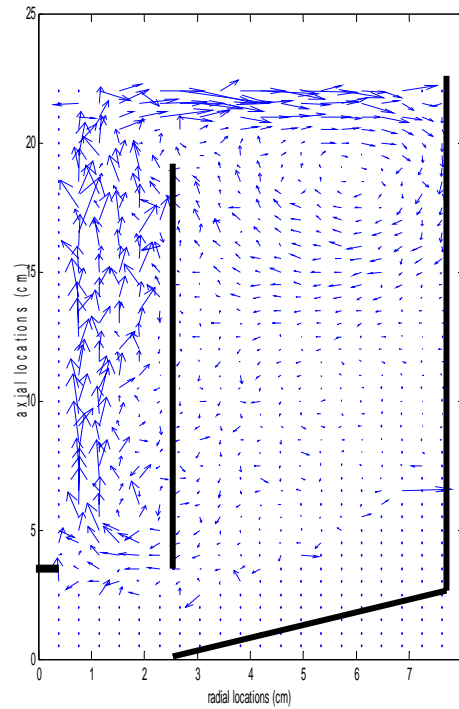


Figure 4.10 Flow pattern for experiment L5
($D/T=0.25$, 1 lpm gas flow rate, single point sparger)

Figure 4.11 shows the possible pattern of gas dispersion in the digester, without considering bubble breakup and coalescence. Definite conclusions about the effect of sparger geometry can be made only when the gas hold-up profile inside the riser is known. CT measurements need to be performed for this purpose.

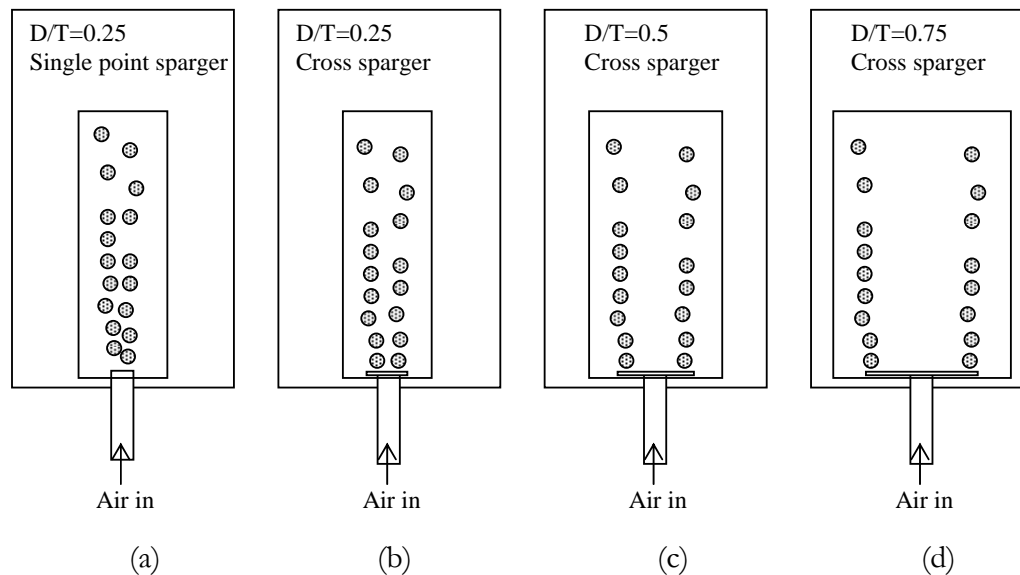


Figure 4.11 Expected effect of sparger geometry and D/T ratio on gas distribution

The effect of sparger on the axial liquid velocity profile is shown in Figure 4.12. The axial liquid velocities are higher for pipe sparger as compared to that for the cross sparger inside the draft tube, whereas the liquid velocities are the same for both the spargers outside the draft tube. The higher velocities can be a result of different gas holdup distribution or change in bubble dynamics. Further confirmation is required from CT measurements to explain effect of sparger design.

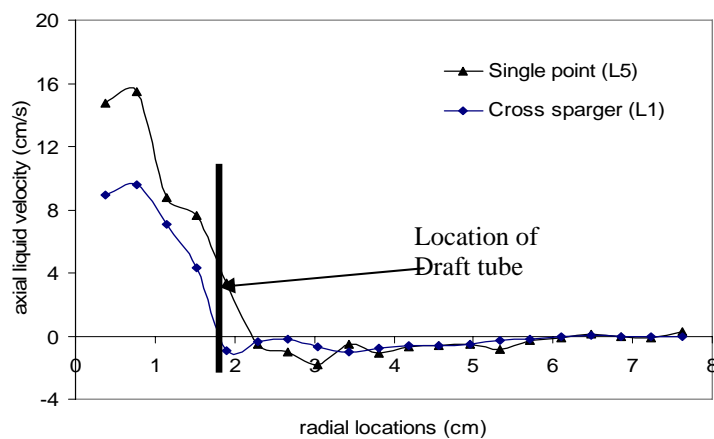


Figure 4.12 Effect of sparger geometry on axial liquid velocity at center of the tank, $z=11$ cm, (experiment L1 and L5).

Volume of Dead Zones or Stagnant Regions

The different configurations of digester can be compared conveniently in terms of dead volume. The dead zones or stagnant zones are the part of the reactor with no flow or very low velocities. Dead zones are undesirable as the dead regions remain secluded from rest of the reactor volume with no mixing thus reducing the effective reactor volume. These are the regions which cause building of pH and temperature, thus degrading the digester performance. Dead zones should also be avoided to prevent solids from settling due to low liquid velocities (Feitkenhauer et al., 2003). Bello-Mendoza and Sharratt (1998) also used volume of dead zones as the mixing parameter for the study of anaerobic digesters.

It is important to select a correct criterion to evaluate the total volume of dead zones. If the settling velocity of the solid particles is known then it can be used as a limiting velocity to define a dead region. The digester slurry contains varying concentration of a variety of solids from different sources such as husk, straw, and fibers coming from the feed, and sand particles, saw dust, wood, shavings, chips, rice hulls from bedding material. The solids are also of different sizes. As the digestion progresses the size of the solids reduces due to the digestion. The microbes form agglomerates and grow on size. Thus it is very hard to specify a representative solids settling velocity.

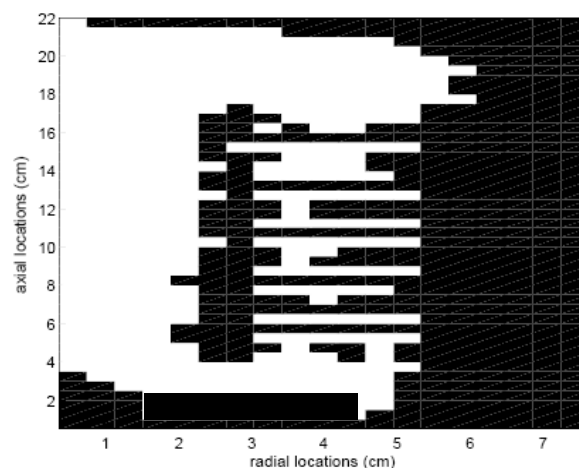
Thus, in the present study the dead zone volume was evaluated by locating the cells with very low velocities (some arbitrary low value, 1 cm/sec was used here), and summing up the volumes of these cells. Table 4.3 shows the dead zone volumes for different digester configurations. The dead zone volume is used only for comparison between different configurations, thus the limiting value of liquid velocity used for calculating dead zone volume is not critical as long as same value is used for all configurations to be compared.

Table 4.3 Dead or stagnant volumes for laboratory-scale digester configurations

Expt no.	Gas flow rate (lpm)	D/T ratio	Sparger	% Dead volume
L1	1	0.25	cross	50
L2	3	0.25	cross	42
L3	1	0.5	cross	30
L4	1	0.75	cross	60
L5	1	0.25	single point	55

Table 4.3 shows that the dead zone volume decreases by increasing the gas flow rate, but it is clear from flow pattern in Figure 4.5 that high liquid velocities are present only inside the draft tube region for D/T of 0.25, thus decrease in dead zone volume does not indicate more homogeneity in this case. Only 30% of the digester volume is inactive/dead in case of D/T of 0.5, whereas this number is highest for D/T of 0.75. Flow patterns shown in Figure 4.10 indicate that the digester with D/T of 0.5 is mixed more homogeneously thorough out the volume than the digester with D/T of 0.75.

It is also very interesting to see the location of dead zones in addition to their total volume. Figure 4.13 shows the map of dead zones in digester with D/T ratio of 0.25. The dead zones exist near the bottom and towards the wall of the digester. This can also be clearly seen in the flow pattern of digester.

**Figure 4.13** Dead zone map for Experiment L1 (dark spaces are the dead zones)

In addition to dead zone volume turbulent diffusivities can also be used to evaluate the mixing performance of digesters, as described in next section.

Eddy diffusivity

The key property of turbulent motion is its ability to transport or mix momentum, energy, scalar quantities, etc. The rates of transfer and mixing in the presence of turbulence are orders of magnitude larger than the rates due to molecular transport. The values of diffusivity at the location near and inside the dead zones will help to understand the diffusion time scales for transfer of material within and through the dead zones. If the material entering the dead zone stays inside the dead zone for a period longer than the time scale of limiting digestion reaction due to low diffusion rate, then the performance of digester will be degraded due to two reasons. First, the effective volume of the digester will be reduced causing the reduction in the effective sludge retention time. Second, if the fatty acids formed in the dead zones are not diffused uniformly as they are formed, they will kill the methanogens.

In the present section, the turbulent eddy diffusivities are defined as measured in a Lagrangian framework. The details of calculation of eddy diffusivities are given by Degaleesan (1997). The radial and axial eddy diffusivities calculated for experiment L1 at the center of the tank are shown in Figure 4.14. The radial diffusivities are very small as compared to axial diffusivities and can be neglected. The distribution of axial diffusivities over the digester volume for experiment L1 is shown in Figure 4.15. The axial diffusivities are very low almost zero inside and near the dead zones. This signifies that the exchange of material through and within the dead zones is very slow.

The axial diffusivities for different configurations are shown in Figure 4.16. The diffusivity increases with increasing gas flow rate. The diffusivity is highest for configuration with D/T ratio of 0.5, indicating better mixing behavior. Sparger design has no effect on the diffusivity.

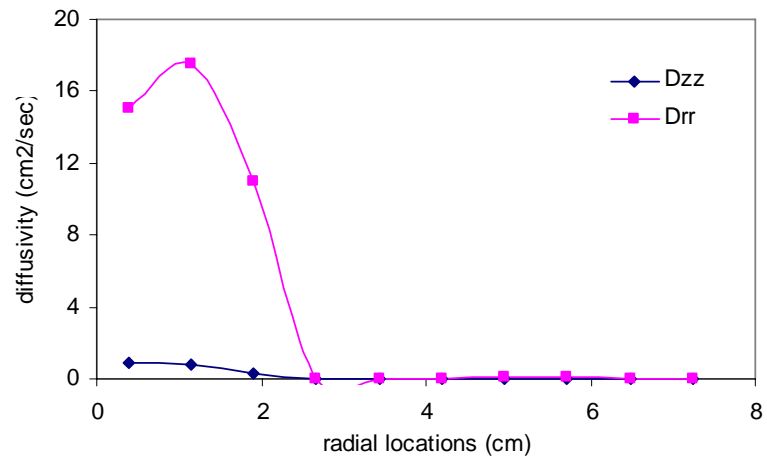


Figure 4.14 Axial and radial eddy diffusivities at the center of the tank for experiment L1

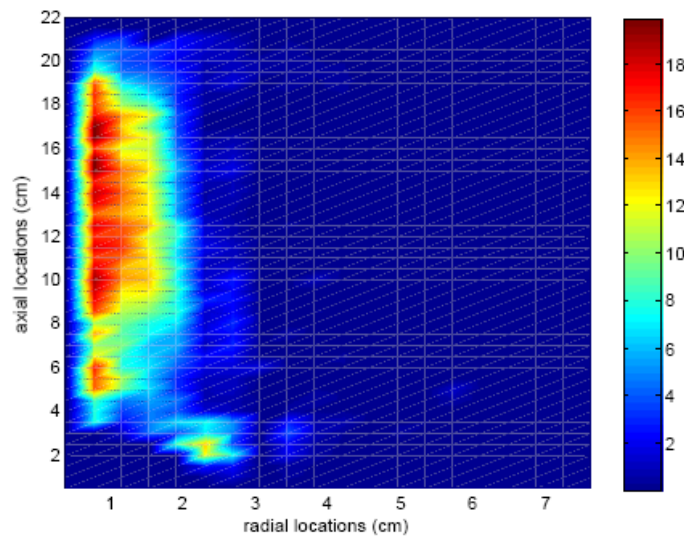


Figure 4.15 Axial diffusivity map for experiment L1

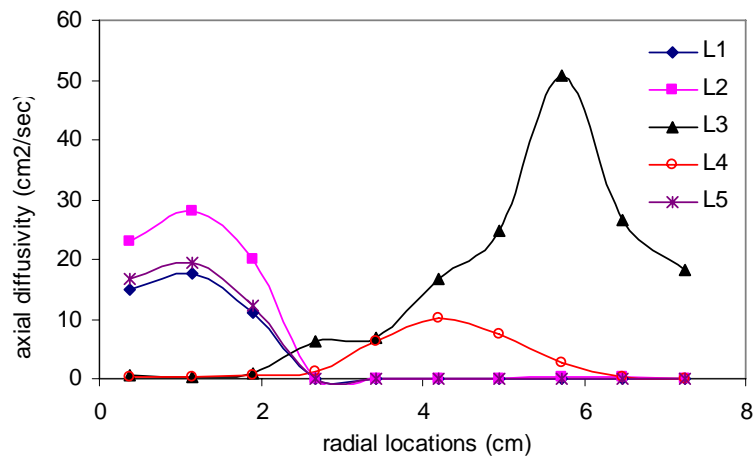


Figure 4.16 Comparison of axial eddy diffusivities for different digester configurations

4.3.2 Pilot-scale

Flow Pattern and Liquid Velocity Profile

Figure 4.17 shows the flow pattern inside the digester for experiment P1 (Table 4.2); digester with D/T ratio of 0.25, cross sparger, and gas flow rate of 4.5 lpm. The overall flow pattern consists of two circulation loops; the bigger circulation loop extends from the top of the digester to the bottom of draft tube, and it is directed upwards inside the draft tube. Another smaller circulation loop exists at the top of the draft tube close to the surface. The liquid moves upward in the riser and downwards in the downcomer. Dead zones exist in the downcomer and close to the digester wall having very low or zero velocities (represented with smaller arrows or dots in Figure 4.17). Similar flow pattern in a small-scale digester has been reported and discussed in detail by Karim et al. (2004). Similar flow patterns were observed for experiment P2 and P3 (Table 4.2), and will be discussed in following sections.

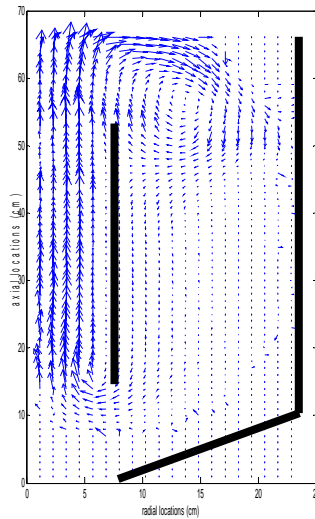


Figure 4.17 Flow pattern for experiment P1 ($D/T=0.25$, 4.5 lpm, cross sparger)

Radial profile of time averaged and azimuthally averaged axial liquid velocity at different axial locations is shown in Figure 4.18. The level of $z=6$ cm represents the horizontal level inside the conical bottom region at 6 cm from the bottom of the digester, similarly $z=12$ cm is just below the draft tube, $z=33$ cm is at the centre of the draft tube or tank, and $z=54$ cm is just above the draft tube. The velocities are high and positive inside the draft tube, where as low and negative outside the draft tube, indicating the upward and downward motion of the liquid respectively. The velocities are zero near the wall region and near the bottom of the digester which shows the location of the dead zones. Higher velocities inside the draft tube are due the turbulence created by the air bubbles rising inside with high velocities.

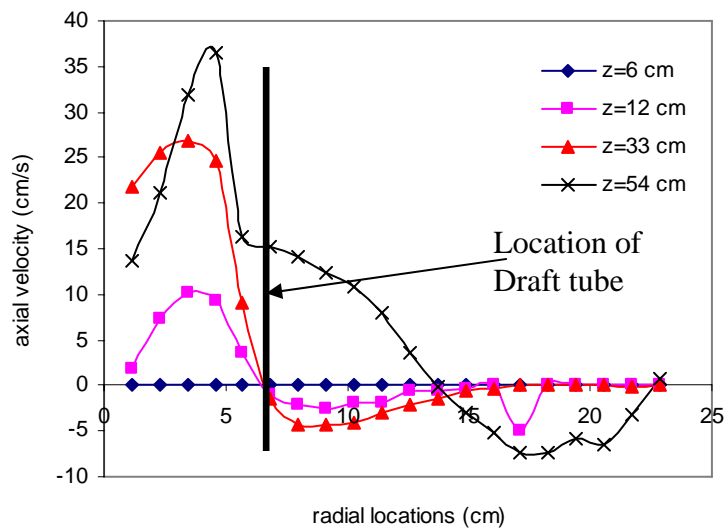


Figure 4.18 Circumferentially averaged axial velocity radial profile for experiment P1 at different axial locations

Effect of gas flow rate

The effect of gas flow rate on the liquid velocity at the center of the tank ($z=33$ cm, all liquid velocity profiles are reported at the center of the tank unless or otherwise mentioned) is shown in Figure 4.19. It is clear from Figure 4.19 that the time averaged axial liquid velocity inside the draft tube increases significantly with the increase in the gas flow rate on liquid velocity. However, there is almost no effect of gas flow rate outside the draft tube. The reasons for this behavior are already discussed in laboratory-scale section of this chapter.

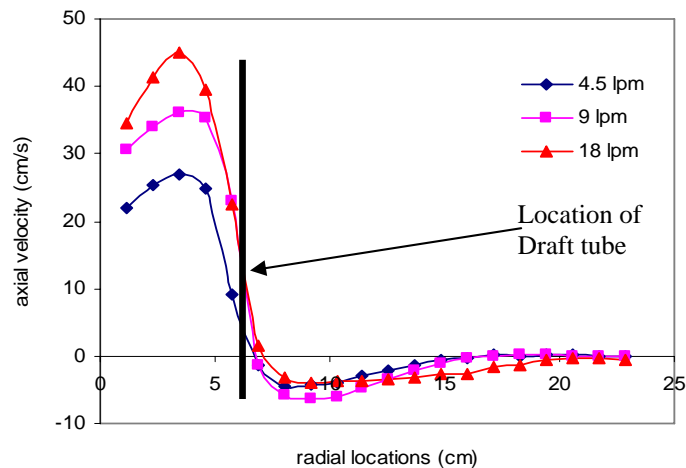


Figure 4.19 Effect of gas flow rate on axial liquid velocity (experiment P1, P2 and P3) at the center of the tank ($z=33$ cm).

Effect of draft tube (riser) diameter

The draft tube diameter to tank diameter ratio (D/T) was varied to 0.75 to see the effect of draft tube diameter. The flow pattern obtained for D/T of 0.75 with cross sparger is shown in Figure 4.20 for gas flow rate of 9 lpm (experiment P5), respectively. The flow patterns are different than the one obtained with D/T ratio of 0.25 (Figure 4.12). Two major circulation loops are seen in Figure 4.20. The liquid flow is directed upwards inside the draft tube by the sparger and then the liquid is distributed into 2 loops. One loop is directed upwards inside the draft tube near the draft tube wall and flows downward in the downcomer region (that is the region between the draft tube and the tank walls). Another loop exists in the riser at the top, which flows downward near the center of the tank and upwards at the region halfway between the draft tube wall and center of the tank. There is significant liquid flow in the downcomer region, which was absent for smaller draft tube diameter as shown in Figure 4.16.

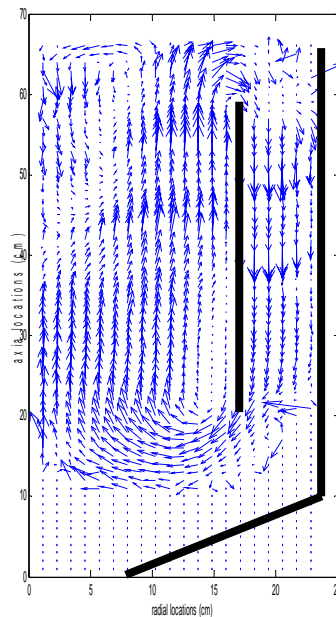


Figure 4.20 Flow pattern for $D/T=0.75$ at gas flow rate of 9 lpm, P5

The circulation loop inside the riser exists because of the combined effect of large riser cross sectional area and cross sparger design. Four holes of sparger are placed at 24 cm from center of the tank for D/T of 0.75. Thus, cross sparger is expected to create dispersed sparging as shown in Figure 4.11d, due to large spacing between the holes. The dispersed sparging created by the cross sparger, creates an additional loop inside the draft tube. This behavior is not seen in the Figure 4.13 for D/T of 0.25. For D/T of 0.25, due to smaller riser diameter and closer spacing of holes (only 7.5 cm from the center, see Figure 4.11b), the gas is expected to be dispersed more uniformly over the smaller cross section of riser as compared to riser of $D/T= 0.75$.

Figure 4.21 shows the radial profile of azimuthally averaged axial liquid velocity at different axial levels for gas flow rate of 9 lpm (experiment P5), respectively. These plots show that the liquid velocity is zero inside the conical bottom region. The positive and the negative values of velocity inside the riser, show that the liquid flows upwards near the center and downwards near the wall of the draft tube.

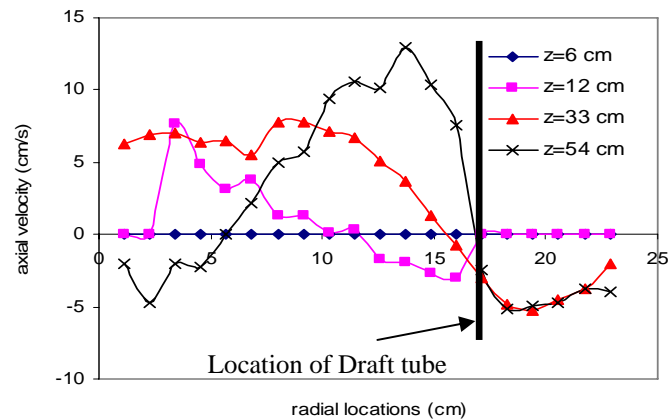


Figure 4.21 Circumferentially averaged axial velocity radial profile for experiment P5

The axial liquid velocity profiles for D/T of 0.25 and 0.75 are compared in Figure 4.18 for different gas flow rates. As the D/T ratio increases, the magnitude of axial velocity inside the riser decreases but it increases in the downcomer region. This is as expected, with same gas flow rate as the area for flow increases with the increasing draft tube diameter the velocity decreases, according to Bernoulli's principle. The higher liquid velocity in downcomer region is an advantage offered by increasing the draft tube diameter. This was also observed by Kojima et al. (1999).

Figure 4.22 also explains the effect of gas flow rate on the axial velocity, increase in the gas flow rate increases the liquid velocity inside the draft tube and hence the circulation in the digester. Similar observations were made by Freitas et al., 1999; Klein et al., 2003a; Lu et al., 1995; Sun et al., 2005; Wen et al., 2005.

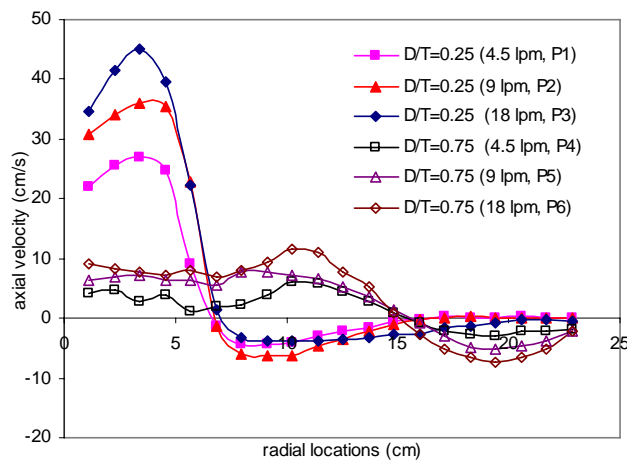


Figure 4.22 Effect of draft tube diameter on the axial liquid velocity at the center of the draft tube at different gas flow rates, (experiments P1 to P6)

Effect of sparger geometry

Cross sparger was replaced with single point sparger to study the effect of sparger on the flow pattern of a digester. Figures 4.23 show the flow patterns obtained for digester with single point sparger and D/T of 0.25 for gas flow rate of 9 lpm (experiment P8), respectively. The flow patterns look similar to one with the cross sparger for experiment P1, P2 and P3 as shown in Figure 4.17. The sparger does not affect the flow pattern significantly for D/T ratio of 0.25 in qualitative manner.

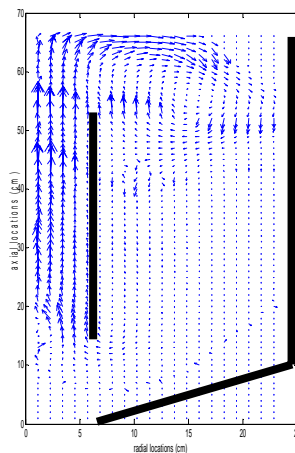


Figure 4.23 Flow pattern for a single point sparger and $D/T=0.25$ at 9 lpm (P8)

Figure 4.24 shows the liquid velocity profile at different axial locations for configurations with single point sparger at gas flow rate of 9 lpm. Figure 4.25 shows the effect of sparger type on the axial liquid velocity for different gas flow rates. For cross sparger the maximum liquid velocity exists away from the centre of the tank, whereas for single point sparger the location of maximum liquid velocity is at the center of the tank. The liquid velocities are higher for single point sparger than cross sparger only in small region at the center of the riser. But for cross sparger, the liquid velocities are higher than single point sparger for majority of annular cross-section of the riser.

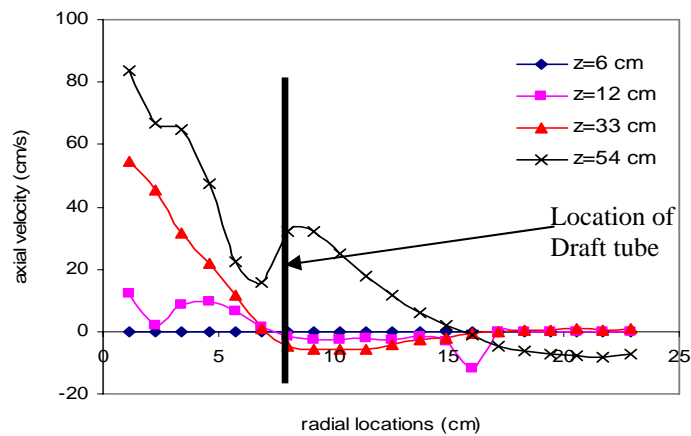


Figure 4.24 Circumferentially averaged axial liquid velocity radial profile for expt P8

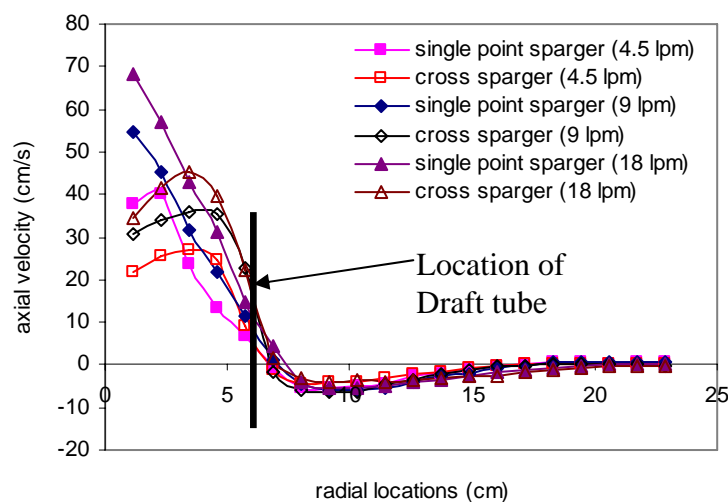


Figure 4.25 Effect of sparger on the axial liquid velocity at the center of the draft tube at different gas flow rates, (experiments P1 to P3 and P7 to P9)

The reason for this behavior is obvious, the holes on the cross sparger are 7.5 cm away from the center of the tank and near the draft tube walls on the arms of the cross sparger for D/T of 0.25, whereas the sparging is done at one localized point at the center of the tank in case of single point sparger. The rising gas bubble from sparging hole accelerates the liquid and creates high liquid velocity. Whereas, cross sparger creates gas dispersion at four separate uniformly spaced point inside the riser. Thus better gas dispersion is expected in case of cross sparger, which creates better liquid circulation and higher average liquid circulation velocities as compared to single-point sparger. The difference in gas holdup distribution can be obtained from CT experiments and this issue can be addressed in more detail.

Effect of solids concentration in the slurry

In three-phase gaslift digesters with very small solid particles, as in present case of dairy manure slurry, a defined flow pattern is obtained along with complete suspension of solids at low gas superficial velocities (Wen et al., 2005). For low density particles (between 1000 to 1600 Kg/m³), the liquid and solid phase are often assumed to be one pseudo-homogeneous phase.

Solids concentration in the slurry was changed from 100 gm/lit (10%) to 50 gm/lit (5%) for a digester with cross sparger and draft tube with D/T ratio of 0.25 at gas flow rate of 9 lpm (experiment P10) to see the effect of solids concentration on the flow pattern of the digester. The flow pattern was not considerably affected by solids concentration, except with a slight increase in the liquid axial velocity for 5% slurry, shown in Figure 4.26 (comparison of axial liquid velocity profile at the center of the tank for different solids concentration, experiment P2 and P10). Higher solids concentration causes the reduction in flow area for the solid and liquid phase thereby increasing the frictional loss and decreasing the velocity. Higher solids concentration also causes the increase in the viscosity of pseudo-homogeneous liquid-solid phase. As discussed earlier, increase in liquid velocity with decreasing solids fraction was also observed by Merchuk (2003) and Sun et al. (2005).

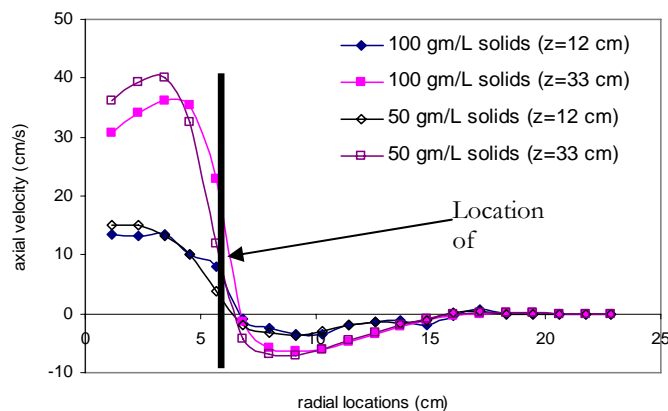


Figure 4.26 Effect of solids concentration on the axial liquid velocity at the center of the draft tube at different gas flow rates, (experiment P1 and P10)

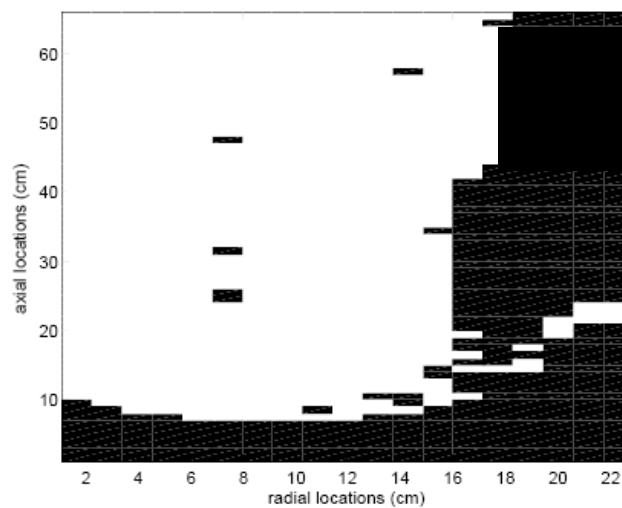
Volume of dead zones or stagnant regions

The different configurations of digester can be compared conveniently in terms of dead volume. Just like laboratory-scale, for pilot-scale also the dead zone volume was evaluated by locating the cells with very low velocities (some arbitrary low value, 1 cm/sec was used here), and summing up the volumes of those cells. Table 4.4 shows the dead zone volumes for different digester configurations. Table 4.4 shows that the dead zone volume decreases upon increasing the gas flow rate for all the configurations. For D/T of 0.25 the higher liquid velocities exist only inside the riser, since decrease in dead zone volume with increasing gas flow rate does not indicate more homogeneity in this case, increased flow rate is not advantageous. The dead zone volume increases with increase in the D/T ratio. The values in the Table 4.4 show that the sparger type and slurry solids concentration does not have an appreciable effect on the dead zone volume, for D/T ratio of 0.25.

Table 4.4 Dead or stagnant volumes for pilot-scale digester configurations

Expt no.	Gas flow rate (lpm)	Total solids in the slurry (g/l)	D/T ratio	Sparger geometry	% Dead volume
P1	4.5	100	0.25	cross	61
P2	9	100	0.25	cross	55
P3	18	100	0.25	cross	50
P4	4.5	100	0.75	cross	65
P5	9	100	0.75	cross	60
P6	18	100	0.75	cross	54
P7	4.5	100	0.25	Single point	63
P8	9	100	0.25	Single point	58
P9	18	100	0.25	Single point	53
P10	9	50	0.25	cross	58

Figure 4.27 shows the map of dead zones in pilot scale configuration P2. Again the dead zones are located near the bottom and towards the wall of the digester and can be easily located from the flow pattern of digester.

**Figure 4.27** Dead zone map for Experiment P2 (dark spaces are the dead zones)

Eddy diffusivity

The radial and axial eddy diffusivities calculated for experiment P1, P2 and P3 at the center of the tank are shown in Figure 4.28. The radial diffusivities are very small as compared to axial diffusivities for all gas flow rates and can be neglected. The distribution of axial diffusivity is shown in Figure 4.29. The diffusivities are very low inside and near the dead zones, as observed for laboratory-scale configuration. The effect of gas flow rate on axial diffusivities for different configurations is shown in Figure 4.30a and 4.30b. The effect of gas flow rate on axial diffusivities is not very clear. The axial diffusivities for different configurations at gas flow rate of 9 lpm are shown in Figure 4.31. The diffusivities are higher for D/T ratio of 0.75 in major portion of the digester as compared to D/T of 0.25. The axial diffusivities are the lowest for the single point sparger. Solids concentration in the slurry has no effect on the axial diffusivities.

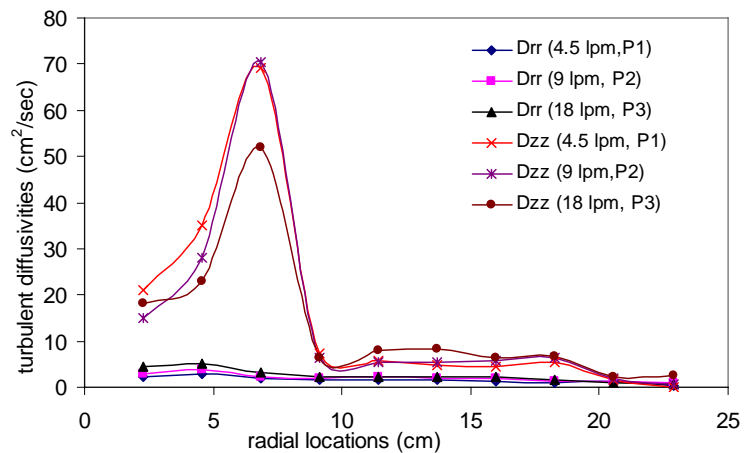


Figure 4.28 Axial and radial eddy diffusivities at the center of the tank for experiment P1, P2 and P3

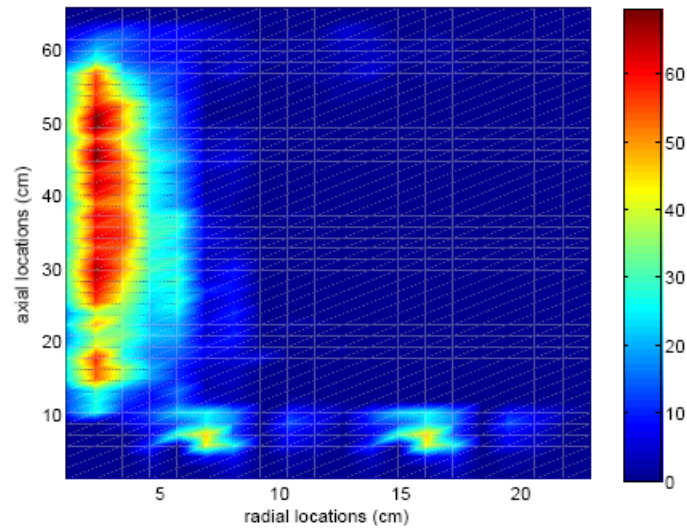


Figure 4.29 Axial diffusivity map for experiment P2

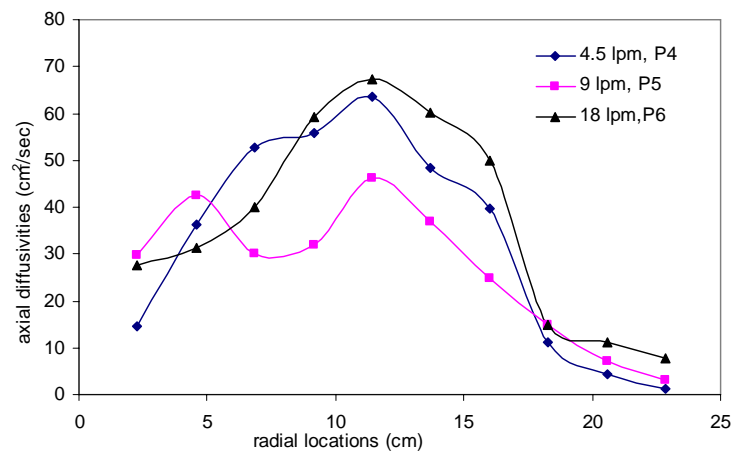


Figure 4.30a Effect of gas flow rate on turbulent axial turbulent diffusivities for configurations with D/T of 0.75 and cross sparger

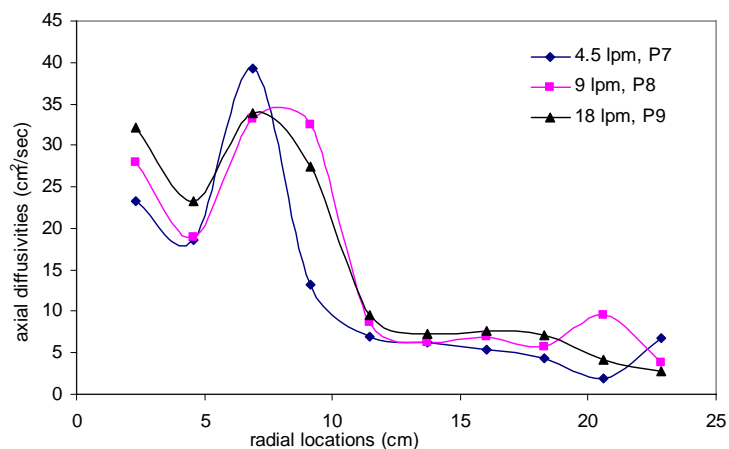


Figure 4.30b Effect of gas flow rate on turbulent axial turbulent diffusivities for configurations with D/T of 0.25 and single point sparger

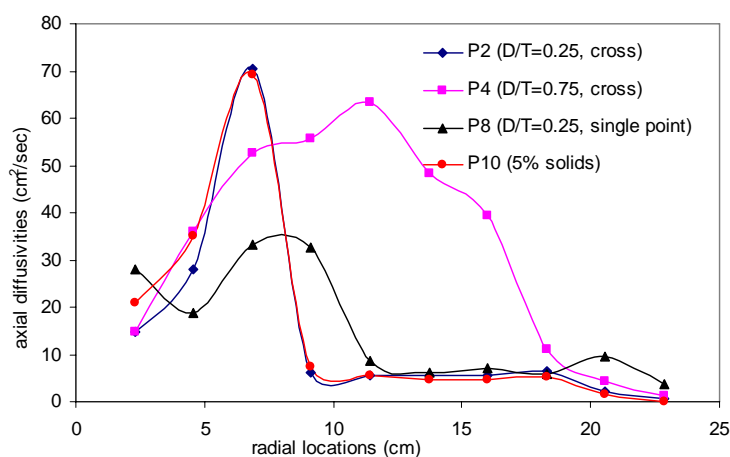


Figure 4.31 Comparison of axial eddy diffusivities for different digester configurations at gas flow rate of 9 lpm

4.3.3 Effect of Scale

The results of laboratory scale and pilot scale CARPT studies were compared to investigate the effect of scale. The working volume of laboratory scale unit was 3.78 L whereas for pilot scale it was 97 L, thus a volumetric scale up factor of approximately 25 was employed. Both the units were geometrically similar; the diameter of pilot unit was three times the diameter of laboratory unit. The gas flow rate of 1 lpm in small scale and

9 lpm in pilot scale corresponds to same superficial gas velocity of 0.91 mm/sec based on tank diameter (14.6 mm/sec based on draft tube diameter for D/T ratio of 0.25 and 1.6 mm/sec for D/T of 0.75).

Thus the laboratory-scale and pilot-scale configurations with cross sparger for D/T of 0.25 and 0.75 with 10% waste and operating with superficial gas velocity if 0.91 mm/sec can be compared to evaluate the effect of scale. Configurations with single point sparger for D/T of 0.25 containing slurry with 10% solids can also be compared; see Table 4.5. While the percentage dead volumes are similar for two scales, the actual volume dead zones in pilot-scale is 25 times larger than in the laboratory-scale.

Table 4.5 Effect of scale on dead or stagnant volumes for different digester configurations

sparger	D/T ratio	% Dead volume	
		Laboratory-scale 1 lpm	Pilot-scale 9 lpm
Cross sparger	0.25	50 (L1)	55 (P2)
Cross sparger	0.75	60 (L4)	65 (P5)
Single point	0.25	55 (L5)	58 (P8)

Comparison of flow patterns of configurations with cross sparger with D/T of 0.25 and superficial gas velocity of 0.91 mm/sec shows that the flow patterns are qualitatively similar. Liquid axial velocity profiles can be compared for quantitative analysis. To facilitate the comparison, the axial liquid velocity is made dimensionless. Axial velocities of laboratory-scale at center of the tank ($z=11\text{cm}$) are divided by the maximum liquid velocity for laboratory-scale at the center of the tank to obtain dimensionless velocity. Similarly, axial velocities for pilot-scale at center of the tank ($z=33\text{ cm}$) are divided by the maximum liquid velocity for pilot-scale at the center of the tank to obtain dimensionless velocity. Figure 4.32 shows the comparison of dimensionless axial liquid velocity profile.

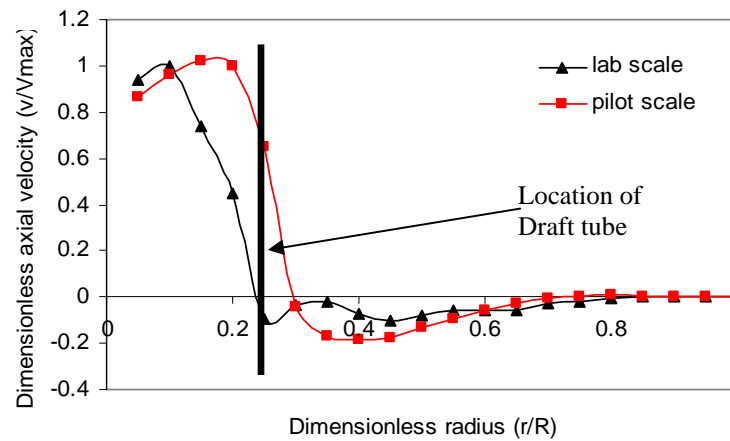


Figure 4.32 Comparison of axial liquid velocity radial profile for laboratory scale and pilot scale digesters (experiment L1 and P2), $D/T=0.25$, cross sparger, 10% slurry and superficial gas velocity of 0.91 mm/sec.

The velocity profile has the same shape and the dimensionless velocities are also comparable. Not only the velocity profiles of two scales should overlap each other for the two scales to be hydrodynamically similar, but their magnitudes of velocities should also match (elaborated further in the following discussion). The velocity profile for pilot scale is shifted to the right (the velocity should be zero at the wall of draft tube, $r/R=0.25$), this can be attributed to the error in the CARPT measurement. The error for laboratory-scale velocity profile is negligible but not for pilot-scale. Larger scale of pilot unit causes more error in reconstruction because of coarser calibration grid and more attenuation of the radiation signal in the system. Thus, if we neglect the error, then the shape of velocity profiles of both the scales match with each other for D/T of 0.25.

Comparison of flow patterns of configurations with single point sparger with D/T of 0.25 and superficial gas velocity of 0.91 mm/sec also shows that the flow patterns are qualitatively similar. The dimensionless velocity profile of both scales matches well, Figure 4.33. The geometry of the laboratory-scale digester with single point sparger did

not allow acquiring enough calibration points inside and near the draft tube. Therefore, the error in the reconstruction in this configuration is more than the other laboratory-scale configurations. So the zero velocity at the draft tube wall is observed at r/R of 0.3 instead of 0.25.

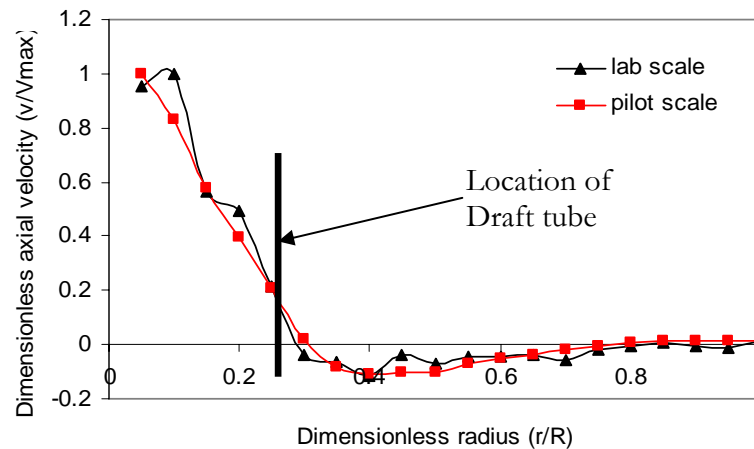


Figure 4.33 Comparison of axial liquid velocity radial profile for laboratory scale and pilot scale digesters (experiment L5 and P8), $D/T=0.25$, single sparger, 10% slurry and superficial gas velocity of 0.91 mm/sec.

Unlike for D/T of 0.25, the flow patterns are quite different for D/T of 0.75. The laboratory-scale digester has only one circulation loop inside the draft tube, with liquid moving down in the center and up towards the wall. For pilot-scale, the circulation pattern is more complex. The liquid moves downwards in the center in upper part of the riser in a smaller independent circulation loop, while the liquid is directed upwards in the center of the riser at the bottom. The dimensionless liquid velocity profiles are compared in Figure 4.34; the profiles are completely different for two scales. This is in accordance with the observations of Blazej et al. (2004), Gavrilescu and Tudose (1998) and Heijnen et al. (1997).

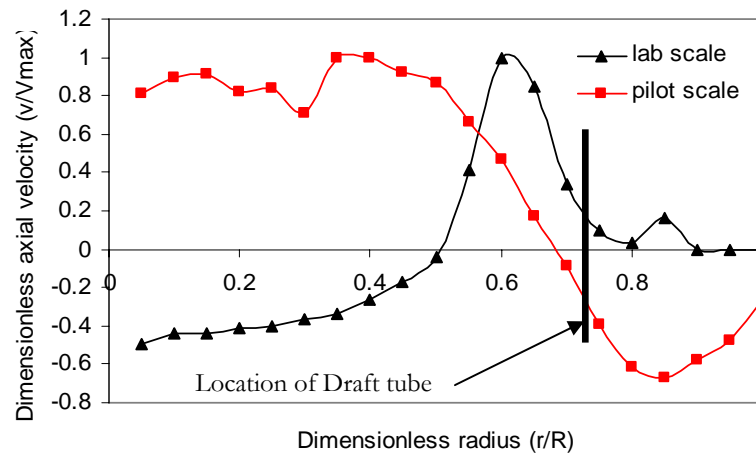


Figure 4.34 Comparison of axial liquid velocity radial profile for laboratory scale and pilot scale digesters, $D/T=0.75$, cross sparger, 10% slurry and superficial gas velocity of 0.91 mm/sec, (experiment L4 and P5).

Figure 4.35a and 4.35b explain the true effect of scale on the axial liquid velocity for experiment L1/P2 and L5/P8, respectively. Since the flow pattern of experiment L4 and P5 are completely different, their axial velocity magnitudes are not compared. In Figure 4.35a and 4.35b, the magnitude of axial velocity is compared rather than dimensionless velocities. The liquid velocities in pilot-scale are about 3 to 4 times higher as compared to laboratory-scale in the riser. The increase liquid velocity is not so significant in downcomer. This has been observed experimentally by Blazej et al. (2004) and Gavrilescu and Tudose (1998).

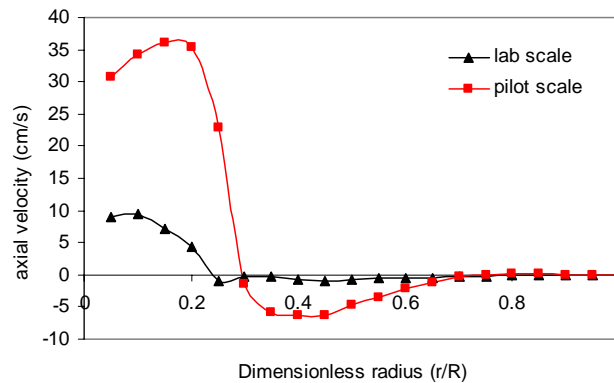


Figure 4.35a Comparison of magnitudes of axial liquid velocity for laboratory scale and pilot scale digesters (experiment L1 and P2), $D/T=0.25$, cross sparger, 10% slurry and superficial gas velocity of 0.91 mm/sec.

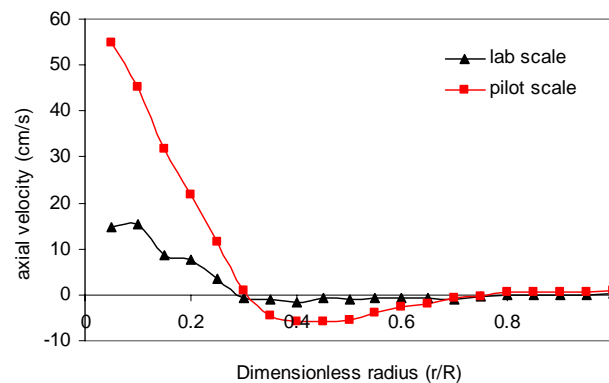


Figure 4.35b Comparison of magnitudes of axial liquid velocity for laboratory scale and pilot scale digesters (experiment L5 and P8), $D/T=0.25$, single point sparger, 10% slurry and superficial gas velocity of 0.91 mm/sec.

Blazej et al. (2004) and Gavrilescu and Tudose (1998) observed increase in liquid circulation velocity and decrease in gas hold up with increasing scale. The frictional losses of the liquid phase encountered in pilot-scale are much lower as compared to small-scale. A significant amount of frictional loss is due to the wall friction, tank walls and the draft tube walls. The surface area of a cylinder per unit volume is inversely proportional to its diameter. Thus the frictional losses per unit volume of liquid in larger

reactors are much less as compared to smaller reactors. These reduced frictional losses in pilot-scale result in increased liquid circulation as compared to laboratory-scale digesters. Blazej et al. (2004) evaluated the frictional loss constants in IGLR using empirical correlations and hydrodynamic model of Heijnen et al. (1997) and proved that the frictional loss constant (proportional to frictional loss) decreases with increasing scale of reactor (from 10.5 liters to 200 liters).

Mixing and hydrodynamics can be characterized by dead zone volume and turbulent eddy diffusivity together. Table 4.5 shows the effect of scale on dead zone volume and mean circulation times. For all three cases, even though the liquid velocities in pilot scale are significantly higher than in laboratory-scale, pilot-scale configuration had significantly higher dead zone volume (25 times larger) and larger size of dead zones than the laboratory-scale configurations. The axial diffusivities in pilot-scale are slightly higher than the laboratory-scale. But the diffusivities in the dead zones are very low for both digester scales. This means that the diffusion or dispersion of material (substrate or intermediates of digestion reaction such as fatty acids) is much slower and poor in pilot-scale digester. Due to smaller size of laboratory-scale digester (and hence smaller size of their dead zones) diffusion to/from the center of dead zone in smaller reactor may be sufficient to maintain significant activity, while that in the larger reactor it may not be sufficient. Higher dead zone volume and low axial diffusivities in the pilot-scale digester can explain its poor performance than the identically operated laboratory-scale digester (Appendix A)

The increase in liquid velocities with scale is significant in riser but insignificant in downcomer. As pointed out before dead zones are observed in downcomer section due to low liquid velocities. Higher liquid velocities only in the riser does not help to reduce to dead zone volume or mean circulation times in pilot-scale. Probably for a scale-up ratio of 25, only 3-4 times increase in liquid velocities in a small section of pilot-scale reactor is not enough to achieve the same mixing intensity that was obtained in small-scale reactors.

Small-scale configurations show better mixing characteristics as compared to large-scale units. Small-scale units are well mixed due to their small size and can be considered to be perfectly or ideally mixed (Bello-Mendoza and Sharratt, 1998; Nielsen and Villadsen, 1992). Schlattmann et al. (2004) studied four different scales of digesters ranging from 2 L to 900 m³ and concluded that the process efficiency of small scale reactors is higher than that for large scale reactors. Residence time distribution studies conducted by Monteith and Stephenson (1981) found only 23% of the reactor volume actively mixed in a large scale digester, indicating inefficient mixing and larger mixing time constants. Performance studies carried out in laboratory-scale and pilot-scale anaerobic digesters (Appendix A) showed that laboratory-scale digester produced more amount of better quality biogas as compared to pilot-scale digester. This may be due to the better mixing performance of laboratory-scale digester as compared to pilot-scale digester, as observed here.

Next question arises, what scale-up criteria should be used to obtain similar performance at different scales of reactor? Geometric similarity is essential but that alone does not guarantee the same hydrodynamic performance. Same superficial gas velocity (power dissipation per unit volume) was used as scale-up criteria in this study. Obviously, same superficial gas velocity did not provide same flow patterns or liquid velocity profiles in geometric similar configurations of experiment L4 and P5. Moreover, sparger geometry did not affect the hydrodynamics with D/T of 0.25 significantly. But sparger geometry had an appreciable effect on the liquid velocities, dead zone volumes, and mean circulation times for pilot-scale configuration with D/T of 0.25. These observations suggest that the superficial gas velocity (energy input per unit volume) may not be the correct scale-up criteria to obtain similar flow patterns in gas recirculation type reactors.

4.4 Summary

The flow pattern and liquid velocity profiles were obtained in a laboratory-scale and pilot-scale gaslift digester operating in regime one. Effect of geometry and operating variables was studied on the liquid velocity, dead zone volume, mean circulation time, and turbulence parameters.

Increased gas flow rate increases the liquid velocity; decreases mean circulation time for all configurations at both the scales, but does not offer any advantage of lowering the dead zone volume significantly. The larger draft tube diameters (with D/T of 0.5 or 0.75) reduce the dead zones and produce relatively homogenous mixing throughout the digester volume. Digester with D/T of 0.5 has minimum percentage of dead volume for laboratory-scale digester. For pilot-scale digester lowest percentage of dead volume was obtained for D/T ratio of 0.75 at highest gas flow rate. Mean circulation time increases with increase in D/T ratio. Decreasing solids content in the slurry decreases the mean circulation time.

If different laboratory-scale configurations of digester are compared on the basis of flow pattern, liquid velocities, dead zone volume and mean circulation time, then the configuration with D/T ratio of 0.5 with low gas flow rate seems to be best configuration for anaerobic digester operation. Because, it provides good liquid circulation throughout the volume of the digester, lowest volume of dead zones and low mean circulation time. Higher gas flow rates can provide more circulation but they are not desirable from the energy consumption consideration.

Flow pattern, liquid velocity profile, dead zone volume and diffusivities were used to evaluate the effect of scale on the hydrodynamics. Geometric similarity and same gas superficial velocity were used as scale-up criteria in this study. Scale of operation affected the flow pattern and liquid velocity profile significantly for D/T of 0.75. The

liquid velocities were significantly higher in pilot-scale in the riser but change was less significant in the downcomer section. Comparing the values of dead zone volume and axial diffusivities to quantify mixing, proved that the mixing performance is better in small-scale digesters as compared to large-scale units in spite of liquid velocities being higher for pilot-scale units. Sparger geometry affected the hydrodynamic performance significantly in pilot-scale but not in laboratory-scale digesters. Thus it can be concluded that only geometric similarity and same gas superficial velocity (energy input per unit volume) does not guarantee similar mixing intensity or hydrodynamic performance at different scales of operation.

Only two D/T ratios were tested in pilot-scale experiments. Thus, the optimum D/T ratio for pilot-scale configuration to provide improved circulation and improved mixing performance was not examined. CFD studies will be carried out for this purpose. The CFD predictions will be first evaluated with CARPT results and then validated CFD code will be used to understand the hydrodynamics of gaslift digesters in detail and to compare additional laboratory-scale and pilot-scale configurations. The CFD studies are presented in Chapter 5.

Chapter 5

Computational Fluid Dynamics Studies: Laboratory-scale and Pilot-scale

5.1 Introduction and Motivation

Advanced non-invasive experimental techniques like CARPT and CT help to understand the hydrodynamics in detail but their application is limited by the time and resource constraints. Thus these techniques cannot be used to evaluate the effect of every parameter on the hydrodynamics. This is where Computational Fluid Dynamics (CFD) can help in such evaluation and for design and scale-up once it is validated.

CFD proves to be a valuable and efficient tool to understand and evaluate hydrodynamics of a flow system. For single-phase systems, CFD models and closures are well established and validated with benchmark experimental data, such that CFD can be used with high level of confidence for simulating single-phase systems. However, this is not the case with multiphase systems. The complex flow structure and interactions within different phases in addition to the turbulence makes it very difficult to develop models for multiphase systems that can mimic reality. The closures used for these equations are modeled hypothetically or correlated from experimental data thus cannot be universally applied to all cases. Therefore multiphase CFD simulations need to be developed for individual situations and validated against experimental data. Once the CFD results are validated for a particular system, CFD can be used to optimize the

system by varying parameters and operating conditions to achieve proper design and scale-up.

Considering the need of evaluating the CFD model with proper experimental data, so that CFD can be used in design and scale-up of gaslift digesters, a 3D two-phase CFD model provided by CFX is used and the simulation predictions are compared with the CARPT data. Ability of CFD to account for the effect of geometry, operating conditions and scale is revisited here.

Karim et al. (2004) performed CARPT studies on 8-inch diameter gaslift digester. Thus, preliminary CFD studies were performed by Vesvikar and Al-Dahhan (2005) to simulate the digester used by Karim et al. (2004) in order to evaluate the predictability of CFD simulations. The experimental data is obtained from CARPT; CARPT studies on two scales of digesters are presented in Chapter 4. This work is an attempt to understand the hydrodynamics of IGLRs with the help of CFD for the configurations and operating conditions of IGLR type anaerobic digester that were not covered by the experiments in Chapter 4.

5.2 Digester Geometry

5.2.1 Laboratory-scale (6-inch diameter digester)

The geometry of 6-inch laboratory-scale digesters used in the performance studies (Chapter 3) and CARPT studies (Chapter 4) was used in these simulations. The details of the digester geometry are given in Figure 4.1. All the laboratory-scale configurations listed in Table 4.1 were simulated along with additional simulations with different geometrical and operating variables. The 6-inch laboratory-scale simulation details are given in Table 5.1 (Acronym LS in simulation number stands for Laboratory-scale Simulation). The additional simulations were performed after validating the CFD code

with the CARPT data reported in Chapter 4. See section 4.2.1 of Chapter 4 for details of experimental conditions and details.

Table 5.1 Simulation details for laboratory-scale (LS) digesters

Simulation no.	D/T ratio	Gas flow rate (lpm)	Gas superficial velocity (mm/sec)	Sparger geometry
LS1, LS2, LS3	0.25	1, 2, 3	0.91, 1.82, 2.84	Cross sparger
LS4, LS5, LS6	0.5	1, 2, 3	0.91, 1.82, 2.84	Cross sparger
LS7, LS8, LS9	0.75	1, 2, 3	0.91, 1.82, 2.84	Cross sparger
LS10, LS11, LS12	0.25	1, 2, 3	0.91, 1.82, 2.84	Single point
LS13, LS14, LS15	0.5	1, 2, 3	0.91, 1.82, 2.84	Single point
LS16, LS17, LS18	0.75	1, 2, 3	0.91, 1.82, 2.84	Single point

5.2.2 Pilot-scale (18-inch diameter digester)

The geometry of 18-inch pilot-scale digesters used in the performance studies (Chapter 3) and CARPT studies (Chapter 4) was used in these simulations. The details of the digester geometry are given in Figure 4.3. All the pilot-scale configurations listed in Table 4.2 were simulated along with additional simulations with different geometrical and operating variables. The pilot-scale simulation details are given in Table 5.2 (Acronym PS in simulation number stands for Pilot-scale Simulation). The additional simulations were performed after validating the CFD code with the CARPT data reported in Chapter 4. See section 4.2.2 of Chapter 4 for details of experimental conditions and details.

Table 5.2 Simulation details for pilot-scale (PS) digesters

Simulation no.	D/T ratio	Gas flow rate (lpm)	Gas superficial velocity (mm/sec)	Sparger geometry
PS1, PS2, PS3	0.25	4.5, 9, 18	0.45, 0.91, 1.82	Cross sparger
PS4, PS5, PS6	0.5	4.5, 9, 18	0.45, 0.91, 1.82	Cross sparger
PS7, PS8, PS9	0.75	4.5, 9, 18	0.45, 0.91, 1.82	Cross sparger
PS10, PS11, PS12	0.25	4.5, 9, 18	0.45, 0.91, 1.82	Single point

5.3 Simulation Details

Density of the (5% or 10%) slurry used in the CARPT experiments was approximately equal to that of the water (see section 4.2.1). The slurry contained microorganism clusters and very small sized solid particles uniformly dispersed in the liquid phase, such that the two-phase solid-liquid slurry can be treated as a single pseudo-homogeneous phase (Klein et al., 2003 and Wen et al., 2003). Oey et al. (2001) also followed the same approach for simulating flow in three-phase IGLR. After obtaining the flow field of pseudo-homogenous liquid phase, Oey et al. (2001) used this flow field to compute the solids distribution inside the mixture by solving a transport equation for the solid volume fraction. This pseudo-two-phase approach is computationally much cheaper than treating the gas, liquid, and solid phases with separate mass and momentum balances and it also circumvents the modeling of even more complicated closure laws. Using this approach, they found that the solids fraction vary locally (in each computational cell) only from 0.81% to 0.99%. Thus, the pseudo-liquid phase was simulated with physical properties of water. The gas phase was simulated with physical properties of air.

The validated CFD code and closures were then used to simulate different geometries of the digester by varying the draft tube diameter, type of sparger and gas flow rate. Table 5.1 and 5.2 lists the CFD simulations performed with different geometries and operating conditions at different scales.

Three dimensional (3D) steady-state simulations were carried out using CFD software version 5.7 for 6-inch and 18-inch digester. van Baten et al. (2003a) compared 2D simulation results with 3D simulation results and found that the assumption of 2D axis symmetry leads to radial profile that have a more parabolic character than that for fully 3D simulations. Mudde and Van Den Akker (2001) also found differences of about 30% in the liquid circulation velocities calculated by 2D and 3D simulations. Sokolichin

et al. (2004) observed that 3D models are able to capture important flow and mixing characteristics. They also observed that 3D dynamic simulations do not require an adjustment through additional lift forces, generally needed in 2D simulations to match the experimental results. Mudde and Van Den Akker (2001) suggested this difference in 2D and 3D simulations results is due to the lower friction in 2D simulations because of absence of front and back wall of the reactor.

The governing equations used in the simulations are shown by Vesvikar and Al-Dahhan (2005). Only drag force term was considered to account for interphase forces, as drag force is dominant as compared to other interphase forces (Kuipers and Swaaij, 1998; Oey et al. 2003; Rafique, et al. 2003; Ranade, 2002). Drag force was modeled with Grace drag model. Preliminary simulations were carried out by Vesvikar and Al-Dahhan using different bubble diameters ranging from 2 to 12 mm, but the change in diameter did not affect their results significantly. The same observation was made by van Baten, et al. (2003) and Sokolichin, et al. (2004). The explanation for the lack of dependence on bubble diameter is that the bubble rise velocity is practically independent of bubble diameter in the range of 3-10 mm. Thus bubble diameter of 10 mm was chosen for the results reported here.

There is a possibility of coalescence of the bubbles generated by the pipe sparger. But the high liquid circulation velocity and low gas fraction in the draft tube maintains high bubble–bubble distance and reduces the bubble coalescence. This was also visually during the experiments.

An Eulerian-Eulerian approach was used to simulate the flow in a three-phase IGLR type anaerobic digesters at two scales. Eulerian method is less computationally intensive as compared to Lagrangian-Lagrangian approach, especially when the void fraction of dispersed phase is high (Oey et al., 2001 and Sokolichin and Eigenberger, 1994). Bagatin et al. (1999), Mudde and Van Den Akker (2001), Oey et al. (2001), van Baten et al. (2003a), and many others used this approach for simulation of three-phase IGLR.

Pseudo-liquid phase was modeled as continuous phase using $k-\epsilon$ (k -epsilon) model, where as gas phase was modeled as dispersed phase using zero equation model. The inlet boundary condition for air was provided by specifying the inlet air velocity at the sparger hole. The outlet boundary condition was the degassing condition for air phase at the surface of water. A no-slip boundary condition was used for air at all the wall boundaries and free-slip boundary condition was applied for air-phase at the draft tube wall.

The mesh was prepared in two stages: a surface mesh of triangular elements is generated and then the volume mesh of tetrahedral elements is generated from the surface mesh. The mesh generated was non uniform. The mesh in the center (i.e. in the region of draft tube) was finer as compared to the region outside the draft tube. Mesh refinement was carried out until a mesh independent solution was obtained as discussed later.

The Finite volume method was used as the numerical technique. The momentum and continuity equations were discretized using finite differences. A first order upwind scheme was used for convective terms. The simulation results are discussed below.

5.4 Simulation Results

5.4.1 Laboratory-scale (6-inch Diameter Digester)

Simulation Results and Comparison with CARPT Data

Figure 5.1a shows the flow pattern obtained from 3D CFD simulation for 6-inch laboratory-scale (simulation LS1). Flow pattern is obtained from velocity vector plot of azimuthally averaged liquid velocities. The main features of the flow pattern shown in Figure 5.1a are exactly similar to flow pattern of 8-inch digester given by Vesvikar and Al-Dahhan (2005).

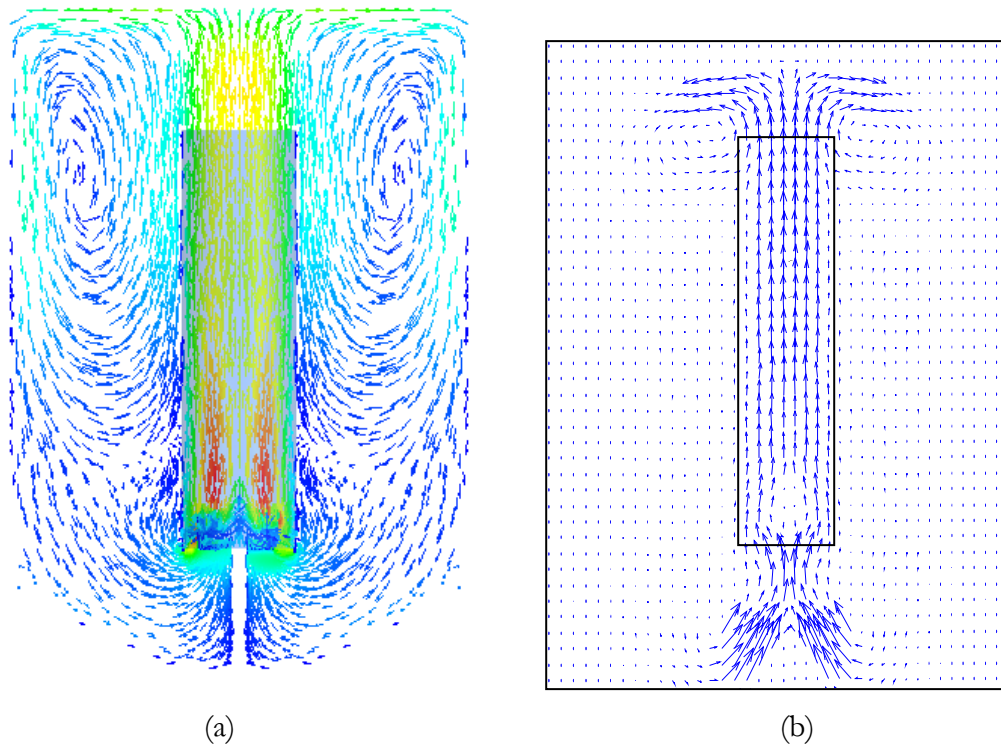


Figure 5.1 Comparison of (a) simulated flow pattern (LS1) and (b) flow pattern obtained from CARPT (L1) for 6-inch digester

Similar flow pattern was obtained from CARPT results. Simulated flow pattern, Figure 5.1a is compared with experimentally obtained flow pattern, Figure 5.1b. Figure 5.1a and 5.1b, shows good qualitative agreement between the simulation and the experimental results for flow pattern, location of stagnant zones, and circulation loops.

The flow pattern obtained agrees with simulation results of Mudde and Van Den Akker (2001), Oey et al. (2001), Oey et al. (2003a), and Svendsen et al. (1992).

Figure 5.2 shows radial profile of azimuthally averaged axial liquid velocities at different axial locations obtained from CFD simulation LS1. The level of $z=2$ cm represents the horizontal level inside the conical bottom region at 2 cm from the bottom of the digester, similarly $z=4$ cm is just below the draft tube, $z=11$ cm is at the centre of the draft tube or tank, and $z=18$ cm is just above the draft tube. Figure 5.2 also presents the quantitative comparison of CFD predictions of liquid velocity with the CARPT results.

The CFD predictions match reasonably with the CARPT experimental data. The trend of velocity profile matches very well with the experimental data, but the values of liquid velocity are over predicted by CFD. The simulated liquid velocities match experimental data better in downcomer section as compared in the riser. This was also reported by Glover et al. (2003) from his 3D simulations. There is still a lot of room for improvement in the CFD predictions. Use of different closures and models for interphase forces should be evaluated for further improvement. The contribution of different interphase forces should also be considered to improve the predictability of CFD models. This will be discussed later.

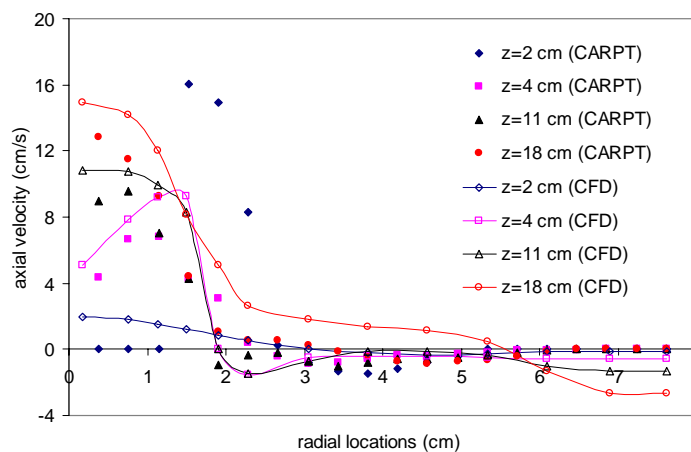


Figure 5.2 Comparison of simulated axial liquid velocity profile for Simulation LS1 with experimental CARPT data (L1)

This level of (dis)agreement between the experimental and CFD simulation results is also reported by Bagatin et al. (1999), Blazej et al. (2004a), Jakobsen et al. (1993), Glover et al. (2003), and Svendsen et al. (1992).

The local gas holdup distribution predicted by CFD for Simulation LS1 is shown in Figure 5.3 (the maximum value of holdup scale is manipulated to improve the readability of plot). The gas is present only in the riser and there is no gas entrainment in the downcomer due to low superficial gas velocity. The gas hold up is maximum at the sparger holes and then gets uniformly distributed in the upper half portion of the

riser. The experimental data for comparison of predicted gas holdup is not available at this time but will be obtained by CT as a part of other doctoral thesis (by Rajneesh Varma). The overall gas hold up is only 0.06%.

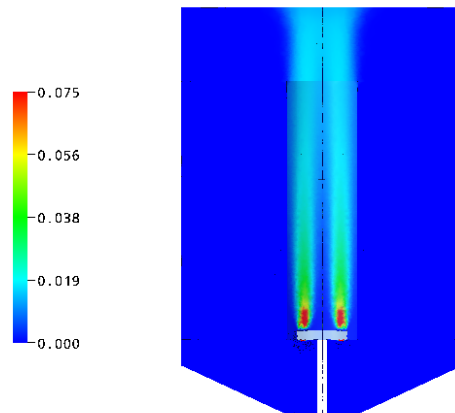


Figure 5.3 Gas hold up distribution predicted by CFD for Simulation LS1

Laboratory-scale Simulations LS3, LS4, LS7, and LS10 were also performed to check the predictability of the CFD simulations. For all these conditions, CFD predictions agree only reasonably with the experimental data on quantitative basis but predict the trends of liquid velocity profile accurately (i.e. good qualitative agreement). The comparison of experimental data and predictions of these simulations is presented in the further discussion.

The dead zone volumes (explained in detail in later section) obtained from CFD simulation results for selected configurations are compared with experimental values in Table 5.3. The agreement between the simulated and experimental values is reasonably accurate.

Table 5.3 Comparison of dead zone volumes predicted by CFD with experimental data for 6-inch laboratory-scale digester

Sparger geometry	D/T	Gas superficial velocity (mm/sec)	% Dead volume	
			CFD	CARPT
Cross sparger	0.25	0.91	46 (LS1)	50 (L1)
		1.82	42 (LS2)	-
		2.74	39 (LS3)	42 (L2)
	0.5	0.91	36 (LS4)	30 (L3)
		1.82	30 (LS5)	-
		2.74	25 (LS6)	-
	0.75	0.91	52 (LS7)	60 (L4)
		1.82	48 (LS8)	-
		2.74	42 (LS9)	-
Single point sparger	0.25	0.91	52 (LS10)	55 (L5)
		1.82	44 (LS11)	-
		2.74	40 (LS12)	-
	0.5	0.91	39 (LS13)	-
		1.82	36 (LS14)	-
		2.74	30 (LS15)	-
	0.75	0.91	55 (LS16)	-
		1.82	51 (LS17)	-
		2.74	49 (LS18)	-

Since the applicability of the CFD simulations to predict the flow pattern and liquid velocities at this scale have been established to match the trend of liquid velocity profiles, these CFD models can be now used to simulate flow in gaslift digesters at other operating conditions listed in Table 5.2 and to evaluate the effect of different operating and geometric variables and the effect of scale.

Effect of Gas (Air) Flow Rate

Effect of air flow rate for a given D/T ratio and a particular type of sparger can be evaluated using the simulations listed in Table 5.2. The flow pattern remains unaffected by the air flow rate (for all D/T ratios and both sparger geometries), only the magnitude of the liquid velocity changes as discussed below. This was also observed for two different gas flow rates from CARPT experiments in Chapter 4.

Figure 5.4 shows the effect of air flow rate on the radial profile of circumferentially averaged axial liquid velocity at the center of the tank ($z=11$ cm, all liquid velocity profiles are reported at the center of the tank unless or otherwise mentioned) for configurations equipped with cross sparger and D/T ratio of 0.5 (Simulations LS1/LS2/LS3). The liquid velocity inside the draft tube (riser) increases with the increasing air flow rate but remains unaffected in the downcomer region. The downcomer region is the region with the low velocities and dead zones, whereas there is good circulation inside the riser even at low liquid velocities. Thus increase in air flow rate offers no advantage in increasing the circulation in the downcomer region. Also for D/T ratio of 0.5 and 0.75, the liquid velocities increased both in riser and downcomer with increasing gas flow rate but the change was marginal as compared to D/T of 0.25. Configurations with single point sparger also showed same effect of gas flow rate; see Figure 5.5.

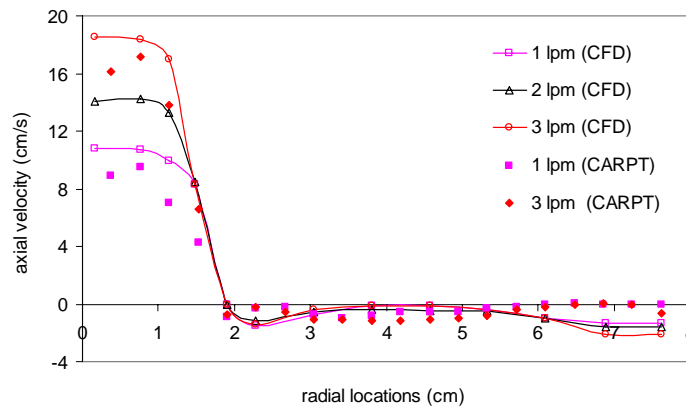


Figure 5.4 Effect of gas flow rate on axial liquid velocity at the center of tank for $D/T=0.25$, cross sparger (LS1, LS2 and LS3)

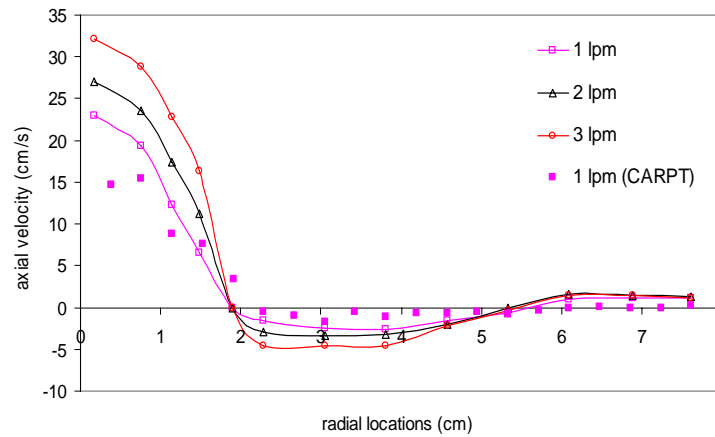


Figure 5.5 Effect of gas flow rate on axial liquid velocity at the center of tank for $D/T=0.25$, single point sparger (LS10, LS11 and LS12)

All three gas flow rates correspond to bubbly flow regime or regime one (no gas entrainment in downcomer). Thus the liquid velocity increases with increasing gas flow rate, this has been proven experimentally also by Freitas et al. (1999), Klein et al. (2003), Lu et al. (1995), Sun et al. (2005) and Wen et al. (2005).

The nature of gas distribution remains the same, only the value of gas holdup increases with increasing gas flow rate. The overall gas holdup increases from 0.1% to 0.16% as gas flow rate increases from 2 lpm to 3 lpm. This increase in gas holdup increases the driving force for liquid circulation. Even at highest gas flow rate of 3 lpm there is no gas entrainment in the downcomer, corresponding to regime one.

Effect of Draft Tube (Riser) Diameter

Effect of draft tube diameter on the flow can be evaluated by changing the draft tube diameter to tank diameter ratio (D/T) at a given gas flow rate and for a particular type of sparger. Flow pattern at air flow rate of 1 lpm, for D/T of 0.25 with cross sparger (simulation LS1) is shown in Figure 5.1a and was discussed earlier. The flow pattern at 1 lpm for D/T ratio of 0.5 and 0.75 (simulation LS4 and LS7) with cross sparger is shown in Figure 5.6a and Figure 5.6b, respectively. Since the flow pattern remains unaffected

by air flow rate, the flow patterns for higher gas flow rates of 2 and 3 lpm are not shown here.

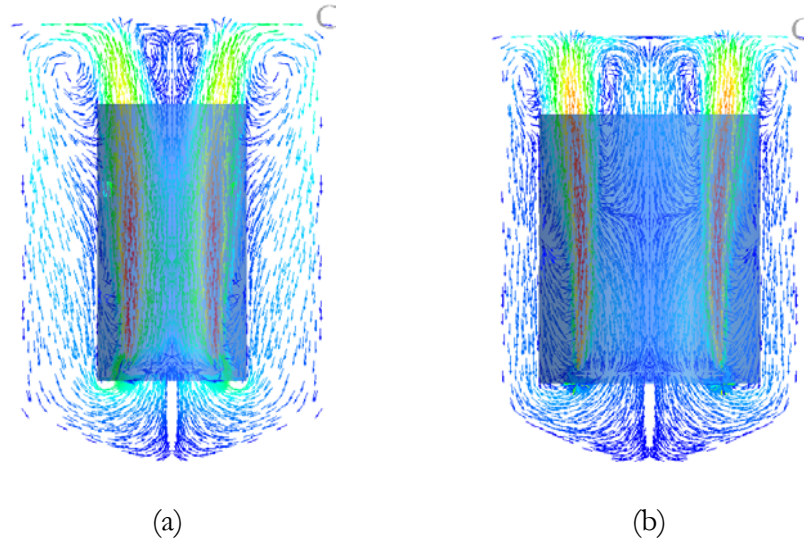


Figure 5.6 Effect of D/T ratio on flow pattern with cross sparger at 1 lpm;
 (a) simulation LS4, $D/T=0.5$ (b) simulation LS7, $D/T=0.75$

The overall flow pattern in digester with larger draft tube diameter is different as compared to the one with smaller draft tube. There is one circulation loop inside the riser in Figure 5.6a and 5.6b, which is absent in digester with smaller draft tube diameter ($D/T=0.25$), Figure 5.1a. This internal circulation loop inside the riser was also observed by Blazej et al. (2004a). There are two other circulation loops present in Figures 5.6a and 5.6b, one stronger loop at the top of the digester and other weaker loop in the downcomer. For more explanation, see Section 4.3.1 of Chapter 4.

The existence of circulation loops inside the riser can be explained by the nature of gas distribution inside the riser, see Figure 5.7a and 5.7b. As D/T increases, the distance between the sparger holes also increases. Thus, gas is sparged towards the riser wall, leaving an unsparged region in the center. This nature of gas distribution initiates the circulation loops inside the riser. More the distance between the sparged regions, stronger is the circulation loop.

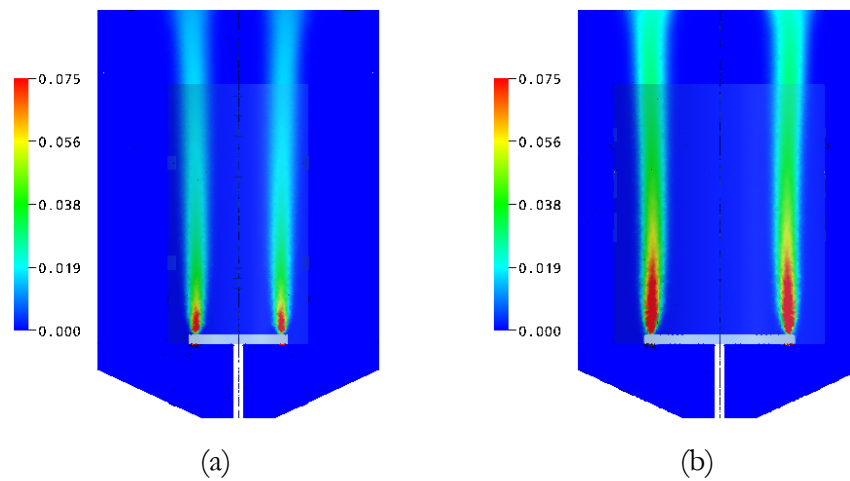


Figure 5.7 Effect of D/T ratio on gas holdup distribution with cross sparger at 1 lpm;
 (a) simulation LS4, $D/T=0.5$ (b) simulation LS7, $D/T=0.75$

As the D/T ratio increases, the magnitude of axial velocity inside the riser decreases. This was expected, with same gas flow rate as the area for flow increases with the increasing draft tube diameter the velocity decreases, according to Bernoulli's principle.

Figure 5.8a to 5.8c shows the flow pattern at 1 lpm for configuration with single point sparger and D/T ratio of 0.25, 0.5, and 0.75 (simulation LS10, LS13, and LS16), respectively. Changing draft tube diameter does not change the flow pattern appreciably for configurations with single point sparger.

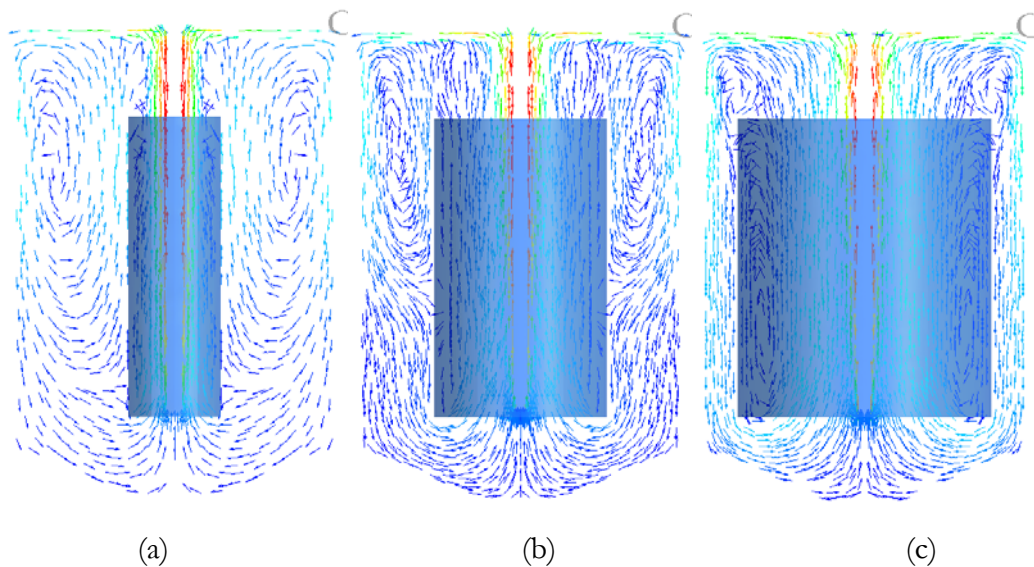


Figure 5.8 Effect of D/T ratio on flow pattern with single point sparger at 1lpm;
 (a) LS10, $D/T=0.25$; (b) LS13 $D/T=0.5$; (c) LS16, $D/T=0.75$

The difference between the flow patterns is mainly due to the different gas distribution. Since, for single point sparger the gas distribution is not affected by the D/T ratio, (see Figure 5.9a, 5.9b and 5.9c) the flow pattern is also not significantly affected by the D/T ratio. Although, as the D/T ratio increases, the unsparged portion of the riser increases and initiates some liquid circulation in the riser due to difference in gas holdup inside the riser at different sections.

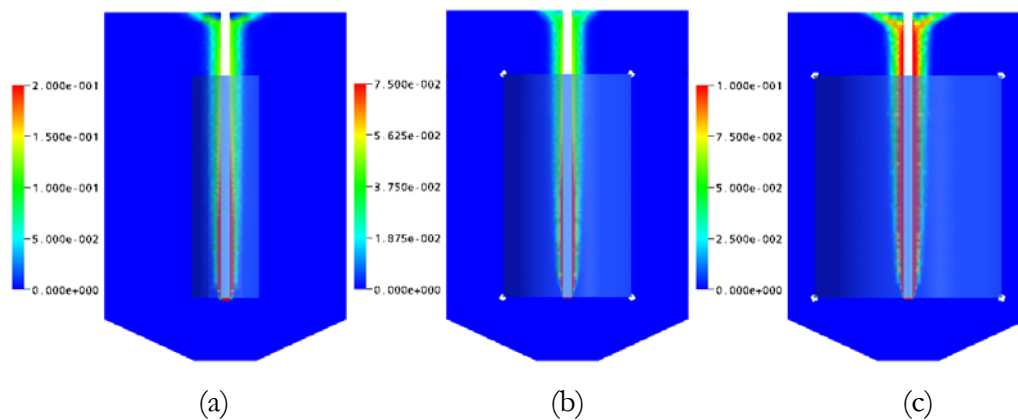


Figure 5.9 Effect of D/T ratio on gas holdup distribution with single point sparger at 1lpm; (a) LS10, $D/T=0.25$; (b) LS13 $D/T=0.5$; (c) LS16, $D/T=0.75$

Effect of D/T ratio on the time averaged liquid axial velocity radial profiles at 1 lpm at the center of the tank is shown in Figure 5.10a and 5.10b for cross sparger and single point sparger, respectively. In Figure 5.10a for configurations with cross sparger the trend of velocity profiles, as well as the magnitude of liquid velocities are different for different D/T ratio. Whereas, in Figure 5.10b for single point sparger, the trend of velocity profiles is same for all D/T ratios. The liquid axial velocities are higher for lower D/T ratios. The negative velocities for D/T of 0.5 and 0.75 in the downcomer, indicates the downward velocities and existence of circulation loop. Draft tube diameter affects the velocity profile for configurations with cross sparger but not with single point sparger. It is due to the nature of gas distribution, which is affected by sparger design.

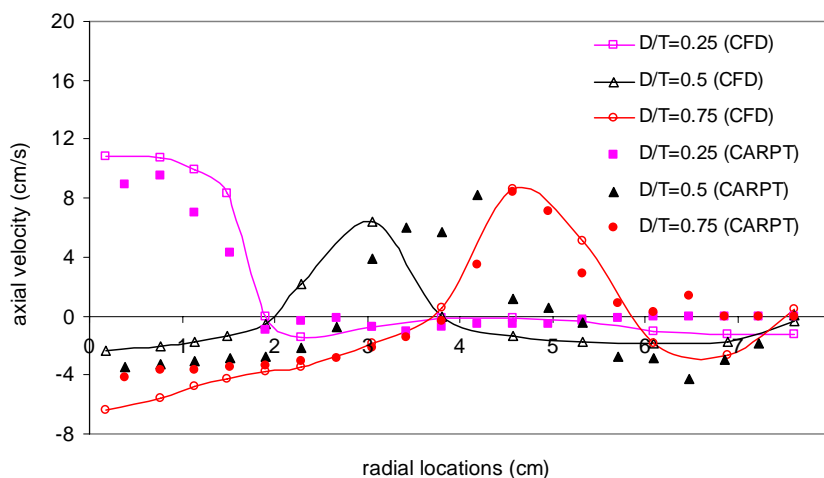


Figure 5.10a Effect of D/T ratio on liquid velocity with cross sparger and 1 lpm gas flow rate (simulation LS1, LS4, and LS7)

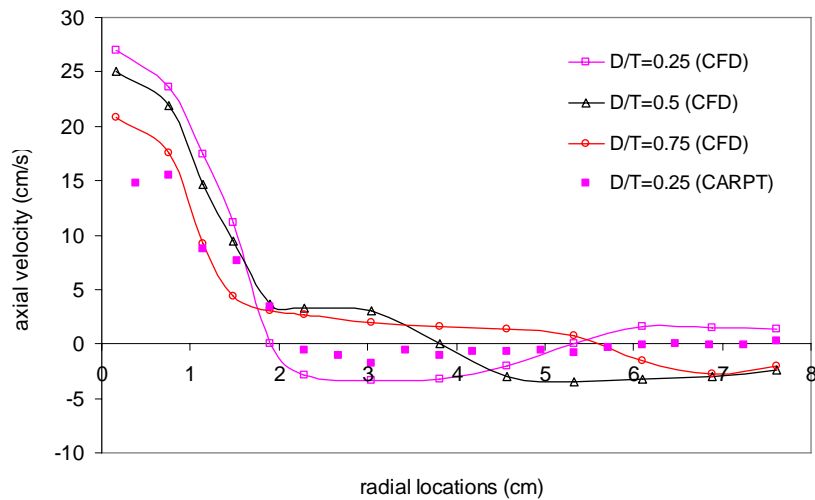


Figure 5.10b Effect of D/T ratio on liquid velocity with single point sparger 1 lpm gas flow rate (simulation LS10, LS13, and LS16)

Effect of Sparger Geometry

The flow patterns are same for both sparger designs at D/T ratio of 0.25. For D/T ratio of 0.5, (Figure 5.6a and Figure 5.8b), the flow patterns are completely different. This is also true for D/T ratio of 0.75 (Figure 5.6b and Figure 5.8c). Sparger does not affect the flow pattern for smaller D/T ratio of 0.25 but does affect appreciably for higher D/T ratios of 0.5 and 0.75.

In simulation LS1 to LS3 and LS10 to LS12, the effect of sparger is not very important due to smaller draft tube diameter (D/T ratio of 0.25). Same observations were made by Mudde and Van Den Akker (2001) in their simulation results, and reasons for this behavior are discussed in Chapter 4.

The effect of sparger on the axial liquid velocity profile is shown in Figure 5.11 for different D/T at 1 lpm gas flow rate for laboratory-scale. It can be observed from Figure 5.11, that the high liquid velocities in case of single point sparger are present only in small central core in the riser. In the annular region near the riser wall and in the downcomer, liquid velocities are higher for cross sparger as compared to single point

sparger. The higher velocities are the result of higher gas flow rate dispersed at one single location by the pipe sparger as opposed to the cross sparger, where only one-fourth of given flow rate is dispersed at each of the four sparger holes. Cross sparger is creates fairly dispersed gas distribution that also results in higher liquid velocities. Becker et al. (1994) observed from his experiments and simulations that multipoint sparger creates higher liquid velocities due to homogeneous gas dispersion as compared to pipe sparger.

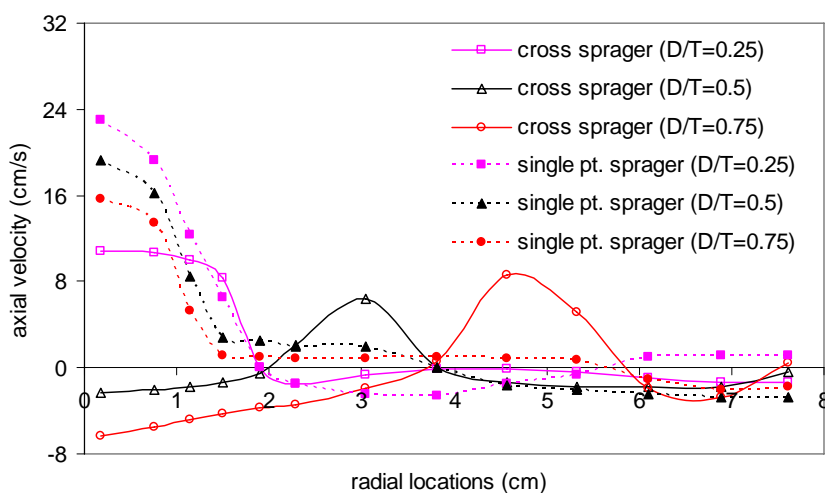


Figure 5.11 Effect of sparger geometry for different D/T ratios on liquid velocity at gas flow rate of 1 lpm (Simulation LS1/LS4/LS7 versus LS10/LS13/LS16)

Volume of Dead Zones or Stagnant Regions

In the present study the dead zones volume was evaluated by locating the cells with very low velocities (1 cm/sec was used here, as this value was used in Chapter 4 using CARPT data), and summing up the volumes of these cells. Table 5.3 shows the dead zone volumes for different digester configurations (the number in the cells represent the percentage dead volume and simulation numbers are given in the bracket).

The dead zone volume decreases by increasing the gas flow rate, but it is clear from the flow patterns that circulation is localized only inside the riser for D/T of 0.25, thus decrease in dead zone volume does not indicate more homogeneity in this case. For

higher D/T ratios (0.5 and 0.75), the effect of gas flow rate on dead volume is not very appreciable.

D/T ratio of 0.75 has highest dead volume, whereas it is lowest for D/T of 0.5. Only 30% of the digester volume is inactive/dead in case of D/T of 0.5, whereas this number is higher for D/T of 0.75. Flow patterns in Figure 5.1 and 5.6 indicate that the digester with D/T of 0.5 is mixed more homogeneously thorough out the volume than the digester with D/T of 0.75.

For D/T ratio of 0.25, the sparger design has no effect on the dead zone volumes. For higher D/T ratios of 0.5 and 0.75, configurations with cross sparger has lower dead zone volume as compared to configurations with single point sparger.

5.4.2 Pilot-scale (18-inch Diameter Digester)

Simulation Results and Comparison with CARPT Data

Figure 5.12a show the flow pattern obtained from 3D CFD simulation for pilot-scale digester (simulation PS2). Similar flow patterns were obtained from CARPT results. Simulated flow patterns, Figure 5.12a is compared with experimentally obtained flow patterns, Figure 5.12b. Figure 5.12a and 5.12b, shows good qualitative agreement between the simulation and the experimental results for flow pattern, location of stagnant zones, and circulation loops.

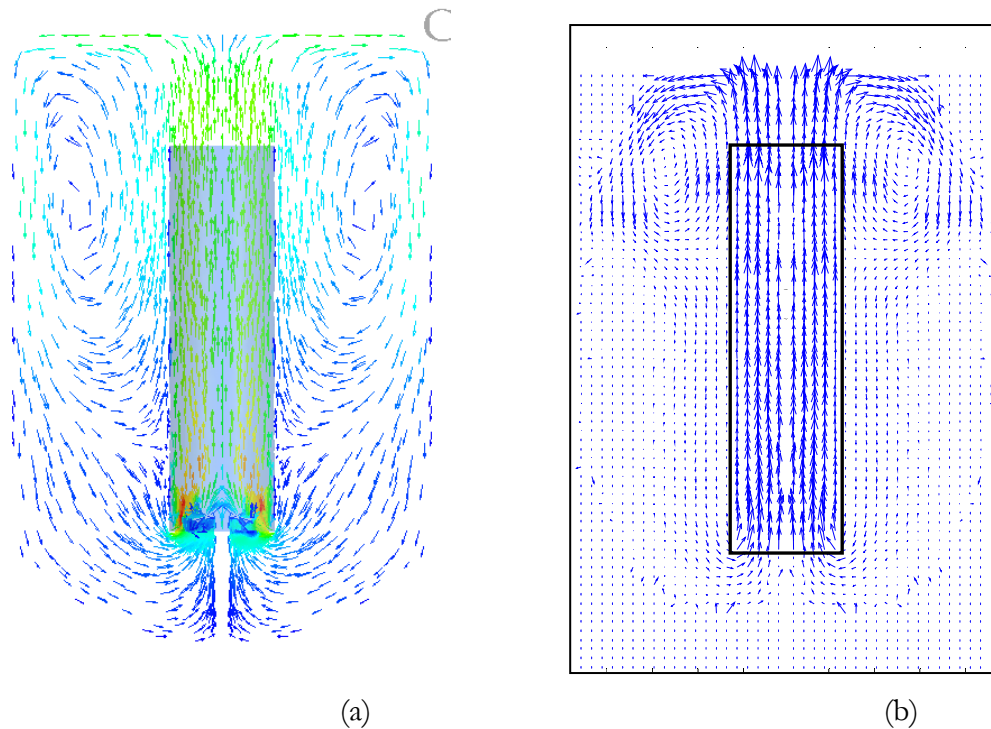


Figure 5.12 Comparison of (a) simulated flow pattern (PS2) and (b) flow pattern obtained from CARPT (P2)

The flow pattern obtained agrees with simulation predictions for 8-inch and 6-inch diameter laboratory-scale digesters.

Figure 5.13 shows radial profile of azimuthally averaged axial liquid velocities at different axial locations obtained from CFD simulation PS2. The level of $z=6$ cm represents the horizontal level inside the conical bottom region at 6 cm from the bottom of the digester, similarly $z=12$ cm is just below the draft tube, $z=33$ cm is at the centre of the draft tube or tank, and $z=54$ cm is just above the draft tube. Figure 5.13 also presents the quantitative comparison of CFD predictions of liquid velocity with the CARPT results. The CFD predictions match reasonably with the CARPT experimental data. The trend of velocity profile matches very well with the experimental data, but the values of liquid velocity are over predicted by CFD. The simulated liquid velocities

match experimental data better in downcomer section as compared in the riser. Just like laboratory-scale simulation predictions.

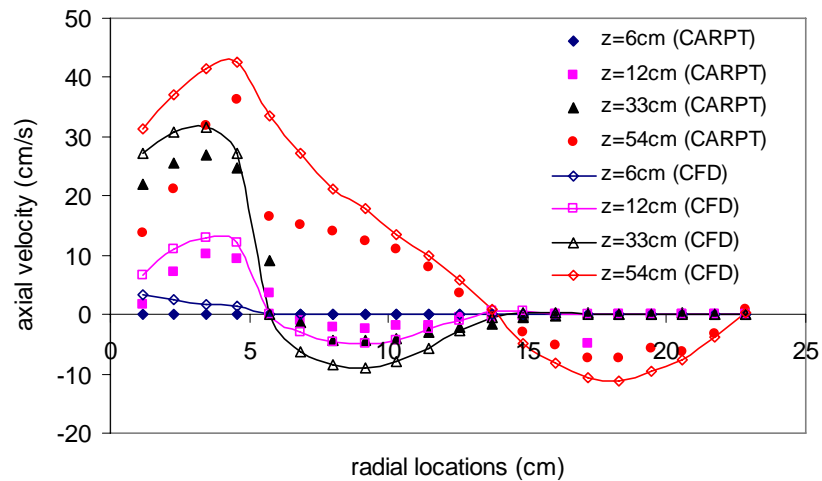


Figure 5.13 Pilot-scale, comparison of simulated axial liquid velocity profile for simulation PS2 with experimental CARPT data.

The gas prediction of Simulation PS2 is shown in Figure 5.14. The same pattern was obtained in similar laboratory-scale configuration (see Figure 5.3). The overall gas holdup is even smaller than the laboratory-scale, only 0.005%.

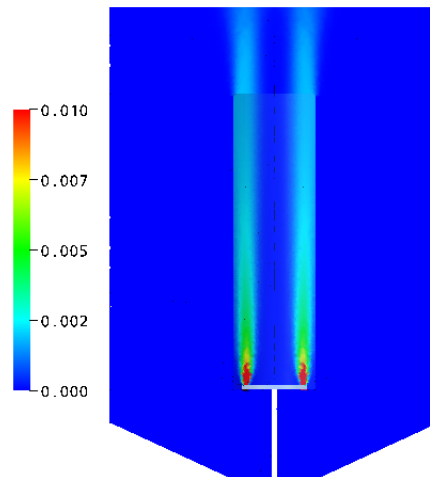


Figure 5.14 Gas hold up distribution predicted by CFD for Simulation PS2

The scale does not affect the accuracy of the predictions of CFD simulations because the simulation grid was made sufficiently small in both scales.

Pilot-scale simulations PS1 to PS3 and PS7 to PS12 were also performed to check the predictability of the CFD simulations. For all these conditions, CFD predictions agree only reasonably with the experimental data on quantitative basis but predict the trends of liquid velocity profile accurately (i.e. good qualitative agreement). The comparison of experimental data and predictions of these simulations will be presented in the further discussion.

The dead zone volumes (explained in detail in later section) obtained from CFD simulation results for selected configurations are compared with experimental values in Table 5.4. The agreement between the simulated and experimental values is reasonably accurate.

Table 5.4 Comparison of dead zone volumes predicted by CFD with experimental data for pilot-scale digester

Sparger geometry	D/T	Gas superficial velocity (mm/sec)	% Dead volume	
			CFD	CARPT
Cross sparger	0.25	0.45	62 (PS1)	61 (P1)
		0.91	58 (PS2)	55 (P2)
		1.82	51 (PS3)	50 (P3)
	0.5	0.45	50 (PS)	-
		0.91	44 (PS5)	-
		1.82	36 (PS6)	-
	0.75	0.45	68 (PS7)	65 (P4)
		0.91	62 (PS8)	60 (P5)
		1.82	59 (PS9)	54 (P6)
Single point sparger	0.25	0.45	60 (PS10)	63 (P7)
		0.91	57 (PS11)	58 (P8)
		1.82	53 (PS12)	53 (P9)

Since the applicability of the CFD simulations to predict the flow pattern and liquid velocities at both the scales have been established to match the trend of liquid velocity profiles, these CFD models can be now used to simulate flow in gaslift digesters at other operating conditions listed in Table 5.2 and to evaluate the effect of different operating and geometric variables.

Effect of Air Flow Rate

Effect of air flow rate for a given D/T ratio and a particular type of sparger can be evaluated using the simulations listed in Table 5.2. The flow pattern remains unaffected by the air flow rate (not shown here), only the magnitude of the liquid velocity changes as discussed below. Similar observations were made for the effect of gas flow rate on liquid velocity for laboratory-scale simulations. The results are shown in Figure 5.15a and 5.15b.

All three gas flow rates correspond to bubbly flow regime or regime one (no gas recirculation in downcomer) for pilot-scale digester also. Thus the liquid velocity increases with increasing gas flow rate.

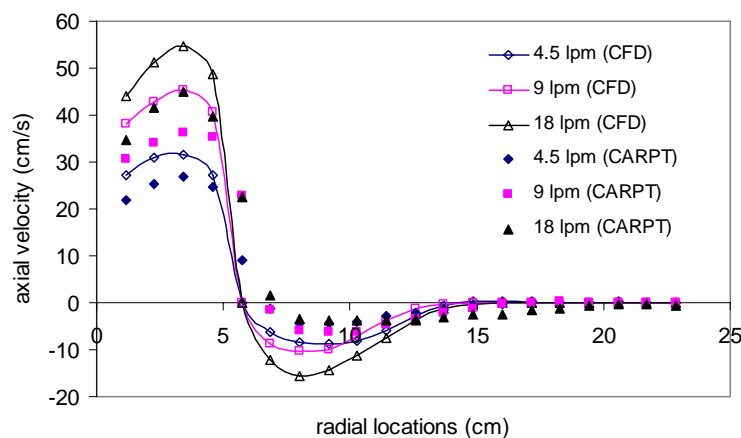


Figure 5.15a Effect of gas flow on axial liquid velocity at the center of tank for $D/T=0.25$, cross sparger (PS1, PS2 and PS3)

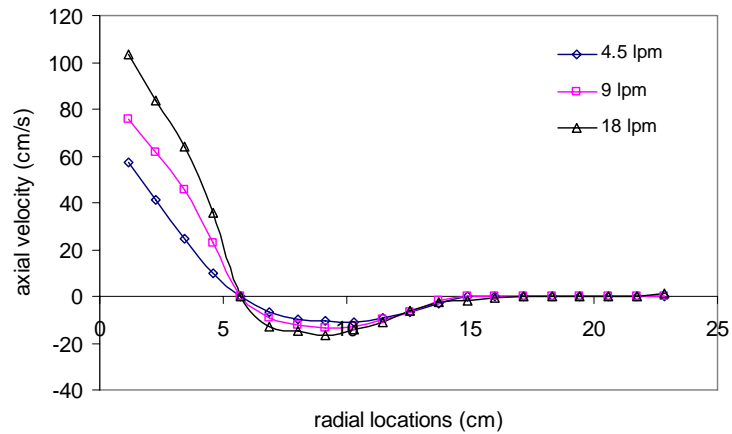


Figure 5.15b Effect of gas flow on axial liquid velocity at the center of tank for $D/T=0.25$, single point sparger (PS10, PS11 and PS12)

Effect of draft tube (riser) diameter

Effect of D/T ratio of axial liquid velocity profile for cross sparger in pilot-scale is shown in Figure 5.16. The discussion for effect of D/T ratio for laboratory-scale simulations also holds for pilot-scale.

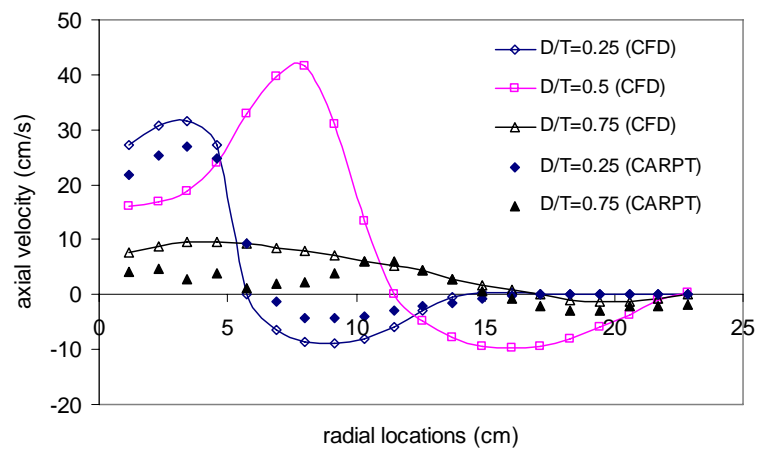


Figure 5.16 Effect of D/T ratio on liquid velocity with cross sparger 4.5 lpm gas flow rate (simulation PS1, PS4, and PS7)

Effect of Sparger Geometry

Effect of sparger geometry for pilot-scale simulations at D/T ratio of 0.25 is same as discussed for laboratory-scale simulations; see Figure 5.17.

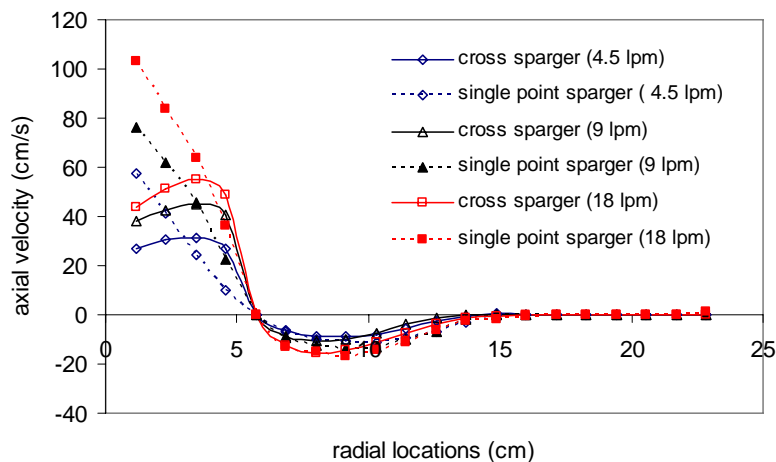


Figure 5.17 Effect of sparger geometry for D/T ratio of 0.25 on liquid velocity at different gas flow rates (simulation PS1, PS2, and PS3 versus PS10, PS11 and PS12)

Volume of dead zones or stagnant regions

Above discussion is applicable to both laboratory-scale and pilot-scale simulations. The discussion for laboratory-scale in Section 5.5.2 is applicable here for pilot-scale also. See Table 5.4 for the values of volume of dead zones.

5.4.3 Effect of Scale (6-inch v/s 18-inch Diameter Digester)

The results of laboratory-scale and pilot-scale CFD simulations can be compared to investigate the effect of scale. The liquid volume in laboratory-scale was 3.78 L whereas for pilot-scale it was 97 L, thus a volumetric scale up factor of approximately 25 was employed. Geometry of simulated digester at both the scales was similar; the diameter of pilot scale digester was three times the diameter of laboratory-scale. The gas flow rate

of 1 lpm and 2 lpm in small scale and gas flow rate of 9 lpm and 18 lpm in pilot scale corresponds to same superficial gas velocity of 0.91 and 1.82 mm/sec, respectively, based on tank diameter (14.6 and 29.2 mm/sec based on draft tube diameter for D/T ratio of 0.25).

Thus the laboratory-scale and pilot-scale configurations with cross sparger for D/T of 0.25, 0.5 and 0.75 operating with superficial gas velocity of 0.91 and 1.82 mm/sec can be compared to evaluate the effect of scale. Configurations with single point sparger for D/T of 0.25 can also be compared.

Comparison of flow patterns of configurations with cross sparger with D/T of 0.25 and superficial gas velocity of 0.91 mm/sec (simulation LS1 and PS2) shows that the flow patterns are qualitatively similar; Figure 5.1a and 6.12a. Liquid axial velocity profiles can be compared for qualitative analysis. To facilitate the comparison, the axial liquid velocity at all the radial locations is made dimensionless. Axial velocities of laboratory-scale at center of the tank are divided by the maximum liquid velocity for laboratory-scale at the center of the tank to obtain dimensionless velocity. Similarly, axial velocities for pilot-scale at center of the tank are divided by the maximum liquid velocity for pilot-scale at the center of the tank to obtain dimensionless velocity. Figure 5.17a shows the comparison of dimensionless axial liquid velocity profile (for simulation LS1 and LS2 versus PS2 and PS3).

The velocity profile has the same shape. Not only the velocity profiles of two scales should overlap each other for the two scales to be hydrodynamically similar, but their magnitudes of velocities should also match (elaborated further in the following discussion). The slight difference between the dimensionless profiles shows the effect of scale on the flow pattern and trend of liquid velocity.

Comparison of flow patterns of configurations with single point sparger with D/T of 0.25 and superficial gas velocity of 0.91 mm/sec (simulation LS10 and PS11) shows that

the flow patterns are qualitatively similar. The dimensionless velocity profile of both scales matches well, Figure 5.17b (simulation LS10 and LS11 versus PS11 and PS12).

Unlike for D/T of 0.25, the laboratory-scale and pilot-scale flow patterns are quite different for higher D/T ratios of 0.5 and 0.75. The laboratory-scale digester has only one circulation loop inside the draft tube, with liquid moving down in the center and up towards the wall. For pilot-scale, the circulation pattern is more complex. The liquid moves downwards in the center in upper part of draft in a smaller independent circulation loop, while the liquid is directed upwards in the center of draft tube at the bottom. Figure 5.17c and 6.17d clearly shows the difference in axial velocity profile due to different flow patterns.

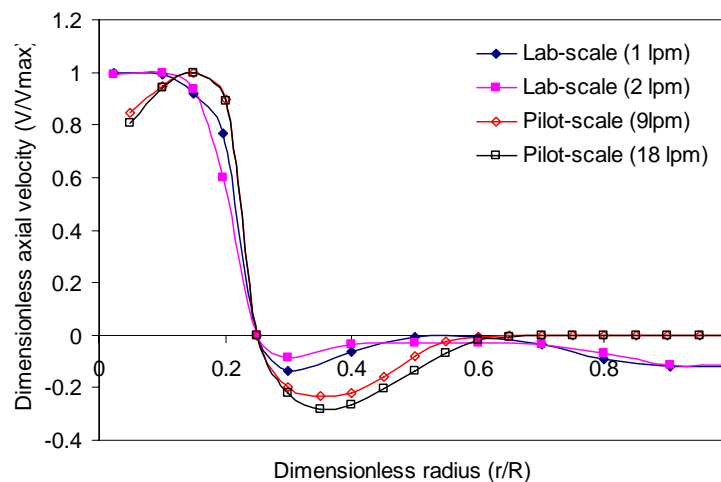


Figure 5.17a Effect of scale on dimensionless axial liquid velocity profile (simulation LS1 and LS2 versus PS2 and PS3, with corresponding maximum liquid velocities of 10.8, 14.2, 45.2 and 54.7, respectively)

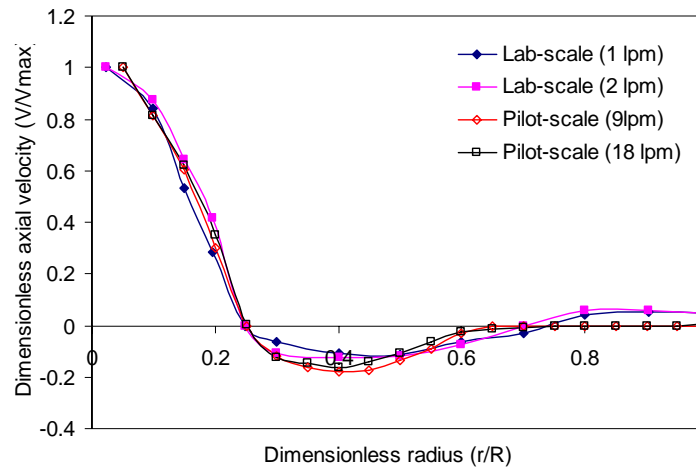


Figure 5.17b Effect of scale on dimensionless axial liquid velocity profile (simulation LS11 and LS12 versus PS12 and PS13, with corresponding maximum liquid velocities of 23, 27, 76 and 103.4, respectively)

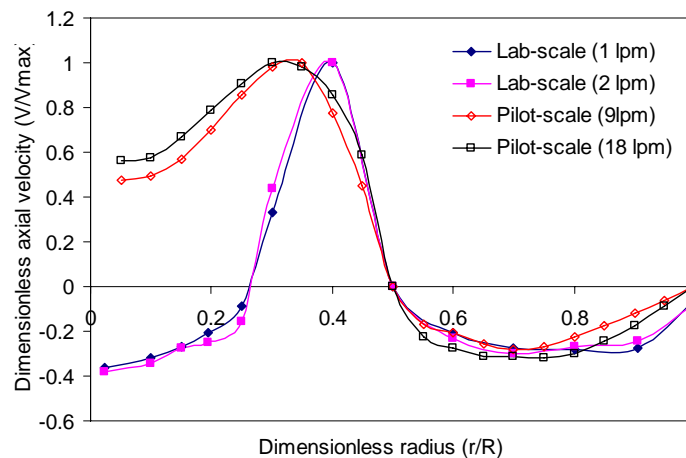


Figure 5.17c Effect of scale on dimensionless axial liquid velocity profile (simulation LS4 and LS5 versus PS5 and PS6, with corresponding maximum liquid velocities of 6.4, 7.6, 50 and 57.2, respectively)

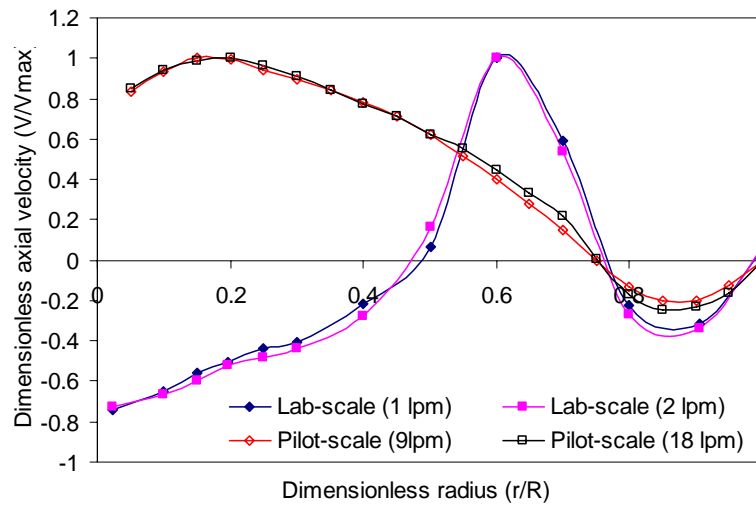


Figure 5.17d Effect of scale on dimensionless axial liquid velocity profile (simulation LS7 and LS8 versus PS8 and PS9, with corresponding maximum liquid velocities of 8.6, 10.1, 12.1 and 14.9, respectively)

Figure 5.18 explains the true effect of scale on the axial liquid velocity for simulation LS1, LS2, PS2 and PS3. In Figure 5.18 the magnitude of axial velocity is compared rather than dimensionless velocities. The liquid velocities in pilot-scale are about 2 to 3 times higher as compared to laboratory-scale. This has been observed experimentally and also by CFD simulations. (For other configurations the difference in the magnitude of liquid velocities can be compared by multiplying the dimensionless velocity with respective maximum axial liquid velocity; the values of corresponding maximum velocities are provided with the Figures 6.17a to 6.17d.)

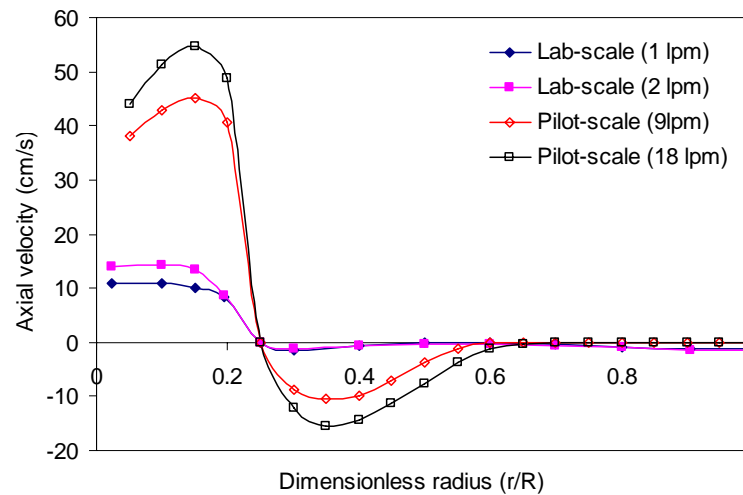


Figure 5.18 Effect of scale on axial liquid velocity profile (simulation LS1 and LS2 versus PS2 and PS3)

Blazej et al. (2004b) and Gavrilescu and Tudose (1998) observed increase in liquid circulation velocity and decrease in gas hold up with increasing scale. van Baten et al. (2003b) found that the radial profiles of gas holdup and liquid velocity simulated by CFD in pilot-scale are much more parabolic in shape as compared to laboratory-scale. The frictional losses of the liquid phase encountered in pilot-scale are much reduced, and this causes much higher liquid circulation and a significantly smaller gas holdup. Blazej et al. (2004b) evaluated the friction factor coefficients in IGLR using empirical correlations and hydrodynamic model of Heijnen et al. (1997) and proved that the friction factor coefficients decreases with increasing scale of reactor (from 10.5 liters to 200 liters). This is explained in detail in Section 4.3.3 of Chapter 4.

The dead zone volumes listed in Table 5.3 and 5.4 can help to understand the effect of scale on dead zones. For pilot-scale the dead zone volumes are higher as compared to laboratory-scale for same superficial gas velocity. Even though the liquid velocities in pilot-scale are higher, it does not help in lowering the dead zones significantly. This is also true for average circulation time (evaluated from CARPT data in Chapter 4 for laboratory-scale and pilot-scale). The mean circulation time (used to quantify mixing) is

higher for pilot-scale as compared to laboratory-scale for same gas superficial velocity. In most of the biological applications of IGLR, gas holdup or mass transfer coefficients are chosen to evaluate the mixing performance. In case of anaerobic digester, gas is sparged only to mix the reactor contents and not for reaction. The mass transfer coefficient is not appropriate criteria to evaluate its mixing performance.

Higher liquid velocities in pilot-scale do not imply that the pilot-scale reactors are better mixed than the laboratory-scale for same energy input per unit volume. (Superficial gas velocity of 0.91 cm/sec corresponds to same power input per unit volume of 8 W/m^3 in both laboratory-scale and pilot-scale.) The scale-up ratio is 25, thus, just 2-3 times increase may not be sufficient to achieve same mixing intensity or same mixing performance at pilot-scale.

Thus the questions one needs to ask in relation to scale-up of IGLRs are: What should be the appropriate scale-up criterion? How can mixing be quantified correctly for a given application? Although this study cannot answer these questions satisfactorily, few points are clear from experimental and CFD results. Such as, same superficial gas velocity or same energy input per unit volume cannot be used as a scale-up criterion in this case. Next issue is about the applicability of CFD for design and scale-up of IGLRs.

CFD simulations were able to account reasonably for the effect of scale for a scale-up factor of 25. The comparison of experimental data and simulation predictions was reasonable for both scales and the predictability of simulations was same at both scales. This may not happen at scales larger than this. Bagatin et al. (1999) observed that the CFD simulations showed high degree of reliability at laboratory and pilot-scale IGLRs, but when reactors of even larger (full-scale) dimension were considered, the agreement was poor. According to them it was due to the poor description of the bubble size distribution using a single-size model.

5.5 Summary

3D CFD simulations were used to predict the flow in gaslift digesters. The CFD predictions showed good qualitative comparison with the experimental data but gave only reasonable quantitative agreement. Different closures and addition of interphase force terms in the CFD model did not improve the CFD predictions.

CFD was able to account for the effect of geometry and operating variables at both laboratory-scale and pilot-scale. The geometrical variations and operating conditions that were not used in experiments to evaluate their effect on hydrodynamics of IGLRs were evaluated with CFD. The increase in the gas flow rate for all configurations of gaslift digesters increased the axial liquid velocities in the riser but showed no added advantage in increasing the dead zone volumes effectively in the downcomer. The flow pattern was affected appreciably by changing the draft tube diameter. The configuration with D/T ratio of 0.5 showed lowest volume of dead zones. From the conclusions of experiments from Chapter 4 and the results of CFD simulations, it becomes clear that the D/T ratio of 0.5 offers better liquid circulation as compared other D/T of 0.25 and 0.75.

Sparger design affects flow pattern for higher D/T ratios of 0.5 and 0.75, but showed no effect for smaller D/T ratio of 0.25. Better gas dispersion created by cross sparger is advantageous in increasing the circulation and decreasing the dead zone volume over the local dispersion created by the single point sparger.

CFD simulations were able to account for the effects of scale. The scale affects the flow pattern and as a result, liquid velocities are also affected. At same superficial gas velocity, the liquid velocities are about 2-3 times higher in pilot-scale as compared to laboratory-scale. Does it imply that the large-scale reactors are better mixed than the small reactors at same energy input? Is 2-3 times increase in liquid velocity for a scale-up

ratio of 25 enough to achieve same intensity of mixing at two scales? If the dead zone volumes and liquid circulation are treated as parameters that quantify mixing, then the answer to above questions is 'No'. Same gas superficial velocity or same energy input per unit volume did not provide same mixing intensities in the two scales of reactor. Thus superficial gas cannot be used a scale-up criterion.

Chapter 6

Summary and Recommendations

6.1 Summary

Anaerobic digestion is a preferable method of animal waste treatment because it reduces the environmental pollution and also provides energy in the form of methane. To reduce the anaerobic digester failure rate and increase its use on the farms, proper understanding of their performance and effect of variables that affect the performance is necessary. Mixing is one of the important variables affecting digester performance. Thus, main objective of this study was to advance the knowledge and understanding of the role of hydrodynamics in the anaerobic digester performance.

In this work the literature was reviewed and the key parameters contributing towards better design of anaerobic digesters were identified. Role of mixing in performance of anaerobic digesters needed more investigation, thus performance experiments to evaluate the contribution of mixing in digesters performance were designed, as explained in Appendix A. From the results of preliminary lab-studies and considering the advantages of low energy consumption and easy operation offered by gaslift internal loop reactor, it was chosen for the performance studies. The results of these performance experiments suggested need of detailed investigation of hydrodynamics of the digesters, which was accomplished through experimental and computational studies.

The important findings of these experimental and computational studies are summarized in this chapter. Detailed summaries of each of these studies are also provided at the end of each chapter from Chapter 3 to Chapter 6.

6.1.1 Development of Multiple-Particle Tracking

MP-CARPT was developed to overcome the limitations of the old single particle CARPT. Newly developed MP-CARPT was successfully validated and tested for tracking of single or two, stationary and moving tracer particles. This technique is now available for implementation on multiphase systems. The main highlights of MP-CARPT are as follows:

- MP-CARPT provides ability to track eight different radioactive tracer particles simultaneously. The radioactive tracers are distinguished on the basis of their gamma energy peaks.
- MP-CARPT is designed such that the data acquisition is faster and free of any interruptions due to nature of flow in the reactor with dead spaces.
- MP-CARPT enables to track more than two solid particles in the system simultaneously, thus the particle-particle interactions can be measured.
- MP-CARPT system is faster, cheaper, compact and advanced as compared to old single particle CARPT system.

MP-CARPT was implemented on a low L/D slurry bubble column reactor to test its ability to track tracers representing different phases (solid and liquid in this case). MP-CARPT successfully provided the flow patterns and velocities of solid and liquid phase in SBCR.

6.1.2 Hydrodynamic Studies: CARPT

Hydrodynamic studies using CARPT were also performed at both laboratory-scale and pilot-scale digester configurations to understand the difference in hydrodynamics at different scales, which can be related to the performance of digesters. CARPT also provided the information about the effect of geometrical and operating variables on the hydrodynamic and turbulent parameters. The main findings were as follows:

- Diameter of draft tube and the geometry of sparger were two important variables that had significant effect on the flow and hydrodynamics in gaslift digester at both the scales.
- Dead zone volume and eddy diffusivity were used to quantify mixing. On basis of these parameters it was found that configuration with draft tube diameter half of the reactor diameter provides good mixing performance. A sparger with uniform distribution of gas over the cross section of riser provides better mixing than the gas dispersion concentrated at a single point.
- Same energy input per unit volume in geometrically similar gas recirculation type digesters was used as a scale-up criterion. The liquid circulation velocities were higher in pilot-scale than the laboratory-scale configurations. But the dead space volume and circulation mixing time were also higher in pilot-scale, suggesting that the laboratory-scale digester shows better mixing performance than the pilot-scale. These findings explain the need of external mixing in case of pilot-scale anaerobic digesters in performance studies.
- Thus, maintaining same energy input and geometric similarity is not sufficient to obtain to the same mixing performance at two scales of operation of gaslift digester.

6.1.3 CFD Studies

CFD studies were performed because of the time and resources constraints associated with CARPT. Before CFD could be used to simulate various geometries of digesters, operating at different operating conditions, the CFD models need to be evaluated against the experimental data. The main findings from the CFD studies were as follows:

- The CFD predictions showed good agreement with the experimental data only qualitatively, whereas the quantitative agreement was only satisfactory or reasonable.
- The CFD predictions also clarified that the draft tube diameter and the sparger geometry are two more important parameters affecting the hydrodynamics of gaslift digesters.
- CFD simulations were able to account for the effect of scale on the geometry and proved that the power input per unit volume is not the correct scale-up criteria.

To summarize, the mixing or hydrodynamics have a significant impact on the performance of large-scale anaerobic digesters. Thus, the effect of mixing should be accounted during the design of anaerobic digesters. The variables that affect the hydrodynamics, such as geometry and type of digester, operating conditions, energy input should also be considered in addition to the factors that affect the anaerobic digestion reaction, such as feed characteristics, pH, temperature, level of toxins and nutrients, etc. The coupling of performance knowledge with the hydrodynamics, as followed in this work, will lead to successful design and scale-up of anaerobic digesters.

6.2 Recommendations for Future Work

Research does not have an end! Solution of one problem raises more questions, provides new goals for investigation of another aspect of same problem or in some cases creates identifies more problems. As any other research project, the work accomplished in this thesis was also constrained by the time and resources. For complete understanding of anaerobic digesters, more research needs to done. Some of the points that need further investigation are listed in the following paragraphs and are identified as future work.

There is still room for improvement of CFD predictions. New closure laws or modified interphase terms should be identified to improve the CFD predictions.

The MP-CARPT system has a great potential to provide important hydrodynamic information of industrially important multiphase reactors. This potential should be exploited to take full advantage of capability of MP-CARPT. For example, in case of gas-solid fluidized beds, the solids occur in different sizes, shapes and properties. Using MP-CARPT hydrodynamics and interaction of these solids of different properties can be evaluated; this information is very valuable for design of such reactors and also for validation of CFD simulations.

The reconstruction of MP-CARPT can be further improved to get more accurate results. Use of new “matrix-calibration” technique can significantly reduce the reconstruction errors. This technique will require modifications to current calibration system. Modification of reconstruction algorithm provided by Bhusarapu (2005) can also increase the reconstruction accuracy. The current reconstruction program is only applicable for tracking two radioactive tracers simultaneously. Slight modifications are needed to extend this program for reconstruction of 2 or more tracers tracked simultaneously.

Appendix A

Performance Studies: Laboratory-scale and pilot-scale

A.1 Introduction

Mixing in anaerobic digester is required for number of important reasons viz. to provide efficient utilization of entire digester volume, to prevent stratification and temperature gradients, to disperse metabolic end products and any toxics contained in the feed, to maintain intimate contact between the bacteria and the substrate, to prevent foaming and scum formation and to avoid solids settling. In short, adequate mixing provides a uniform environment, one of the keys to good digestion.

In spite of the crucial role of mixing in digester operation, contradictory findings are reported in the literature about the necessity of mixing and the required mixing intensity to enhance the digester performance. There are many reasons for these controversies and uncertainties. One of them is, mixing is not adequately quantified and characterized in these systems. Another important reason is, most of these digester performance studies are performed in small laboratory-scale reactors and/or using low solids concentration. These approaches do not contribute greatly in understanding influence of mixing on digester performance or in providing criteria for full scale digester design.

Laboratory-scale reactors are valuable in estimating kinetic parameters, in estimation of nutrient and alkalinity requirements and discovering potential problems like toxicity, because they are easy to control, efficient mixing and uniform environment can be guaranteed. On the other hand, experimentation on a large scale digester is necessary to elucidate the operational problems and difficulties like effects of improper mixing, clogging of feed and outlet ports, solids accumulation, foaming and so on.

A.2 Objectives

1. To study the effect of mixing on the performance of anaerobic digester.
2. To demonstrate the effect of digester size on the role of mixing by comparing the lab-scale and pilot-scale digester performance.

A.3 Results and Discussion

Two identical laboratory-scale digesters with working volume of 3.87 liters (6 inches in diameter) were used. One was mixed by gas recirculation at a rate of 1 l/min; digester was equipped with draft tube with diameter one fourth of digester diameter and a multipoint sparger to facilitate mixing. Another digester was unmixed; unmixed condition implies that no mixing is provided by external means, but digester is naturally mixed due to the evolution of biogas bubbles and addition of feed and effluent removal. Pilot scale digester had working volume of 97 liters (18 inches in diameter) and was geometrically similar to the laboratory-scale digester. The pilot-scale digester operation was started with biogas recirculation. After 70 days of operation of the pilot-scale digester in mixed condition, biogas recirculation was stopped and it was operated in unmixed condition for more than 70 days. Again the biogas recirculation was started and the digester was operated in mixed condition for more than 12 days, this was done to check the reproducibility of the results obtained. The biogas recirculation rate in pilot-scale digester was 9.07 l/min, resulting in an input energy density of 8 W/m³, which corresponds to 1 l/min biogas recirculation rate in the 6-inch laboratory scale unit at same energy input rate.

Both the digesters were operated in same manner using same cow manure collected from a local dairy farm in the Oak Ridge, TN area. The raw sludge was processed and diluted with water to obtain 6.6% total volatile solids (total solids of about 12-13%) concentration. This feeding rate was maintained corresponding to a hydraulic retention time of 16 days. Gas samples were analyzed for methane and carbon dioxide content. Slurry samples were analyzed for total solids (TS), total volatile solids (TVS), Volatile Fatty acids (VFA), and total alkalinity (TA).

Table A.1 shows the results of the performance results of two scales of digesters, whereas Figure A.1 compares their cumulative methane production rates. Laboratory-scale digester produced more biogas with higher methane content than the pilot-scale digester. The TS, TVS and VFA content in the effluent of laboratory-scale was also lower than the pilot-scale digester. The laboratory-scale digester in mixed and unmixed condition showed same performance in terms of methane production. Pilot-scale digester in mixed condition performed significantly better than in unmixed condition with approximately 100% higher methane production. Increase in VFA in the effluent reaching the values of feed VFA indicated that unmixed pilot-scale digester was failing.

Since the rate of bioreaction is low, anaerobic digesters are kinetically controlled. But, still sufficient amount of mixing is required to maintain a uniform environment inside the digester to guarantee efficient distribution of substrate, pH and temperature. Even the small amount of mixing produced by the motion of evolving gas bubbles and the addition of feed in the unmixed digester is sufficient for efficient operation of the laboratory scale digester. Since the reaction is kinetically controlled, any additional amount of mixing does not further improve the performance of the mixed laboratory-

scale digester over an unmixed digester. As the size of the reactor increases, difficulty in achieving complete mixing increases, and additional mixing is required. Since, no additional mixing was provided in pilot-scale unmixed reactor, it showed poorer performance than the pilot-scale mixed reactor.

Table A.1 Effect of mixing on performance of laboratory-scale and pilot-scale anaerobic digester

Scale	Laboratory-scale (6-inch, 3.78 L)		Pilot-scale (18-inch, 97 L)	
	Mixed	Unmixed	Mixed	Unmixed
Gas recirculation rate (L/min)	1	-	9	-
Feed/effluent rate ($L/2\ days$)	0.470	0.470	12	12
Biogas production rate ($L/L/day$)	1.2	1.1	0.55	0.3
Methane content (%)	76	73	65	52
Cumulative methane production rate (L/day)	3.3	3.1	40	20
Cumulative methane production rate per unit volume ($L/L/day$)	0.87	0.82	0.41	0.2

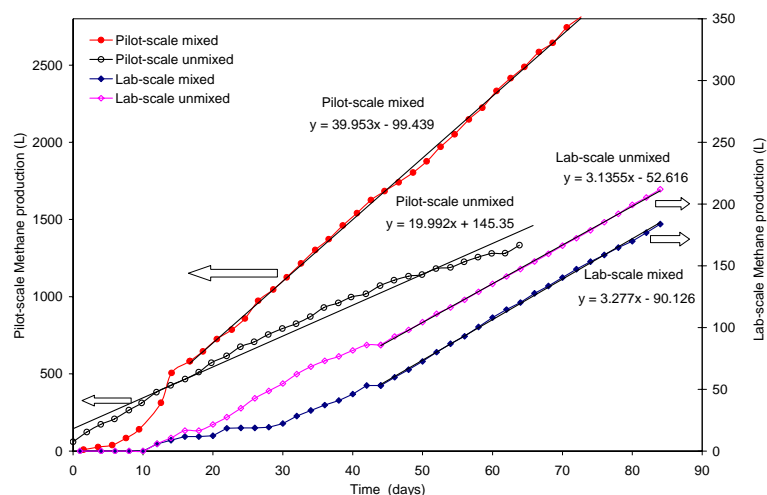


Figure A.1 Comparison of cumulative methane production rates for laboratory-scale and pilot-scale digesters

A.4 Summary

Significant differences between the results obtained for mixed and unmixed condition in the pilot-scale digester were observed. Mixing provided in the digester results in its efficient operation and avoids its failure. Mixing played no significant role in the

performance if laboratory-scale digesters. At the smaller scale the mixing created by the evolution of gas bubbles is sufficient for proper operation of the unit. Any additional amount of mixing does not benefit the digesters to create more gas, necessarily because the digestion process is kinetically controlled. Excessive amount of mixing is also not recommended as mixing needs energy and spending more energy will not be profitable. This concludes that large scale operation of digester is necessary to obtain meaningful results and findings that can be used for proper design of commercial scale units.

The following essential question arises: what is the best or optimum mixing intensity to ensure efficient or less energy input to maximize the energy output obtained from the biogas. This question is yet to be answered and it needs further investigation using large scale digester is currently in progress. The findings in the pilot scale digester and their comparison with those obtained with 6-inch digester suggest that laboratory scale digesters are of no use to determine the optimum mixing intensity needed for efficient digester performance.

Appendix B

MP-CARPT Manual

B.1 Background

Concept for MP-CARPT is based on energy discrimination. By using a different isotope (with different gamma peaks) for each particle, it should be possible to discriminate which particle a detected gamma came from. Before examining the method for doing this, it is useful to review a few aspects of single-particle CARPT. Figure B.1 shows a detector channel used for single-particle CARPT, while Figure B.2 shows an idealized spectrum for a hypothetical isotope. The detector channel registers one count for each detected gamma exceeding the discriminator threshold. This arrangement rejects lower energy gammas that are due to Compton scattering or background sources (depending on how close to the peak the discriminator threshold is set.)

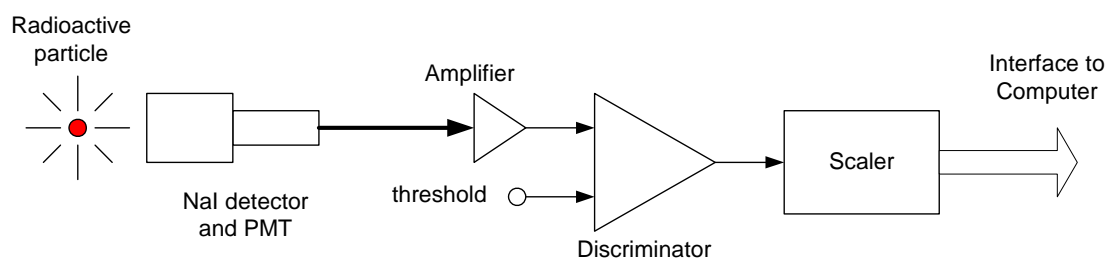


Figure B.1 Single particle CARPT detector channel.

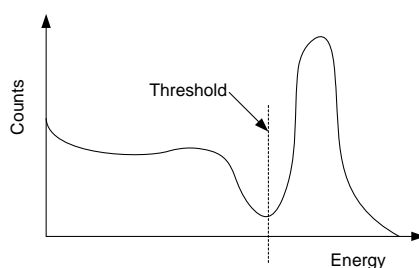


Figure B.2 Idealized NaI spectrum.

B.2 MP-CARPT Concept

Figure B.3 shows a concept for a MP-CARPT (MP-CARPT) detector channel. The detected and amplified signal is introduced to an energy analyzer that can sort the events according to non-overlapping energy windows. For example, gammas with energies between 1 and 1.2 MeV would be events counted by scaler 1 while gammas with energies between 0.7 and 0.9 MeV would be events counted by scaler 2. Figure B.4 shows the NaI spectrum for two hypothetical isotopes individually and combined. It also shows the range of the two energy windows. This illustrates only two particles and two isotopes, but the concept could be extended to greater numbers. For those familiar with conventional NIM electronics, the energy analyzer could be implemented as multiple single-channel analyzers (SCA) – one per each isotope or energy window. This would be a very costly approach for CARPT where multiple detectors (16 or more) are used and 2 or more isotopes would be used. An alternative approach would be to use multi-channel analyzers (MCA). A standard multi-channel analyzer determines the energy of each detected gamma and sorts them into multiple energy windows (called channels). Generally these windows are evenly spaced, and there are usually 2000 or more of them. This type of instrument is generally used for spectroscopy, but the spectral data could be processed in software to reduce the many windows to the few needed for MP-CARPT. This is still a complex and costly approach as commercially-available MCAs generally have far more capabilities than needed (and therefore more cost), and they are generally meant to be used singly or in very small numbers – it would be difficult to interface to 16 or more of them.

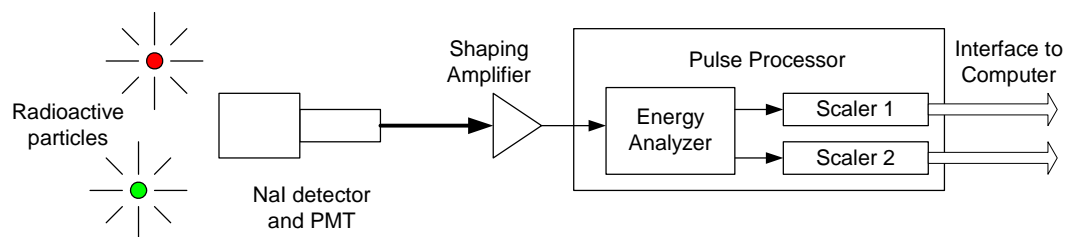


Figure B.3 MP-CARPT detector channel.

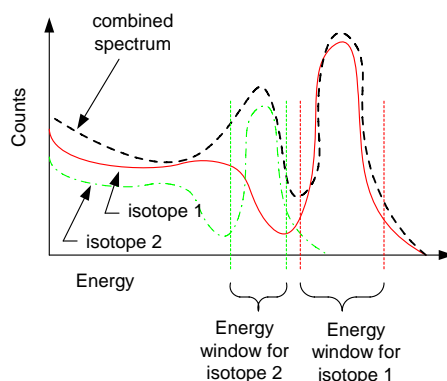


Figure B.4 Idealized NaI spectrum for two isotopes.

B.3 Proof of Concept Experiments

As a proof of the energy discrimination concept, an experiment was set up based on the old CAMAC and NIM electronics. This experiment allowed CARPT to be extended to two particles with a minimum of additional hardware. Figure B.5 shows a detector channel modified for dual-particle CARPT, while Figure B.6 shows an idealized spectrum for two different hypothetical isotopes. Gammas resulting from one of the particles or background are detected by the NaI detector and photomultiplier, and are then amplified by a timing-filter amplifier (TFA). The signal from the TFA is split into two equal parts and these are input to two discriminators. As shown in Figure B.6, the two thresholds are different. The threshold for discriminator 1 (threshold 1) is set just below the photopeak for isotope 1. This insures that the counts recorded by scaler 1 will be mainly due to isotope (and particle) 1. The threshold for discriminator 2 (threshold 2) is set just below the photopeak for isotope 2. This means that the counts recorded by scaler 2 will be due to isotope (and particle) 2 plus those of particle 1. By subtracting the counts of scaler 1 from those of scaler 2, we get the counts that are due to particle 2 alone.

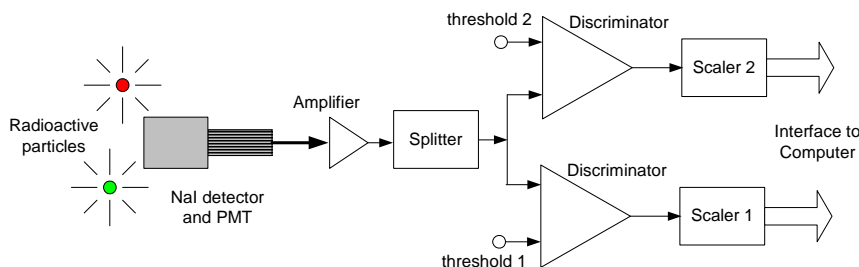


Figure B.5 Dual particle CARPT detector channel.

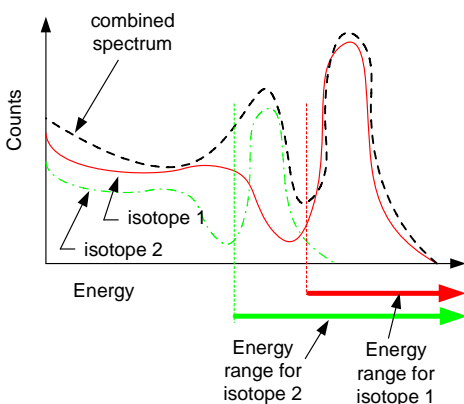


Figure B.6 Idealized NaI spectrum for two isotopes.

Figure B.7 shows the modules and their connections for the dual particle experiment. Up to 16 detectors may be used. The existing single particle CARPT data acquisition program was modified slightly to allow setting the two different thresholds.

We were able to use one detector in the dual-particle setup to distinguish the two peaks of Scandium-46. The Sc-46 spectrum resembles Figure B.2, and by setting the two discriminators to values corresponding to the valley below each peak we were able to get about twice as many counts in one scaler than the other. (The two peaks are equally intense.) This would indicate that the scaler corresponding to the higher threshold counted only the upper peak, while the scaler with the lower threshold counted both peaks.

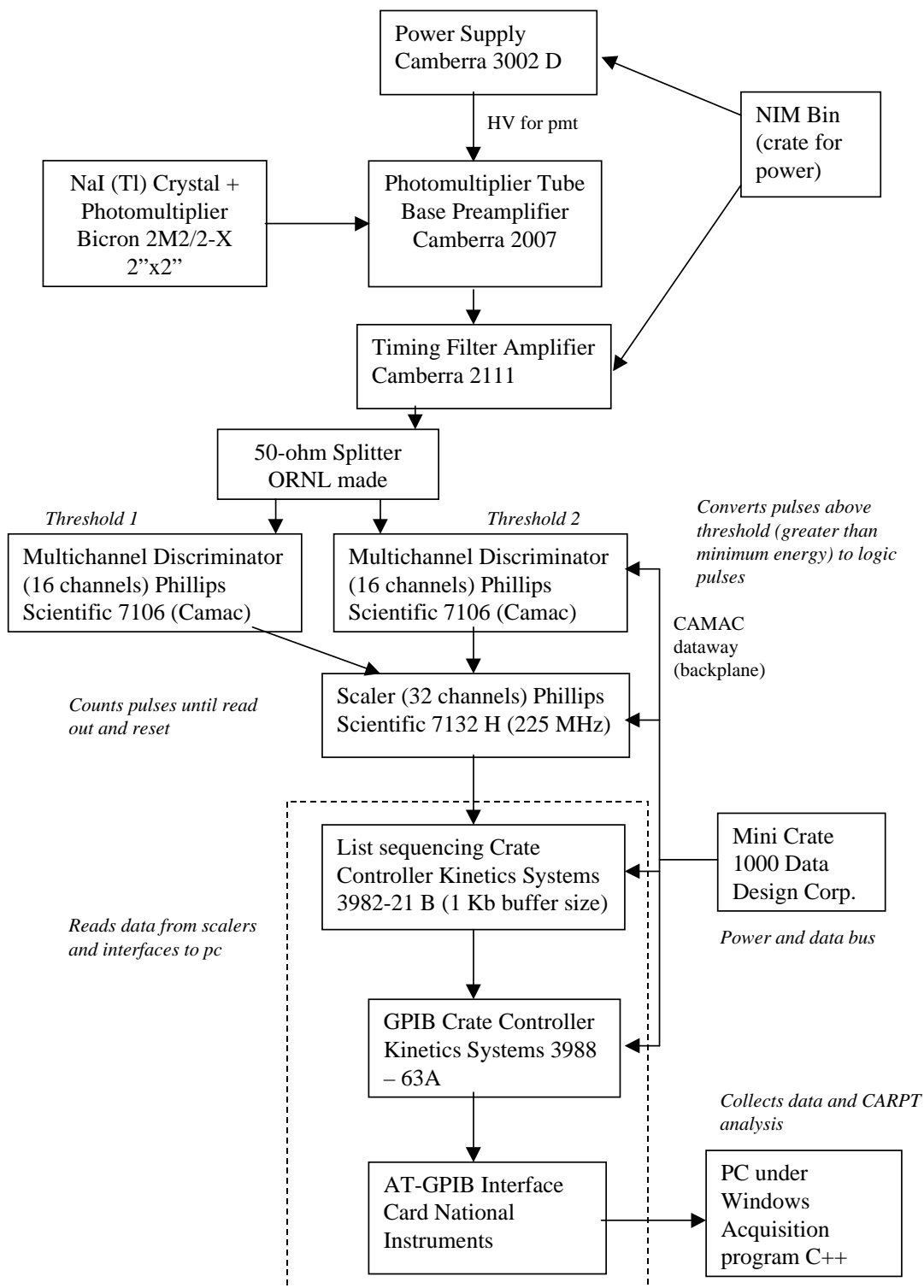


Figure B.7 Dual-particle CARPT electronics showing NIM and CAMAC elements.

B.4 NaI Detector Readout Concept

Many physics experiments require a large number of detector channels (hundreds, thousands or even tens of thousands.), and due to the large number of channels, each must be relatively inexpensive and have a good computer interface. For the Spallation Neutron Source, it is expected that there will be several thousand He3 detectors to read out. This readout was being developed at ORNL. Fortunately, the signal from the preamp used with those detectors resembles the signal from the NaI detectors and photomultipliers used for CARPT. Figure B.8 shows an experimental setup using a NaI detector and part of the SNS He3 readout electronics.

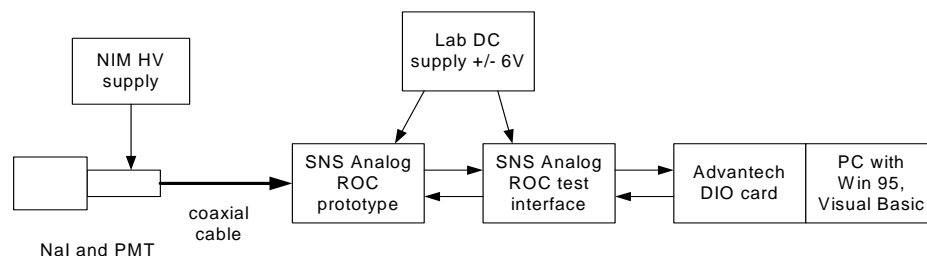


Figure B.8 NaI readout using SNS He3 electronics.

Initial tests of this setup use it as an MCA to view energy spectra. It operates in the following way. The PC arms ROC card, making it ready to process pulses from the photomultiplier (PMT). Pulses from the PMT are detected by a discriminator in the Analog Readout Card (ROC). The discriminator threshold is programmable and is set just above the system noise level. When a pulse is detected (this corresponds to a gamma), the pulse is integrated and the integrated value is digitized. This digital value is proportional to the energy of the gamma. The digital value is sent to the PC via the digital input/output (DIO) card. This sequence terminates by disarming the ROC. The software in the pc controls how many pulses are processed. The software also histograms the events and writes the results to a file. The software could be easily re-written to categorize the values according to two or more energy windows.

Figure B.9 shows the Analog ROC prototype card and the ROC interface. These were used along with a 3-inch NaI detector to obtain the spectrum shown in Figure B.10. The peak near channel 260 is due to Potassium-40.

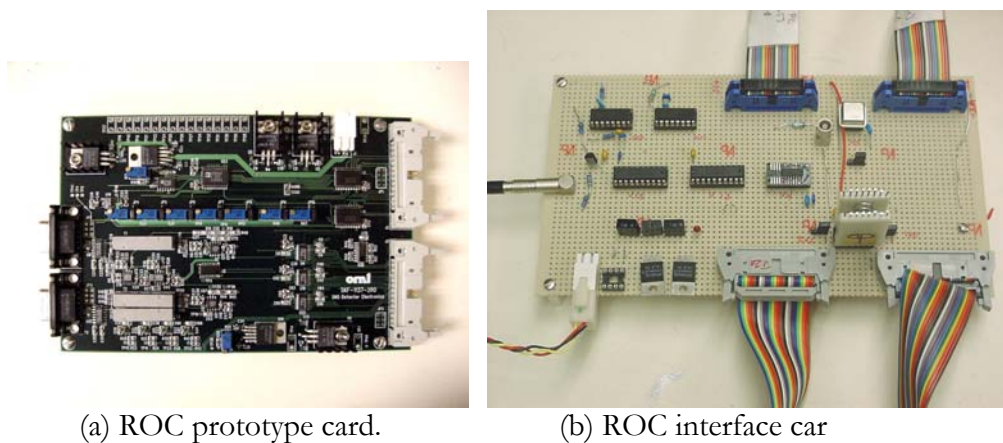


Figure B.9

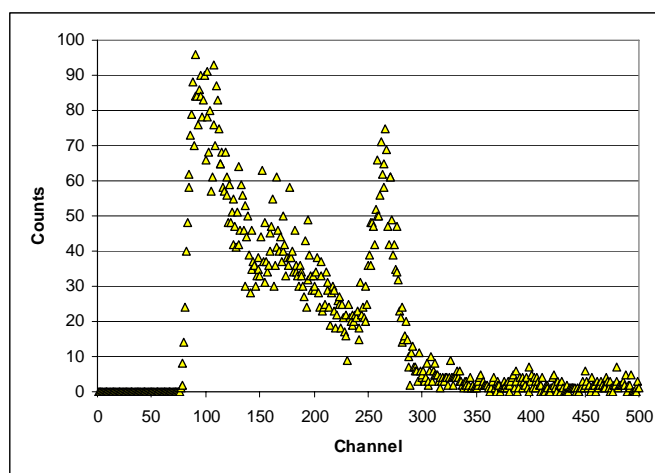


Figure B.10 Spectrum of Potassium-40 obtained using prototype electronics

A.5 Readout Electronics and Data Acquisition

The readout electronics and data acquisition for MP-CARPT consists of timing filter/shaping amplifiers, pulse processor or NaI readout modules, a crate and a PC as shown in Figure B.11. The shaping amplifiers are used to increase the signal levels before pulse processing occurs. The readout modules perform the pulse processing and energy discrimination and are comprised of analog, digital and interface sections. Several readout modules are plugged into a CPCI crate. The crate contains single board PC that controls the readout modules and communicates to a network via Ethernet. These modules and other elements are discussed in more detail in the following subsections.

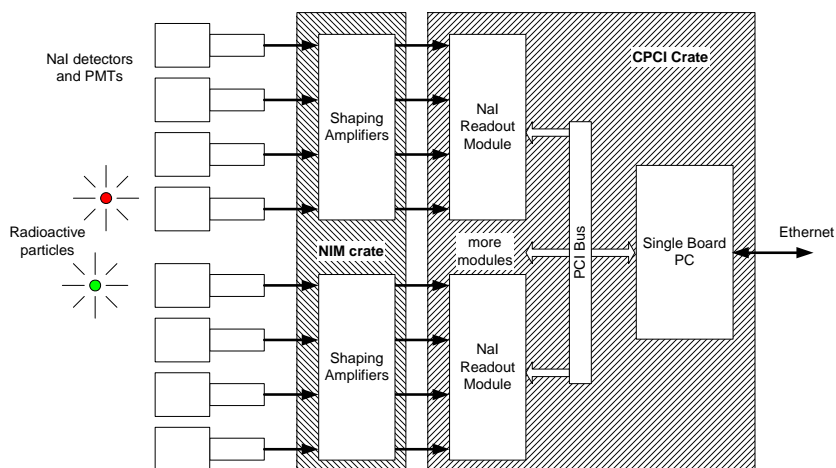


Figure B.11 MP-CARPT arrangement using NIM and CPCI format NaI readout electronics

B.5.1 Timing Filter Amplifier

Introduction

In single particle CARPT experiments, a commercial timing filter amplifier (TFA) is used. This amplifier is normally adjusted to provide an adjustable gain on the order of 100 and to provide minimal filtering to the signal from the NaI detector. (Nominal settings are 50-ns integration and no differentiation.) The TFA is capable of a wide variety of time-constants for filtering, but that ability is not required for this application, and a much simpler amplifier would serve as well.

A prototype timing filter or shaping amplifier was developed as a possible replacement for the NIM timing filter amplifiers. (The large number of single-channel TFAs needed for a CARPT experiment is a considerable expense.) The prototype shaping amp has four channels, a maximum gain of 100 and filtering that is equivalent to 50 ns integration and no differentiation. The gain of each channel is continuously adjustable from 100 to <1 . The prototype operates from a ± 6 Vdc power supply. It was evaluated during the dual particle CARPT experiments and found to be the functional equivalent of the TFAs.

Currently, an 8-channel version of the shaping amplifier is developed. This amplifier is housed in a NIM module and is designed for use with the NaI pulse processor module. Following sections describe it and explain its use.

Design Overview

Figure B.12 shows a block diagram of a single channel of the shaping amplifier. It consists of a differential receiver amplifier, an adjustable attenuator, and a differential line driver plus input and output connectors. The differential receiver has two

functions: it provides gain and allows the polarity of the input signal to be reversed. The adjustable attenuator allows the signal level to be reduced as needed to set the overall gain. The gain stage also has two functions: it provides gain and serves as a low-pass filter. (Low-pass filtering is the pulse shaping function.) The differential line driver converts the signal from the gain stage to a differential signal that can be transmitted through a twisted pair cable.

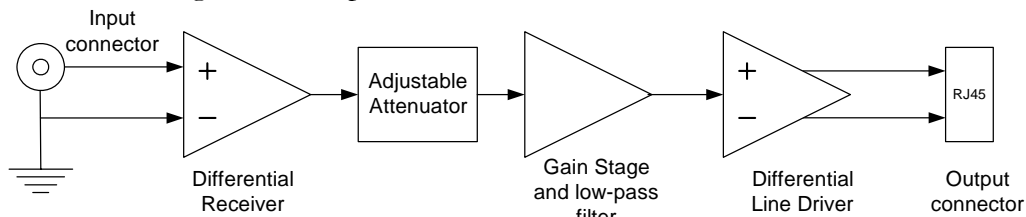


Figure B.12 Block diagram of shaping amplifier channel.

Figure B.13 is a circuit diagram for one channel of the shaping amplifier. Integrated circuits U1 is the differential receiver, RP1 is the adjustable attenuator, U2 is the core of the gain stage and U3 is the differential line driver. These circuits will be described in more detail in the remainder of this section.

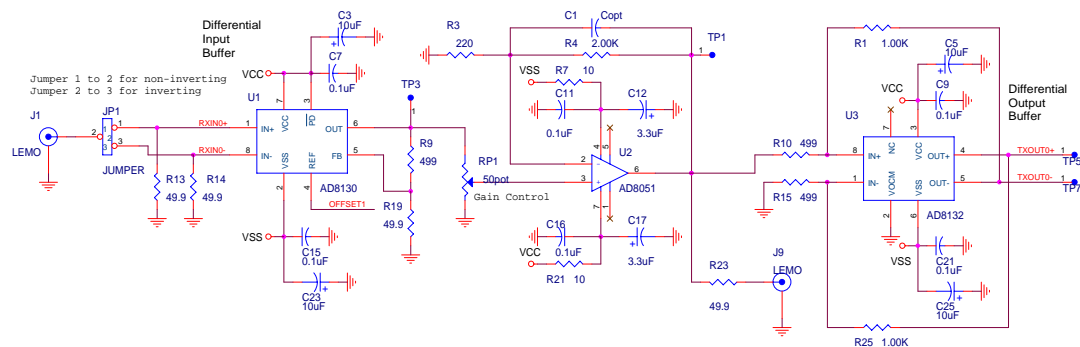


Figure B.13 Circuit diagram of one shaping amplifier channel.

Differential receiver U1 uses an Analog Devices AD8130 differential amplifier to provide a gain of 11. The AD8130 has a bandwidth of approximately 10 MHz when connected for a gain of 10, so that the bandwidth of the receiver amplifier should be just slightly less than 10 MHz. The signal polarity can be reversed by using jumper JP1 to connect the input signal to the inverting input of the amplifier (pin 8) instead of the non-inverting input (pin 1). The receiver circuit also includes 50-ohm input resistors that properly terminate the coaxial cable used to bring the signal from the detector to the shaping amplifier. The signal from the differential receiver passes through potentiometer RP1 to the input of the gain stage. Depending upon the position of the wiper, the signal may not be attenuated or it may be attenuated by as much as a factor of 100.

The gain stage uses an AD8051 opamp connected for a non-inverting gain of 10. According to the data sheet, the AD8051 has a bandwidth of approximately 7 MHz for that gain. Combined with the bandwidth of the receiver amplifier, this gives an overall

bandwidth of about 6 MHz and that corresponds to a shaping time of approximately 25 ns. The line driver is implemented using an AD8132 differential amplifier that is connected to provide a gain of two. The AD8132 has a gain-bandwidth of approximately 300 MHz, so that the bandwidth of the line driver amplifier is approximately 150 MHz, which is large enough to have a negligible effect on the overall shaping amplifier bandwidth.

Module Implementation and Use

The shaping amplifier is using a 4-layer printed circuit board (SKF-1166-4R0) and is housed in a single-wide NIM module. Figure B.14 shows the module with the side panel removed. The eight channels are arranged linearly with channel 1 at the top and channel 8 at the bottom. The Lemo input connectors are visible at the right and extend through the front panel. The potentiometers (blue rectangles) used for gain adjustment are located just below each input connector. The RJ-45 output connectors are visible at the left, above the NIM power connector. Channels 1 through 4 use the upper RJ-45 connector, while channels 5 through 8 use the lower one. Figure B.15 shows the front and rear panels of the module.

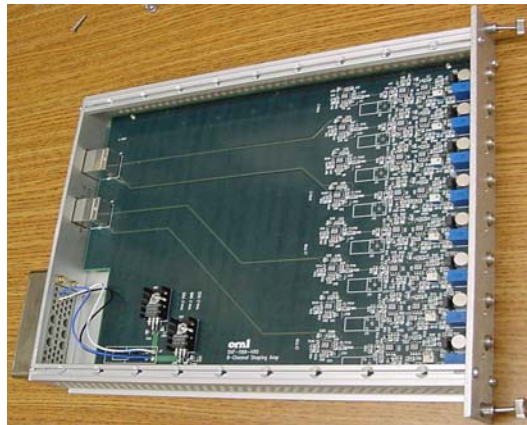


Figure B.14 Side view of shaping amplifier module

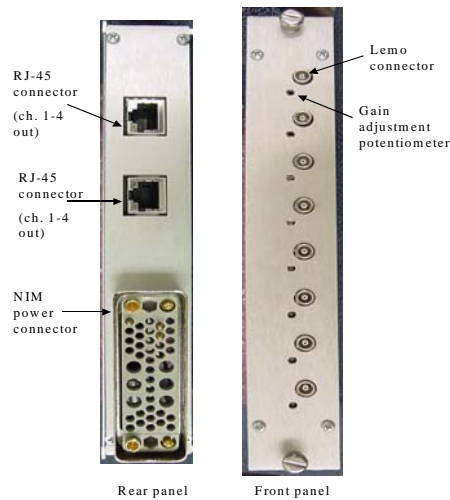


Figure B.15 Shaping amplifier module front and rear panels

Gain adjustments to the channels are made using the variable attenuators accessible through the front panel. The full range of adjustment is 20 turns, and a clockwise rotation increases the gain. The potentiometers idle if turned past the upper or lower limit, so there is no damage to the module from turning the control too far. Each channel has a DC offset adjustment that allows adjusting the dc output voltage to zero. This affects the baseline of an amplified pulse and should be done prior to setting discriminator levels. To use this control, the side cover of the NIM module must be removed to gain access. Figure B.16 shows the location of the DC offset adjustment potentiometer for a typical channel. It is immediately to the left of the blue gain-adjust potentiometer for the corresponding channel.

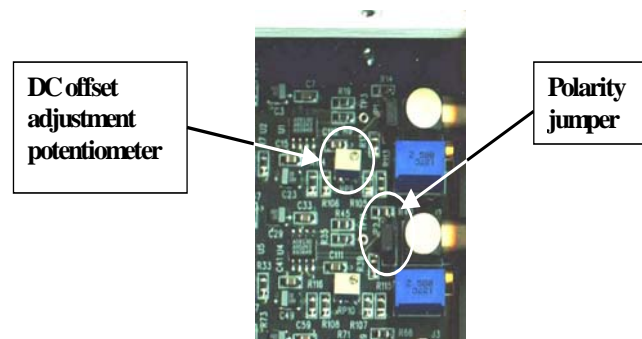


Figure B.16 Close-up view of circuit board showing adjustment locations.

The shaper amplifier module is initially set to provide non-inverting gain. If the polarity of the pulse needs to be inverted (to match the detector to the discriminator or other circuits following the shaper), it can be accomplished by changing a jumper setting. The polarity jumper for each channel is located just behind the input Lemo connector for that channel. For non-inverting gain, the jumper should be set on the lower two pins of the 3-pin header (lower meaning towards the bottom of the NIM module). For

inverting gain, the jumper should be set on the upper two pins of the 3-pin header (upper meaning towards the top of the NIM module).

Specifications

DC power supply	+/-6V @ 230mA
Input impedance	50 ohms nominal
Output capability	up to +/-4 V into 100 ohms differential load
Gain	2 to 200, adjustable via front panel potentiometers
Shaping time constant	25 ns (integration)
DC offset adjustment	via internal potentiometers

B.5.2 Pulse Processor Module/NaI readout Module

Introduction

The pulse processor module for MP-CARPT separates pulses through energy discrimination. It integrates detected and amplified pulses in order to produce a voltage that is proportional to the detected energy. This voltage is digitized and introduced to an energy analyzer that can sort the events according to non-overlapping energy windows. The pulse processor module keeps a count of how many pulses fall into each energy window.

A simplified diagram of this equipment is shown in Figure B.3. As an example of its use for MP-CARPT, consider the NaI spectrum for two hypothetical isotopes individually and combined that is shown in Figure B.4. Isotope 1 has a peak around 1.1 MeV while isotope 2 has a peak around 0.8 MeV. If two energy windows like those shown in Figure B.4 are set in the pulse processor, then gammas with energies between 1 and 1.2 MeV will be routed to scaler 1, and gammas with energies between 0.7 and 0.9 MeV would be events counted by scaler 2. Thus scaler 1 will count primarily events due to isotope 1 and scaler 2 will count mainly events due to isotope 2. This illustrates the concept of counting energy-discriminated events using only two particles and two isotopes, but the concept can be extended to greater numbers.

For particle tracking, the pulse processor module must acquire energy discriminated data multiple time intervals and for multiple detectors. For example, counts might be accumulated for 50 ms before being read out and the counter reset. This process would be repeated over and over again for the duration of the experiment, which might last minutes or even hours. Determination of the particle's position requires using multiple, spatially separate detectors, typically 8 to 32.

Design Overview

Figure B.17 is a block diagram of the pulse processor module. It has 8 channels with each consisting of an analog section, an ADC and a digital section implemented using a

Field-Programmable Gate Array (FPGA). One channel is used with each detector. Each channel is connected to another FPGA that controls the operation of the module. This FPGA controls the counting intervals, downloads setup parameters to the channel FPGAs and collects data from them. In turn, the control FPGA is connected to an IC (PLX9030) that interfaces to the PCI bus. The PLX9030 handles the PCI bus protocol allowing data transfers to and from the PC that is the bus master. These circuits are discussed in greater detail in the following subsections.

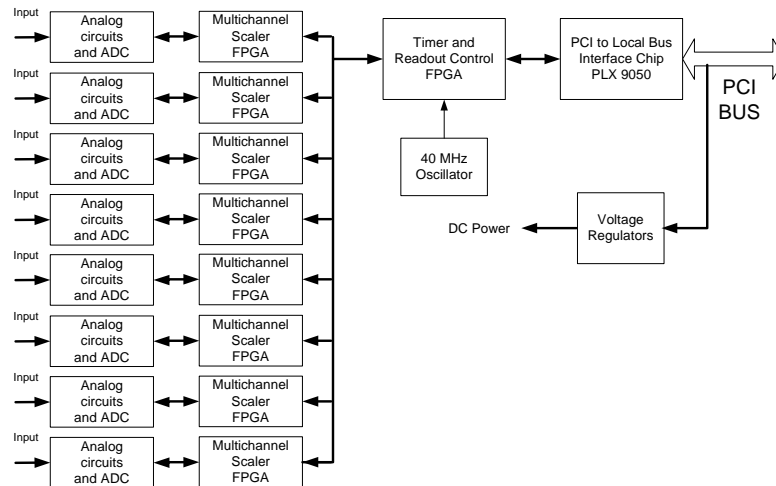


Figure B.17 Block diagram of the pulse processor module.

Pulse Processor Module Analog Circuits

Figure B.18 is a block diagram of one channel of the analog section showing connections to the shaping amplifier and to the digital section. Each channel has a differential receiver followed by both a gain stage and a delay line. The output of the gain stage is compared the initial limit threshold by a discriminator. If a pulse exceeds this threshold, it is assumed that it might be due to a suitable pulse (and not just noise), and the pulse processing process is started. An example of this type of event is shown as a timing diagram in Figure B.19. The gain stage output is low-pass filtered and discriminated again (this is the minimum discriminator.) If minimum discriminator fires within approximately 200 ns of the initial discriminator firing, it is assumed that the pulse was due to a real pulse and processing of the event should continue. If the second discriminator does not fire, then it is assumed that first discriminator fired on noise and the event should be rejected and not processed.

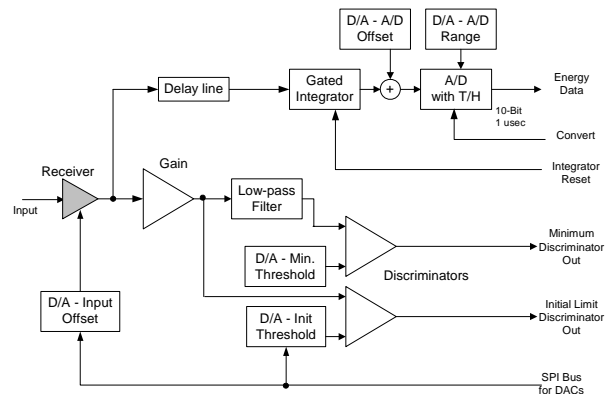


Figure B.18 Analog electronics for one channel.

The differential receiver also drives a delay line of approximately 400 ns in length. The delay line is then followed by a gated integrator. The use of delay lines allows the pulse height discriminators to gate the integrators on without losing any signal due to delays in gating. As seen in the timing diagram, the digital logic times from the initial pulse discriminator and opens the integrator reset switch after approximately 300 ns. (Several of these parameters are programmable and are discussed further in the section on the pulse processor digital circuits.) This delay plus the discriminator delay should be less than the length of the delay line so the pulse is completely integrated. If the Minimum discriminator output does not go true during the 300 ns delay, the integrators are reset and the system waits for another pulse. If it does go true, the integrators are not reset until after they are sampled by their ADCs.

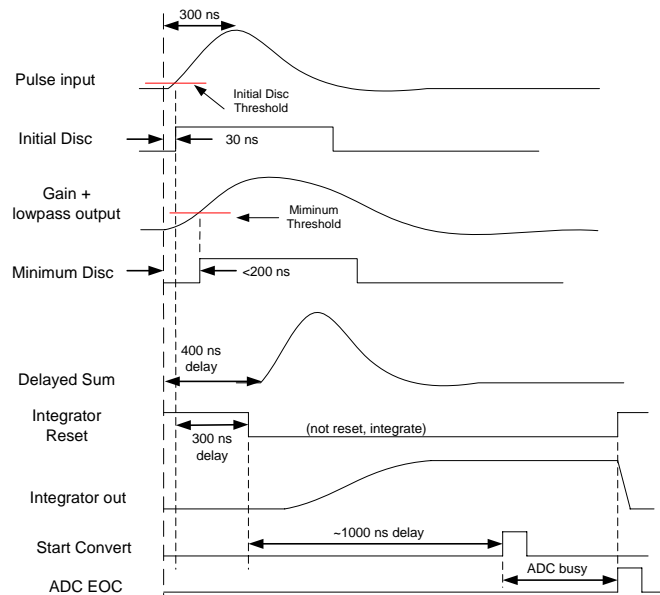


Figure B.19 Pulse Processor Timing Diagram.

After sufficient integration time (this is programmable), the integrator output is sampled by the 10-bit ADC. This is shown in the timing diagram by the Start Convert signal for the case of a 1-microsecond integration time. The conversion takes approximately half a microsecond, and when the converter is finished, it gives an End of Conversion (EOC) signal. This signal causes the logic to reset the integrators, and the pulse processor channel is ready to process another pulse. The time taken between pulse detection and EOC is approximately 2 microseconds for this arrangement.

Pulse Processor Module Digital Channel Circuits

A digital portion implemented using a single FPGA follows the analog portion of the channel circuits. Figure B.20 shows the block diagram of the channel FPGA. The timing control block determines when a pulse is detected and controls the integration and digitization process. The energy window logic accepts digitized pulses and determines which scaler(s) should be incremented. The interface to the module controller transfers data to from the channel to the controller and control parameters from the module controller to the channels.

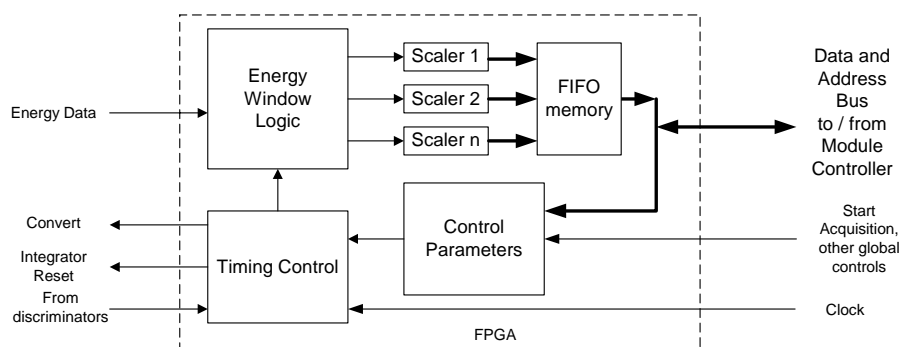


Figure B.20 Digital electronics for one channel.

The timing control logic uses the output of the initial discriminator to start a sequence of events. The pulse from this discriminator indicates that an input pulse has been detected. (See Figure B.19.) Shortly after this, the timing control releases the integrator reset (allow it to start integration) and then waits for the minimum discriminator to fire. If it fires within the prescribed amount of time, the process continues, if not, the process is aborted. After the integration is complete, the timing control logic starts the analog-to-digital converter and resets the integrator.

The logic that implements this process uses a 20-MHz clock (the acquisition clock). Figure B.21 shows the timing diagram for the pulse acquisition process. The acquisition process starts with rising edge of the initial discriminator being synchronized to the acquisition clock. Because of the synchronization, starting the acquisition time counter (at 20 MHz) is delayed by 1 to 2 clock cycles (one clock cycle is 50 ns). All acquisition time parameters (Pulse Timeout, Integrator release time, and Sampling time) are based on the acquisition time counter. This counter is zeroed before the pulse acquisition process begins and counts increments of 50 ns. The Pulse Timeout parameter defines

how long the process is to wait for the minimum discriminator signal (MIN_DISC) to occur. If the MIN_DISC signal does not occur, then the input pulse is defined as invalid and the process is reset. Otherwise, the integrated value of the input pulse will be converted and sent to the energy window logic. The integrator release time is the acquisition count value (+1) where the integrator is released (changed from reset to not reset) to start the integration process. The sampling time (+1) is the acquisition count value where the integrator analog input is sampled. After the analog input has been sampled, the integrator is reset. The ADC conversion process takes 14 acquisition clock cycles, and the energy windowing (binning) process takes either 1 clock cycle in coarse mode or 6 clock cycles in fine mode to finish the process. The total time for the acquisition process is approximately the Sampling Time + 22 acquisition clock cycles. Any input pulses occurring more closely spaced than this value will result in distorted data.

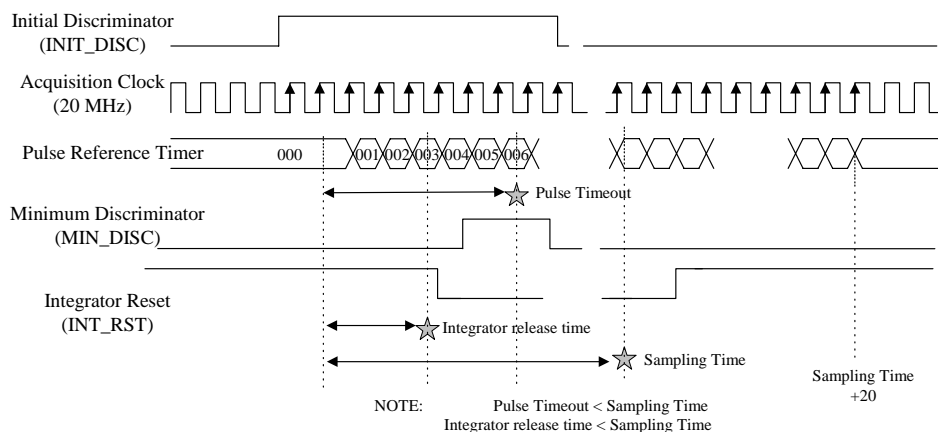


Figure B.21 Timing diagram for pulse acquisition in a channel.

Upon completion of the conversion, the digitized energy data goes to the energy window logic. This logic sorts the energy into windows. The pulse processor has two modes of sorting and counting pulses – coarse and fine windows. The coarse window mode takes data in the format needed for CARPT, while the fine window mode allows the processor to function as a multi-channel analyzer (MCA). The coarse mode will be described first.

In the coarse mode, for example, one window might correspond to the range of 1 to 1.2 MeV while another could be the range of 0.7 to 0.9 MeV. Each time a pulse is processed and if its energy falls within a window, the corresponding scaler is incremented by one count. The coarse mode has eight windows with independently adjustable upper and lower limits. Window limits are given in terms of ADC values (0 to 1023). If desired, the windows may overlap. Pulses are processed and counts accumulated as long as the module controller dictates. Each scaler can accumulate up to 65,535 counts ($2^{16} - 1$) before overflowing or being reset. An overflow condition is indicated by a count of 65,535 – the counters do not rollover.

In the coarse mode, data is taken over multiple time intervals (sampling sessions) before being read out by the module controller. At the end of each time interval, the scaler values are transferred to a FIFO (first-in, first-out) memory that is part of the FPGA. The scalers are then reset and a new counting interval starts with minimal dead time. The size of the FIFO (4 Kbytes) limits the number of intervals to a maximum of 256 between readouts.

In the fine mode, the channel logic is used in a slightly different way to collect MCA-type data and to transfer it to the computer. Pulses are acquired and digitized in exactly the same way as in the coarse mode, but the energy window logic uses the FIFO to simply record how many times each possible ADC value (bin) occurred during the experiment. Each bin (memory location) can accumulate up to 65,535 counts before overflowing. The fine mode is a very useful feature as it allows collecting an energy spectrum that can be used to set up the energy windows for CARPT.

In fine mode, data is taken over one time interval (sampling session) before being read out by the module controller. This is due to the size of the FIFO memory holding the data. This memory is arranged as 1024 two-byte words.

Bus Interface

Figure B.22 shows a computer bus interface that is needed to transfer data for analysis and for adjustment of instrument parameters. Several interface and packaging formats were considered for the NaI readout electronics. It seemed most useful if the circuit cards were made as modules and plugged into a crate. One possibility was CAMAC. That had the advantage that the existing CARPT equipment uses CAMAC and the bus interface is relatively simple to design. However, there are a number of disadvantages. The CAMAC bus is relatively slow and interfacing the CAMAC crate to a pc or workstation generally requires conversion to another interface such as GPIB and then another conversion to the native bus for the pc or workstation used for data analysis. Another disadvantage is that the CAMAC format is not up to date and is increasing less commonly used.

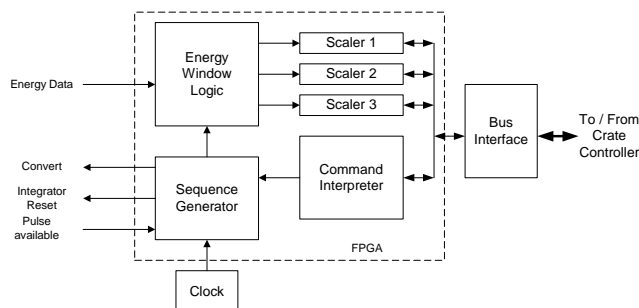


Figure B.22 Digital portion of NaI readout electronics.

Ultimately, it was decided to build the NaI readout electronics using a compact PCI (CPCI) format. This is an up-to-date standard that is more suited to the modern pc world and allows fast data transfers. This implementation uses commercially available

crates and processor cards (Figure B.23). A big advantage of this arrangement is that a single board computer (SBC) can serve both as crate controller and as a data analysis engine.



Figure B.23 PCI crate and single board computer.

Module control and Bus Interface

The module controller FPGA (Figure B.24) handles the interface to the PLX chip and the FPGA channels. For both interfaces, a 32-bit bus is used with a variety of address and enabling signals. The controller also configures all DACs in the system via an SPI bus interface. These DACs set analog values such as thresholds and offsets. The controller's other function is to define general acquisition parameters and modes for the eight FPGA channels (global control signals). For example, the signal that enables counting is broadcast from the module controller FPGA to the channel FPGAs. The module controller FPGA also contains FIFO memory that is used to buffer data on readout of the channel FPGAs.

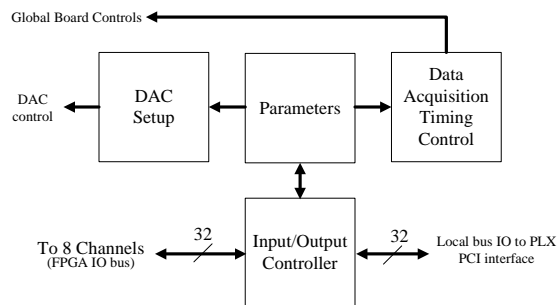


Figure B.24 Module Controller FPGA block diagram.

When the module controller enables the channel FPGAs to start counting pulses, it starts its own counter that counts cycles of a clock with a 6.4 microsecond period. The time interval (sampling session) duration is 6.4 microseconds times the value programmed into the sequence acquisition time register. This value may range from 1 to 2.15×10^9 ($2^{31} - 1$) that corresponds to a time interval of 6.4 microseconds to 3.8 hours. Smaller values (on the order of milliseconds) are appropriate for CARPT while larger

values (minutes or hours) are appropriate for acquiring energy spectra. The contents of the various control registers are given fully in the section on module programming. The number of time intervals for which counts are to be acquired is given by the number of sequences parameter in the Modes and Sequence Definition Register. The parameter may range from 0 to 255 if the coarse mode is selected. The actual number of intervals is one plus the value in the register. When the programmed number of intervals is reached, the data must be read out before any more can be taken. This results in a small amount of dead time.

The module controller can also operate in a “fake trigger mode” which causes data to be taken, analyzed, counted and read out with no input pulses. This is useful for adjusting offsets, measuring system noise and debugging the module. In this mode, the module functions normally, except that the module controller periodically provides a “trigger” that takes the place of the signals from the initial and minimum discriminators. The integrator and ADC are operated normally. The rate of fake triggers can be programmed via the Trigger Firing Count register.

PCI Bus Interface

The interface to the PCI bus is through a PLX PCI9030. This IC has a non-multiplexed local bus (separate address and data lines) connecting it to the module controller FPGA. It also provides a 32-bit, 33-MHz connection to the PCI bus and handles the PCI bus protocol. Commands and set-up parameters pass through the PCI bus to the module while data is transferred from the module through the PCI bus to the host pc.

B.5.3 MP-CARPT Electronics Arrangement

A somewhat more detailed picture of the MP-CARPT electronics is shown in Figure B.25. This drawing indicates the parts of the arrangement that are the same as in single-particle CARPT and those that are different. It also indicates the main functions of the different elements.

Module Implementation and Use

Figure B.26 is a photograph of the pulse processor module. It is a 6U Compact PCI module. The connections to the shaping amplifier are made using the two RJ-45 connectors on the front panel while the connections to the PCI bus are via the P1 connector at the rear of the module. The module is not hot-swap compliant, and the CPCI crate should be powered down to remove or insert a pulse processor module. The pulse processor is designed to be used as part of a radiation detection system. A detailed diagram of electronics for a MP-CARPT experiment is shown in Figure B.25. This drawing indicates the parts of the arrangement that are the same as in single-particle CARPT and those that are different. It also indicates the main functions of the different elements.

B.6 Module Programming and Data Access

Operation of the module is memory mapped. Set-up and the initiation of data acquisition are accomplished by PCI-bus write operations, while data are acquired from the module via PCI-bus read operations. All data transfers use 32-bit (4 byte) words and are done in PCI non-bursting mode.

Normal data taking involves writing the various set-up parameters to the module and initiating data collection with write to the appropriate address. The software can monitor a status bit indicating when data collection has finished or may simply wait long enough before starting to read out data. The data may be read out by multiple reads to the appropriate address. (One read per data word.) Data collection may then be started again.

Reading address 110 or any address 800000H through FFFFFFFH represents a data acquisition read once the module is collecting data. Each data acquisition read operation reads one data word. The next read operation reads the next word, etc. Data acquisition read operations are always sequential regardless of the address specified. For example, reading address 2000000H instead of 3000000H will not change the contents of the read. The address space was partitioned in this manner so bursting operations would be possible if required. When the acquired data from the pulse processor module is being readout, the configuration parameters should NOT be read.

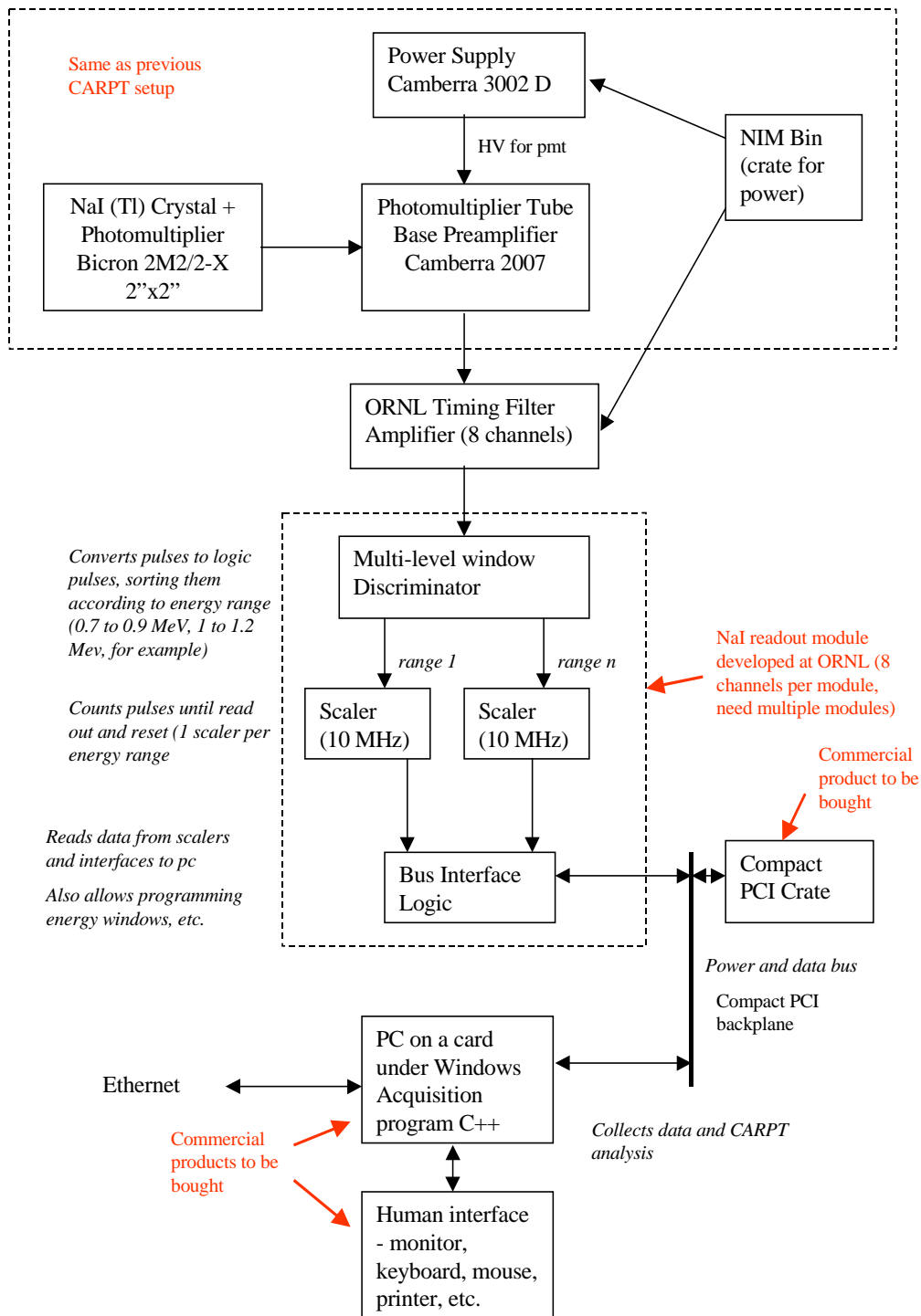


Figure B.25 MP-CARPT electronics showing NIM and CPCI elements.

The register addresses to access a particular parameter or to start an operation are shown in Table B.1. These are the local-bus addresses for 4-byte words – each one corresponds to four PCI (1 byte) addresses. Some of register addresses store two or more parameters due to the parameters requiring less than 32 bits.



Figure B.26 Pulse processor module.

Table B.1-a Channel 0 parameters

ADDR (Hex)	Description
000	Channel 0 Coarse BIN0 Threshold HIGH (31:16) Coarse BIN0 Threshold LOW (15:0)
001	Channel 0 Coarse BIN1 Threshold HIGH (31:16) Coarse BIN1 Threshold LOW (15:0)
002	Channel 0 Coarse BIN2 Threshold HIGH (31:16) Coarse BIN2 Threshold LOW (15:0)
003	Channel 0 Coarse BIN3 Threshold HIGH (31:16) Coarse BIN3 Threshold LOW (15:0)
004	Channel 0 Coarse BIN4 Threshold HIGH (31:16) Coarse BIN4 Threshold LOW (15:0)
005	Channel 0 Coarse BIN5 Threshold HIGH (31:16) Coarse BIN5 Threshold LOW (15:0)
006	Channel 0 Coarse BIN6 Threshold HIGH (31:16) Coarse BIN6 Threshold LOW (15:0)
007	Channel 0 Coarse BIN7 Threshold HIGH (31:16) Coarse BIN7 Threshold LOW (15:0)
008	Channel 0 Valid pulse timeout. This parameter is represents maximum time after INIT_DISC for MIN_DISC to occur so the pulse is deemed valid. Each bit corresponds to 50ns. (15:0)
009	Channel 0 Sample time. Define the sample time for the ADC with respect to INIT_DISC. Each bit corresponds to 50ns. (15:0)
00a	Channel 0 Integrator release time. Define the time with respect to INIT_DISC where the integrator is enabled. Each bit corresponds to 50ns. (15:0)

Table B.1-b Channel 1 parameters

ADDR (Hex)	Description
020	Channel 1 Coarse BIN0 Threshold HIGH (31:16) Coarse BIN0 Threshold LOW (15:0)
021	Channel 1 Coarse BIN1 Threshold HIGH (31:16) Coarse BIN1 Threshold LOW (15:0)
022	Channel 1 Coarse BIN2 Threshold HIGH (31:16) Coarse BIN2 Threshold LOW (15:0)
023	Channel 1 Coarse BIN3 Threshold HIGH (31:16) Coarse BIN3 Threshold LOW (15:0)
024	Channel 1 Coarse BIN4 Threshold HIGH (31:16) Coarse BIN4 Threshold LOW (15:0)
025	Channel 1 Coarse BIN5 Threshold HIGH (31:16) Coarse BIN5 Threshold LOW (15:0)
026	Channel 1 Coarse BIN6 Threshold HIGH (31:16) Coarse BIN6 Threshold LOW (15:0)
007	Channel 1 Coarse BIN7 Threshold HIGH (31:16) Coarse BIN7 Threshold LOW (15:0)
028	Channel 1 Valid pulse timeout. This parameter is represents maximum time after INIT_DISC for MIN_DISC to occur so the pulse is deemed valid. Each bit corresponds to 50ns. (15:0)
029	Channel 1 Sample time. Define the sample time for the ADC with respect to INIT_DISC. Each bit corresponds to 50ns. (15:0)
02a	Channel 1 Integrator release time. Define the time with respect to INIT_DISC where the integrator is enabled. Each bit corresponds to 50ns. (15:0)

Table B.1-c Channel 2 parameters

ADDR (Hex)	Description
040	Channel 2 Coarse BIN0 Threshold HIGH (31:16) Coarse BIN0 Threshold LOW (15:0)
041	Channel 2 Coarse BIN1 Threshold HIGH (31:16) Coarse BIN1 Threshold LOW (15:0)
042	Channel 2 Coarse BIN2 Threshold HIGH (31:16) Coarse BIN2 Threshold LOW (15:0)
043	Channel 2 Coarse BIN3 Threshold HIGH (31:16) Coarse BIN3 Threshold LOW (15:0)
044	Channel 2 Coarse BIN4 Threshold HIGH (31:16) Coarse BIN4 Threshold LOW (15:0)
045	Channel 2 Coarse BIN5 Threshold HIGH (31:16) Coarse BIN5 Threshold LOW (15:0)
046	Channel 2 Coarse BIN6 Threshold HIGH (31:16) Coarse BIN6 Threshold LOW (15:0)
047	Channel 2 Coarse BIN7 Threshold HIGH (31:16) Coarse BIN7 Threshold LOW (15:0)
048	Channel 2 Valid pulse timeout. This parameter is represents maximum time after INIT_DISC for MIN_DISC to occur so the pulse is deemed valid. Each bit corresponds to 50ns. (15:0)
049	Channel 2 Sample time. Define the sample time for the ADC with respect to INIT_DISC. Each bit corresponds to 50ns. (15:0)
04a	Channel 2 Integrator release time. Define the time with respect to INIT_DISC where the integrator is enabled. Each bit corresponds to 50ns. (15:0)

Table B.1-d Channel 3 parameters

ADDR (Hex)	Description
060	Channel 3 Coarse BIN0 Threshold HIGH (31:16) Coarse BIN0 Threshold LOW (15:0)
061	Channel 3 Coarse BIN1 Threshold HIGH (31:16) Coarse BIN1 Threshold LOW (15:0)
062	Channel 3 Coarse BIN2 Threshold HIGH (31:16) Coarse BIN2 Threshold LOW (15:0)
063	Channel 3 Coarse BIN3 Threshold HIGH (31:16) Coarse BIN3 Threshold LOW (15:0)
064	Channel 3 Coarse BIN4 Threshold HIGH (31:16) Coarse BIN4 Threshold LOW (15:0)
065	Channel 3 Coarse BIN5 Threshold HIGH (31:16) Coarse BIN5 Threshold LOW (15:0)
066	Channel 3 Coarse BIN6 Threshold HIGH (31:16) Coarse BIN6 Threshold LOW (15:0)
067	Channel 3 Coarse BIN7 Threshold HIGH (31:16) Coarse BIN7 Threshold LOW (15:0)
068	Channel 3 Valid pulse timeout. This parameter is represents maximum time after INIT_DISC for MIN_DISC to occur so the pulse is deemed valid. Each bit corresponds to 50ns. (15:0)
069	Channel 3 Sample time. Define the sample time for the ADC with respect to INIT_DISC. Each bit corresponds to 50ns. (15:0)
06a	Channel 3 Integrator release time. Define the time with respect to INTT_DISC where the integrator is enabled. Each bit corresponds to 50ns. (15:0)

Table B.1-e Channel 4 parameters

ADDR (Hex)	Description
080	Channel 4 Coarse BIN0 Threshold HIGH (31:16) Coarse BIN0 Threshold LOW (15:0)
081	Channel 4 Coarse BIN1 Threshold HIGH (31:16) Coarse BIN1 Threshold LOW (15:0)
082	Channel 4 Coarse BIN2 Threshold HIGH (31:16) Coarse BIN2 Threshold LOW (15:0)
083	Channel 4 Coarse BIN3 Threshold HIGH (31:16) Coarse BIN3 Threshold LOW (15:0)
084	Channel 4 Coarse BIN4 Threshold HIGH (31:16) Coarse BIN4 Threshold LOW (15:0)
085	Channel 4 Coarse BIN5 Threshold HIGH (31:16) Coarse BIN5 Threshold LOW (15:0)
086	Channel 4 Coarse BIN6 Threshold HIGH (31:16) Coarse BIN6 Threshold LOW (15:0)
087	Channel 4 Coarse BIN7 Threshold HIGH (31:16) Coarse BIN7 Threshold LOW (15:0)
088	Channel 4 Valid pulse timeout. This parameter is represents maximum time after INIT_DISC for MIN_DISC to occur so the pulse is deemed valid. Each bit corresponds to 50ns. (15:0)
089	Channel 4 Sample time. Define the sample time for the ADC with respect to INIT_DISC. Each bit corresponds to 50ns. (15:0)
08a	Channel 4 Integrator release time. Define the time with respect to INIT_DISC where the integrator is enabled. Each bit corresponds to 50ns. (15:0)

Table B.1-f Channel 5 parameters

ADDR (Hex)	Description
0a0	Channel 5 Coarse BIN0 Threshold HIGH (31:16) Coarse BIN0 Threshold LOW (15:0)
0a1	Channel 5 Coarse BIN1 Threshold HIGH (31:16) Coarse BIN1 Threshold LOW (15:0)
0a2	Channel 5 Coarse BIN2 Threshold HIGH (31:16) Coarse BIN2 Threshold LOW (15:0)
0a3	Channel 5 Coarse BIN3 Threshold HIGH (31:16) Coarse BIN3 Threshold LOW (15:0)
0a4	Channel 5 Coarse BIN4 Threshold HIGH (31:16) Coarse BIN4 Threshold LOW (15:0)
0a5	Channel 5 Coarse BIN5 Threshold HIGH (31:16) Coarse BIN5 Threshold LOW (15:0)
0a6	Channel 5 Coarse BIN6 Threshold HIGH (31:16) Coarse BIN6 Threshold LOW (15:0)
0a7	Channel 5 Coarse BIN7 Threshold HIGH (31:16) Coarse BIN7 Threshold LOW (15:0)
0a8	Channel 5 Valid pulse timeout. This parameter is represents maximum time after INIT_DISC for MIN_DISC to occur so the pulse is deemed valid. Each bit corresponds to 50ns. (15:0)
0a9	Channel 5 Sample time. Define the sample time for the ADC with respect to INIT_DISC. Each bit corresponds to 50ns. (15:0)
0aa	Channel 5 Integrator release time. Define the time with respect to INIT_DISC where the integrator is enabled. Each bit corresponds to 50ns. (15:0)

Table B.1-g Channel 6 parameters

ADDR (Hex)	Description
0c0	Channel 6 Coarse BIN0 Threshold HIGH (31:16) Coarse BIN0 Threshold LOW (15:0)
0c1	Channel 6 Coarse BIN1 Threshold HIGH (31:16) Coarse BIN1 Threshold LOW (15:0)
0c2	Channel 6 Coarse BIN2 Threshold HIGH (31:16) Coarse BIN2 Threshold LOW (15:0)
0c3	Channel 6 Coarse BIN3 Threshold HIGH (31:16) Coarse BIN3 Threshold LOW (15:0)
0c4	Channel 6 Coarse BIN4 Threshold HIGH (31:16) Coarse BIN4 Threshold LOW (15:0)
0c5	Channel 6 Coarse BIN5 Threshold HIGH (31:16) Coarse BIN5 Threshold LOW (15:0)
0c6	Channel 6 Coarse BIN6 Threshold HIGH (31:16) Coarse BIN6 Threshold LOW (15:0)
0c7	Channel 6 Coarse BIN7 Threshold HIGH (31:16) Coarse BIN7 Threshold LOW (15:0)
0c8	Channel 6 Valid pulse timeout. This parameter is represents maximum time after INIT_DISC for MIN_DISC to occur so the pulse is deemed valid. Each bit corresponds to 50ns. (15:0)
0c9	Channel 6 Sample time. Define the sample time for the ADC with respect to INIT_DISC. Each bit corresponds to 50ns. (15:0)
0ca	Channel 6 Integrator release time. Define the time with respect to INIT_DISC where the integrator is enabled. Each bit corresponds to 50ns. (15:0)

Table B.1-h Channel 7 parameters

ADDR (Hex)	Description
0e0	Channel 7 Coarse BIN0 Threshold HIGH (31:16) Coarse BIN0 Threshold LOW (15:0)
0e1	Channel 7 Coarse BIN1 Threshold HIGH (31:16) Coarse BIN1 Threshold LOW (15:0)
0e2	Channel 7 Coarse BIN2 Threshold HIGH (31:16) Coarse BIN2 Threshold LOW (15:0)
0e3	Channel 7 Coarse BIN3 Threshold HIGH (31:16) Coarse BIN3 Threshold LOW (15:0)
0e4	Channel 7 Coarse BIN4 Threshold HIGH (31:16) Coarse BIN4 Threshold LOW (15:0)
0e5	Channel 7 Coarse BIN5 Threshold HIGH (31:16) Coarse BIN5 Threshold LOW (15:0)
0e6	Channel 7 Coarse BIN6 Threshold HIGH (31:16) Coarse BIN6 Threshold LOW (15:0)
0e7	Channel 7 Coarse BIN7 Threshold HIGH (31:16) Coarse BIN7 Threshold LOW (15:0)
0e8	Channel 7 Valid pulse timeout. This parameter is represents maximum time after INIT_DISC for MIN_DISC to occur so the pulse is deemed valid. Each bit corresponds to 50ns. (15:0)
0e9	Channel 7 Sample time. Define the sample time for the ADC with respect to INIT_DISC. Each bit corresponds to 50ns. (15:0)
0ea	Channel 7 Integrator release time. Define the time with respect to INIT_DISC where the integrator is enabled. Each bit corresponds to 50ns. (15:0)

Table B.1-i System parameters

ADDR (Hex)	Description	
100	Sequence acquisition time in 6.4 μ s increments. (31:0)	
101	Modes and Sequence Definition	
	7:0	Number of sequences. If NS is the number of sequences defined, then a total of NS+1 sequences will be run.
	8	Acquisition type 0=Coarse, 1=Fine
10:9	Acquisition mode 00=Normal 01=Fixed coarse pattern. (for module testing only) 10=Fake trigger mode. 11=Normal	
102	Acquisition Status	
	18:0	Word count (number of 32 bit words) read by the host computer.
	19	Data Ready for transfer. 1=Ready
	20	BIOMASS card FIFO empty.
	21	Acquisition enabled.
	22	FIFO hold-off. BIOMASS FIFO has occurred sufficient data to be read.
	23	FIFO Full Error. The BIOMASS card had a FIFO go full.
31:24	Channel error indicators.	
103	Start Acquisition. Writing any data to this address starts the acquisition. Reading this address returns the last word written to the card.	
104	Stop Acquisition. (abort current operation)	
105	Write DAC. The parameters stored in the control FPGA (Addresses 180H to 1A7H) are written to the DACs via the board SPI bus. Changing the DAC values requires first writing new values to the appropriate addresses (180H, etc.)	
106	Trigger Firing Count. In Fake trigger mode, this value defines how often a channel fakes valid pulse and begins the integration process. Specifically, this variable is used in calibration and debugging modes.	
108	Word Count value at end of Channel 0 (bits 18:0) DEBUGGING	
109	Word Count value at end of Channel 1 (bits 18:0) DEBUGGING	
10a	Word Count value at end of Channel 2 (bits 18:0) DEBUGGING	
10b	Word Count value at end of Channel 3 (bits 18:0) DEBUGGING	
10c	Word Count value at end of Channel 4 (bits 18:0) DEBUGGING	
10d	Word Count value at end of Channel 5 (bits 18:0) DEBUGGING	
10e	Word Count value at end of Channel 6 (bits 18:0) DEBUGGING	

Table B.1-j Analog Control Parameters

Address (Hex)	Description
180	DAC Parameter DACSEL=1, ADDR=0: Input offset Channel 0
181	DAC Parameter DACSEL=1, ADDR=1: Input offset Channel 1
182	DAC Parameter DACSEL=2, ADDR=0: Input offset Channel 2
183	DAC Parameter DACSEL=2, ADDR=1: Input offset Channel 3
184	DAC Parameter DACSEL=3, ADDR=0: Input offset Channel 4
185	DAC Parameter DACSEL=3, ADDR=1: Input offset Channel 5
186	DAC Parameter DACSEL=4, ADDR=0: Input offset Channel 6
187	DAC Parameter DACSEL=4, ADDR=1: Input offset Channel 7
188	DAC Parameter DACSEL=5, ADDR=0: Minimum Threshold Channel 0
189	DAC Parameter DACSEL=5, ADDR=1: Minimum Threshold Channel 1
18a	DAC Parameter DACSEL=5, ADDR=2: Minimum Threshold Channel 2
18b	DAC Parameter DACSEL=5, ADDR=3: Minimum Threshold Channel 3
18c	DAC Parameter DACSEL=5, ADDR=4: Minimum Threshold Channel 4
18d	DAC Parameter DACSEL=5, ADDR=5: Minimum Threshold Channel 5
18e	DAC Parameter DACSEL=5, ADDR=6: Minimum Threshold Channel 6
18f	DAC Parameter DACSEL=5, ADDR=7: Minimum Threshold Channel 7
190	DAC Parameter DACSEL=6, ADDR=0: Initial Threshold Channel 0
191	DAC Parameter DACSEL=6, ADDR=1: Initial Threshold Channel 1
192	DAC Parameter DACSEL=6, ADDR=2: Initial Threshold Channel 2
193	DAC Parameter DACSEL=6, ADDR=3: Initial Threshold Channel 3
194	DAC Parameter DACSEL=6, ADDR=4: Initial Threshold Channel 4
195	DAC Parameter DACSEL=6, ADDR=5: Initial Threshold Channel 5
196	DAC Parameter DACSEL=6, ADDR=6: Initial Threshold Channel 6
197	DAC Parameter DACSEL=6, ADDR=7: Initial Threshold Channel 7
198	DAC Parameter DACSEL=5, ADDR=8: Full scale reference Channel 0
199	DAC Parameter DACSEL=5, ADDR=9: Full scale reference Channel 1
19a	DAC Parameter DACSEL=5, ADDR=10: Full scale reference Channel 2
19b	DAC Parameter DACSEL=5, ADDR=11: Full scale reference Channel 3
19c	DAC Parameter DACSEL=6, ADDR=8: Full scale reference Channel 4
19d	DAC Parameter DACSEL=6, ADDR=9: Full scale reference Channel 5
19e	DAC Parameter DACSEL=6, ADDR=10: Full scale reference Channel 6
19f	DAC Parameter DACSEL=6, ADDR=11: Full scale reference Channel 7
1A0	DAC Parameter DACSEL=7, ADDR=0: ADC offset Channel 0
1A1	DAC Parameter DACSEL=7, ADDR=1: ADC offset Channel 1
1A2	DAC Parameter DACSEL=7, ADDR=2: ADC offset Channel 2
1A3	DAC Parameter DACSEL=7, ADDR=3: ADC offset Channel 3
1A4	DAC Parameter DACSEL=7, ADDR=4: ADC offset Channel 4
1A5	DAC Parameter DACSEL=7, ADDR=5: ADC offset Channel 5
1A6	DAC Parameter DACSEL=7, ADDR=6: ADC offset Channel 6
1A7	DAC Parameter DACSEL=7, ADDR=7: ADC offset Channel 7

Table B.1-k System ID and data acquisition

ADDR (Hex)	Description
110	Read-only. The acquisition information.
111	Read-only. BIOMASS fixed ID-1 (0x89ABCDEF)
112	Read-only. BIOMASS fixed ID-2 (0x12345678)
113	Read-only. BIOMASS fixed ID-3 (0xB77BEFDF)
0800000 to 0FFFFFFF	Read-only. The acquisition information.

The default values for the different thresholds and other module parameters are defined in Table B.2. Data in this system is always read and written as a 32-bit word – these values are padded with zeroes to fill out the word. The default values are loaded into the module control FPGA on power up. As shown in Table 1, many of these parameters, such as valid pulse timeout or Integrator release time, can be set independently on a per channel basis, but the same default values are used for all eight channels.

Table B.2 Parameter default values (in hexadecimal).

Parameter	Default value in Hex
BIN0 Threshold LOW (15:0)	000
BIN0 Threshold HIGH (31:16)	07F
BIN1 Threshold LOW (15:0)	080
BIN1 Threshold HIGH (31:16)	0FF
BIN2 Threshold LOW (15:0)	100
BIN2 Threshold HIGH (31:16)	17F
BIN3 Threshold LOW (15:0)	180
BIN3 Threshold HIGH (31:16)	1FF
BIN4 Threshold LOW (15:0)	200
BIN4 Threshold HIGH (31:16)	27F
BIN5 Threshold LOW (15:0)	280
BIN5 Threshold HIGH (31:16)	2FF
BIN6 Threshold LOW (15:0)	300
BIN6 Threshold HIGH (31:16)	37F
BIN7 Threshold LOW (15:0)	380
BIN7 Threshold HIGH (31:16)	3FF
Valid pulse timeout	6
Sample time	28
Integrator release time	1
Sequence acquisition time	3000
Acquisition Mode & number of sequences	0
Input Offset Channel	80
Minimum Threshold	80
Initial Threshold	80
Full Scale Reference	80
ADC offset	80

B.7 Software

The “BIOMASS” software for the pulse processor module is written in C code. This code provides a simple interface to configure parameters on each pulse processor module and acquire information from all pulse processor module (s). These software routines handle all communications with the Window’s PLX API via the PLX DLL. A different subroutine is used at each step of the procedure, so integration with higher-level code is possible. At present, all input and output functions of the software are file based, i.e., setup parameters are taken from a file and downloaded to the module, and data from the module is written to a file without graphical or other display.

B.7.1 Initial module set-up

To set-up pulse processor modules for the first time, you insert the modules in the crate (power must be off) and make certain they are seated properly and latched. You then turn on the power. Windows should start and a message box should say that new hardware (PCI bridge device) has been found. Another message box will indicate that it is “OEM custom PCI9030”. Click “ok” as needed.

Next the PLXMON program is used to set-up the API for PLX cards. When this starts, a window pops up and should say that a driver is detected. This window closes by itself, and the next window says that PCI devices don’t have listings. This window lists the number of cards and some other information. Click “ok” and this window goes away. Next, the properties window appears. Once again, click “ok” to exit this window. You can now exit the program – the card set-up is complete.

B.7.2 Module configuration

A configuration file is used to set-up the pulse processor module for data taking. This section describes the generation, modification and use of configuration files.

The pulse processor modules in the CPCI crate are located and configured by using the BIOMASS program with the configuration option. The command to create a configuration file is “BIOMASS -C CONFIG_FILE” where CONFIG_FILE is the name of the output file where the configuration data is stored for future use. This command also runs a test procedure that adjusts the input and ADC offsets in the module using the corresponding DACs. For this procedure, the shaping amplifiers should be powered on and connected to the pulse processor module(s). If detectors are connected to the shaping amplifiers, they should not be powered up so as to prevent any pulses from detectors disturbing the adjustment procedure.

The configuration procedure generates a configuration file (CONFIG_FILE.ACQ) that contains energy window limits, integration time, thresholds, ADC full-scale and offsets for each channel of each card. The file also contains the parameters acquisition time, acquisition mode, acquisition type and acquisition number of samples. These *global* parameters apply to all pulse processor modules in a crate. Table B.3 describes the global parameters.

Table B.3 Configuration file global parameters.

Parameter	Description	Values Hex or (decimal)	module address (Hex)
Acquisition time	time interval for data taking – time is this integer value multiplied by 6.4 μ s	1 to 3FFFFFFF (1 to 2147483647)	100
Acquisition mode	Determines type of data taking	0 = normal 1 = fixed pattern 2 = fake trigger	101, bits 9 and 10
Acquisition type	Determines if coarse or fine bins are used	0 = coarse 1 = fine	101, bit 8
Acquisition number of samples	Number of time intervals during which data is to be acquired before module readout	0 to 7F (0 to 127)	101, bits 0 to 7

The configuration file is an ordinary text file and may be manually edited to set-up the parameters for a given experiment. Parameters such as energy window limits and the global parameters would generally be modified for a particular experiment. Parameters such as integration time, discriminator thresholds, and ADC full-scale might need to be adjusted to allow for detector variations or for other optimization needs. Generally, the automatically determined offset values should be sufficient and not need to be adjusted manually. Appendix A.1 is a sample configuration file.

A.7.3 Data Acquisition

Once the modules are initialized and a configuration file is created and modified as needed, data acquisition is simple. An experiment can be run by using the command “BIOMASS -R-I CONFIG_FILE -O OUT_FILE”. This command runs the program in the normal run mode (-R option) with input file (-I option) “CONFIG_FILE” and output file (-O option) “OUT_FILE”. Please note that a .LOG extension is added to the name of the output file.

Presently, there are two possible output file formats for the pulse processor card available in the software. One mode has CARD and CHANNEL information in the columns with BIN and SAMPLE information in block rows as shown in Table 4. This format should be useful for a fine-mode (MCA type) experiment. For example, if two cards used in the fine mode with one sampling interval, the output file will have 16 columns of data with 1024 rows. The other mode has SAMPLE information in the

columns with the CARD, CHANNEL, and BIN information in the rows in Table 5. The name of the mode reflects what values are stored in the columns.

The output file format can be set with the file format option (*-f value*). The format shown in Table B.4 (Samples in columns, Cards and Channels in rows) is the default format (*-f 0*). To use the format shown in Table B.5 (Samples in rows, Cards and Channels in columns), you specify *-f 1* when running the program. Running the BIOMASS program with the *-h* option will give “help” information on various options. To do this, type “BIOMASS *-H*”. Table 6 gives a list of suggested configuration values for MP-CARPT.

Table B.4 Readout scheme for the CARD and CHANNEL mode

Time interval #1																
	Card #0							ETC	Card #N							
	0	1	2	3	4	5	6		7	0	1	2	3	4	5	6
BIN 0 (Sample 1)																
BIN 1 (Sample 1)																
ETC																
BIN X (Sample 1)																
Time interval #2																
Channels	Card #0							ETC	Card #N							
	0	1	2	3	4	5	6		7	0	1	2	3	4	5	6
BIN 0 (Sample 1)																
BIN 1 (Sample 1)																
ETC																
BIN X (Sample 1)																
(data from additional time intervals)																
Time interval #S																
Channels	Card #0							ETC	Card #N							
	0	1	2	3	4	5	6		7	0	1	2	3	4	5	6
BIN 0 (Sample S)																
BIN 1 (Sample S)																
ETC																
BIN X (Sample S)																

Table B.5 Readout scheme for SAMPLES mode

Card #0				ETC	Sample S
	Sample 1	Sample 2			
Channel 0 BIN 0					
Channel 0 BIN 1					
ETC					
Channel 0 BIN X					
Channel 1 BIN 0					
Channel 1 BIN 1					
ETC					
Channel 1 BIN X					
* ETC *					
Channel 7 BIN 0					
Channel 7 BIN 1					

ETC			
Channel 7 BIN X			
Card #1			
Channel 0 BIN 0			ETC
* ETC *			
Channel 7 BIN X			
** ETC **			
Card #N			
Channel 0 BIN 0			ETC
* ETC *			
Channel 7 BIN X			

Table B.6 Suggested Parameter values (in hexadecimal).

Parameter	Suggested value in Hex	Comment
BIN Thresholds LOW and HIGH	?	Set as needed
Valid pulse timeout	6	default
Sample time	28	Default, s□ 2
Integrator release time	1	Default
Sequence acquisition time	30D	~5 ms per interval
Acquisition mode	0	Normal data
Acquisition type	0	Coarse mode
Acquisition Mode & number of sequences	FF	256 intervals
Input Offset Channel	A0	mid scale, program will autose
Minimum Threshold	8	Lower values are possible
Initial Threshold	8	Lower values are possible
Full Scale Reference	FF	Lower value to increase gain
ADC offset	80	mid scale, program will autose

B.7.4 Summary of the Programming Procedure

The procedure for setting up and acquiring data is described in the following sequence:

- 1) Use the PLXMON program from PLX to setup the API for the PLX cards. You will need to use this program each time a new pulse processor card is added to the system.
- 2) Initialize the pulse processor cards in the system and create a configuration file. The command is "BIOMASS -C CONFIG_FILE" where CONFIG_FILE is the name of the output file.
- 3) Modify the control parameters for each card in the configuration file. Be sure and set the mode to fine.
- 4) Connect the detectors to the amplifiers and/or turn on detectors.
- 5) Take data using each radioactive source one at a time. Plot energy spectra and determine desired energy windows.
- 6) Modify the control parameters for each BIOMASS card in the configuration file for normal (CARPT-type) acquisition. Remember to change the ACQ_MODE back to 0! It

may be useful to save different versions of the configuration file for similar, but slightly different experiments (like one for MCA mode and another for CARPT).

7) Run the experiment. The command is “BIOMASS -R-I CONFIG_FILE -O LOG_FILE”. Please note that a .LOG extension is added to the name of the output log file.

B.7.5 Test Mode Operation

There are a couple of test modes that are useful. The “fake trigger” mode is useful to determine the system noise and mean value for a zero signal. This can be accomplished by setting the module for fine mode and “fake trigger” mode and running a short experiment. In the “fake trigger” mode, the module controller causes the channels to fake the detection of a valid input pulse, so the integration and digitization process is started and the resulting data stored. This process is repeated according to the TRIGGER FIRING COUNT parameter. The time between “fake triggers” is 25 ns times the TRIGGER FIRING COUNT. The default value is 32 μ s, so sufficient data can be taken in a few seconds.

If this experiment is run without a shaping amplifier connected to pulse processor module (the module may need to be configured without the shaping amplifier), essentially all the counts should be in one or two bins. If the shaping amplifier is connected, the noise level will be greater and the counts will be spread over perhaps 20 bins.

B.7.6 Sample Data

Figure B.27 shows spectra resulting from using the shaping amplifier and pulse processor module with two 2-inch NaI detectors and naturally-occurring Potassium-40 (in salt substitute). The peak for this isotope is 1.46 MeV, and it occurs at channel 950 for one detector and channel 400 for the other due to the detector gains not being balanced. (Both detectors used the same high voltage and same shaping amplifier gain.) The same source was counted for approximately 16 hours and the data shown in Figure B.28 was obtained. Other well-known background peaks are labeled.

The “fake trigger” mode was used to obtain the plot shown in Figure B.29. The distributions show the level of amplifier noise. (Ideally all counts would occur in a single bin as the input is a constant – zero.) The root-mean-square (rms) variation for the typical channel is about 6 bins. This variation is significantly less than the variation due to the NaI detectors, so it is sufficiently good to not effect peaks like those shown in Figure B.27. Two channels show significantly lower rms variations. These channels have modified shaping amplifiers. These modifications may be included in future shaping amplifier modules.

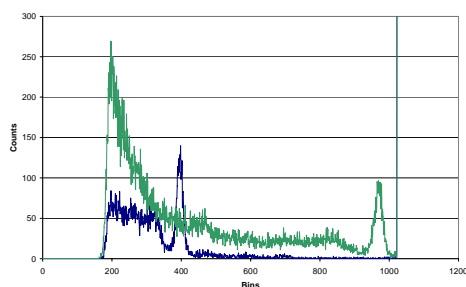


Figure B.27 ^{40}K spectrum

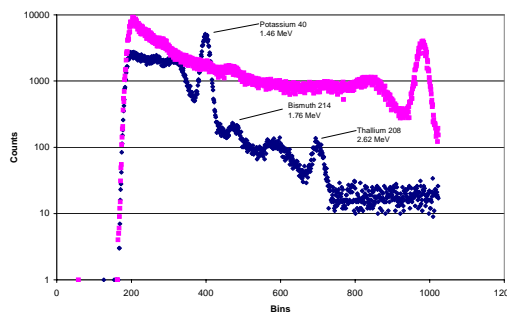


Figure B.28 ^{40}K spectrum with log scale.

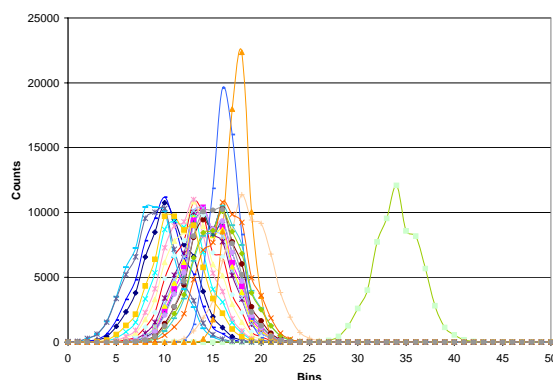


Figure B.29 Shaper amplifier noise.

B.8 Problems encountered with MP-CARPT

B.8.1 Problems

The principle of MP-CARPT is based on the energy discrimination. Two or more radioactive particles can be distinguished from each other based on their gamma energy peaks. Co-60 has its energy peaks at 1.17 and 1.33 MeV and Sc-46 has its peaks at 0.889 and 1.12 MeV. With the adjustment in gain of the timing amplifiers, the peaks of Co-60 and Sc-46 can be shifted together horizontally but not independently. During the course of normal operation this peak should remain at the same position, given that all other settings (like gain etc.) in data acquisition electronics are kept constant, irrespective of the position of the radioactive particle and the intensity of the gamma ray counts received. This property is essential for the success for the MP-CARPT.

The limits of energy windows during the experiment phase are set such that only the high energy Co-60 peak is captured in one window and in the other window both Co-60 and Sc-46 peaks are captured. This approach helps in distinguishing between the counts obtained from different sources. For this to succeed, the position of the energy peaks

must remain the same for different locations of radioactive source. Hence the variation in the intensity of the gamma ray counts (due to changing distance) shouldn't affect the location of the peaks on the energy (bins) scale.

However, during experimentation it was discovered that this was not the case with the electronics developed at the ORNL which is currently in use for MP-CARPT. The Figure B.30 below shows the shift in energy peaks of Co-60 and Sc-46 for two different source locations (hence gamma ray counts intensity). For a location of the particles closer to the detector the peaks shift towards a higher energy (towards the right on the scale). The number of gamma ray photon counts obtained by the detectors is dependent on the distance of the source from the detector. Therefore, more counts are obtained for source near the detector and less photon counts for longer distances. In this data acquisition system the change in counts brings about a shift in the location of the peak. Hence the photo peak shifts out of the energy window when the particle location is closer to the detector. This causes a drop in the counts detected for particle locations close to the detector. This is counter intuitive to the basic principles.

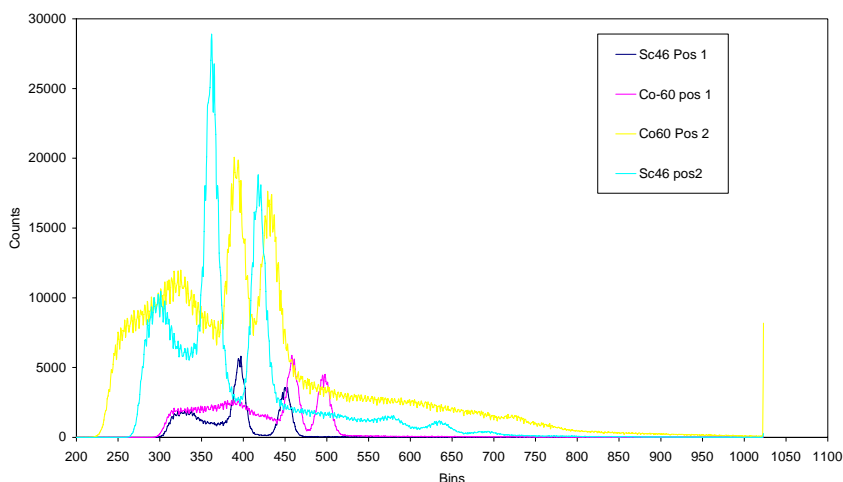


Figure B.30 Shift in gamma ray energy spectrum of the ^{60}Co and ^{46}Sc at two different locations of the particles.

Another problem encountered has been explained with the aid of Figure B.31. The counts obtained from two separate single sources independently should add up to the total gamma counts obtained with 2 sources together (provided their locations remain unchanged). When this experiment was carried out, it was found that they don't add up with this set up. Figure B.31 shows the gamma ray photon peaks for Co-60 and Sc-46, taken simultaneously and separately with the current MP-CARPT data acquisition system. It can be seen that the peaks of the individual source are not superimposed when the scans are obtained simultaneously. This shift creates problems during the data processing, as the counts of Sc-46 are obtained by subtracting the counts of Co-60 alone from the total counts of Sc-46 and Co-60 together.

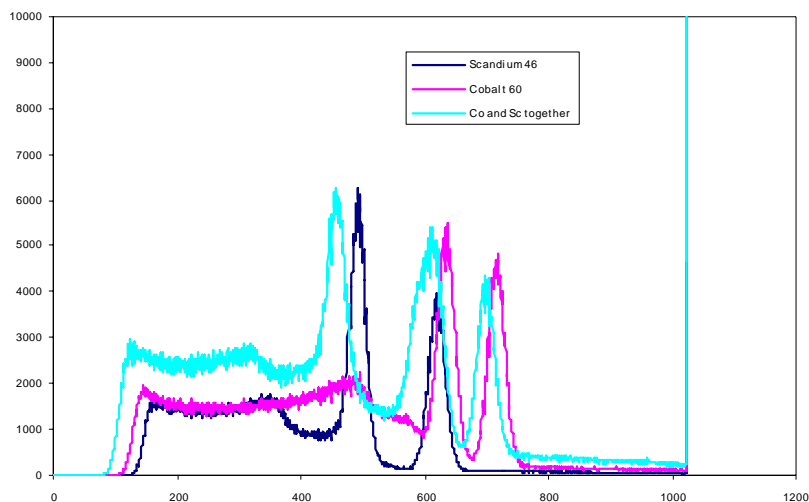


Figure B.31 Photo peaks of ^{46}Sc and ^{60}Co taken with individual source both separately and together. Notice a shift in the spectrum of the combined sources.

B.8.2 Rectification of Problems

Above problems can be solved by changing the parameters in the configuration file, which provides input to the data acquisition program.

Figure B.31 shows the problem of shifting of gamma peak with changing distance of Sc-46 and Co-60 sources from the detector. The value of parameter “sample_time” was changed from 40 to 16, this value was decided after a trial and error procedure to eliminate the shifting of gamma peaks. Figure B.33 shows the gamma peaks of Sc-46 and Co-60 obtained separately for different positions, position 1 is closer to the detector whereas position 2 is farther. The shifting of the peak is almost eliminated by changing the value of sample_time.

Figure B.32 shows the shift in the gamma spectrum when Sc-60 and Co-60 are scanned together with respect to their individual spectrum. This suggests that the counts are not additive. With the change of sample_time, the Sc-46 and Co-60 counts were found to be additive as shown in Figure B.33. Counts were obtained for Sc-46 and Co-60 separately and together. The counts of Sc-46 and Co-60 were added to examine the overlap with counts that were obtained by placing Sc-46 and Co-60 together at the same location. The summed counts match very well with the counts of Sc-46 and Co-60 scanned together, indicating that the superposition rule of gamma peaks for different sources is satisfied.

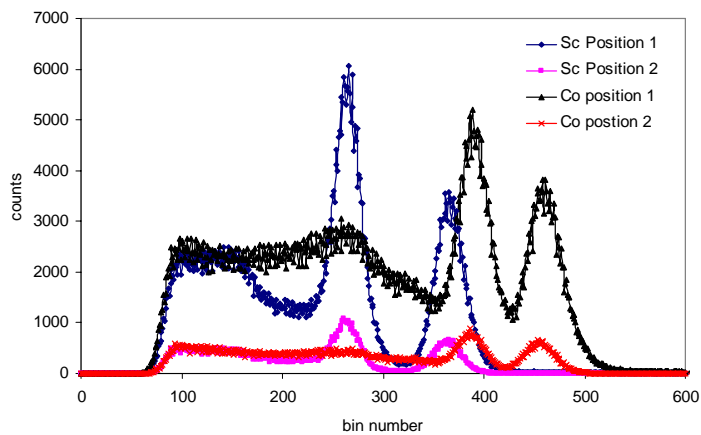


Figure B.32 Individual Gamma peaks of Sc-46 and Co-60 placed at different locations

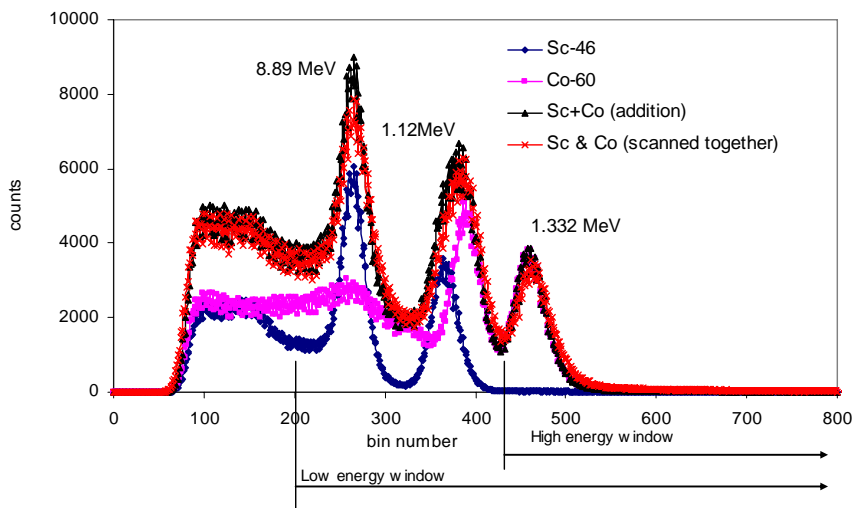


Figure B.33 Gamma peaks of Sc-46 and Co-60 individually and together, and summation of individual counts

Appendix B.1

Example Configuration File.

```

# BIOMASS control file config4
# biomass version 1.1
#
# This file was generated using the biomass program and its -C option.
#
#
# *****
#
# Define the CARD definitions
#
# *****

# -----
## CARD [SerialNum=Pci9030-1 - bus 02 slot 0c device=9030 vendor=10b5 ]
# -----
CARD Pci9030-1 ON
    set CHAN0_BIN0_LOW H0
    set CHAN0_BIN0_HIGH H7f
    set CHAN0_BIN1_LOW H80
    set CHAN0_BIN1_HIGH Hff
    set CHAN0_BIN2_LOW H100
    set CHAN0_BIN2_HIGH H17f
    set CHAN0_BIN3_LOW H180
    set CHAN0_BIN3_HIGH H1ff
    set CHAN0_BIN4_LOW H200
    set CHAN0_BIN4_HIGH H27f
    set CHAN0_BIN5_LOW H280
    set CHAN0_BIN5_HIGH H2ff
    set CHAN0_BIN6_LOW H300
    set CHAN0_BIN6_HIGH H37f
    set CHAN0_BIN7_LOW H380
    set CHAN0_BIN7_HIGH H3ff
    set CHAN1_BIN0_LOW H0
    set CHAN1_BIN0_HIGH H7f
    set CHAN1_BIN1_LOW H80
    set CHAN1_BIN1_HIGH Hff
    set CHAN1_BIN2_LOW H100
    set CHAN1_BIN2_HIGH H17f
    set CHAN1_BIN3_LOW H180
    set CHAN1_BIN3_HIGH H1ff
    set CHAN1_BIN4_LOW H200
    set CHAN1_BIN4_HIGH H27f
    set CHAN1_BIN5_LOW H280
    set CHAN1_BIN5_HIGH H2ff
    set CHAN1_BIN6_LOW H300
    set CHAN1_BIN6_HIGH H37f
    set CHAN1_BIN7_LOW H380
    set CHAN1_BIN7_HIGH H3ff
    set CHAN2_BIN0_LOW H0

```

```
set CHAN2_BIN0_HIGH H7f
set CHAN2_BIN1_LOW H80
set CHAN2_BIN1_HIGH Hff
set CHAN2_BIN2_LOW H100
set CHAN2_BIN2_HIGH H17f
set CHAN2_BIN3_LOW H180
set CHAN2_BIN3_HIGH H1ff
set CHAN2_BIN4_LOW H200
set CHAN2_BIN4_HIGH H27f
set CHAN2_BIN5_LOW H280
set CHAN2_BIN5_HIGH H2ff
set CHAN2_BIN6_LOW H300
set CHAN2_BIN6_HIGH H37f
set CHAN2_BIN7_LOW H380
set CHAN2_BIN7_HIGH H3ff
set CHAN3_BIN0_LOW H0
set CHAN3_BIN0_HIGH H7f
set CHAN3_BIN1_LOW H80
set CHAN3_BIN1_HIGH Hff
set CHAN3_BIN2_LOW H100
set CHAN3_BIN2_HIGH H17f
set CHAN3_BIN3_LOW H180
set CHAN3_BIN3_HIGH H1ff
set CHAN3_BIN4_LOW H200
set CHAN3_BIN4_HIGH H27f
set CHAN3_BIN5_LOW H280
set CHAN3_BIN5_HIGH H2ff
set CHAN3_BIN6_LOW H300
set CHAN3_BIN6_HIGH H37f
set CHAN3_BIN7_LOW H380
set CHAN3_BIN7_HIGH H3ff
set CHAN4_BIN0_LOW H0
set CHAN4_BIN0_HIGH H7f
set CHAN4_BIN1_LOW H80
set CHAN4_BIN1_HIGH Hff
set CHAN4_BIN2_LOW H100
set CHAN4_BIN2_HIGH H17f
set CHAN4_BIN3_LOW H180
set CHAN4_BIN3_HIGH H1ff
set CHAN4_BIN4_LOW H200
set CHAN4_BIN4_HIGH H27f
set CHAN4_BIN5_LOW H280
set CHAN4_BIN5_HIGH H2ff
set CHAN4_BIN6_LOW H300
set CHAN4_BIN6_HIGH H37f
set CHAN4_BIN7_LOW H380
set CHAN4_BIN7_HIGH H3ff
set CHAN5_BIN0_LOW H0
set CHAN5_BIN0_HIGH H7f
set CHAN5_BIN1_LOW H80
set CHAN5_BIN1_HIGH Hff
set CHAN5_BIN2_LOW H100
set CHAN5_BIN2_HIGH H17f
set CHAN5_BIN3_LOW H180
```

```
set CHAN5_BIN3_HIGH H1ff
set CHAN5_BIN4_LOW H200
set CHAN5_BIN4_HIGH H27f
set CHAN5_BIN5_LOW H280
set CHAN5_BIN5_HIGH H2ff
set CHAN5_BIN6_LOW H300
set CHAN5_BIN6_HIGH H37f
set CHAN5_BIN7_LOW H380
set CHAN5_BIN7_HIGH H3ff
set CHAN6_BIN0_LOW H0
set CHAN6_BIN0_HIGH H7f
set CHAN6_BIN1_LOW H80
set CHAN6_BIN1_HIGH Hff
set CHAN6_BIN2_LOW H100
set CHAN6_BIN2_HIGH H17f
set CHAN6_BIN3_LOW H180
set CHAN6_BIN3_HIGH H1ff
set CHAN6_BIN4_LOW H200
set CHAN6_BIN4_HIGH H27f
set CHAN6_BIN5_LOW H280
set CHAN6_BIN5_HIGH H2ff
set CHAN6_BIN6_LOW H300
set CHAN6_BIN6_HIGH H37f
set CHAN6_BIN7_LOW H380
set CHAN6_BIN7_HIGH H3ff
set CHAN7_BIN0_LOW H0
set CHAN7_BIN0_HIGH H7f
set CHAN7_BIN1_LOW H80
set CHAN7_BIN1_HIGH Hff
set CHAN7_BIN2_LOW H100
set CHAN7_BIN2_HIGH H17f
set CHAN7_BIN3_LOW H180
set CHAN7_BIN3_HIGH H1ff
set CHAN7_BIN4_LOW H200
set CHAN7_BIN4_HIGH H27f
set CHAN7_BIN5_LOW H280
set CHAN7_BIN5_HIGH H2ff
set CHAN7_BIN6_LOW H300
set CHAN7_BIN6_HIGH H37f
set CHAN7_BIN7_LOW H380
set CHAN7_BIN7_HIGH H3ff
set ACQ_TRIGGER_CNT H80
set CHAN0_INPUT_OFFSET Ha0
set CHAN1_INPUT_OFFSET H9e
set CHAN2_INPUT_OFFSET H95
set CHAN3_INPUT_OFFSET H99
set CHAN4_INPUT_OFFSET H9b
set CHAN5_INPUT_OFFSET H92
set CHAN6_INPUT_OFFSET H9e
set CHAN7_INPUT_OFFSET H99
set CHAN0_INIT_THRESHOLD H08
set CHAN1_INIT_THRESHOLD H40
set CHAN2_INIT_THRESHOLD H40
set CHAN3_INIT_THRESHOLD H40
```

```

set CHAN4_INIT_THRESHOLD H40
set CHAN5_INIT_THRESHOLD H40
set CHAN6_INIT_THRESHOLD H40
set CHAN7_INIT_THRESHOLD H40
set CHAN0_MIN_THRESHOLD H08
set CHAN1_MIN_THRESHOLD H20
set CHAN2_MIN_THRESHOLD H20
set CHAN3_MIN_THRESHOLD H20
set CHAN4_MIN_THRESHOLD H20
set CHAN5_MIN_THRESHOLD H20
set CHAN6_MIN_THRESHOLD H20
set CHAN7_MIN_THRESHOLD H20
set CHAN0_ADC_OFFSET H94
set CHAN1_ADC_OFFSET Hbc
set CHAN2_ADC_OFFSET He3
set CHAN3_ADC_OFFSET Hd6
set CHAN4_ADC_OFFSET Ha2
set CHAN5_ADC_OFFSET He2
set CHAN6_ADC_OFFSET Ha5
set CHAN7_ADC_OFFSET Hcf
set CHAN0_FULL_SCALE Hff
set CHAN1_FULL_SCALE Hff
set CHAN2_FULL_SCALE Hff
set CHAN3_FULL_SCALE Hff
set CHAN4_FULL_SCALE Hff
set CHAN5_FULL_SCALE Hff
set CHAN6_FULL_SCALE Hff
set CHAN7_FULL_SCALE Hff

# -----
## CARD [SerialNum=Pci9030-0 - bus 02 slot 0b device=9030 vendor=10b5 ]
# -----
CARD Pci9030-0 ON
set CHAN0_BIN0_LOW H0
set CHAN0_BIN0_HIGH H7f
set CHAN0_BIN1_LOW H80
set CHAN0_BIN1_HIGH Hff
set CHAN0_BIN2_LOW H100
set CHAN0_BIN2_HIGH H17f
set CHAN0_BIN3_LOW H180
set CHAN0_BIN3_HIGH H1ff
set CHAN0_BIN4_LOW H200
set CHAN0_BIN4_HIGH H27f
set CHAN0_BIN5_LOW H280
set CHAN0_BIN5_HIGH H2ff
set CHAN0_BIN6_LOW H300
set CHAN0_BIN6_HIGH H37f
set CHAN0_BIN7_LOW H380
set CHAN0_BIN7_HIGH H3ff
set CHAN1_BIN0_LOW H0
set CHAN1_BIN0_HIGH H7f
set CHAN1_BIN1_LOW H80
set CHAN1_BIN1_HIGH Hff
set CHAN1_BIN2_LOW H100

```



```
set CHAN1_BIN2_HIGH H17f
set CHAN1_BIN3_LOW H180
set CHAN1_BIN3_HIGH H1ff
set CHAN1_BIN4_LOW H200
set CHAN1_BIN4_HIGH H27f
set CHAN1_BIN5_LOW H280
set CHAN1_BIN5_HIGH H2ff
set CHAN1_BIN6_LOW H300
set CHAN1_BIN6_HIGH H37f
set CHAN1_BIN7_LOW H380
set CHAN1_BIN7_HIGH H3ff
set CHAN2_BIN0_LOW H0
set CHAN2_BIN0_HIGH H7f
set CHAN2_BIN1_LOW H80
set CHAN2_BIN1_HIGH Hff
set CHAN2_BIN2_LOW H100
set CHAN2_BIN2_HIGH H17f
set CHAN2_BIN3_LOW H180
set CHAN2_BIN3_HIGH H1ff
set CHAN2_BIN4_LOW H200
set CHAN2_BIN4_HIGH H27f
set CHAN2_BIN5_LOW H280
set CHAN2_BIN5_HIGH H2ff
set CHAN2_BIN6_LOW H300
set CHAN2_BIN6_HIGH H37f
set CHAN2_BIN7_LOW H380
set CHAN2_BIN7_HIGH H3ff
set CHAN3_BIN0_LOW H0
set CHAN3_BIN0_HIGH H7f
set CHAN3_BIN1_LOW H80
set CHAN3_BIN1_HIGH Hff
set CHAN3_BIN2_LOW H100
set CHAN3_BIN2_HIGH H17f
set CHAN3_BIN3_LOW H180
set CHAN3_BIN3_HIGH H1ff
set CHAN3_BIN4_LOW H200
set CHAN3_BIN4_HIGH H27f
set CHAN3_BIN5_LOW H280
set CHAN3_BIN5_HIGH H2ff
set CHAN3_BIN6_LOW H300
set CHAN3_BIN6_HIGH H37f
set CHAN3_BIN7_LOW H380
set CHAN3_BIN7_HIGH H3ff
set CHAN4_BIN0_LOW H0
set CHAN4_BIN0_HIGH H7f
set CHAN4_BIN1_LOW H80
set CHAN4_BIN1_HIGH Hff
set CHAN4_BIN2_LOW H100
set CHAN4_BIN2_HIGH H17f
set CHAN4_BIN3_LOW H180
set CHAN4_BIN3_HIGH H1ff
set CHAN4_BIN4_LOW H200
set CHAN4_BIN4_HIGH H27f
set CHAN4_BIN5_LOW H280
```

```
set CHAN4_BIN5_HIGH H2ff
set CHAN4_BIN6_LOW H300
set CHAN4_BIN6_HIGH H37f
set CHAN4_BIN7_LOW H380
set CHAN4_BIN7_HIGH H3ff
set CHAN5_BIN0_LOW H0
set CHAN5_BIN0_HIGH H7f
set CHAN5_BIN1_LOW H80
set CHAN5_BIN1_HIGH Hff
set CHAN5_BIN2_LOW H100
set CHAN5_BIN2_HIGH H17f
set CHAN5_BIN3_LOW H180
set CHAN5_BIN3_HIGH H1ff
set CHAN5_BIN4_LOW H200
set CHAN5_BIN4_HIGH H27f
set CHAN5_BIN5_LOW H280
set CHAN5_BIN5_HIGH H2ff
set CHAN5_BIN6_LOW H300
set CHAN5_BIN6_HIGH H37f
set CHAN5_BIN7_LOW H380
set CHAN5_BIN7_HIGH H3ff
set CHAN6_BIN0_LOW H0
set CHAN6_BIN0_HIGH H7f
set CHAN6_BIN1_LOW H80
set CHAN6_BIN1_HIGH Hff
set CHAN6_BIN2_LOW H100
set CHAN6_BIN2_HIGH H17f
set CHAN6_BIN3_LOW H180
set CHAN6_BIN3_HIGH H1ff
set CHAN6_BIN4_LOW H200
set CHAN6_BIN4_HIGH H27f
set CHAN6_BIN5_LOW H280
set CHAN6_BIN5_HIGH H2ff
set CHAN6_BIN6_LOW H300
set CHAN6_BIN6_HIGH H37f
set CHAN6_BIN7_LOW H380
set CHAN6_BIN7_HIGH H3ff
set CHAN7_BIN0_LOW H0
set CHAN7_BIN0_HIGH H7f
set CHAN7_BIN1_LOW H80
set CHAN7_BIN1_HIGH Hff
set CHAN7_BIN2_LOW H100
set CHAN7_BIN2_HIGH H17f
set CHAN7_BIN3_LOW H180
set CHAN7_BIN3_HIGH H1ff
set CHAN7_BIN4_LOW H200
set CHAN7_BIN4_HIGH H27f
set CHAN7_BIN5_LOW H280
set CHAN7_BIN5_HIGH H2ff
set CHAN7_BIN6_LOW H300
set CHAN7_BIN6_HIGH H37f
set CHAN7_BIN7_LOW H380
set CHAN7_BIN7_HIGH H3ff
set ACQ_TRIGGER_CNT H80
```

```
set CHAN0_INPUT_OFFSET Ha4
set CHAN1_INPUT_OFFSET Ha7
set CHAN2_INPUT_OFFSET Ha5
set CHAN3_INPUT_OFFSET Ha5
set CHAN4_INPUT_OFFSET H9c
set CHAN5_INPUT_OFFSET Ha4
set CHAN6_INPUT_OFFSET H9d
set CHAN7_INPUT_OFFSET Ha1
set CHAN0_INIT_THRESHOLD H40
set CHAN1_INIT_THRESHOLD H40
set CHAN2_INIT_THRESHOLD H40
set CHAN3_INIT_THRESHOLD H40
set CHAN4_INIT_THRESHOLD H40
set CHAN5_INIT_THRESHOLD H40
set CHAN6_INIT_THRESHOLD H40
set CHAN7_INIT_THRESHOLD H40
set CHAN0_MIN_THRESHOLD H20
set CHAN1_MIN_THRESHOLD H20
set CHAN2_MIN_THRESHOLD H20
set CHAN3_MIN_THRESHOLD H20
set CHAN4_MIN_THRESHOLD H20
set CHAN5_MIN_THRESHOLD H20
set CHAN6_MIN_THRESHOLD H20
set CHAN7_MIN_THRESHOLD H20
set CHAN0_ADC_OFFSET H87
set CHAN1_ADC_OFFSET H96
set CHAN2_ADC_OFFSET Hce
set CHAN3_ADC_OFFSET Hcf
set CHAN4_ADC_OFFSET Hff
set CHAN5_ADC_OFFSET Hc4
set CHAN6_ADC_OFFSET Hd0
set CHAN7_ADC_OFFSET H94
set CHAN0_FULL_SCALE Hff
set CHAN1_FULL_SCALE Hff
set CHAN2_FULL_SCALE Hff
set CHAN3_FULL_SCALE Hff
set CHAN4_FULL_SCALE Hff
set CHAN5_FULL_SCALE Hff
set CHAN6_FULL_SCALE Hff
set CHAN7_FULL_SCALE Hff

## *****
# Define GLOBAL definitions (to all cards)
## *****
global PULSE_TIMEOUT H6
global SAMPLE_TIME H28
global INT_REL_TIME H1
global ACQ_TIME H8000
global ACQ_MODE 0
global ACQ_TYPE 1
global ACQ_NUM_SAMPLES H0
```

References

Angenent, L.T.; Sung S., Raskin, L., 2002. Methanogenic population dynamics during start up of a full scale anaerobic sequencing batch reactor treating swine waste. *Water Res.*, 36(18), 762-770.

Bagatin, R.; Andriago, P.; Protto, L.; Meastri, F.; Di Muzio, F.; Masi, M.; Carraa, P., 1999. Fluid Dynamics of Gas-Liquid Airlift Reactors through CFD Packages. PVP, 397-1, Computational Technologies for Fluid/Thermal/Structural/Chemical Systems with Industrial Applications, ASME, 293-303.

Becker, S.; Sokolichin, A.; Eigenberger, G., 1994. Gas-Liquid Flow in Bubble Columns and Loop Reactors: Part II. Comparison of Detailed Experiments and Flow Simulations. *Chem. Eng. Sci.*, 49(24B), 5747-5762.

Bello-Mendoza, Ricardo; Sharratt, Paul N., 1998. Modeling the effects of imperfect mixing on the performance of anaerobic reactors for sewage sludge treatment. *Journal of Chemical Technology & Biotechnology*, 71(2), 121-130.

Ben-Hasson, R.M.; Ghaly, A.E.; Singh, R.K., 1985. Design and evaluation of no-mix energy efficient anaerobic digester. Proceedings, Annual Meeting, Canadian Society of Agricultural Engineering, June 23-27, Charlottetown, P.E.I.

Bhusarapu, Satish, 2005. Solids flow mapping in gas-solid risers. Ph.D. thesis, Washington University, St. Louis, MO, USA

Blazej, M.; Cartland Glover, G.M.C.; Generalis, S.C.; Markos, J., 2004a. Gas-liquid simulation of airlift bubble column reactor. *Chemical Engineering and Processing*, 43, 137-144.

Blazej, M.; Kisa, M.; Markos, J., 2004b. Scale influence on the hydrodynamics of an internal loop airlift reactor. *Chemical Engineering and Processing*, 43(12), 1519-1527.

CARPT Manual, 2005. Prepared by Chemical Reaction Engineering Laboratory (CREL), Washington University, St. Louis, MO, USA

Carroll, W.D.; Ross, R.D., 1984. A full scale comparison of confined and unconfined gaslift mixing systems in anaerobic digesters. *Sewage Sludge stabilization and disinfection, Wat. Res. Cent. Conf.* 1984, 146-157.

Casey, T.J., 1986. Requirements and methods for mixing un anaerobic digesters. *Anaerobic digestion of sewage sludge and organic agricultural wastes*, 90-103.

- Chen, T.; Chynoweth, D.P.; Biljetina, R., 1990. Anaerobic digestion of municipal solid waste in a nonmixed solids concentrating digester. *Appl. Biochem. Biotechnol.* 24/25, 533-544.
- Choi, K. H.; Chisti, Y.; Moo-Young, M., 1996. Comparative evaluation of hydrodynamic and gas-liquid mass transfer characteristics in bubble column and airlift slurry reactors. *Chemical Engineering Journal*, 62(3), 223-229.
- Chynoweth, D.P.; Turick, C.E.; Owens, J.M.; Jerger, D.E.; Peck, M.W., 1993. Biochemical methane potential of biomass and waste feedstocks. *Biomass and Bioenergy*, 5(1), 95-111.
- Cockx, A.; Line, A.; Roustan, M.; Do_Quang, J.; Lazarova, V., 1997. Numerical Simulation and Physical Modeling of the Hydrodynamics in an Air-Lift Internal Loop Reactor. *Chem. Eng. Sci.*, 52 (21/22), 3787-3792.
- Dague, R.R.; McKinney, R.E.; Pfeffer, J.T., 1970. Solids retention in anaerobic waste treatment systems. *J. Water Pollut. Control Fed.* 42 Part 2, R29-R46.
- Degaleesan, S., 1997. Fluid dynamic measurements and modeling of liquid mixing in bubble columns. D.Sc. Thesis, Washington University, St. Louis.
- Demirer, G. N.; Chen, S., 2004. Effect of retention time and organic loading rate on anaerobic acidification and biogasification of dairy manure. *Journal of Chemical Technology and Biotechnology*, 79(12), 1381-1387.
- Feitkenhauer, H.; Maleski, R.; Maerkl, H., 2003. Airlift-reactor design and test for aerobic environmental bioprocesses with extremely high solid contents at high temperatures. *Wat. Sci. Tech.*, 48(8), 69-77.
- Freitas, Carla; Fialova, Maria; Zahradnik, Jindrich; Teixeira, Jose A., 1999. Hydrodynamic model for three-phase internal- and external-loop airlift reactors. *Chemical Engineering Science*, 54(21), 5253-5258.
- Garcia-Calvo, E.; Leton, P.; Arranz, M. A., 1996. Theoretical prediction of gas holdup in bubble columns with Newtonian and non-Newtonian liquids. *Chemical Engineering Communications*, 143, 117-132.
- Garcia-Calvo, E.; Rodriguez, A.; Prados, A.; Klein, J., 1999. A fluid dynamic model for three-phase airlift reactors. *Chemical Engineering Science*, 54(13-14), 2359-2370.
- Gavrilescu, M.; Tudose, R. Z., 1998a. Concentric-tube airlift bioreactors Part I: Effects of geometry on gas holdup. *Bioprocess Engineering*, 19(1), 37-44.
- Gavrilescu, M.; Tudose, R. Z., 1998b. Concentric-tube airlift bioreactors Part II: Effects of geometry on liquid circulation. *Bioprocess Engineering*, 19(2), 103-109.

Ghosh, S., 1977. Anaerobic Digestion For Renewable Energy and Environmental Restoration. The 8th Intern. Conference on Anaerobic Digestion, Sendai International Center, Sendai, Japan, Ministry of Education Japan.

Glover, Cartland, G.M.C.; Blazej, M.; Generalis, S.C.; Markos, J., 2003. Three-dimensional gas-liquid simulation of airlift bubble column reactor. *Chemical papers*, 57(6), 387-392.

Gunaseelan, V. N., 1997. Anaerobic digestion of biomass for methane production: a review. *Biomass and Bioenergy*, 13(1/2), 83-114.

Heijnen, J. J.; Hols, J.; Van Der Lans, R. G. J. M.; Van Leeuwen, H. L. J. M.; Mulder, A.; Weltevrede, R., 1997. A simple hydrodynamic model for the liquid circulation velocity in a full-scale two- and three-phase internal airlift reactor operating in the gas recirculation regime. *Chemical Engineering Science*, 52(15), 2527-2540.

Hill, D.T., 1982. A comprehensive dynamic model for animal waste methanogenesis. *Trans. ASAE* 25(5), 1374-1380.

Ho, C.C.; Tan, Y.K., 1985. Anaerobic treatment of palm oil mill effluent by tank digesters. *J. Chem. Tech. Biotechnol.* 35B, 155-164.

Hoffmann, R., 2005. The effect of shear on the performance and microbial ecology of anaerobic digesters treating cow manure from dairy farms. MS thesis. Washington University, St. Louis, MO, USA.

Jakobsen, H.A.; Svendsen, H.F.; Hjarbo, K.W., 1993. On the prediction of local flow structure in internal loop bubble column reactors using a two-fluid model. *European Symposium on computer aided process design*, 7, 531-536.

James, S.; Wiles, C.; Swartzbaugh, J.; Smith, R., 1980. Mixing in large-scale municipal solid waste-sewage sludge anaerobic digesters. *Biotechnology and Bioengineering Symposium*, 10, 259-272.

Karim, K.; Hoffman, R.; Klasson, T.; Al-Dahhan, M.H.; 2005b. Anaerobic digestion of animal waste: Waste strength versus impact of mixing. *Bioresource Tech.*, 96(16), 1771-1781.

Karim, K., Klasson, T., Hoffman, R., Drescher, S.R., Depaoli, D.W., Al-Dahhan, M.H., 2005a. Anaerobic digestion of animal waste: effect of mixing. *Bioresource Tech.* 96(14), 1607-1612

Karim, Khursheed; Varma, Rajneesh; Vesvikar, Mehul; Al-Dahhan, M. H., 2004. Flow pattern visualization of a simulated digester. *Water Research*, 38(17), 3659-3670.

- Kennard, Malcolm; Janekeh, Massoud., 1991. Two- and three-phase mixing in a concentric draft tube gas-lift fermentor. *Biotechnology and Bioengineering*, 38(11), 1261-70.
- Klein, J.; Godo, S.; Dolgos, O.; Markos, J., 2001. Effect of gas-liquid separator in the hydrodynamics and circulation flow regimes in internal loop airlift reactors. *J. Chem Technol. Biotechnol.*, 76, 516-524.
- Klein, J.; Vicente, A.A.; Teixeira, J.A., 2003a. Hydrodynamics of a three-phase airlift reactor with an enlarged separator - application to high cell density systems. *Canadian Journal of Chemical Engineering*, 81(3-4), 433-443.
- Klein, J.; Vicente, A.A.; Teixeira, J.A., 2003b. Hydrodynamic considerations on optimal design of a three-phase airlift bioreactor with high solids loading. *Canadian Journal of Chemical Engineering*, 81(3-4), 433-443.
- Kojima, Hiromitsu; Sawai, Jun; Uchino, Hidetoshi; Ichige, Takakazu, 1999. Liquid circulation and critical gas velocity in slurry bubble column with short size draft tube. *Chemical Engineering Science*, 54(21), 5181-5185.
- Kontandt, H.G.; Roediger, A.G., 1977. Engineering operation and economics of methane gas production. In: Schlegel, H.G. and Barnea, J. (ed.), *Microbial energy conversion*. Pergamon Press, 379-392.
- Kuipers J.A.M.; van Swaaij, W.P.M., 1998. *Computational Fluid Dynamics Applied to Chemical Reaction Engineering*. *Advances in Chemical Engineering*, 24.
- Lee, L.; Chandrasekaran, B.; Hulme, I.; Kantzas, A., 2005. A Non-Invasive Hydrodynamic Study of Gas-Solid Fluidised Bed of Linear Low Density Polyethylene *CJChE*, 83(1), 119-126.
- Lee, S.R.; Cho, N.K.; Maeng, W.J., 1995. Using the pressure of biogas created during anaerobic digestion as the source of mixing power. *J. Ferment. Bioengng.*, 80(4), 415-417.
- Lu, Wen-Jang; Hwang, Shyh-Jye; Chang, Chun-Min., 1995. Liquid velocity and gas holdup in three-phase internal loop airlift reactors with low-density particles. *Chemical Engineering Science*, 50(8), 1301-10.
- Luo, Hu Ping, 2005. Analyzing and modeling of airlift photobioreactors for microalgal and cyanobacteria cultures. Ph.D. thesis, Washington University, St. Louis, MO, USA
- Lusk, P., 1998. *Methane Recovery from Animal Manures: A Current Opportunities Casebook*. 3rd Edition. NREL/SR-580-25145. Golden, CO: National Renewable Energy Laboratory. Work performed by Resource Development Associates, Washington, DC.

- McNeil Tech. Inc., 2005. Colorado Agriculture IOF Technology Assessments: Anaerobic Digestion. Prepared for Colorado Agriculture IOF Technology Assessments: Anaerobic Digestion, September 2005.
- Merchuk, J. C.; Ladwa, N.; Cameron, A.; Bulmer, M.; Pickett, A., 1994. Concentric-tube airlift reactors: effects of geometrical design on performance. *AIChE Journal*, 40(7), 1105-17.
- Merchuk, J.C., 2003. Airlift bioreactors: review of recent advantages. *Can. J. Chem. Eng.*, 81, 324-337.
- Merchuk, J.C.; Gluz, M., 1999. Bioreactor, Airlift reactors from *The encyclopedia of bioprocess technology: fermentation, biocatalysis, and bioseparation*. Wiley, NY, 320-353.
- Merchuk, J.C.; Seigel, M.H., 1988. Air-lift reactors in chemical and biological technology. *J. Chem. Technol. Biotechnol.*, 41, 105-120.
- Merchuk, J.C.; Shechter, R., 2003. Modeling of an airlift reactor with floating solids for wastewater treatment. *CJChE*, 81, 900-905.
- Merchuk, J.C.; Stein, Y., 1981. Local holdup and liquid velocity in airlift reactors. *AIChE J.*, 27, 377-381.
- Merchuk, Jose C.; Ladwa, Narendra; Cameron, Angus; Bulmer, Marc; Berzin, Isaac; Pickett, Andy M., 1996. Liquid flow and mixing in concentric tube air-lift reactors. *Journal of Chemical Technology & Biotechnology*, 66(2), 174-182.
- Meynell, P.J., 1976. *Methane: Planning a Digester*. Prism Press, London, 55-57.
- Miron, A. Sanchez; Garcia, M.-C. Ceron; Camacho, F. Garcia; Grima, E. Molina; Chisti, Y., 2004. Mixing in bubble column and airlift reactors. *Chemical Engineering Research and Design*, 82(A10), 1367-1374.
- Monteith, H.D.; Stephenson, J.P., 1981. Mixing efficiencies in full-scale anaerobic digesters by tracer methods. *J. WPCF* 53, 78-84.
- Morgan, J.W.; Evison, L.M.; Forster, C.F., 1991. Changes to the microbial ecology in anaerobic digesters treating ice cream wastewater during start-up. *Water Research*, 25(6), 639-53.
- Morgan, P.F.; Neuspiel, P.J., 1958. Environmental control of anaerobic digestion with gas diffusion. In: McCabe, J. and Eckenfelder, W.W. (ed.), *Biological treatment for sewage and industrial wastes*, v2, Reinhold, New York.

- Moser, M.A.; Roos, K.F., 1997. AgSTAR Program: Three commercial-scale anaerobic digester systems for animal waste. Third Biomass Conference of the Americas, Montreal, Quebec, 2, 1221-1227.
- Mudde, R. F.; van den Akker, 2001. Two-Fluid Model Simulations of an Internal Airlift reactor. PVP-Vol. 424-1, Computational Technologies for Fluid/ Thermal/ Structural/ Chemical systems with Industrial Applications, Vol. 1, 101-108.
- Nielsen, J.; Villadsen, J., 1992. Modelling of Microbial Kinetics. Chem. Eng. Sci. 47, 4225-4276.
- Novica, Rados, 2003. Slurry bubble column hydrodynamics. Ph.D. thesis, Washington University, St. Louis, MO, USA
- Oey, R. S.; Mudde, R. F.; Portela, L. M.; van den Akker, H. E. A., 2001. Simulation of a slurry airlift using a two-fluid model. Chemical Engineering Science, 56(2), 673-681.
- Oey, R. S.; Mudde, R. F.; van den Akker, 2003a. Numerical Simulations of an Oscillating Internal-loop Airlift Reactor. The Can. J. Chem. Eng., 81, 684-691.
- Oey, R. S.; Mudde, R. F.; van den Akker, H. E. A., 2003b. Sensitivity study on interfacial closure laws in two-fluid bubbly flow simulations. AIChE Journal, 49(7), 1621-1636.
- Parkin, G.F.; Owen, W.F., 1986. Fundamentals of anaerobic digestion of wastewater sludges. J. Env. Engg. 112(5), 867-921.
- Petersen, Erin E.; Margaritis, Argyrios, 2001. Hydrodynamic and mass transfer characteristics of three-phase gas-lift bioreactor systems. Critical Reviews in Biotechnology, 21(4), 233-294.
- Pierkiel, A.; Lanting, J., 2004. The effect of shear power on anaerobi sewage sludge digestion: a pilot study. Anaerobic digestion 2004, 10th World congress, Montreal, Canada, Vol. 2, 851-855.
- Pironti, F. F.; Medina, V. R.; Calvo, R.; Saez, A. E., 1995. Effect of draft tube position on the hydrodynamics of a draft tube slurry bubble column. Chemical Engineering Journal, 60(1-3), 155-60.
- Rammohan, A.; Kemoun, A.; Al-Dahhan, M.; Dudukovic, M.; Larachi, F., 2001. CARPT dynamic bias studies: evaluation of accuracy of position and velocity measurements. Recents Progres en Genie des Procedes, 15(79), 59-67.
- Rammohan, Aravind, 2003. Characterization of single and multiphase flows in stirred tank reactors. Ph.D. thesis, Washington University, St. Louis, MO, USA.

- Ranade, V.V., 2002. Computational Flow Modeling for Chemical Reactor Engineering”, Process Systems Engineering, 5, Academic Press.
- Rousseau, I. ; Bu’Lock, J.D., 1980. Biotechnol. Lett., 2(11), 475.
- Saez, A. Eduardo; Marquez, Marco A.; Roberts, George W.; Carbonell, Ruben G., 1998. Hydrodynamic model for gas-lift reactors. AIChE Journal, 44(6), 1413-1423.
- Sawyer, C.N.; Grumbling, A.M., 1960. Fundamental consideration in high-rate digestion. Inc. Sew. Eng. Div. ASCE, 86-92.
- Schlattmann, M.; Speckmaier, M.; Lebhun, M.; Gronauer, A., 2004. Comparison of anaerobic digestion in laboratory, pilot and full scale fermenters loaded with agricultural substrates. Proc. Anaerobic Digestion 2004 10th World Congress Montreal, Canada 3, 1828-1832.
- Siegel, M. H.; Robinson, C. W., 1992. Applications of airlift gas-liquid-solid reactors in biotechnology. Chemical Engineering Science, 47(13-14), 3215-29.
- Smith, L.C.; Elliot, D.J.; James, A., 1996. Mixing in upflow anaerobic filters and its influence on performance and scale-up. Water Research, 30(12), 3061.
- Sokolichin, A.; Eigenberger, G.;Lapin, A.; 2004. Simualtion of Buoyancy Driven Bubbly Flow: Established Simplifications and Open Questions. AIChE J., 50(1), 24-45.
- Speece, R.E., 1996. Anaerobic Biotechnology for Industrial Wastewaters. Vanderbilt University, Arachae Press.
- Stroot, P.G.; McMohan, K.D.; Mackie, R.I.; Raskin, L., 2001. Anaerobic codigestion of municipal solid waste and biosolids under various mixing conditions—I. Digester performance. Water Res. 67(3), 294-301.
- Sun, S.; Bao, X.; Liu, C.; Wei, W., 2005. Hydrodynamic model for three-phase annulus airlift reactors. Ind. Eng. Chem. Res. (2005), 44(19), 7550-7558.
- Svendsen, H.F.; Jakobsen, H.A.; Torvik, R., 1992. Local Flow Structures in Internal Loop and Bubble Column Reactors. Chem. Eng. Sci., 47 (13/14), 3297-3304.
- Tilche, A.; Vieira, S.M.M., 1991. Discussion report on reactor design of anaerobic filters and sludge bed reactors. Wat. Sci. Tech., 24(8), 193-206.
- Trilleros, D.A.; Diaz, R.; Redendo, R., 2005. Three phase airlift internal loop reactor: correlations for predicting the main fluid dynamic parameters. J Chem. Tech. Biotech., 80, 515-522.

US EPA, 1979. Process design manual for sludge treatment and disposal. EPA 625/1-79-011, Cincinnati, OH.

USDA, <http://www.scorecard.org/env-releases/aw/us.td>, 2003.

van Baten, J.M.; Ellenberger, J.; Krishna, R., 2003b. Hydrodynamics of Internal Air-Lift Reactors: experiments versus CFD simulations. *Chem. Eng. and Proc.*, 42, 733-742.

van Baten, J.M.; Ellenberger, J.; Krishna, R., 2003. Using CFD to Describe the Hydrodynamics of Internal Air-Lift Reactors. *The Can. J. of Chem. Eng.*, 81, 660-668.

Van Benthum, W. A. J.; Van der Lans, R. G. J. M.; Van Loosdrecht, M. C. M.; Heijnen, J. J., 1999. Bubble recirculation regimes in an internal-loop airlift reactor. *Chemical Engineering Science*, 54(18), 3995-4006.

Vesvikar, M.S.; Al-Dahhan, M.H., 2005. Flow pattern visualization in a mimic anaerobic digester using CFD. *Biotech. Bioengg.*, 89(6), 719-732.

Vial, C.; Bendjaballah-Lalaoui, N.; Poncin, S.; Wild, G.; Midoux, N., 2003. Comparison, combination and validation of measuring techniques for local flow and turbulence analysis in bubble columns and airlift reactors. *Can. J. Chem. Eng.*, 81, 741-755.

Wang, Yen, 1969. Handbook of radioactive nuclides. The Chemical Rubber Co., Ohio, USA

Wei, Chaohai; Xie, Bo; Xiao, Hongliang; Wang, Dongsheng, 2000. Volumetric mass transfer coefficient of oxygen in an internal loop airlift reactor with a convergence-divergence draft tube. *Chemical Engineering & Technology*, 23(7), 597-603.

Weiland, P.O., 1984. *Ger. Chem. Eng.*, 7, 374.

Wen, J.P.; Jia, X.Q.; Feng, W., 2005. Hydrodynamic and mass transfer of gas-liquid-solid three phase internal loop airlift reactors with nanometer solid particles. *Chem. Eng. Technol.*, 28(1), 53-60.

Vita

Mehul S. Vesvikar

Date of Birth	August, 19 th 1976
Place of Birth	Mumbai, India
Degrees	B.E., Chemical Engineering, May 1998 M.Chem.Engg., Chemical Engineering, August 2001 D.Sc., Chemical Engineering, August 2006

Publications

- Mehul S. Vesvikar, Borole A., Klasson T., Karim K., Al-Dahhan M.H. 2005. Performance study of a pilot scale anaerobic digester and comparison with laboratory scale units. Sent for review to *Bioresource Technology*.
- Mehul S. V. and Al-Dahhan M.H. 2005. Flow pattern visualization in a mimic anaerobic digester using CFD. *Biotechnology and Bioengineering*, 89(6), 719-732.
- Mehul S. Vesvikar, Varma R., Karim K., Al-Dahhan M.H. 2005. Flow pattern visualization in a mimic anaerobic digester: Experimental and Computational Studies. *Water Science and Technology*, 52(1-2), 537-543.
- Mehul S. Vesvikar, Varma R., Karim K., Al-Dahhan M.H. 2005. Flow pattern visualization in a mimic anaerobic digester: Experimental and computational studies. *Anaerobic Digestion 2004 Proceedings*, Vol 1, 123-128.
- Hoffman R., Varma R., Vesvikar M., Karim K., Al-Dahhan M.H., Angenent L.T. 2004. Effect of shear rate on hydrodynamics, performance, and microbial community dynamics for an anaerobic digester treating cow waste. *Anaerobic Digestion 2004 Proceedings*, Vol 3, 1755.
- Karim K., Varma R., Vesvikar M. and Al-Dahhan M. H. 2004. Flow pattern visualization of a simulated digester. *Water Research*, **38**(17), 3659-3670.
- Mehul S. Vesvikar, Roy S., Ramachandran P.A., Dudukovic M.P. 2003. Modeling of solid liquid circulating fluidized beds for alkylation reactions. *AIChE, Sixth international conference of refinery and second international aromatics proceedings*, 447-455.

Proceedings and Presentations

Mehul S Vesvikar, and Al-Dahhan M.H., Effect of mixing and scale on the performance and hydrodynamics of anaerobic digesters, Bioenergy I, 2006, Tomar, Portugal.

Mehul S. Vesvikar, and Al-Dahhan M.H., Effect of mixing and scale on the performance of anaerobic digesters, AIChE Annual meeting, 2005, Cincinnati, OH.

Mehul S. Vesvikar, Al-Dahhan M.H., Effect of mixing and scale on the performance of anaerobic digesters. MAEEC meeting, Sept. 2005, Washington University in St. Louis, MO.

Mehul S. Vesvikar, Varma R., Karim K., Al-Dahhan M.H., Flow pattern visualization in a mimic anaerobic digester: Experimental and Computational Studies. Anaerobic Digestion 2004, 10th World Congress, Montreal, Canada.

Mehul S. Vesvikar, Al-Dahhan M.H., Flow pattern visualization in a mimic anaerobic digester using CFD. AIChE Annual meeting, 2003, San-Francisco, CA.

Mehul S. Vesvikar, Varma R., Karim K., Al-Dahhan M.H., Flow pattern visualization in a mimic anaerobic digester: Experimental and computational studies, AIChE Annual meeting, 2003, San-Francisco, CA.

Mehul S. Vesvikar and Muthanna Al-Dahhan, Flow pattern visualization in a mimic anaerobic digester using CFD. Poster presentation, Computational Fluid Dynamics in Chemical Reaction Engineering III, May 25-30, 2003, Davos, Switzerland.

August 2006

Short Title: Design of Anaerobic Digesters

Vesvikar M.S., D.Sc., 2006